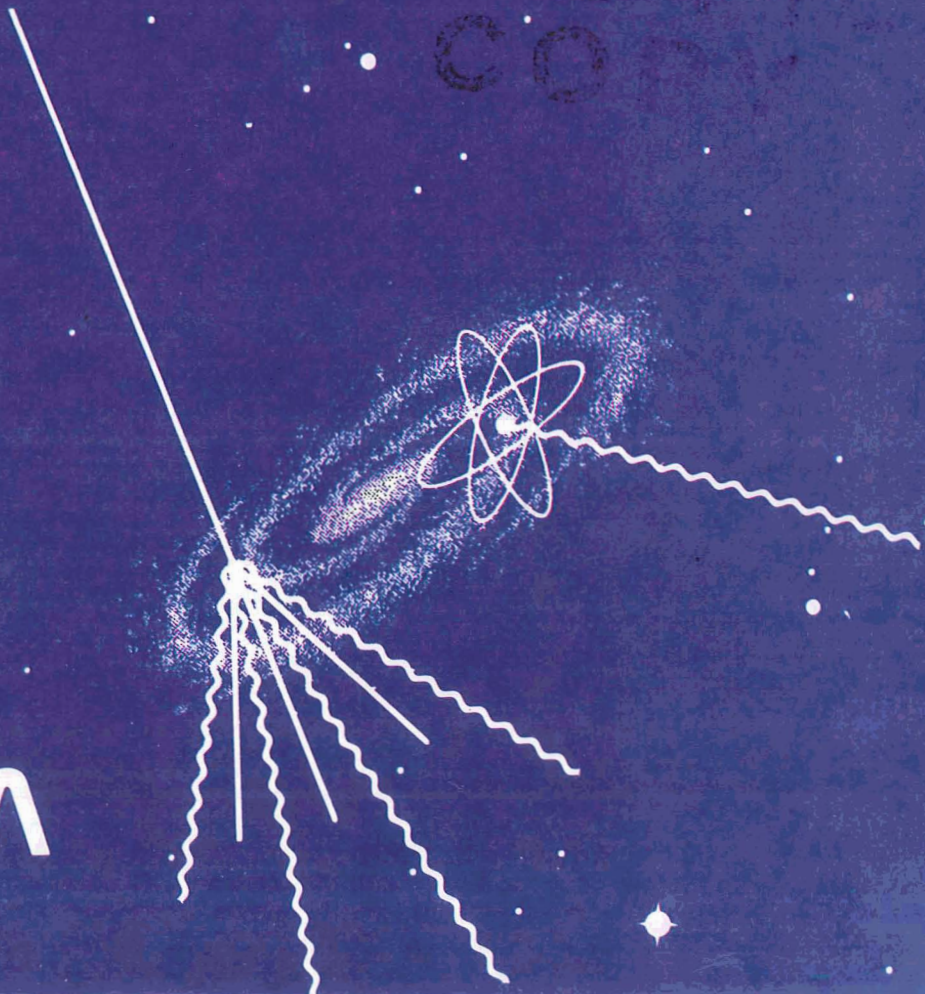


# GAMMA RAY ASTROPHYSICS

New Insight  
into the Universe

CASE FILE  
COMPILED

NASA



**GAMMA RAY ASTROPHYSICS**  
New Insight into the Universe

NASA SP-453

**GAMMA RAY ASTROPHYSICS**  
New Insight into the Universe

Carl E. Fichtel and Jacob I. Trombka  
*NASA Goddard Space Flight Center*

**NASA** Scientific and Technical Information Branch 1981  
National Aeronautics and Space Administration  
Washington, DC

---

For sale by the Superintendent of Documents  
U.S. Government Printing Office, Washington, D.C. 20402  
Library of Congress Catalog Card Number 81-600116



## Foreword

Our aim in writing this book on the new field of  $\gamma$ -ray astronomy is to provide a text which describes the astrophysical significance of these highest energy celestial photons, and to assemble in one place a treatment on  $\gamma$ -rays emitted from bodies in the solar system, from within our galaxy, and from beyond our galaxy. The special importance of  $\gamma$ -ray astronomy has long been realized by astronomers and physicists, and theorists have pursued many aspects of this field in some detail. Hence, it is possible to describe the significance of several problems in  $\gamma$ -ray astrophysics and discuss the potential implications of anticipated results, as well as existing ones.

Gamma ray astronomy has already yielded several surprises, including  $\gamma$ -ray bursts of unknown origin and intense pulsed  $\gamma$ -radiation from radio pulsars. Not only was the strong pulsed radiation a surprise, but in at least one case the phase is quite different from that in the radio range. Further there are observed  $\gamma$ -ray emitting objects for which the originating mechanism can only be determined with certainty after improved measurements are made.

This book is intended for those in astrophysics who wish to have the opportunity to learn more about the evolving field of  $\gamma$ -ray astronomy and its relationship to the high energy, evolutionary processes occurring in the universe. We have assumed that the readers will have had basic undergraduate courses in physics, including electromagnetic, atomic, and nuclear theory, and will be familiar with the rudiments of astronomy. We have attempted to write those portions where reference to the content of more advanced astronomy and physics courses is appropriate in such a way that the general flow of thought will not be interrupted in a significant way for readers unfamiliar with the details of the particular theories involved, yet those with a full understanding of the theories will see the validity and qualifications clearly.

We considered whether to discuss the  $\gamma$ -ray production and interaction processes together near the beginning of the book or to describe each as it occurred in a development built around astrophysical subjects. After considerable thought and the experience of teaching courses in X-ray and  $\gamma$ -ray astrophysics and

planetary physics, the latter approach was chosen. This decision resulted partially from the natural development of the theory in terms of specific applications, partially from the assumption that the readers have already had the basic physics and astronomy background, and partially from what appears to be the students enthusiasm and our own for studying the astrophysical phenomena under consideration and, therefore, allowing the needed supporting calculations to be derived or introduced as they are required.

We have left to the end of the book a general discussion of the experimental aspects of the field which, for the most part, seem best treated together, separately from the development of the astrophysical aspects of  $\gamma$ -ray astronomy.

The present time seems to be particularly appropriate for a new book on  $\gamma$ -ray astrophysics in view of the existing pause between the satellite and other experiments of the 1970's whose results have formed the foundation for this field and the major advances that should occur in the late 1980's. Also, as noted earlier, the relevant theoretical work is at hand so that meaningful discussions of the results and future expectations are possible.

This book would not have been possible without the cooperation of a large number of individuals. We gratefully acknowledge the use of information supplied to us by several scientists before it appeared in the open literature. We would especially like to acknowledge the following individuals for their help: C. Andre of the Smithsonian Institution; J. Arnold of the University of California, San Diego; E. Chupp of the University of New Hampshire; J. Lapidus of the National Institutes of Health; A. Metzger of the Jet Propulsion Laboratory; R. Reedy of the Los Alamos Scientific Laboratory; G. Steigman of the Bartol Research Foundation; and T. Weekes of the Mount Hopkins Observatory; A. Opp of NASA Headquarters; D. Bertsch, C. Crannell, R. Hartman, D. Kniffen, J. O'Keefe, D. Thompson; and L. Yin of the Goddard Space Flight Center; for their supplying special materials or critically reviewing the text; R. Tanner of the Goddard Space Flight Center and Eileen Sapcaru of the Systems and Applied Sciences Corporation for their valuable efforts in scientific editing; Elaine Brown, Candy Clark, Rose Ramberg, Teri Wernick, and especially Jaci Mills for their patience and

good humor in typing the manuscript; David Okamoto and John Mathes for preparing a number of the graphs and patiently reviewing the nuclear tables. Our special thanks are given to J. Brandt and F. McDonald of the Goddard Space Flight Center and A. Opp and W. Quaide for their interest and support of this work. We wish also to thank Elsie Trombka for her cheerfulness and help over this trying period of our writing this book.



# Contents

Chapter

## PART I - INTRODUCTION

1	GAMMA RAY ASTRONOMY IN PERSPECTIVE . . .	3
---	--	---

## PART II - THE SOLAR SYSTEM

2	GAMMA RAY OBSERVATIONS OF THE SOLAR SYSTEM . . . . .	19
	Introduction . . . . .	19
	Models of Solar System Evolution. . . . .	20
	Solar System Gamma Ray Astronomical Observations . . . . .	21
3	PLANETS, COMETS, AND ASTEROIDS. . . . .	25
	Introduction . . . . .	25
	Interaction Processes. . . . .	26
	Primary and Secondary Galactic Cosmic Ray Interactions . . . . .	33
	Experimental Results . . . . .	49
4	SOLAR OBSERVATIONS . . . . .	67
	Introduction . . . . .	67
	Interaction Processes. . . . .	68
	Experimental Results . . . . .	86

Chapter

PART III – THE GALAXY

5	THE INTERSTELLAR MEDIUM AND GALACTIC STRUCTURE . . . . .	99
	Introduction . . . . .	99
	Interaction Processes . . . . .	99
	Galactic Matter Distribution . . . . .	107
	Galactic Cosmic Ray Distribution . . . . .	110
	Current Gamma Ray Results and Their Interpretation . . . . .	113
6	COMPACT OBJECTS . . . . .	131
	Neutron Stars and Pulsars . . . . .	132
	Supernovae . . . . .	140
	Black Holes . . . . .	143
	Other High Energy Gamma Ray Sources . . . . .	146
	Low Energy Gamma Ray Bursts . . . . .	148

PART IV – EXTRAGALACTIC RADIATION

7	GALAXIES . . . . .	165
	Normal Galaxies . . . . .	165
	Introduction to Active Galaxies . . . . .	168
	Seyfert Galaxies . . . . .	171
	Radio Galaxies . . . . .	173
	Quasars . . . . .	174
	BL Lacertae Objects . . . . .	178
	Concluding Remarks . . . . .	180
8	COSMOLOGY . . . . .	187
	Introduction . . . . .	187
	Diffuse Radiation . . . . .	189

Chapter		
	The Values of $H_0$ and $q_0$ .....	195
	Matter-Antimatter Symmetry or Asymmetry .....	197
9	DIFFUSE RADIATION .....	203
	Introduction .....	203
	Observations .....	203
	Possible Contributors to the Diffuse Radiation .....	208
	Summary .....	219

#### PART V - INSTRUMENTATION

10	GAMMA RAY INTERACTION PROCESSES .....	229
	Introduction .....	229
	Photoelectric Effect and Fluorescence Radiation .....	232
	Pair Production and Annihilation Radiation .....	233
	Compton Scattering .....	242
	Electron Leakage and Bremsstrahlung .....	244
11	DETECTORS FOR ENERGIES LESS THAN 10 MeV .....	247
	Introduction .....	247
	Properties of Detectors .....	248
	Detector Response to Monoenergetic Radiation .....	264
	Detector Efficiency .....	274
	Detector Flight Systems .....	287

Chapter

12	DETECTORS FOR ENERGIES GREATER THAN 10 MeV .....	305
	Introduction and History .....	305
	The High Energy Gamma Ray Interaction.....	312
	Experimental Approach .....	315
	Angular Resolution.....	324
	Energy Resolution.....	329
	Instrument Performance and Data Analysis.....	331
13	ANALYSIS OF OBSERVATIONAL SPECTRA .....	337
	Introduction .....	337
	General Formulation.....	337
	Calculation of Errors.....	341
	Methods of Solution .....	344
	Compensation for Gain Shift and Zero Drift .....	346
	Analysis of Mixture of Discrete Lines and Continuum .....	349
	Analysis of High Energy Resolution Discrete Line Spectra .....	352
	Sources of Gamma Ray Background .....	356

PART VI - THE FUTURE

14	PROSPECTS FOR GAMMA RAY ASTRONOMY ...	385
	LIST OF SYMBOLS .....	391
	SUBJECT INDEX .....	393

# **PART I**

# **INTRODUCTION**

## *Chapter 1*

### *Gamma Ray Astronomy in Perspective*



# Chapter 1

## Gamma Ray Astronomy in Perspective

As we begin the study of gamma ray (hereafter  $\gamma$ -ray) astronomy and the astrophysical phenomena whose secrets these highest energy photons best reveal, it is important to remember that throughout most of history our view of the heavens was restricted to the visible portion of the electromagnetic spectrum. Our concept of the universe even now is strongly influenced by knowledge gained from this very important, but quite small wavelength band. Many major advances in our understanding of the universe have come in this century as optical telescopes have grown larger. For example, in the 1920's, it became clear that many galaxies beyond our own exist and that the Sun is not even at the center of our galaxy, but is in fact far from the galactic center. These findings destroyed the prevalent belief that our solar system was the center of the universe. Soon after the discovery of the existence of other galaxies, of which there are now known to be billions, it was found that they are systematically receding from each other. This discovery led to the present "big bang" theory of the universe. It was further realized that our Sun is a rather ordinary star and that many galaxies release far more energy than our own.

Still, our present knowledge of the universe would be much more restricted if the visible wavelength range had remained the sole source of information. Many phenomena can be understood or even revealed only by the investigation of emission in other parts of the electromagnetic spectrum. The first region of the spectrum beyond the optical to be explored was the radio range.

Although radio emission from the galaxy was detected in the 1930's, it was not until the 1950's that radio astronomy began to have a major impact. Studies of the 21 cm line, resulting from the hyperfine splitting of the ground state of atomic hydrogen, produced the first picture showing that our galaxy has a spiral structure.

The 21 cm line emission, which reveals the galactic atomic hydrogen distribution, and the continuum radio emission generally accepted to be synchrotron radiation which indicates the presence and distribution of relativistic electrons, are two examples of astrophysical information to come from a wavelength region outside the familiar visible one.

As a result of the advent of the space age which permitted instruments to be carried above the Earth's atmosphere, most of the remainder of the electromagnetic spectrum has now been examined, at least in a preliminary way. Some portions, such as the ultraviolet, have been extensively studied. Studies in the infrared have expanded our knowledge of molecules in interstellar space, and X-ray observations have revealed much about the hotter regions to be studied in astrophysics.

Gamma ray astronomy is the last major wavelength range to yield its wealth of information. This late development grew from a combination of factors including the need to place  $\gamma$ -ray telescopes above the Earth's atmosphere, the requirement to develop rather complex instruments, and the relatively low intensity of  $\gamma$ -ray photons particularly in relation to the charged particle cosmic ray intensity rather than from a failure of scientists to realize its unique and significant potential contributions. (Even though the photon intensity is low, the energy emitted in the  $\gamma$ -ray range may be, and in several cases is, quite high because each photon carries a large amount of energy and the  $\gamma$ -ray frequency range is very broad.)

There are several aspects of the universe to which  $\gamma$ -ray astronomy speaks more clearly than observations at other wavelengths, and for some astrophysical studies  $\gamma$ -rays carry unique information about the source. Gamma ray astronomy permits the direct study of the largest transfers of energy occurring in astrophysical processes, including rapid expansion processes, explosions, high energy particle acceleration, gravitational accretion onto superdense objects, the fundamental process of the

building of the elements, and even particle-antiparticle annihilation, should antimatter be sufficiently abundant anywhere. Recently synthesized nuclear material can reveal its presence through the emission of characteristic  $\gamma$ -ray lines from certain excited nuclei. The nucleonic cosmic rays, representing one of the three approximately equal expansion pressures (the others resulting from the magnetic fields and the kinetic motion of matter) in the galaxy, reveal themselves uniquely through the high energy  $\gamma$ -rays emitted by the  $\pi^0$  mesons which are formed in nuclear interactions between cosmic rays and interstellar matter. High energy cosmic ray electrons reveal themselves through interactions with matter and photons. The region around a black hole is predicted to emit very characteristic  $\gamma$ -rays, and the death of a black hole should reveal itself with the emission of a very specific type of  $\gamma$ -ray burst. Matter-antimatter annihilation produces another specific type of  $\gamma$ -ray spectrum.

Gamma ray astronomical observations also find important applications in studies of the evolution of our solar system, the nature of high energy processes in the Sun's atmosphere, and their relation to the basic problems of solar activity. A knowledge of the overall elemental composition of a given body can be related to the mechanisms of condensation and accumulation of materials from the primordial solar nebula. Analyses of characteristic X-rays and  $\gamma$ -rays from planetary surfaces can be used to infer global distribution of major and, in some cases, minor and trace elements.

Another attractive feature of  $\gamma$ -ray astronomy is that the universe is largely transparent to  $\gamma$ -rays. They can reach the solar system from the galactic center, distant parts of the universe, and dense regions near the centers of active galaxies—regions which cannot be viewed in the optical or low energy X-ray region. However, in contrast to optical photons which penetrate easily through the Earth's atmosphere, only the total amount of matter and not its form is relevant for  $\gamma$ -ray interactions. Thus, for example, the Earth's atmosphere has too much total matter for  $\gamma$ -rays to reach the Earth's surface. (It is primarily the dust of interstellar space which absorbs the optical photons in the galactic disk.) Further, cosmic ray interactions in the upper atmosphere produce  $\gamma$ -rays copiously, creating an undesirable background and adding to the need to place  $\gamma$ -ray detectors above the

Earth's atmosphere. It is also necessary to have the  $\gamma$ -ray telescope in a region of space where the particle radiation is low. Hence, a satellite orbit below the charged particles trapped in the geomagnetic field of the Earth is desired.

Once these difficulties are removed, the universe is found to be marvelously clear when viewed in the  $\gamma$ -ray frequency range. A more specific illustration of the penetrating power of this radiation is the following: a high energy  $\gamma$ -ray passing through the diameter of the central plane of the galactic disk has about a 1 percent chance of interacting, for a typical path. By contrast an optical photon can only penetrate about one-tenth the distance from the galactic center to the Earth in the central plane of the disk. A high energy  $\gamma$ -ray also can typically travel to the Earth from the outer part of the universe with less than a 1 percent chance of interacting; in this case there is a red shift. This remarkable window extends from a few times  $10^7$  eV, below which it begins to close slowly as the energy decreases so that as the X-ray region is reached the distant parts of the galaxy are quite opaque, to  $10^{15}$  eV, at which point there begins a 1- to 2-decade region in energy where in  $\gamma$ -ray interactions with the blackbody radiation are important.

The scientific potential of  $\gamma$ -ray astronomy and its direct relationship to the highest energy processes occurring in astrophysics was recognized by theoreticians well before fruitful experiments became possible. As early as 1952, Hayakawa (1952) noted the effect of meson-producing nuclear interactions between cosmic rays and interstellar gas. In the same year Hutchinson (1952) discussed the production of bremsstrahlung radiation by cosmic rays. Even earlier, Feenberg and Primakoff (1948) examined the astrophysical significance of the Compton effect in regard to cosmic ray electrons. Morrison (1958) wrote a very extensive article describing many of the  $\gamma$ -ray production processes which are still thought to be important in astrophysics. Colgate and White (1966) proposed the possibility of a  $\gamma$ -ray burst in association with a supernova explosion, and several papers discussed the importance of  $\gamma$ -ray lines in studying rapid nucleosynthesis in supernovae. Recently, as the first results on galactic  $\gamma$ -rays became available, there has been a great expansion of the number of theoretical papers on the interrelationship between galactic structure, cosmic ray origin, cosmic ray pressure in the galaxy, and  $\gamma$ -rays.

As has been noted, the experimental development of  $\gamma$ -ray astronomy has been slow. Several experimental attempts to detect  $\gamma$ -rays with less complex instruments flown on balloons in the years before 1960 were unsuccessful. The failure to obtain positive results led experimenters to develop the larger, more sophisticated detector systems of the 1960's and fly them on the larger, high altitude balloons that were being developed during this period. The increase in size was dictated by the realization that the intensities of  $\gamma$ -rays were quite low, and the increased sophistication was demanded both by the need to detect the rare  $\gamma$ -rays in a high background, primarily of charged cosmic ray particles, and by the inherent nature of  $\gamma$ -ray interactions.

The first certain detection of high energy celestial  $\gamma$ -rays was made by Kraushaar et al. (1972), who observed  $\gamma$ -rays with energies above 50 MeV from the galactic disk, with a peak intensity toward the galactic center. However, the limited spectral and spatial resolution of this pioneering experiment left many unanswered questions. About the same time a few confirmed positive results, mostly related to a general enhancement in the galactic center region, were obtained with high altitude balloon experiments.

On November 15, 1972, a  $\gamma$ -ray telescope with approximately 12 times the sensitivity of the third Orbiting Solar Observatory (OSO-3) and angular resolution of a few degrees was launched on the second Small Astronomy Satellite (SAS-2). This instrument provided results which have led to a much better picture of the  $\gamma$ -ray sky, including fair detail on the galactic plane (e.g., Fichtel et al., 1975; Bignami et al., 1979). Another  $\gamma$ -ray instrument with approximately equal sensitivity and angular resolution, Cosmic Ray Satellite (COS-B), was launched on August 8, 1975, and provided information which further expanded our knowledge (e.g., Mayer-Hasselwander et al., 1980).

With the results from these satellites,  $\gamma$ -ray astrophysics proceeded from the discovery phase to the exploratory phase. These data showed the rich character of the galactic plane diffuse emission with its potential for the study of the forces of change in the galaxy, the study of the origin and expansion of the cosmic ray gas, and the study of the galactic structure. When examined in detail the longitudinal and latitudinal distribution appear generally correlated with galactic structural

features, including spiral arm segments. With the observations of discrete sources, some of which are associated with supernovae and pulsars and others apparently not correlated with radiation at other wavelengths, point-source  $\gamma$ -ray astronomy has also begun. It offers the opportunity for obtaining direct information on the processes occurring in neutron stars, black holes, pulsars, and supernovae. As an example the energy emitted in  $\gamma$ -rays ( $E > 50$  MeV) from the pulsar PSR 0531+21 in the Crab nebula exceeds  $10^{34}$  ergs  $s^{-1}$ —an impressive amount when scientists realize that it almost certainly comes from charged particles accelerated to relativistic energies. There have also been some surprises. The Vela pulsar, PSR 0833-45, exhibits two pulses in the  $\gamma$ -ray region, as opposed to one in the radio region, neither of them in phase with the radio pulse. One of the strongest  $\gamma$ -ray sources is observed at  $L = 195$ ,  $b = +5$ , yet there is no obvious counterpart seen at other wavelengths.

Although nuclear  $\gamma$ -ray lines whose origin lies outside our solar system have great astrophysical significance, their detection is especially difficult because the predominant interaction process in this energy range is the Compton process and because there is a high level of locally produced  $\gamma$ -rays and neutrons. Solar nuclear  $\gamma$ -ray lines have been detected, however, by Chupp et al. (1973) from the large solar flares of August 4, and 7, 1972, with an instrument flown on OSO-7. Also, the detection of a  $\gamma$ -ray line from the galactic center has been reported (Johnson and Haymes, 1973; Leventhal, MacCallum, and Strong, 1978).

Successful measurements of X-ray,  $\gamma$ -ray, and  $\alpha$ -particle emissions from the Moon, Mars, and Venus have been carried out during both U.S. and Soviet spaceflight missions. The most extensive orbital and in situ measurements have been conducted at the Moon. Rangers 3, 4, and 5 in 1961 and 1962 carried the first  $\gamma$ -ray spectrometer into space. Results were obtained on the spacecraft and cosmic background (Metzger et al., 1964). The first measurement of a  $\gamma$ -ray spectrum near the Moon was obtained by the Soviet Luna orbiter in 1966 which recognized a compositional distinction between mare and terra provinces (Vinogradov et al., 1967). The first successful in situ measurement of composition was the  $\alpha$ -backscatter experiment carried by Surveyor 5 in 1967 (Turkevich et al., 1969). During the Apollo 15 and Apollo 16 flights in 1971 and 1972  $\gamma$ -ray, X-ray, and

$\alpha$ -particle spectrometers were carried on the orbiting Command and Service Modules. Approximately 20 percent of the lunar surface was mapped for magnesium, aluminum, thorium, potassium, uranium, silicon, titanium, and oxygen (Metzger et al., 1973; Adler et al., 1972; and Bjorkholm et al., 1973). The two Soviet Lunakhod roving vehicles carried X-ray fluorescence experiments (Kocharov and Viktorev, 1976). A  $\gamma$ -ray spectrometer aboard the Soviet Mars-5 orbiter obtained several hours of data, from an altitude of about 2300 km, indicating that the average potassium, uranium, and thorium content of the regions surveyed corresponds to that of terrestrial rocks like oceanic basalts (Surkov et al., 1976). The two NASA Viking Landers carried an X-ray spectrometer for the fluorescence analysis of selectable soil and rock samples (Clark et al., 1977). The finely divided samples of the two landing sites were remarkably similar, with high iron and sulfur content and little potassium. Three Soviet spacecraft, Venera 8, 9, and 10, have carried a  $\gamma$ -ray spectrometer to measure potassium, uranium, and thorium at the surface of Venus by detecting thorium decay of these naturally radioactive elements (Surkov, 1977). In addition, Venera 10 had a second  $\gamma$ -ray instrument on board to measure the bulk density of the surface materials.

Also, in the low energy  $\gamma$ -ray region of the spectrum, there has been the discovery of the low energy  $\gamma$ -ray bursts (Klebesadel, Strong, and Olsen, 1973). These bursts are short, typically observable for a few seconds to tens of seconds, and have energies concentrated in the low energy  $\gamma$ -ray region. The origin and nature of these  $\gamma$ -ray burst sources remain an unsolved puzzle.

In the very high energy region of the  $\gamma$ -ray spectrum, ground based Čerenkov light reflector telescopes have good evidence of  $\gamma$ -ray emission from the Crab Nebula, Pulsar 0531+21 (Helmken, Grindlay, and Weekes, 1975; and Gupta et al., 1978), the Vela Pulsar PSR 0833-45 (Bhat et al., 1980), Cygnus X-3 (Vladimirsky et al., 1975), and Centaurus-A (Grindlay et al., 1975) above  $10^{11}$  eV. The implications with regard to the sources of these extremely energetic photons are obviously impressive.

In the following chapters of this book, the role that  $\gamma$ -ray astronomy plays in astrophysics will be studied starting with the closest objects, those of the solar system, expanding to the

galaxy and the stellar objects in it, and onward to other galaxies, cosmology, and the diffuse  $\gamma$ -radiation. The last chapters of the book will discuss the approaches to the detection of astrophysical  $\gamma$ -rays. Production and absorption processes associated with  $\gamma$ -rays will be developed individually as the need arises.

In general, the  $\gamma$ -ray region will be defined as the energy realm above 0.1 MeV, but the division between X-rays and  $\gamma$ -rays is not sharp. There are some phenomena such as  $\gamma$ -rays from  $\pi^0$  mesons produced in high energy interactions, nuclear  $\gamma$ -ray lines, and matter-antimatter annihilation  $\gamma$ -rays, which belong solely to the  $\gamma$ -ray realm; however, other phenomena such as bremsstrahlung from electrons interacting with matter span the two regions. In addition, results from X-ray astronomy and from other wavelength ranges will be discussed as appropriate for the understanding of the astrophysical problems under consideration.

## REFERENCES

- Adler, I., Trombka, J., Gerard, J., Lowman, P., Schmadebeck, R., Yin, L., Blodget, H., Eller, E., Lamothe, R., Gorenstein, P., and Bjorkholm, P., 1972, *Science*, **175**, 436.
- Bhat, P. N., Gupta, S. K., Ramana Murthy, P. V., Sreekantan, B. V., Tonwar, S. C., and Viswanath, P. R., 1980, *Astron. Astrophys.*, **81**, L3.
- Bignami, G. F., Fichtel, C. E., Hartman, R. C., and Thompson, D. J., 1979, *Ap. J.*, **232**, 649.
- Bjorkholm, P., Golub, L., and Gorenstein, P., 1973, *Proc. Fourth Lunar Planet. Sci. Conf.*, **3**, 2803.
- Chupp, E. L., Forrest, D. J., Higbie, P. R., Suri, A. N., Tsai, C., and Dunphy, P. P., 1973, *Nature*, **241**, 333.
- Clark, B. C., III, Baird, A. K., Rose, H. J., Jr., Toulmin, P., III, Christian, R. P., Kelliher, W. C., Castro, A. J., Rowe, C. D., Keil, K., and Huss, G. R., 1977, *J. Geophys. Res.*, **82**, 4577.
- Colgate, S. A., and White, R. H., 1966, *Ap. J.*, **143**, 626.
- Feenberg, E., and Primakoff, H., 1948, *Phys. Rev.*, **73**, 449.
- Fichtel, C. E., Hartman, R. C., Kniffen, D. A., Thompson, D. J., Bignami, G. F., Ogelman, H. B., Ozel, M. E., and Tumer, T., 1975, *Ap. J.*, **198**, 163.
- Grindlay, J. E., Helmken, H. F., Brown, H. R., Davis, J., and Allen, L. R., 1975, *Ap. J. (Letters)*, **197**, L9.
- Gupta, S. K., Ramana Murthy, P. V., Sreekantan, B. V., and Tonwar, S. C., 1978, *Ap. J.*, **221**, 268.
- Hayakawa, S., 1952, *Prog. Theor. Phys.*, **8**, 571.
- Helmken, H. F., Grindlay, J. E., and Weekes, T. C., 1975, *Proc. of the 14th Int. Cosmic Ray Conf.*, **1**, 123.

- Hutchinson, G. W., 1952, *Phil. Mag.*, **43**, 847.
- Johnson, W. N., III, and Haymes, R. C., 1973, *Ap. J.*, **184**, 103.
- Klebesadel, R. W., Strong, I. B., and Olsen, R. A., 1973, *Ap. J. (Letters)*, **182**, L85.
- Kocharov, G., and Viktorev, S. V., 1974, *Doklady Academy of Sciences, USSR*, **214**, 71.
- Kraushaar, W. L., Clark, G. W., Garmire, G. P., Borken, R., Higbie, P., Leong, C., and Thorsos, T., 1972, *Ap. J.*, **177**, 341.
- Levanthal, M., MacCallum, C. J., and Strong, P. D., 1978, *Ap. J. (Letters)*, **225**, L11.
- Mayer-Hasselwander, H. A., Bennett, K., Bignami, G. F., Burcheri, R., D'Amico, N., Hermsen, W., Kanbach, G., Lebran, F., Lichti, G. G., Masnou, J. L., Paul, J. A., Pinkau, K., Scarsi, L., Swanenberg, B. N., Wills, R. D., 1980, *Annals of the New York Academy of Sciences, Proc. of the Ninth Texas Sym.*, **336**, 211.
- Metzger, A. E., Anderson, E. C., Van Dilla, M. A., and Arnold, J. R., 1964, *Nature*, **204**, 766.
- Metzger, A. E., Trombka, J. I., Peterson, L. E., Reedy, R. C., and Arnold, J. R., 1973, *Science*, **179**, 800.
- Morrison, P., 1958, *Nuovo Cimento*, **7**, 858.
- Surkov, Y. A., 1977, *Proc. Eighth Lunar Planet. Sci. Conf.*, 265.
- Surkov, Y. A., Moskalyova, L. P., Kirnozov, F. F., Khyarkukova, V. P., Manvelyan, O. S., and Shchelov, O. P., 1976, *Space Research XVI* (Berlin: Akademie-Verlag, COSPAR, 1976).
- Turkevich, A. L., Franzgrote, E. J., and Patterson, J. H., 1969, *Science*, **165**, 277.

Vinogradov, A. P., Surkov, Y. A., Chernov, G. M., Kirnozov, F. F., and Nazarkina, G. B., 1967, *Cosmic Res.*, **5**, 741.

Vladimirsky, B. M., Neshpur, Yu. I., Stepanian, A. A., and Fomin, N. P., 1975, *Proc. of the 14th Int. Cosmic Ray Conf.*, **1**, 118.



# **PART II**

## **THE SOLAR SYSTEM**

*Chapter 2*  
*Gamma Ray Observations of the Solar System*

*Chapter 3*  
*Planets, Comets, and Asteroids*

*Chapter 4*  
*Solar Observations*



## PART II

# THE SOLAR SYSTEM

*The detailed exploration of the solar system is becoming a reality as we look at the spaceflight results during this third decade of the space age. Observational data have been obtained from ground-based instruments, spaceflight programs, and meteorite studies that allow certain constraints to be imposed on the theoretical models relative to the origin and evolution of the solar system. Gamma ray astrophysical observations have made a significant contribution to these data. Various theoretical approaches can now be evaluated in terms of their observational tests, and more rigorous models can be developed. Both chronology and the present-day dynamics of the Sun and solar system can be examined critically with  $\gamma$ -ray astronomical observations.*

*In Chapter 2, we have briefly outlined some of the more prevalent theoretical models concerning the origin of the solar system. The  $\gamma$ -ray observational results can then be considered in this context. Detailed considerations of  $\gamma$ -ray emission processes and experimental results obtained during spaceflight missions are presented in Chapter 3 concerning solar system bodies excluding the Sun and in Chapter 4 concerning the Sun itself.*



## Chapter 2

# Gamma Ray Observations of the Solar System

### INTRODUCTION

The question of the origin of the solar system has attracted much attention. Such interest is evident throughout the history of mankind. Many models have evolved but when the basic assumptions underlying such models, no matter how mathematically elegant, cannot be related to actual observed phenomena, there is no method to discriminate between truth and fiction. In the last two decades, however, observational data have been obtained from both spaceflight programs and meteorite studies that allow certain constraints to be imposed on the theoretical models for the origin and evolution of the solar system. Further, various theoretical approaches can now be evaluated in terms of their observational tests, and more rigorous models can be developed.

The present structure of the solar system should be understood as the product of a long series of complicated processes. A major aim of the solar system exploration program and the subsequent attempt to develop theoretical models is to reconstruct the early history of the solar system based on present-day observations. In order to comprehend the relationship between  $\gamma$ -ray astronomical measurements and the development of theoretical models one must understand, at least in broad outline, the general hypothesis relating to solar system evolution.

## MODELS OF SOLAR SYSTEM EVOLUTION

Regarding the evolution of the solar system, the approaches fall into two general categories: the dualistic view, the planetesimal approach; and the monistic view, the nebular hypothesis. The dualistic approach has led to the development of a number of models. One model suggests that the Sun passed very near another star at some time and drew out material from it. These filaments of material ultimately condensed into separate planets. Another dualistic model hypothesizes that the Sun was originally a member of a binary system. The other star, having suffered a direct collision with a third star, broke up and the planets were formed from the resulting fragments.

A number of objections can be raised with respect to the two dualistic views just considered. In the first case, when considering materials being drawn from the Sun by the attraction of a passing star, there is a failure to account for the peculiar distribution of angular momentum in the solar system, which is mainly carried by the outer planets of far less mass than the Sun. Considering the binary system hypothesis, rather high temperatures would be expected causing the material to stream out into space rather than condense into planets. The dualistic view in one form or another seemed the most plausible explanation for the genesis of the solar system for, until recently, it was believed that the Sun and planets could hardly represent the remains of independent condensing in a primeval nebula, their masses being too unequal to be suspect of any such explanations.

Recent evidence of the following has revived interest in the monistic view, the nebular hypothesis: the common age of solar and planetary evolution derived from the distribution of materials, and the comparison of that age to stellar evolution derived from astrophysical observation.

The nebular hypothesis of the origin of the solar system can be briefly described as follows: at a great distance from the galactic center along the curved arms of our spiral galaxy, a great cloud of gas and dust contracted, occurring, it is believed, some 4.6 billion years ago. The cloud collapsed and spun more rapidly, forming a disk. A star, our Sun, was formed at some time later when a massive, dense, and hot body collected at the center of the disk and a nebular fusion reaction was ignited. Later, the

surrounding dust particles accreted to form the planets bound in orbit around the Sun and satellites bound in orbit around some of the planets.

Using this hypothesis as a basis and moving from the present time back to the early history of the solar system, five stages can be used to trace and understand the evolution of the solar system (Alfvén and Arrhenius, 1976).

1. Most recently—during the last 3 to 4 billion years—a slow evolution of the primeval planets, satellites, and asteroids produced the present state of the bodies in the solar system. By studying this latest phase of evolution (post-accretional evolution), we prepare a basis for reconstructing the states established by earlier processes.

2. Preceding the post-accretional stage there is an evolution of condensed grains which move in Kepler orbits to form planetesimals. The planetesimals continue to grow in size by accretion. These planetesimals are the embryonic precursors of the bodies found today in the solar system. By clarifying the accretional processes, attempts can be made to reconstruct the chemical and dynamical properties of the early population of grains.

3. To account for grains moving in Kepler orbits around the Sun and the protoplanets, transfer of angular momentum from these primary bodies to the surrounding medium must have occurred in the stage of evolution preceding accretion.

4. During this pre-accretional stage there must have been an emplacement of gas and dust to form a medium around the magnetized central bodies in the regions where the planet and satellite groups later accreted.

5. The Sun must have formed as the primary body to accrete from the source cloud of the solar system.

Detailed discussions of the various theories concerning solar system evolution can be found in such references as Adler and Trombka (1970), Sagan (1975), Cameron (1975), Alfvén and Arrhenius (1976), and Greeley and Carr (1976).

## **SOLAR SYSTEM GAMMA RAY ASTRONOMICAL OBSERVATIONS**

Considering the proposed models of the dynamic evolution of the solar system, how can  $\gamma$ -ray astrophysical observations

contribute to our understanding of solar system evolution? Gamma ray spectroscopic observations of planetary bodies will allow for the global determination of elemental surface composition. The problem of the origin and evolution of the solar system can thus be considered in a geochemical context. The problems have been examined in two works, Adams et al. (1967, 1979).

In order to determine the stages in the evolution of the solar system when chemical fractionation took place, some questions must be examined: Are the individual terrestrial planets and satellites chemically uniform or nonuniform? Did the final accretion result in the present array of planets and satellites, or in an array that was subsequently altered? Was the cloud chemically homogenous at the time of final accretion? What was the state of the Sun-cloud system when it first became an identifiable unit? Were there large-scale elemental and isotropic nonuniformities in the contracted nebula? Answers depend ultimately on chemical measurements as well as mineralogy and petrology. Assumptions cannot be made a priori that a given planet is chemically homogeneous and that an analysis at a given site is representative of the whole planet. Thus the remote orbital  $\gamma$ -ray and X-ray remote sensing system will address these questions.

The only accessible part of a planet—its near-surface—may be totally nonrepresentative of the planet as a whole. It is necessary to have a general understanding of the planet, and this can be achieved effectively only by studying the processes that may have caused—and may yet be causing—redistribution of materials within the planet. Only if these processes are understood can valid general conclusions be drawn regarding the significance of specific measurements. The sampling or type of measurements made on a planet, therefore, should be guided by the need to understand geologic processes.

In the above discussion, surface properties are considered. Of equal importance in understanding solar system evolution is the relationship of the surface to the planets, internal heterogeneities and conditions. Chemical determinations of materials from the interiors obviously cannot be made directly; nevertheless, inferences are possible from measurements of physical properties. The value of any particular physical parameter is not

important, since it depends on local conditions; its importance lies in the fact that it places limits on chemical composition and internal conditions, and provides data on internal processes. Stratigraphy is concerned directly with documentation of crystal heterogeneity. Even though the surface rocks constitute a minute part of the total mass of the planet, it is the part on which a great many measurements are made. Thus, an understanding of surface materials is crucial and how variegated the surface rocks are and how they are formed must be known. The mode of formation is particularly important, for different processes vary in the extent to which they cause chemical change. Consequently, to understand the broader implications of surface analyses, we should know the distribution and mode of formation of the rocks analyzed, as well as the degree to which they typify all other materials of the planet.

Of course the central body of interest of the solar system is the Sun. There can be no theory for the origin and evolution of the solar system without an understanding of the nature of the Sun, its chronology, and present-day dynamics. Furthermore, the Sun is of great astrophysical interest because it is the star that the astronomer can study in greatest detail. The study of solar transient phenomena yields significant information on solar dynamics. Therefore,  $\gamma$ -ray astronomy, as applied to the observation of the Sun, has the specific objective of considering high energy processes that take place in the outer region of the Sun's atmosphere and the relationship of these phenomena to the basic problems of solar activity. A measurement of the spectra of discrete  $\gamma$ -ray line emission will reveal the detailed dynamics and time structure of solar flares and energetic particle acceleration and release. Such measurements should also yield qualitative, and in some cases quantitative, information on the composition of specific ambient or transient nuclides in the outer regions of the Sun's atmosphere.

In the next two chapters, remote  $\gamma$ -ray geochemical sensing systems for planetary surface observations and solar  $\gamma$ -ray observations during flares will be discussed in detail.

## REFERENCES

- Adams, J. B., Conel, J. E., Dunne, J. A., Fanale, F., Holstrom, G. B., and Loomis, A. A., 1967, "Scientific Strategy, Objectives and Experiments for Mariner Missions from 1970 through 1973," Calif. Inst. Tech., Jet Prop. Lab. Doc. 900-94 (internal document).
- Adams, J. B., Conel, J. E., Dunne, J. A., Fanale, F., Holstrom, G. B., and Loomis, A. A., 1969, *Rev. Geophys.*, 7, 623.
- Adler, I., and Trombka, J. I., 1970, *Physics and Chemistry in Space*, vol. 3, J. G. Roderer and J. Zahringer, eds. (New York: Springer-Verlag, 1970).
- Alfvén, H., and Arrhenius, G., 1976, *Evolution of the Solar System*, NASA SP-345 (Washington, D.C.: U.S. Government Printing Office, 1976).
- Cameron, A. G. W., 1975, *Scientific American*, 233, 33.
- Greeley, R., and Carr, M. H., eds., 1976, *A Geological Basis for the Exploration of the Planets*, NASA SP-417 (Springfield, Va.: National Technical Services, 1976).
- Sagan, C., 1975, *Scientific American*, 233, 23.

## Chapter 3

# Planets, Comets, and Asteroids

### INTRODUCTION

An important part of the investigation of planetary evolution is the determination of the chemical composition of the surfaces of planets, comets, and asteroids. The abundance of certain elements with different condensation temperatures and with various types of geochemical behavior can provide important data relative to the origin and evolution of these bodies. The global planetary composition is characteristic of the nature of its formation during the accretion from the solar nebula. Furthermore, early condensation processes are indicated by certain key elements, e.g., uranium (a refractory element), iron (condensed as metallic iron-nickel), and magnesium (the first silicate formed). In the course of planetary evolution, the elemental distribution is greatly modified by such processes as core and crust formation during differentiation and later magma formation and emplacement. Evolutionary processes can be studied, for example, by determining the K/U ratio (remelting of the primordial condensates) and the Th/U ratio (relative abundance of volatiles). A detailed discussion of the use of geochemical information in the study of the formation and evolution of planetary bodies can be found for example in Anders (1977).

In this chapter, methods for remote sensing of elemental composition of surfaces will be considered. A number of processes which modified the elemental composition must be understood in order to interpret the compositional maps determined from

the remote sensing observations. The surfaces of most planets usually involve a regolith consisting of most fragments and reworked material such as glasses. The extent to which regolith material has been transported away from its origin influences the geochemical distribution. Transport mechanisms possible on various planets include volcanism, meteoroid impact, water and wind movement, and particle transport due to electrostatic charge processes. Remote geochemical information obtained by X-ray and  $\gamma$ -ray spectroscopic measurements combined with photo-geological maps can be used to infer information about both horizontal and vertical elemental composition relative to the problems just considered.

Both X-ray and  $\gamma$ -ray remote sensing techniques will be considered. It is the combination of these techniques which is required for a more complete understanding of the remote sensing method. Combinations of X-ray and  $\gamma$ -ray spectrometers or a  $\gamma$ -ray spectrometer alone have been successfully flown on a number of planetary spaceflight missions. In U.S. spaceflight programs, such spectrometers were included aboard Apollo 15 and Apollo 16 (Adler et al., 1972; Metzger et al., 1973), and in the Soviet space program on a number of Luna missions, Mars 4 and Mars 5, and the Venera missions (Vinogradov et al., 1966; and Surkov et al., 1976).

## INTERACTION PROCESSES

Measurements of discrete line X-ray and  $\gamma$ -ray emission from condensed bodies in space can be used to obtain both qualitative and quantitative elemental composition information. Discrete line emission in this energy domain ( $\sim 0.2$  keV to  $\sim 10$  MeV) can be attributed to a number of processes such as natural radioactivity, solar X-ray fluorescence, and cosmic ray primary and secondary induced activity. Figure 3-1 summarizes the major processes for X-ray and  $\gamma$ -ray emissions from the Moon. The elements that are listed produce significant X-ray and  $\gamma$ -ray fluxes because of their abundance, interaction cross sections, and magnitude of exciting flux. Also indicated in the figure are the depths at which the interactions occur and the depth from which the discrete line X-ray and  $\gamma$ -ray photons can escape through the planetary surface and can be detected from orbit. Both alpha particle

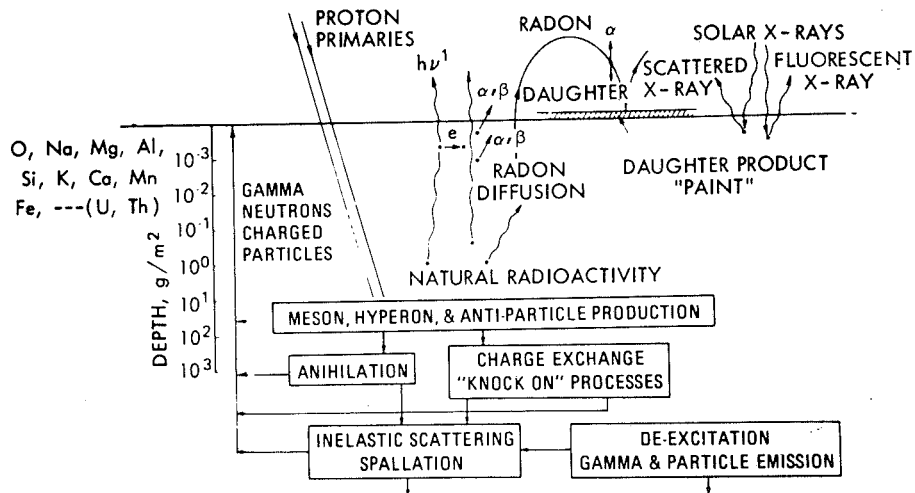


Figure 3-1. Radiation environment at the lunar surface.

emission and neutron albedo can also be used to determine elemental composition. Each of the major emission processes are considered below.

### Solar X-Ray Fluorescence

The major radiation source for remote orbital X-ray elemental analysis is that produced by characteristic X-rays following the interaction of solar X-rays with the surface of the given body being studied. Figure 3-2 shows a so-called "quiescent" solar X-ray emission spectrum characteristic of that observed during Apollo 15. The spectrum shown was produced by a semiempirical method. Data obtained from the solar observatory, "Solrad," were com-

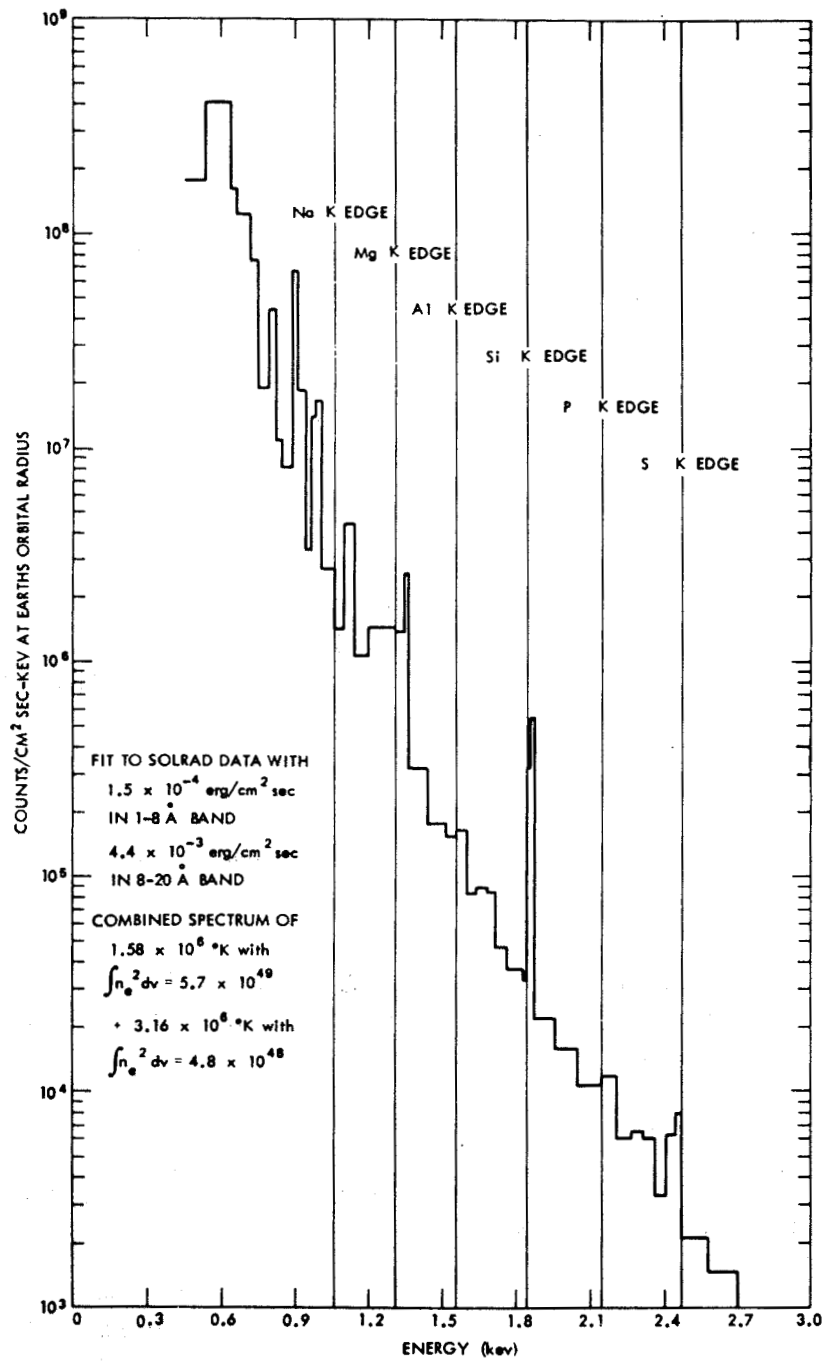


Figure 3-2. Solar X-ray spectrum at the Earth's orbital radius (1AU).

bined with a theoretical calculation based on a model developed by Tucker and Koren (1971). The calculation was predicated on combining a coronal temperature of  $\sim 1.5 \times 10^8$  K with a hot spot temperature of about  $\sim 3 \times 10^6$  K in proportions determined from Solrad measurements during Apollo 15.

The expected fluorescence emission can be calculated using the following relation (Jenkins and DeVries, 1967):

$$I_j = \left[ \omega_j g_j \left( \frac{r_j^{-1}}{r_j} \right) \frac{d\Omega C_j}{4\pi} \right] \times \left\{ \frac{\int_{\lambda_{\min}}^{\lambda_{\max}} J(\lambda) \mu_i(\lambda) d\lambda}{\sum_1^n C_i \left[ \mu_i(\lambda) + \mu_i(\lambda_j) \left( \frac{\cos \alpha}{\cos \beta} \right) \right]} \right\}, \quad (3-1)$$

where  $I_j$  is the expected fluorescent flux for element  $j$  in the irradiated surface in photons per second per fraction solid angle,

$J(\lambda)$  is incident for exciting differential energy flux as a function of wavelength;

$\mu_i(\lambda)$  is the mass absorption coefficient as a function of wavelength for element  $i$ ;

$C_i$  is the percent of atomic concentration for element  $i$ ;

$\omega_j$  is the fluorescence yield for element  $j$ ;

$r_j$  is the absorption jump for element  $j$ ;

$g_j$  is the probability of a particular electron transfer (e.g., K-alpha) in a particular shell (e.g., K-series);

$d\Omega/4\pi$  is the differential fraction of a solid for emission (assumed isotropic in these calculations);

$\lambda_{\text{edge}}$  is the wavelength at the absorption edge;

$\lambda_{\text{min}}$  is the shortest wavelength or highest energy for the incident or exciting flux;

$\mu_i(\lambda_j)$  is the mass absorption coefficient for element  $i$  for the excited X-ray fluorescence of wavelength  $\lambda_j$ ;

$\alpha$  is the complement of the angle of the incident flux;

$\beta$  is the complement of the so-called take off angle (angle of emission) of the secondary flux; and  
 $n$  is the number of elements in the sample.

The above equation holds for the case of a thick target, infinite in terms of the absorption of the wavelengths of interest, for example, remote X-ray sensing.

A major source of background in remote X-ray analysis can be attributed to the X-rays emitted from an irradiated surface because of the coherent scattering of the incident flux  $S(\theta, \lambda)$ . This component can be calculated from the following relationship (Hubbell, 1969):

$$S(\theta, \lambda) = 0.239 [\cos^2 \theta + 1] J(\lambda) \frac{\sum_1^n \left[ \frac{C_i}{W_i} f_i^2 \right] d\Omega}{\sum_1^n \left[ \mu_i(\lambda) \left( 1 + \frac{\cos \alpha}{\cos \beta} \right) \right]}, \quad (3-2)$$

where  $S(\theta, \lambda)$  is the differential angular and wavelength scattered flux,

$\theta$  is the backscatter angle (only X-rays scattered out of the surface will be detected); the constant 0.0239 is the product of  $N$  (Avogadro's number) and  $r^2/2$  where  $r$  is the electron radius;  
 $W_i$  is the atomic weight of element  $i$ ; and  
 $f_i$  probability for coherent scattering.

The other factors are the same as those defined in Equation (3-1). Results for such a calculation for a possible comet-like material at 2 AU from the Sun are given in Table 3-1. The solar spectrum shown in Figure 3-1 and Equations (3-1) and (3-2) were used in the calculation. The fluxes shown can be observed at orbital altitudes. In fact from Equations (3-1) and (3-2) the calculated X-ray fluxes were consistent with the results obtained during Apollo 15 and Apollo 16 (Adler and Trombka, 1977).

**Table 3-1**  
**Expected X-Ray Fluorescence and Scattering from a Comet Surface**

Element	Line Energy (keV)	Comet 2 AU from the Sun	
		Line Flux (photons cm <sup>-2</sup> s <sup>-2</sup> )	Coherent Scattered X-rays (photons cm <sup>-2</sup> s <sup>-2</sup> keV <sup>-1</sup> )
C	0.277	2.1 × 10	6.3 × 10 <sup>2</sup>
O	0.525	1.9 × 10	4.1
Mg	1.254	7.8 × 10 <sup>-3</sup>	2.3 × 10 <sup>-2</sup>
Al	1.487	2.7 × 10 <sup>-4</sup>	7.9 × 10 <sup>-3</sup>
Si	1.740	1.4 × 10 <sup>-3</sup>	3.0 × 10 <sup>-3</sup>
S	2.308	2.2 × 10 <sup>-4</sup>	4.4 × 10 <sup>-4</sup>
Ca	3.692	3.7 × 10 <sup>-6</sup>	2.1 × 10 <sup>-5</sup>
Fe	6.404	4.2 × 10 <sup>-6</sup>	4.6 × 10 <sup>-7</sup>

**Note:** The surface soil material was assumed to have a one-to-one solid-plate ice concentration. The solid material was assumed to be chondritic in nature.

The X-ray emission is strongly dependent on the elemental composition and on the distance from the Sun. It should also be noted that the higher *Z* elements are not shown. The expected emission flux from these elements would be too low to be detectable from orbit. Both elemental composition of these elements and the fast—almost a power law—decrease in solar differential energy spectrum accounts for this low intensity. These results were based on results for the so-called “quiescent Sun.” There can be variations in the solar activity and thus in both the magnitude and spectral distribution of the solar X-ray spectrum which will affect the spectral quality of the X-ray emission flux from the surface.

An increase in solar activity and possibly in temperatures, tends to harden the solar spectrum. This hardening enhances the intensities of the emissions of the heavier elements relative to the lighter elements. The increase in intensity also increases the absolute magnitude of the fluorescent X-ray flux. Whenever X-ray orbital measurements are used to obtain elemental composition, simultaneous observations must be made of the incident solar

X-ray spectrum and the planetary X-ray emission spectrum in order to infer both qualitative and quantitative information.

Characteristic X-ray emission can be produced by charged particle interactions with condensed matter. These interactions may be of interest for possible remote chemical composition sensing of the Galilean satellites of Jupiter. X-ray fluorescence from such key elements as magnesium, aluminum, silicon, and iron may be excited by the interactions of charged particles (e.g., the Jovian radiation belt) with the satellite surfaces. Of particular interest will be electron and proton interactions. The processes of interest will be briefly considered here. The preponderance of useful characteristic X-rays are generated by the inner shell ionization due to electron impact. The inner shell ionization cross sections from protons can become comparable to electron cross section if the protons have energies about 1000 times that of electrons. For example 5 keV electrons and 4 MeV protons both have a cross section of  $\sim 2 \times 10^{-20}$  cm<sup>2</sup> in the K-shell ionization of an aluminum target (Brandt, 1972; Toburen, 1972).

Finally, the mean free path of these soft X-rays are very short with respect to the density of materials found on planetary surfaces. Thus, the elemental composition obtained by utilizing the X-ray fluorescent method is characteristic of the composition for only about 100  $\mu$  in depth. Furthermore, any significant atmosphere around a planetary body will absorb the solar X-ray flux, thus eliminating any chance of surface fluorescence. Thus, the technique can only be used for atmosphereless bodies such as our Moon, comets, asteroids, and Mercury.

### **Charged Particle X-Ray Fluorescence**

Progressing to the outer planets, it is found that the solar X-ray flux has decreased to such an extent that the emission produced by solar X-ray excitation is negligible. For the outer planets and specifically for the Galilean satellites of Jupiter, charged particle X-ray fluorescence as discussed above may produce sufficient fluxes of characteristic X-rays so as to allow for remote analysis.

### **Natural Radioactivity**

One of the major sources of  $\gamma$ -ray emission from planetary surfaces is attributable to the decay of the so-called natural radioactive

elements. These are the naturally occurring primordial radioactive elements  $^{40}\text{K}$ ,  $^{138}\text{La}$ ,  $^{176}\text{Lu}$  and the uranium and thorium decay. The  $\gamma$ -ray energies, half-lives, and yields (i.e., gammas per disintegration of the parent radionuclide) for these nuclides are shown in Table 3-2 (Reedy, 1978).

Not all the energies listed in Table 3-2 can be observed at orbital altitudes. The major lines are used to infer the distribution of the nuclear species enumerated. For this case it can be assumed that the  $\gamma$ -rays are emitted at a steady and predictable rate. A so-called secular equilibrium is assumed among the parent and daughter products, an equilibrium that can be disturbed by radon emanation which can change the ratio of parent-to-daughter  $\gamma$ -ray emission. This disequilibrium can be used to measure the chronology and time extent of such emission processes. In order to obtain information on disequilibrium,  $\gamma$ -ray lines from both the parent and daughter nuclides must be detected.

## PRIMARY AND SECONDARY GALACTIC COSMIC RAY INTERACTIONS

The bombardment of a body of condensed matter by the primary galactic cosmic rays produces many interactions and numerous secondary particles. The spectra of primary and secondaries are discussed in detail by Reedy and Arnold (1972). The approximately 90 percent proton component of the cosmic ray flux is of most interest in this section. Numerous secondary particles are produced by the primary cosmic ray interactions. Most secondary charged particles have low enough energies that they are stopped before they can induce nuclear reactions. However, this is not true for the secondary neutrons produced by ionization energy losses. Thus, these neutrons become the major flux of particles capable of exciting  $\gamma$ -ray emission.

The majority of secondary neutrons produced in this manner have energies from  $\sim 0.5$  MeV to  $\sim 20$  MeV. They can be further slowed down in the planetary surface to produce significant fluxes of thermal neutrons. Calculations of the secondary neutron flux produced by the incident primary cosmic ray flux and moderated by the planetary material have been carried out by a number of investigators (Lingenfelter et al., 1961; Lingenfelter et al., 1972; Korblum and Fireman, 1974; Lapidés et al., 1980; and Spergel

**Table 3-2**  
**Natural Radioactive Elements of Interest in Remote**  
 **$\gamma$ -Ray Sensing of Planetary Bodies**

Element	Nuclide	Energy (MeV)	Yield	Half-Life
K	$^{40}\text{K}$	1.4608	0.1048	$1.250 \times 10^9\text{y}$
La	$^{138}\text{La}$	1.4359	0.671	$1.35 \times 10^{11}\text{y}$
	$^{138}\text{La}$	0.7887	0.329	$1.35 \times 10^{11}\text{y}$
Lu	$^{176}\text{Lu}$	0.3069	0.940	$3.6 \times 10^{10}\text{y}$
	$^{176}\text{Lu}$	0.2018	0.850	$3.6 \times 10^{10}\text{y}$
Th	$^{208}\text{Tl}$	2.6146	0.360	3.10m
	$^{228}\text{Ac}$	1.6304	0.019	6.13h
	$^{212}\text{Bi}$	1.6205	0.016	60.60m
	$^{228}\text{Ac}$	1.5879	0.037	6.13h
	$^{228}\text{Ac}$	1.4958	0.010	6.13h
	$^{228}\text{Ac}$	1.4592	0.010	6.13h
	$^{228}\text{Ac}$	0.9689	0.175	6.13h
	$^{228}\text{Ac}$	0.9646	0.054	6.13h
	$^{228}\text{Ac}$	0.9111	0.290	6.13h
	$^{208}\text{Tl}$	0.8605	0.045	3.1m
	$^{228}\text{Ac}$	0.8402	0.010	6.13h
	$^{228}\text{Ac}$	0.8356	0.018	6.13h
	$^{228}\text{Ac}$	0.7948	0.048	6.13h
	$^{212}\text{Bi}$	0.7854	0.010	60.60m
	$^{228}\text{Ac}$	0.7721	0.016	6.13h
	$^{228}\text{Ac}$	0.7552	0.011	6.13h
	$^{212}\text{Bi}$	0.7271	0.070	60.60m
	$^{208}\text{Tl}$	0.5831	0.307	3.1m
	$^{228}\text{Ac}$	0.5623	0.010	6.13h
	$^{208}\text{Tl}$	0.5107	0.083	3.1m
	$^{228}\text{Ac}$	0.4630	0.046	6.13h
	$^{228}\text{Ac}$	0.4094	0.022	6.13h
	$^{228}\text{Ac}$	0.3384	0.120	6.13h
	$^{228}\text{Ac}$	0.3280	0.034	6.13h
	$^{212}\text{Pb}$	0.3000	0.031	10.64h
	$^{208}\text{Tl}$	0.2774	0.024	3.1m
	$^{228}\text{Ac}$	0.2703	0.038	6.13h
$^{224}\text{Ra}$	0.2410	0.038	3.64d	
$^{212}\text{Pb}$	0.2386	0.470	10.64h	

**Table 3-2 (continued)**  
**Natural Radioactive Elements of Interest in Remote**  
 **$\gamma$ -Ray Sensing of Planetary Bodies**

Element	Nuclide	Energy (MeV)	Yield	Half-Life
U	$^{228}\text{Ac}$	0.2094	0.045	6.13h
	$^{214}\text{Bi}$	2.4477	0.016	19.7m
	$^{214}\text{Bi}$	2.2041	0.050	19.7m
	$^{214}\text{Bi}$	2.1185	0.012	19.7m
	$^{214}\text{Bi}$	1.8474	0.021	19.7m
	$^{214}\text{Bi}$	1.7645	0.159	19.7m
	$^{214}\text{Bi}$	1.7296	0.031	19.7m
	$^{214}\text{Bi}$	1.6613	0.012	19.7m
	$^{214}\text{Bi}$	1.5092	0.022	19.7m
	$^{214}\text{Bi}$	1.4080	0.025	19.7m
	$^{214}\text{Bi}$	1.4015	0.014	19.7m
	$^{214}\text{Bi}$	1.3777	0.040	19.7m
	$^{214}\text{Bi}$	1.2810	0.015	19.7m
	$^{214}\text{Bi}$	1.2381	0.059	19.7m
	$^{214}\text{Bi}$	1.1552	0.017	19.7m
	$^{214}\text{Bi}$	1.1203	0.150	19.7m
	$^{214}\text{Bi}$	0.9341	0.032	19.7m
	$^{214}\text{Bi}$	0.8062	0.012	19.7m
	$^{214}\text{Pb}$	0.7859	0.011	26.8m
	$^{214}\text{Bi}$	0.7684	0.049	19.7m
	$^{214}\text{Bi}$	0.6655	0.016	19.7m
	$^{214}\text{Bi}$	0.6093	0.461	19.7m
	$^{214}\text{Pb}$	0.3519	0.371	26.8m
$^{214}\text{Pb}$	0.2952	0.192	26.8m	
$^{214}\text{Pb}$	0.2419	0.075	26.8m	
	$^{226}\text{Ra}$	0.1860	0.055	$1.602 \times 10^3\text{y}$
	$^{235}\text{U}$	1.1857	0.540	$7.04 \times 10^8\text{y}$

**Note:** y = years, d = days, h = hours, m = minutes, s = seconds.

et al., 1980). The neutron production mechanisms used in the calculation involve such processes as evaporation and knock-on. Detailed descriptions of these mechanisms can be found in Lingenfelter et al. (1961), Lingenfelter et al. (1972), and Korblum and Fireman (1974).

Results for thermal neutron distributories are shown in Figure 3-3 and Figure 3-4 (Lapides et al., 1980; Lapides, 1981). In Figure 3-3, the spatial distribution for thermal neutrons are shown for the Apollo 11 landing site-type material and a Carbonaceous Chondrite material (CCN). The curve marked source indicates the spatial dependence of a given energy group. The magnitude of this curve has been chosen only to be able to compare the spatial dependence of the Apollo 11 and CCN curves. The source term reflects the cosmic ray produced secondary neutrons the depth is measured in terms of  $\text{gm cm}^{-2}$  in order to generalize the solution. As can be seen, the spatial dependence of the thermal flux near the surface of a planetary will be quite different from a source term due to leakage from the surface but at depths greater than about  $150 \text{ g cm}^{-2}$  the source, Apollo 11, and CCN spectrum seems to have the same spatial dependences. The flux intensity is presented in terms of flux per neutron produced. For this case, the magnitude of the thermal flux in the Apollo 11-type material is larger than in the CCN. The macroscopic neutron absorption cross section is larger in the CCN material thus leading to the depression in thermal neutron flux.

Figure 3-4 shows the spatial dependence of the thermal flux as a function of hydrogenous content. The thermal flux reaches a maximum closer to the surface of a planet for those cases in which the hydrogen content increases. This is due to the increase in thermalization due to the presence of hydrogen. Hydrogen is also an excellent absorber of thermal neutron. Thus, although the thermalization increases, there is a point where the absolute magnitude of the flux decreases with increasing hydrogen as can be seen in Figure 3-4. The spatial shape and flux magnitude of the thermal neutrons affects the shape and magnitude of the  $\gamma$ -ray emission from the surface. A knowledge of the exciting flux will be required to obtain geochemical information from a determination of the  $\gamma$ -ray emission. Methods for performing such analyses can be found for example in Reedy and Arnold (1972), Reedy et al. (1973), Lapides et al. (1980), and Lapides

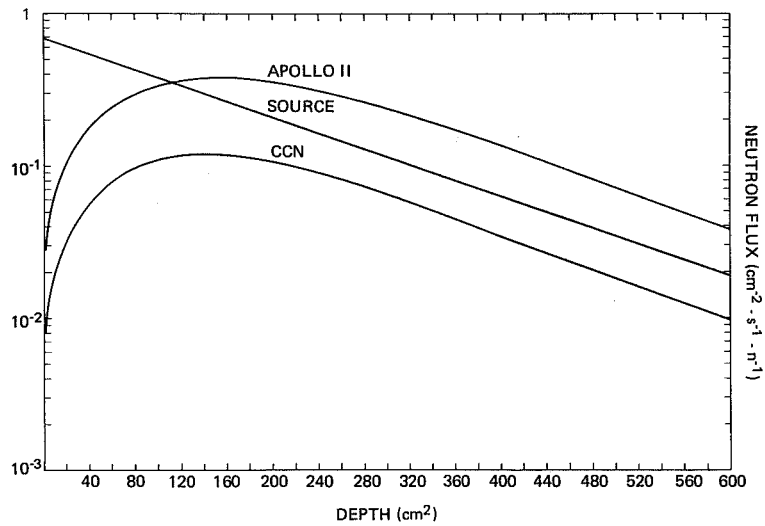


Figure 3-3. Spatial dependence of the thermal neutron flux in a lunar-type material (Apollo 11) and a carbonaceous chondrite material (CCN). The source neutrons are produced by cosmic ray interactions in the surface materials. The spatial dependence of the source neutrons is also indicated. The shape is shown only as a comparison for the Apollo 11 and CCN (Lapides, 1981). The magnitude is arbitrary and depends on the particular energy group.

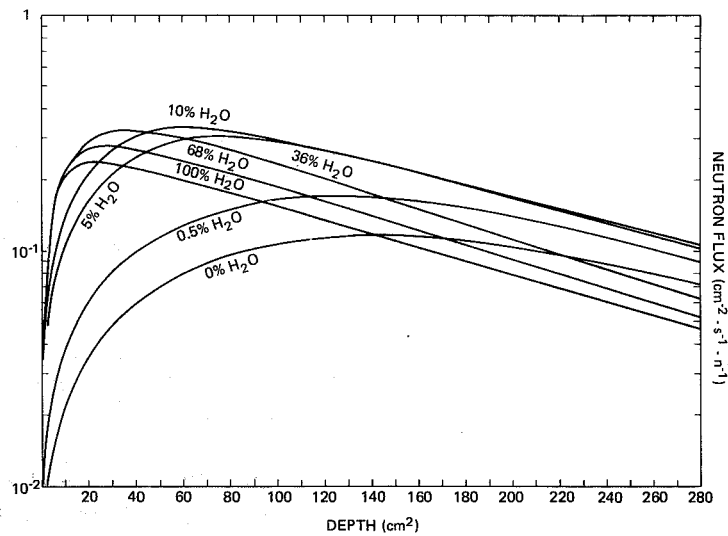
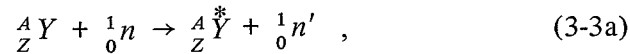


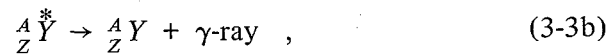
Figure 3-4. Calculated thermal flux in a planetary surface as a function of depth in the surface. The affect of the addition of hydrogen (in the form of water) is shown for a number of different hydrogen concentrations.

(1981). Experimental neutron flux determinations have been obtained during the Apollo 17 mission by Woolum et al. (1975). These results are consistent with those shown in Figure 3-3.

Neutrons with energies greater than or equal to 1 MeV can produce  $\gamma$ -ray exciting levels of nuclei through inelastic scattering reactions of the  $(n, x\gamma)$  type, where  $x$  is usually a neutron but can be another particle. For the case where  $x$  is a neutron the reaction can be described as follows:



then



where

$Y$  is a given nuclide;

$Z$  is the atomic number;

$A$  is the atomic weight;

${}^1_0 n$  is a neutron;

$\dot{Y}^*$  is the excited state of the nuclide; and

${}^1_0 n'$  stands for the neutron with energy reduced from the incident energy.

The emission in this case is prompt. The major  $\gamma$ -ray lines expected from materials of interest in planetary exploration are listed in Table 3-3. The yields are strongly dependent on the spectral distributions of the exciting neutrons. That is, the  $\gamma$ -ray energy produced depends on the energy levels that can be excited. Assume a neutron spectral distribution corresponds to the lunar case; the yields are then the fraction of  $\gamma$ -rays with given energy produced per deexcitation of the excited level. Another source of  $\gamma$ -ray emission is also included in Table 3-3: the primary galactic cosmic ray interactions with the surface materials. These interactions are due to the very high energy protons (above  $\sim 100$  MeV). This type of

**Table 3-3**  
**Major Discrete Line  $\gamma$ -Ray Emission due to Neutron Inelastic Scatter and**  
**Primary Galactic Cosmic Ray Interactions with a Lunar-Type Surface**

Element	Source	Energy (MeV)	Yield	Half-Life (where applicable)
C	$^{12}\text{C}(n,n\gamma)$	4.4383	1.00	
N	$^{14}\text{N}(n,n\gamma)$	5.1049	0.80	
	$^{14}\text{N}(n,\alpha\gamma)$	4.4441	1.00	
	$^{14}\text{N}(n,n\gamma)$	2.3127	1.00	
	$^{14}\text{N}(n,\alpha\gamma)$	2.1245	1.00	
	$^{14}\text{N}(n,n\gamma)$	1.6348	1.00	
O	$^{16}\text{O}(n,n\gamma)$	8.8691	0.072	
	$^{16}\text{O}(n,n\gamma)$	7.1170	1.00	
	$^{16}\text{O}(n,n\gamma)$	6.9172	1.00	
	$^{16}\text{O}(n,n\gamma)$	6.1294	1.00	
F	$^{16}\text{N}$	6.1294	0.69	7.14s
	$^{16}\text{O}(n,n\gamma)$	4.9490	0.40	
	$^{16}\text{O}(n,n\alpha\gamma)$	4.4383	1.00	
	$^{16}\text{O}(n,n\gamma)$	4.161	0.44	
	$^{16}\text{O}(n,\alpha\gamma)$	3.854	0.691	
	$^{16}\text{O}(n,n\gamma)$	3.833	1.00	
	$^{16}\text{O}(n,\alpha\gamma)$	3.6842	1.00	
	$^{16}\text{O}(n,\alpha\gamma)$	3.086	1.00	
	$^{16}\text{O}(n,n\gamma)$	2.7408	0.76	
	$^{16}\text{O}(n,n\gamma)$	1.753	0.126	
F	$^{19}\text{F}(n,n\gamma)$	1.3569	1.00	
	$^{19}\text{F}(n,n\gamma)$	1.2358	1.00	
	$^{19}\text{F}(n,n\gamma)$	0.1971	1.00	
Na	$^{23}\text{Na}(n,n\gamma)$	2.6396	1.00	
	$^{23}\text{Na}(n,n\gamma)$	1.6364	1.00	
	$^{20}\text{F}$	1.6337	1.00	11.56s
	$^{22}\text{Na}$	1.2745	1.00	2.62y
	$^{23}\text{Na}(n,n\gamma)$	0.4399	1.00	
Mg	$^{24}\text{Mg}(n,n\gamma)$	4.238	0.76	
	$^{24}\text{Mg}(n,n\gamma)$	3.8671	0.983	
	$^{24}\text{Na}$	2.7539	0.9995	14.96h
Mg	$^{24}\text{Mg}(n,n\gamma)$	2.7539	1.00	

**Table 3-3 (continued)**  
**Major Discrete Line  $\gamma$ -Ray Emission due to Neutron Inelastic Scatter and  
Primary Galactic Cosmic Ray Interactions with a Lunar-Type Surface**

Element	Source	Energy (MeV)	Yield	Half-Life (where applicable)
	$^{26}\text{Mg}(n,n\gamma)$	1.8087	1.00	
	$^{25}\text{Mg}(n,n\gamma)$	1.6117	1.00	
	$^{24}\text{Mg}(n,n\gamma)$	1.3686	1.00	
	$^{24}\text{Na}$	1.3686	1.00	14.96h
	$^{24}\text{Na}$	1.2745	1.00	14.96h
	$^{22}\text{Na}$	1.2745	0.9994	2.62y
	$^{26}\text{Mg}(n,n\gamma)$	1.1297	0.90	
Al	$^{27}\text{Al}(n,n\gamma)$	4.580	0.75	
	$^{27}\text{Al}(n,n\gamma)$	4.409	0.70	
	$^{27}\text{Al}(n,n\gamma)$	3.9556	0.88	
	$^{27}\text{Al}(n,n\gamma)$	3.2103	0.87	
	$^{27}\text{Al}(n,n\gamma)$	3.004	0.91	
	$^{27}\text{Al}(n,n\gamma)$	2.981	1.00	
	$^{24}\text{Na}$	2.7539	0.9995	14.96h
	$^{27}\text{Al}(n,n\gamma)$	2.734	0.24	
	$^{27}\text{Al}(n,n\gamma)$	2.2997	0.76	
	$^{26}\text{Al}$	1.8087	0.997	$7.4 \times 10^5\text{y}$
	$^{27}\text{Al}(n,d\gamma)$	1.8087	1.00	
	$^{27}\text{Al}(n,n\gamma)$	1.7195	0.76	
	$^{24}\text{Na}$	1.3686	1.00	14.96h
	$^{22}\text{Na}$	1.2745	0.9994	2.62y
	$^{27}\text{Al}(n,n\gamma)$	1.0144	0.97	
	$^{27}\text{Al}(n,n\gamma)$	0.8438	1.00	
	$^{27}\text{Mg}$	0.8438	0.71	9.46m
Si	$^{28}\text{Si}(n,n\gamma)$	7.4162	0.90	
	$^{28}\text{Si}(n,n\gamma)$	6.8777	0.65	
	$^{28}\text{Si}(n,n\gamma)$	5.6012	0.61	
	$^{28}\text{Si}(n,n\gamma)$	5.1094	1.00	
	$^{28}\text{Si}(n,n\gamma)$	5.0992	0.35	
	$^{28}\text{Si}(n,n\gamma)$	4.4972	0.91	
	$^{28}\text{Si}(n,n\gamma)$	3.2000	1.00	
	$^{28}\text{Si}(n,n\gamma)$	2.8387	1.00	

**Table 3-3 (continued)**  
**Major Discrete Line  $\gamma$ -Ray Emission due to Neutron Inelastic Scatter and**  
**Primary Galactic Cosmic Ray Interactions with a Lunar-Type Surface**

Element	Source	Energy (MeV)	Yield	Half-Life (where applicable)
	$^{24}\text{Na}$	2.7539	0.9995	14.96h
	$^{30}\text{Si}(n,n\gamma)$	2.2354	1.00	
	$^{26}\text{Al}$	1.8087	0.997	$7.4 \times 10^5\text{y}$
Si	$^{28}\text{Si}(n,n\gamma)$	1.7788	1.00	
	$^{28}\text{Al}$	1.7788	1.00	2.31m
	$^{24}\text{Na}$	1.3686	1.00	14.96h
	$^{22}\text{Na}$	1.2745	0.9994	2.62y
	$^{29}\text{Si}(n,n\gamma)$	1.2733	1.00	
P	$^{31}\text{P}(n,n\gamma)$	2.2337	1.00	
	$^{31}\text{P}(n,n\gamma)$	1.2661	1.00	
S	$^{32}\text{S}(n,n\gamma)$	2.2301	1.00	
Cl	$^{35}\text{Cl}(n,n\gamma)$	1.7632	1.00	
	$^{35}\text{Cl}(n,n\gamma)$	1.2194	1.00	
Ar	$^{40}\text{Ar}(n,n\gamma)$	1.4608	1.00	
K	$^{39}\text{K}(n,n\gamma)$	2.8137	1.00	
	$^{39}\text{K}(n,n\gamma)$	2.5225	1.00	
Ca	$^{40}\text{Ca}(n,n\gamma)$	5.2486	0.79	
	$^{40}\text{Ca}(n,n\gamma)$	3.9044	1.00	
	$^{40}\text{Ca}(n,n\gamma)$	3.7366	1.00	
	$^{40}\text{Ca}(n,\alpha\gamma)$	1.6112	1.00	
	$^{40}\text{Ca}(n,p\gamma)$	1.1589	0.86	
	$^{44}\text{Ca}(n,n\gamma)$	1.1569	1.00	
	$^{40}\text{Ca}(n,p\gamma)$	0.8916	1.00	
	$^{40}\text{Ca}(n,p\gamma)$	0.7705	1.00	
Ti	$^{48}\text{Ti}(n,n\gamma)$	1.3117	1.00	
	$^{48}\text{Ti}(n,n\gamma)$	0.9834	1.00	
	$^{46}\text{Ti}(n,n\gamma)$	0.8892	1.00	
	$^{46}\text{Sc}$	0.8892	1.00	83.9d
Cr	$^{52}\text{Cr}(n,n\gamma)$	1.5308	1.00	
	$^{52}\text{Cr}(n,n\gamma)$	1.4342	1.00	
	$^{52}\text{Cr}(n,n\gamma)$	1.3338	1.00	
	$^{52}\text{Cr}(n,n\gamma)$	0.9356	1.00	

**Table 3-3 (continued)**  
**Major Discrete Line  $\gamma$ -Ray Emission due to Neutron Inelastic Scatter and**  
**Primary Galactic Cosmic Ray Interactions with a Lunar-Type Surface**

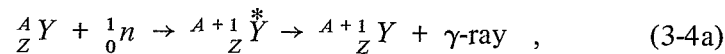
Element	Source	Energy (MeV)	Yield	Half-Life (where applicable)
	$^{55}\text{Mn}(n,n\gamma)$	1.5289	1.00	
	$^{55}\text{Mn}(n,n\gamma)$	1.1160	1.00	
	$^{55}\text{Mn}(n,n\gamma)$	0.8583	1.00	
	$^{54}\text{Mn}$	0.8348	1.00	303d
	$^{55}\text{Mn}(n,n\gamma)$	0.1260	1.00	
Fe	$^{56}\text{Fe}(n,n\gamma)$	3.6019	0.69	
	$^{56}\text{Fe}(n,n\gamma)$	2.601	1.00	
	$^{56}\text{Fe}(n,n\gamma)$	2.5231	0.87	
Fe	$^{56}\text{Fe}(n,n\gamma)$	2.1129	1.00	
	$^{56}\text{Fe}(n,n\gamma)$	1.8109	1.00	
	$^{54}\text{Fe}(n,n\gamma)$	1.4077	1.00	
	$^{56}\text{Fe}(n,2n\gamma)$	1.3164	1.00	
	$^{56}\text{Fe}(n,n\gamma)$	1.2383	1.00	
	$^{56}\text{Fe}(n,n\gamma)$	1.0380	1.00	
	$^{56}\text{Fe}(n,2n\gamma)$	0.9312	1.00	
	$^{56}\text{Fe}(n,n\gamma)$	0.8467	1.00	
	$^{54}\text{Mn}$	0.8348	1.00	303d
Ni	$^{58}\text{Ni}(n,n\gamma)$	1.4544	1.00	
	$^{60}\text{Ni}(n,n\gamma)$	1.3325	1.00	
	$^{58}\text{Co}$	0.8106	1.00	71.3d
Sr	$^{88}\text{Sr}(n,n\gamma)$	1.8360	1.00	
Y	$^{88}\text{Y}$	1.8360	0.994	108.1d
	$^{89}\text{Y}(n,n\gamma)$	1.7445	1.00	
	$^{89}\text{Y}(n,n\gamma)$	1.5074	1.00	
	$^{89}\text{Y}(n,n\gamma)$	0.9092	1.00	
Zr	$^{90}\text{Zr}(n,n\gamma)$	2.1865	1.00	
	$^{92}\text{Zr}(n,n\gamma)$	0.9345	1.00	
	$^{94}\text{Zr}(n,n\gamma)$	0.9182	1.00	
	$^{89}\text{Zr}$	0.9092	1.00	78.4h
Ba	$^{138}\text{Ba}(n,n\gamma)$	1.4359	1.00	

**Note:** y = years, d = days, h = hours, m = minutes, s = seconds.

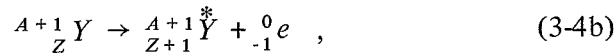
interaction leads to the production of radionuclides by spallation. The latter process is of much greater importance when considering the solar  $\gamma$ -rays and activation of  $\gamma$ -ray detectors during spaceflight and will therefore be considered in greater detail in Chapter 4 and Chapter 12.

Secondary neutrons with energies below the first excited level of the nuclei in a condensed medium irradiated by the incident cosmic rays can be elastically scattered by various nuclei, and can either escape the media or be captured by other nuclei.

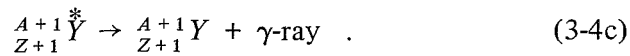
Another important process leading to  $\gamma$ -ray emission can be described as follows:



then for example, if  ${}^A_Z Y^{A+1}$  is an unstable nucleus



and possibly



The  $\gamma$ -ray emission accompanying the process in Equation (3-4a) is prompt and will be referred to as a prompt capture process. The  $\gamma$ -ray emitted by the decay of the radioactive nuclide shown in Equations (3-4b) and (3-4c) follows the decay of the electron ( ${}^0_{-1} e$ ). The energy involved in the prompt capture is comparable to the binding energy of the nucleus and thus, in most cases, is higher than the energy of the  $\gamma$ -rays with the given energy produced by inelastic interaction or by the decay of radionuclides. Table 3-4 is a compilation of prompt capture lines and activation lines. The yield is the fraction of  $\gamma$ -rays with the given energy produced per excitation of the excited level. Table 3-5 is a tabulation of spallation products of interest in planetary exploration.

**Table 3-4**  
**Major Discrete Line Emission due to Prompt Capture and**  
**Neutron Activation in Lunar-Type Material**

Element	Source	Energy (MeV)	Yield	Half-Life (where applicable)
H	$^1\text{H}(n,\gamma)$	2.2233	1.00	
N	$^{14}\text{N}(n,\gamma)$	10.8295	0.135	
	$^{14}\text{N}(n,\gamma)$	6.3225	0.184	
	$^{14}\text{N}(n,\gamma)$	5.5334	0.185	
	$^{14}\text{N}(n,\gamma)$	5.298	0.217	
	$^{14}\text{N}(n,\gamma)$	5.2693	0.311	
	Na	$^{23}\text{Na}(n,\gamma)$	6.395	0.20
$^{24}\text{Na}$		2.7539	0.9995	14.96h
$^{24}\text{Na}$		1.3686	1.00	14.96h
$^{23}\text{Na}(n,\gamma)$		0.4723	1.00	
Mg		$^{24}\text{Mg}(n,\gamma)$	3.918	0.48
	$^{24}\text{Mg}(n,\gamma)$	2.8285	0.36	
Al	$^{27}\text{Al}(n,\gamma)$	7.724	0.30	
	$^{27}\text{Al}(n,\gamma)$	7.694	0.045	
	$^{27}\text{Al}(n,\gamma)$	4.735	0.057	
	$^{27}\text{Al}(n,\gamma)$	4.2600	0.06	
	$^{27}\text{Al}(n,\gamma)$	4.1340	0.065	
	$^{27}\text{Al}(n,\gamma)$	3.0345	0.08	
	$^{27}\text{Al}(n,\gamma)$	2.960	0.09	
	$^{28}\text{Al}$	1.7788	1.00	2.31m
	Si	$^{28}\text{Si}(n,\gamma)$	7.200	0.08
$^{28}\text{Si}(n,\gamma)$		6.381	0.13	
$^{28}\text{Si}(n,\gamma)$		4.934	0.61	
$^{28}\text{Si}(n,\gamma)$		3.5395	0.66	
$^{28}\text{Si}(n,\gamma)$		2.0931	0.20	
$^{28}\text{Si}(n,\gamma)$		1.2733	0.19	
S	$^{32}\text{S}(n,\gamma)$	5.424	0.55	
	$^{32}\text{S}(n,\gamma)$	2.379	0.40	
Cl	$^{35}\text{Cl}(n,\gamma)$	7.791	0.09	
	$^{35}\text{Cl}(n,\gamma)$	7.415	0.11	
	$^{35}\text{Cl}(n,\gamma)$	6.621	0.09	
	$^{35}\text{Cl}(n,\gamma)$	6.111	0.21	

**Table 3-4 (continued)**  
**Major Discrete Line Emission due to Prompt Capture and**  
**Neutron Activation in Lunar-Type Material**

Element	Source	Energy (MeV)	Yield	Half-Life (where applicable)
K	$^{35}\text{Cl}(n,\gamma)$	1.951	0.20	
	$^{39}\text{K}(n,\gamma)$	7.770	0.07	
	$^{39}\text{K}(n,\gamma)$	5.7525	0.07	
	$^{39}\text{K}(n,\gamma)$	5.697	0.07	
	$^{39}\text{K}(n,\gamma)$	5.381	0.09	
Ca	$^{39}\text{K}(n,\gamma)$	0.7705	0.58	
	$^{40}\text{Ca}(n,\gamma)$	6.4200	0.40	
	$^{40}\text{Ca}(n,\gamma)$	5.9005	0.07	
	$^{40}\text{Ca}(n,\gamma)$	4.419	0.18	
	$^{40}\text{Ca}(n,\gamma)$	2.0015	0.18	
Ti	$^{40}\text{Ca}(n,\gamma)$	1.9427	0.80	
	$^{48}\text{Ti}(n,\gamma)$	6.7615	0.40	
	$^{48}\text{Ti}(n,\gamma)$	6.557	0.04	
	$^{48}\text{Ti}(n,\gamma)$	6.419	0.28	
	$^{48}\text{Ti}(n,\gamma)$	4.967	0.03	
	$^{48}\text{Ti}(n,\gamma)$	4.882	0.05	
	$^{48}\text{Ti}(n,\gamma)$	1.7620	0.045	
	$^{48}\text{Ti}(n,\gamma)$	1.5853	0.09	
	$^{48}\text{Ti}(n,\gamma)$	1.4983	0.04	
	$^{48}\text{Ti}(n,\gamma)$	1.3815	0.82	
Cr	$^{48}\text{Ti}(n,\gamma)$	0.3419	0.38	
	$^{53}\text{Cr}(n,\gamma)$	9.719	0.10	
	$^{53}\text{Cr}(n,\gamma)$	8.8840	0.24	
Mn	$^{52}\text{Cr}(n,\gamma)$	7.939	0.11	
	$^{55}\text{Mn}(n,\gamma)$	7.244	0.10	
	$^{55}\text{Mn}(n,\gamma)$	7.058	0.09	
Fe	$^{56}\text{Mn}$	1.8109	0.29	2.576h
	$^{56}\text{Mn}$	0.8467	0.988	2.576h
	$^{54}\text{Fe}(n,\gamma)$	9.299	0.034	
	$^{56}\text{Fe}(n,\gamma)$	7.6457	0.22	
	$^{56}\text{Fe}(n,\gamma)$	7.6313	0.24	
	$^{56}\text{Fe}(n,\gamma)$	7.279	0.05	

**Table 3-4 (continued)**  
**Major Discrete Line Emission due to Prompt Capture and**  
**Neutron Activation in Lunar-Type Material**

Element	Source	Energy (MeV)	Yield	Half-Life (where applicable)
	$^{56}\text{Fe}(n,\gamma)$	6.019	0.08	
	$^{56}\text{Fe}(n,\gamma)$	5.921	0.08	
	$^{56}\text{Fe}(n,\gamma)$	4.810	0.018	
	$^{56}\text{Fe}(n,\gamma)$	4.2185	0.04	
	$^{56}\text{Fe}(n,\gamma)$	1.725	0.09	
Fe	$^{56}\text{Fe}(n,\gamma)$	1.6126	0.07	
	$^{56}\text{Fe}(n,\gamma)$	0.6921	0.08	
Ni	$^{58}\text{Ni}(n,\gamma)$	8.999	0.37	
	$^{58}\text{Ni}(n,\gamma)$	8.534	0.18	
Sr	$^{87}\text{Sr}(n,\gamma)$	1.8360	0.45	
Y	$^{89}\text{Y}(n,\gamma)$	6.080	0.40	
Nd	$^{143}\text{Nd}(n,\gamma)$	0.697	0.65	
Sm	$^{149}\text{Sm}(n,\gamma)$	0.4395	0.40	
	$^{149}\text{Sm}(n,\gamma)$	0.3340	0.70	
Eu	$^{152g}\text{Eu}$	1.409	0.15	12.7y
	$^{152g}\text{Eu}$	1.113	0.09	12.7y
Gd	$^{157}\text{Gd}(n,\gamma)$	6.747	0.02	
	$\text{Gd}(n,\gamma)$	1.187	0.11	
	$^{157}\text{Gd}(n,\gamma)$	0.945	0.07	
	$^{157}\text{Bd}(n,\gamma)$	0.182	0.22	

**Note:** y = years, d = days, h = hours, m = minutes, s = seconds.

**Table 3-5**  
**Spallation Products of Interest in Planetary Exploration**

Element	Source	Energy (MeV)
Mg	$^{20}\text{Ne}^*$	1.6337
Al	$^{23}\text{Na}^*$	1.6364
	$^{20}\text{Ne}^*$	1.6337
	$^{24}\text{Mg}^*$	1.3686
Si	$^{27}\text{Al}^*$	2.2104
	$^{20}\text{Ne}^*$	1.6337
	$^{24}\text{Mg}^*$	1.3686
	$^{27}\text{Al}^*$	1.0144
Ca	$^{39}\text{K}^*$	2.8137
	$^{39}\text{Ca}^*$	2.793
	$^{32}\text{S}^*$	2.2301
	$^{36}\text{Ar}^*$	1.9704
Fe	$^{52}\text{Cr}^*$	1.4342

For the activation products in Table 3-4 the yield is the fraction of  $\gamma$ -rays emitted per decay of the radionuclide. The half-lives of the radionuclides are also indicated. It must be remembered that the nature of the primary cosmic ray flux and thus the secondary particle flux can be strongly influenced by the presence of a magnetic field and atmosphere about a planetary body. Therefore calculation of induced  $\gamma$ -ray emission will be different for various planetary bodies in our solar system.

### Solar Proton Interactions

Both charged and neutral particles are released from the Sun during strong solar flares. About 90 percent of these particles are protons. For the purpose of this discussion only proton interactions will be considered. The spectral shape and intensity of the solar proton flux arriving at a planetary surface will depend on the distance from the Sun, and the presence of a magnetic field, and of an atmosphere about the planetary body. The solar proton flux is much lower in average energy than the cosmic ray flux. Thus, the induced  $\gamma$ -ray emission can be determined

from an analysis of the primary particle interaction, since the secondary particles produced will not be significant.

The solar protons will travel only a few centimeters in planetary materials. They will slow down by such interaction as inelastic scatter. Capture can also occur. Prompt and delayed  $\gamma$ -ray emission can be produced. In terms of remote  $\gamma$ -ray analysis, only the delayed  $\gamma$ -ray emission which is produced by the decay of a radioactive nuclide will be detectable since the prompt emission will be coincidental with the arrival of the solar proton flux. During large solar events, protons will tend to saturate the  $\gamma$ -ray detectors. Observation can therefore be made only after the proton flux has stopped.

The magnitude and spectral distribution of  $\gamma$ -ray emission due to the solar proton flux activation of a planetary surface will depend not only on the most recent event leading to proton irradiation, but also on the previous history of all other such events. From the half-lives of the activated species one can infer how far back in time the particular event produces nuclides of importance in remote  $\gamma$ -ray sensing. Some of the more important activated species observed on the Moon during Apollo 15 and 16 are shown in Table 3-6. The target nucleus is indicated as well as the activated radionuclides. Details for calculation of the solar proton flux and the radionuclides produced in the Moon can be found in Reedy and Arnold (1972), Reedy et al. (1973), and Reedy (1978).

**Table 3-6**  
**Solar Proton Induced  $\gamma$ -Ray Emission Observed**  
**During Apollo 15 and Apollo 16**

Element	Nuclide	Energy (MeV)	Half-Life
Mg	$^{22}\text{Na}$	1.2745	2.6y
Al	$^{26}\text{Al}$	1.8087	$7.5 \times 10^5\text{y}$
	$^{22}\text{Na}$	1.2745	2.6y
Si	$^{26}\text{Al}$	1.8087	$7.5 \times 10^5\text{y}$
	$^{22}\text{Na}$	1.2745	2.6y
Fe	$^{56}\text{Co}$	1.2383	78d
	$^{56}\text{Co}$	0.8467	78d
	$^{54}\text{Mn}$	0.8348	303d

**Note:** y = years, d = days.

## EXPERIMENTAL RESULTS

One of the early objectives of the space program has been understanding the origin, development, and present-day dynamics of the solar system. Remote orbital and in situ observations of X-rays,  $\gamma$ -rays, and particle emission from the surfaces of planetary bodies has provided new information relative to these objectives. In Chapter 2, a number of questions regarding the understanding of the evolution of the solar system were presented. It was indicated that the determination of a global distribution of the major, minor, and trace elements in such bodies as the planets, comets, and asteroids can significantly contribute to the development of evolutionary models of the solar system. For example, a knowledge of the overall elemental composition of a given body can be related to the mechanism of condensation and accumulation from the primordial solar nebula. Subsequent to accretion, the bulk distribution of elements has usually been affected by evolutionary processes. Thus, inferences can be made concerning early processes from a study of the present distributions.

During the manned and unmanned missions to the Moon and planets, X-ray and  $\gamma$ -ray remote sensing systems have been flown and successful measurements achieved. The combination of remote sensing, in situ analysis, and returned sample analysis has allowed us to obtain extensive global geochemical data on the Moon. In addition, the combination of orbital measurements and surface sampling has enabled us to verify the remote analysis measurement system.

A brief review of the missions in which successful measurements of X-ray,  $\gamma$ -ray, and  $\alpha$ -particle emission were accomplished will now be presented. Some of the more significant results relating to the development of models of solar evolution will also be indicated. Because it will be impossible to detail the results from all such flights, results from the remote sensing X-ray and  $\gamma$ -ray experiments aboard Apollo 15 and Apollo 16 will be considered in greater detail. In this way it is hoped that the power of these remote sensing techniques can be demonstrated and understood.

Rangers 3, 4, and 5 in 1961-1962 carried the first  $\gamma$ -ray spectrometer in space. Although the spacecraft did not come close enough to the Moon to measure emissions from the surface,

results were obtained on the spacecraft and cosmic backgrounds. The first indication of an isotropic diffuse cosmic  $\gamma$ -ray background was found as a result of an analysis of the Ranger  $\gamma$ -ray data (Metzger et al., 1964). In 1966 the Soviet lunar orbiter mission, Luna, carried a  $\gamma$ -ray spectrometer, and the first  $\gamma$ -ray spectrum near the Moon was obtained. Detailed spectral information was not obtained because of the poor energy resolution of the detector and the background problems, but compositional distinctions between mare and terra provinces were recognized (Vinogradov et al., 1967). The first successful in situ measurement on the Moon was the  $\alpha$ -backscatter experiment carried by Surveyor 5 in 1967. The surface composition at the landing site was found to be basaltic in nature. Measurements using this experiment on a number of Surveyor missions consistently indicated that the mare areas at the landing site were also basaltic (Turkevich, 1969). During the Apollo 15 and 16 flights in 1971 and 1972,  $\gamma$ -ray, X-ray, and  $\alpha$ -particle spectrometers were carried on the orbiting Command and Service Modules. Approximately 20 percent of the lunar surface was mapped for magnesium, aluminum, thorium, potassium, uranium, silicon, titanium and oxygen (Adler et al., 1972; Metzger et al., 1973; and Bjorkholm et al., 1973). The results obtained for the  $\gamma$ -ray and X-ray spectrometer experiments will be considered in detail in the following sections. Two Soviet Lunakhod roving vehicles carried X-ray fluorescence experiments. These detection systems were used to screen materials for selection for return flights to the Earth (Kocharov and Viktorov, 1974).

Remote nuclear techniques have been applied to Mars and Venus, though less extensively than to the Moon. A  $\gamma$ -ray spectrometer aboard the Soviet Mars 5 orbiter obtained several hours of data from an altitude of about 2300 km, indicating that the average potassium, uranium, and thorium content of the regions surveyed corresponds with that of terrestrial rocks like oceanic basalts (Surkov et al., 1976). The two Viking Landers carried an X-ray spectrometer for the fluorescence analysis of selected soil and rock samples (Clark et al., 1977). The finely divided samples at the two landing sites were remarkably similar, with high iron and sulfur content, and little potassium.

Three Soviet spacecraft, Venera 8, 9, and 10, have carried a  $\gamma$ -ray spectrometer to measure  $^{40}\text{K}$ , uranium and thorium at

the surface of Venus by detecting the decay of these naturally radioactive elements (Surkov, 1977). In addition, Venera 10 had a second  $\gamma$ -ray instrument on board to measure the bulk density of the surface materials. High abundances were found for potassium, uranium and thorium at the Venera 8 site, the potassium value being comparable to granitic rocks on Earth, while the uranium and thorium values are similar to those of alkali basalts. The Th/U ratio agrees with that found for major rock types on Earth, on the Moon, and in chondritic meteorites. The subsequent landings of Venera 9 and 10 measured sites with much lower  $\gamma$ -ray activity, with values for potassium and uranium similar to those of terrestrial oceanic basalt rocks.

### **Apollo X-Ray Spectrometer Results**

The Apollo X-ray spectrometer consists of three large area proportional detectors; a set of large area filters for energy discrimination among the characteristic X-rays of aluminum, silicon, and magnesium; collimators; and data-handling electronics for obtaining 8-channel pulse-height spectra. These three detectors are pointed at the lunar surface while taking measurements. A fourth proportional counter that looked in the direction opposite to the three large area proportional counters was used as a solar monitor.

The characteristic X-ray emission flux variation reflects the changes in nature of the different surface elemental composition overflow. A number of other factors can also produce variation in the observed X-ray emission flux from orbit. The variation in intensity because of changes in the incident solar flux was monitored by measuring the solar differential energy spectra incident on the lunar surface. Correction methods for solar flux variation have been developed (e.g., Clark, 1979). Other sources of variation can be attributed to such factors as matrix effects, solar illumination angle, and surface roughness. Those effects are about the same for the magnesium, aluminum and silicon X-ray emission processes. These other factors can be substantially removed by the use of the intensity ratios, Al/Si and Mg/Si (Adler et al., 1972), which provide information on the magnesium and aluminum variation because the silicon variation is relatively small over the lunar surface covered by Apollo 15 and 16.

When considering the results obtained, three other factors must be kept in mind. First, the depth of surface materials sampled corresponds to tens of micrometers. Second, the collimators used on the detector system allowed observations to be made with spatial resolution of about 10 km on the lunar surface when the Apollo orbiter was at about 100 km from this surface; most of the measurements were obtained at about this altitude. Finally, observations can be obtained on the sunlit portions of the Moon since only X-rays from the Sun produce the fluorescence.

Figures 3-5 and 3-6 show Al/Si and Mg/Si ratio profiles along a northern track observed during the Apollo 15 mission (Alder et al., 1972). The ratios for various analyzed materials are shown along the right-hand axis for reference. Each point on the graph represents 16 seconds of data accumulation. A number of observations can be drawn from a study of these figures.

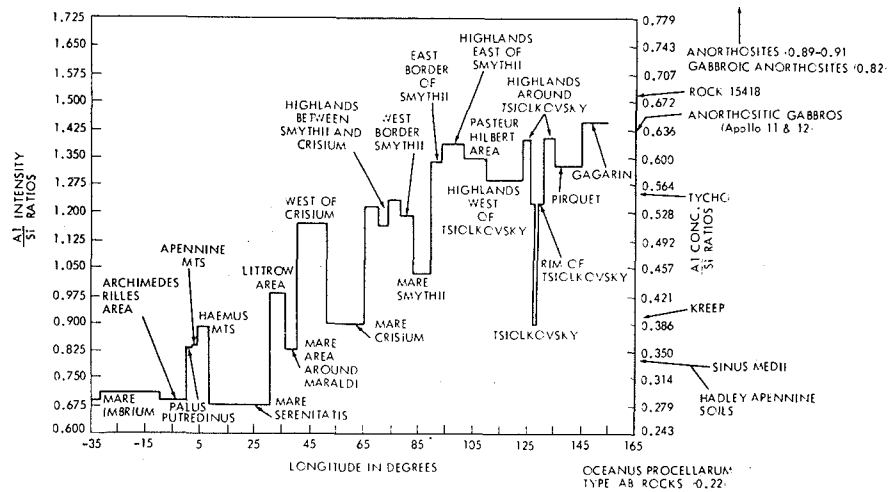


Figure 3-5. Al/Si ratio as a function of longitude for an Apollo 15 ground track. The values for some reference materials are indicated on the right-hand axis.

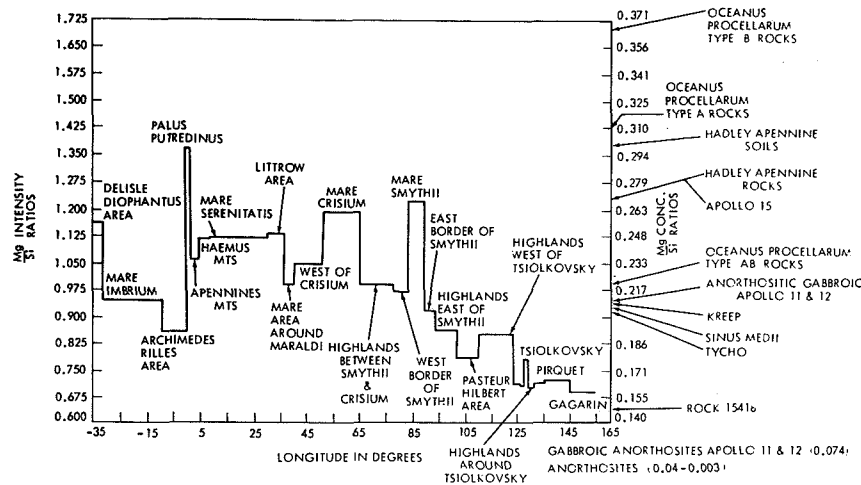


Figure 3-6. The Mg/Si ratio as a function of longitude for an Apollo 15 ground track. The values for some reference material are indicated on the right-hand axis.

- The Al/Si ratios are high in the highlands and are considerably lower in the mare areas. The extreme variation is about a factor of two. The Mg/Si concentration ratios generally show the opposite relationship.
- There is a general tendency for Al/Si ratio values to increase from the western mare areas to the eastern limb highlands.
- There are distinct chemical contrasts between such features as the small mare basins and the highland rims (note, for example, the crater Tsiolkovsky in Figure (3-5)). The rim areas are intermediate between the mare areas and the surrounding highlands.

- There was agreement between the  $\text{Al}_2\text{O}_3$  content of the returned Apollo samples and that inferred from the X-ray measurements. This demonstrated that the orbital measurements are a reliable guide to at least this aspect of the lunar surface chemistry. Furthermore, a remarkable factor can be inferred regarding the vertical profile, that is the dust surface is characteristic of the composition below.

The above represents merely a few of the results obtained, but with these results the following observations can be made: This experiment clearly demonstrated that the Moon's crust is chemically differentiated. The global features can be used to define the extent of differentiation and clearly distinguish the mare basalt (low aluminum) from the highland anorthosites (high aluminum material). On a medium scale, it is seen that the terra and mare are increasingly aluminous from west to east, suggesting an inhomogeneous lunar crust.

Figure 3-7 shows a color coded map of all the X-ray data obtained during Apollo 15 and 16 missions. The Al/Si ratio is plotted (Andre et al., 1977). If one carefully studies this map, the ray structure due to meteor impact can be seen. This information can be used to obtain data on the vertical distribution of elemental composition, since these craters can disclose layers deep below the surface.

Finally, on a smaller scale ( $\sim 20$  km), details of cratering on the Moon can be investigated. Figure 3-8 shows impact cratering effects near the mare Crisium area. Here the Mg/Al ratio is plotted. Because of the intermittent inverse correlation between these elements, the change in elemental composition is emphasized. Such craters as Picard and others and a significant chemical contrast relative to the surroundings (Andre et al., 1978) are shown. This contrast is a surface expression of the excavation of the sub-surface material of different compositions. Higher magnesium is shown as an increase in red, while higher aluminum is shown as an increase in blue. The dark red area indicates a deep penetration into the surface. The surrounding material is blue, characteristic of highland material as compared with the basaltic material characterized by the red.

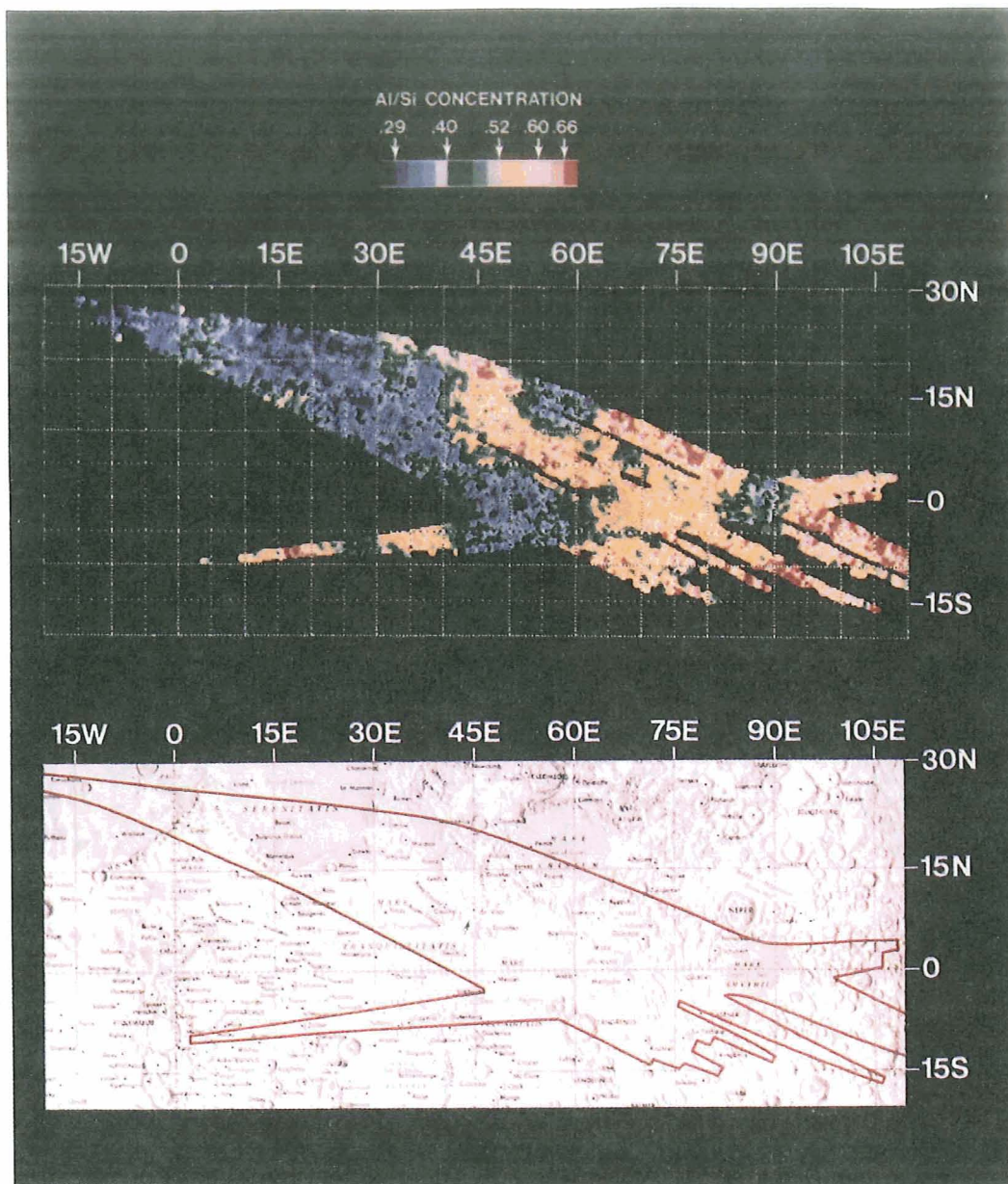


Figure 3-7. Color coded Al/Si map of all of the X-ray fluorescence data obtained during Apollo 15 and Apollo 16 (Andre et al., 1977).

### The Apollo $\gamma$ -Ray Spectrometer

The Apollo  $\gamma$ -ray detector consisted of a  $7 \times 7$  cm right cylindrical NaI (Tl) crystal detector surrounded by a plastic anti-coincidence mantle for suppressing events due to charged  $\alpha$ -particles. The electronic processor consisted of a 512-channel pulse-height analyzer including an amplifier but no memory. The information was transmitted channel by channel, either in realtime or

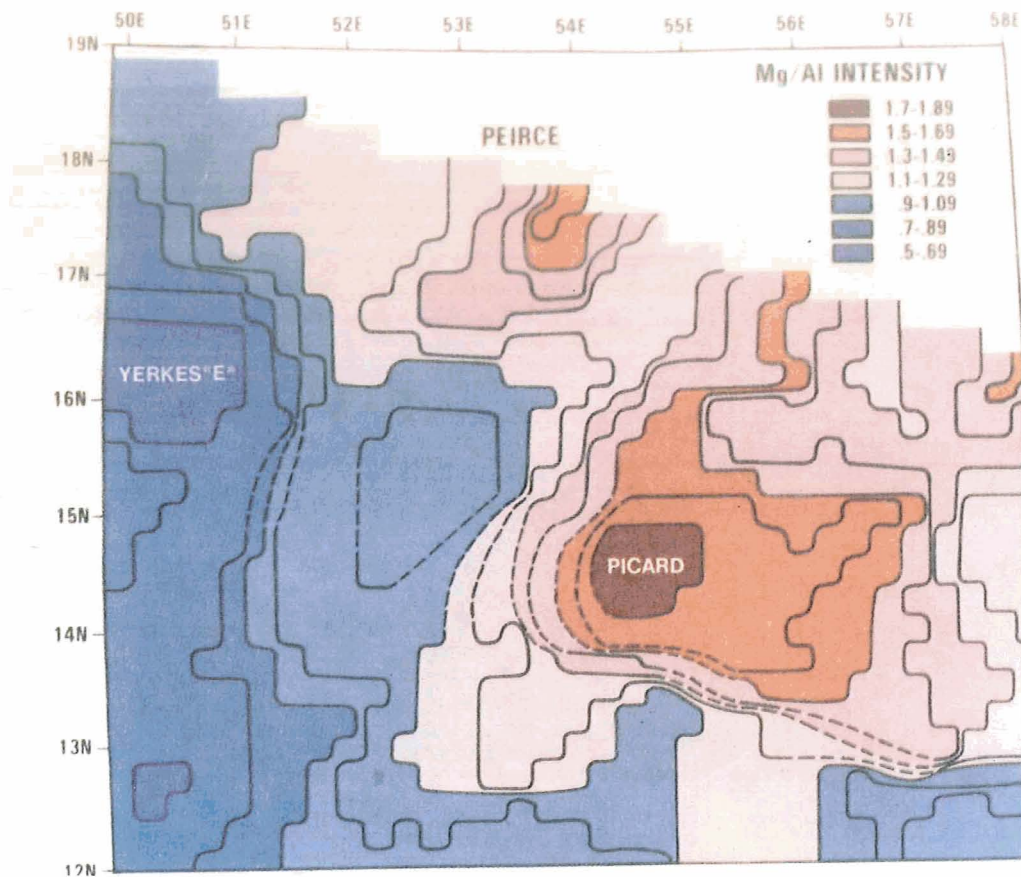


Figure 3-8. Color coded Mg/Al ratio map in the mare Crisium area showing lunar surface cratering on a  $\sim 20$  km resolution scale (Andre et al., 1978).

stored on magnetic tape for subsequent transmission. Spectra were obtained by sorting the received pulses for various time periods. Approximately 30 minutes of data accumulation is required to obtain a statistically significant spectrum. The detector was deployed on a boom some 8.3 m from the spacecraft in order to minimize the background  $\gamma$ -radiation produced on the spacecraft by cosmic ray interactions. The instrument design and data analysis and the background problems will be discussed in Chapter 12 and Chapter 13. Details on detector design can be found in papers by Arnold et al. (1972) and Harrington et al. (1974).

Figure 3-9 is an energy loss or pulse-height spectrum of the discrete line emission from the Moon. By the energy loss or pulse height, we mean the discrete line spectrum as observed by the scintillation detector. There have been no corrections for detector response and efficiency as a function of energy. The conversion to energy from pulse height is 19.5 keV/channel. The energy

region up to approximately channel 140 is dominated by the  $\gamma$ -rays produced by the natural radioactive components  $^{40}\text{K}$ , thorium, and uranium. Thus, the integrated counts up to this energy will reflect the variation in these radioactive elements. Figure 3-10 is a color coded map indicating the variation in intensity of natural radioactive emission of the Moon for those areas observed during Apollo 15.

Low radioactivity is indicated in blue and increases in intensity to red. Because of the higher count rate, the best spatial resolution maps can be obtained for these components. Similar maps have been obtained for iron and lithium. More complete elemental compositions have been obtained over much larger areas of the Moon. Table 3-7 shows a number of more complete elemental analysis over a few areas of the Moon. As can be seen in Figure 3-10 the area measured by the  $\gamma$ -ray spectrometer system is much larger than that covered by the X-ray system. Remember

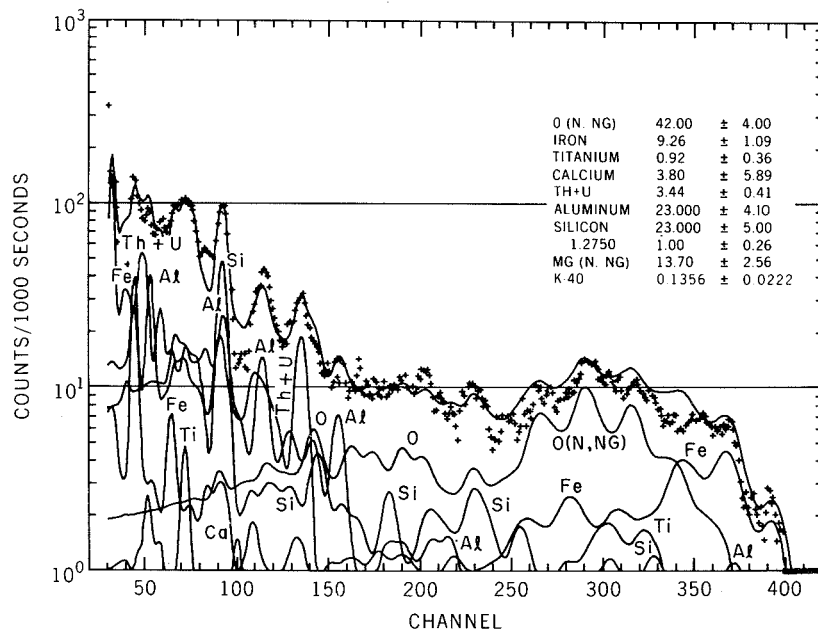
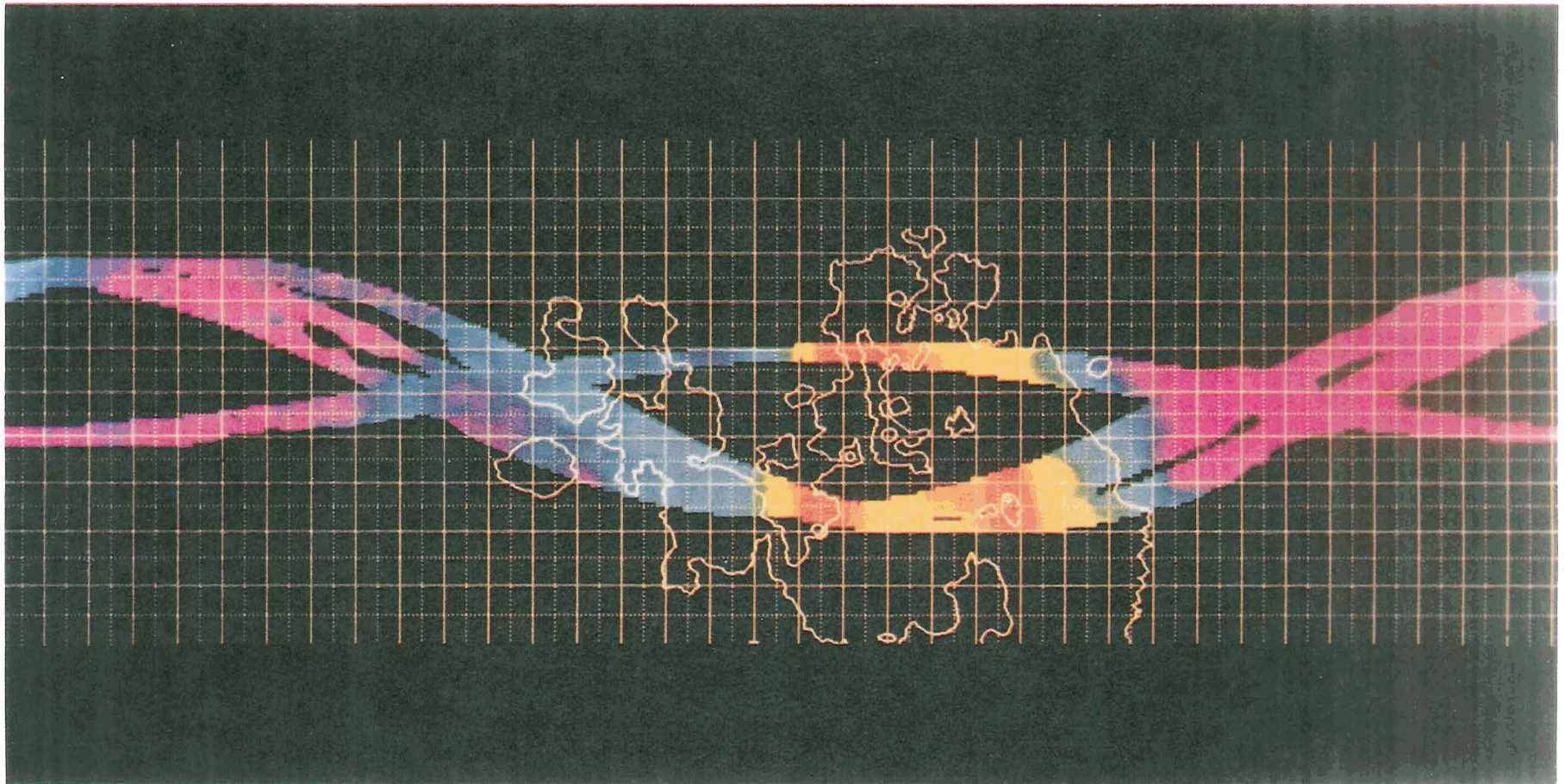


Figure 3-9. Discrete line spectrum measured by the Apollo  $\gamma$ -ray spectrometer during Apollo 15. The background has been subtracted. The characteristic  $\gamma$ -ray signature for each of the elements contributing a significant photon flux are also shown. The energy to pulse-height conversion is approximately 19.5 keV per channel.



*Figure 3-10. Distribution of naturally radioactive elements potassium, thorium, and uranium over the region overflowed by the Apollo 15 and Apollo 16 Command and Service Modules. The count rate which is proportional to the concentration of the radioactive elements is color coded: blue for low count rate to red for the highest count rate.*

**Table 3-7**  
**Elemental Composition of Selected Lunar Sites as Determined**  
**from the Apollo 15 Remote Sensing  $\gamma$ -Ray Experiment**

Lunar Feature	Coordinate Boundary Region	Element Concentration in				
		Fe(%)	Mg(%)	Ti(%)	Th(ppm)	K(ppm)
Van de Graff	168°W - 168°E	7.7	3.8	0.1	2.3	1600
Highland East	88°E - 60°E	6.5	4.5	1.3	1.0	940
Mare						
Fecunditatis	60°E - 42°E	11.3	7.0	2.2	1.2	1400
Mare Imbrium	15°W - 39°W	13.6	6.2	1.4	5.8	1700
Aristarchus						
Region	54°W - 81°W	9.6	4.9	2.2	6.9	2500
Highland West	81°W - 68°W	5.7	3.5	1.5	0.4	950
Average over all of Apollo 15 Orbit		8.7	4.8	1.5	2.2	1230

**Note:** ppm = parts per million.

**Source:** Trombka et al. (1977).

that the  $\gamma$ -ray emission is caused by natural radioactive and cosmic ray-induced activation and thus is independent of the position of the Sun relative to the Moon.

A number of characteristics of the elemental distributions shown in Figure 3-10 and Table 3-7 should be pointed out. Some of the factors are considered relative to the analysis of returned lunar samples. Details of the analysis carried out on the lunar samples can be found in the yearly Proceedings of the Lunar Science Conference, from 1968 to the present. The articles are too numerous to list here. The observations cannot be extended to the whole Moon; however, they represent the areas overflowed during the Apollo 15 and Apollo 16 missions only.

The regions within and bounding the western maria (Oceanus Procellarum) show higher levels of radioactivity than any others elsewhere on the lunar surface. There is a striking contrast between this region and the rest of the Moon, particularly the eastern maria. Further, there is a detailed structure in the distribution of radioactivity within the high radioactivity regions. The highest

concentration, shown in red on Figure 3-10, were in the Aristarchus region in the high ground west of the Apollo 15 landing site and south of Archimedes and in the area south of the Fra Mauro crater. The Fra Mauro site overflow is about  $7^\circ$  south of the Apollo 14 landing site. The soil from the landing sites showed levels comparable to the orbital data.

The eastern maria show evidence of local enhancement although the radioactivity is lower than the western maria. The highland regions showed relatively low radioactivity except on the borders of the western maria, where lateral mixing may have occurred. The eastern far side highlands ( $180^\circ$  to  $90^\circ$  east) are measurably more radioactive than the western highlands ( $90^\circ$  to  $180^\circ$  west). A small maximum in activity was found near Van de Graff, where a major magnetic anomaly exists.

Laser altimeter profiles were obtained during the Apollo mission (Sjogren and Wollenhaupt, 1973). Comparison between the Al/Si ratio data shown in Figure 3-5, the distribution of radioactivity Figure 3-10, and the laser altimeter data (Trombka et al., 1973) reveal the following observations: the Al/Si ratio profile directly correlates with the laser altimeter data. With the exception of the Imbrium Procellarium area marked inverse correlation can be seen between the natural radioactivity and the elevation. While this inverse correlation is also broadly true of the Imbrium Procellarium region, it does not hold up with regard to the detailed structure in the variation in radioactivity. On the far side, this inverse correlation extends to an observation of greater east-west asymmetry—around  $180^\circ$  for the Apollo 16 trajectory than that of the Apollo 15: an asymmetry which exists for both elevation and natural radioactivity. This correlation and the inverse correlation appear to reflect the nature and extent of major lunar differentiation processes. If the Moon is in an isostatic equilibrium, then the more extensive the early anorthositic differentiation (characterized by lower densities and lower concentrations of the naturally radioactive nuclides compared to the mare), the higher the aluminum concentration and the lower the radioactivity.

The major depression, which occurs in the vicinity of the crater Van de Graff, exhibits the sharpest contrast in elevation to the adjacent highlands, a difference of the order of about 8 km. The same area is also the site of the only major far side enhancement in natural radioactivity. A strong magnetic feature is also

observed in this area by magnetometers aboard the Apollo subsatellite (Coleman et al., 1973). Thus, over this portion of the lunar surface as scanned up to date, are the largest surface remnant magnetic field, one of the deepest depressions, and the only significant far side enhancement in radioactivity. All such features been observed within about 150 km of each other. This Van de Graff area is quite notable and, to date, quite a singular exception to the general conditions prevailing on the lunar far side. When understood, it is likely to contribute significantly to our understanding of lunar evolution. From the chemical composition shown in Table 3-7, the Van de Graff shows a difference from any thus far observed on the Moon. The other mare and highland-like composition have been found abundantly in returned lunar samples. For the Van de Graff composition, the major elements are highland-like, though the iron concentration is a little high. The concentration of potassium and thorium are very similar to the eastern mare. One returned lunar sample, a "granite-" like rock (12013) contained what might be similar to the Van de Graff composition even though this region is on the far side of the Moon. The origin of this rock may be from this region.

Early interpretations of the  $\gamma$ -ray results were presented in terms of three components: mare basalts, KREEP (mare-type materials high in potassium (K), rare earths (RE) and phosphorus (P)), and a low radioactivity highland component (Metzger et al., 1973). The Van de Graff component does not fit this model but otherwise the components shown in Table 3-7 do follow this pattern. The so-called KREEP material may have their origin in the region of the hot spots shown in Figure 3-10. Most returned sample compositions can be inferred from a mixture of these basic components.

The large highland regions are not entirely uniform. The iron shows a notable east-west asymmetry. The iron concentration is higher in the eastern regions. The values of titanium found on the far side highlands are also high and are possibly another example of inhomogeneity in broad highland areas. There are also titanium differences in the maria and KREEP regions.

A most interesting result can be found in the ratio of K/Th. Potassium is a volatile material and thorium is a refractory. Thus, this ratio can be used to measure the volatile-to-refractory material variation. In both missions this ratio varied around the

Moon and was found to be consistently lower than that found on Earth. This reflects a global depletion of volatiles for the Moon as compared to the Earth.

In the above two sections, a review of the results of the remote sensing  $\gamma$ -ray and X-ray results has been presented. The detailed summary of the early analysis can be found in Trombka et al. (1977). Again, many papers have been published including more detailed analyses. It is impossible to list all the relevant articles. The reader is referred to the results published each year in the Proceedings of the Lunar and Planetary Science Conference for more detailed results and interpretation of these data.

With these experiments as a beginning, detailed geochemical maps of bodies of our solar systems can be obtained. Once these results are obtained, theories of the evolution and dynamics of our solar system can be constructed.

## REFERENCES

- Adler, I., and Trombka, J.I., 1977, *Phys. and Chem. of the Earth*, 10, 17.
- Adler, I., Trombka, J., Gerard, J., Schmadebeck, R., Lowman, P., Blodget, H., Yin, L., Eller, E., Lamothe, R., Gorenstein, P., Bjorkholm, P., Harris, B., and Gursky, H., 1972, *Preliminary Science Report*, NASA SP-289, p. 436.
- Anders, E., 1977, *Phil. Trans. Roy., Soc. London*, A285, p. 23.
- Andre, C.G., Bielefeld, M.J., Eliason, E., Soderblom, L.A., Adler, I., and Philpotts, J.A., 1977, *Science*, 197, 986.
- Andre, G.W., Wolfe, R.W., and Adler, I., 1978, in *Mare Crisium: A View from Luna 24*, ed. R. Merrill (New York: Pergamon Press, 1978), p. 1.
- Arnold, J.R., Peterson, L.E., Metzger, A.E., and Trombka, J.I., 1972, *Preliminary Science Report*, NASA SP-289.
- Bjorkholm, P., Golub, L., and Gorenstein, P., 1973, *Proc. Fourth Lunar Planet. Sci. Conf.*, 3, 2803.
- Brandt, W., 1972, *Proc. Int. Conf. on Inner Shell Ionization Phenomena*, USAEC Conf. 720404, 2, 948.
- Clark, B.C., III, Baired, A.K., Rose, H.J., Jr., Toulmin, P., III, Christian, R.P., Kelliher, W.C., Castro, A.J., Rowe, C.D., Keil, K., and Huss, G.R., 1977, *J. Geophys. Res.*, 82, 4577.
- Clark, P.E., 1979, "Corrections, Correlation and Theoretical Considerations of Lunar X-Ray Fluorescence Intensity Ratios," Ph. D. Diss., University of Maryland.
- Coleman, P.J., Jr., Lichtenstein, B.R., Russell, C.T., Schubert, G., and Sharp, L.R., 1973, *Apollo 16 Preliminary Science Report*, NASA SP-315, p. 23-1.

- Harrington, T.M., Marshall, J.H., Arnold, J.R., Peterson, L.E., Trombka, J.I., and Metzger, A.E., 1974, *Nucl. Instr. and Meth.*, **118**, 401.
- Hubbell, J.H., 1969, *Photon Cross-Sections, Attenuation Coefficients, and Energy Absorption Coefficients from 10 keV to 100 GeV*, NSDRS-NBS 29 (Washington, D.C.: National Bureau of Standards, 1969).
- Jenkins, R., and DeVries, J., 1967, *Practical X-Ray Spectrometry* (New York: Springer-Verlag, Inc., 1967).
- Kocharov, G. Ye, and Viktorev, S.V., 1974, *Doklady Academy of Sciences, USSR*, **214**, 71.
- Kornblum, J.J., and Fireman, E.L., 1974, *Preprint No. 51* (Washington, D.C.: Smithsonian Astrophysical Observatory, Center for Astrophysics, 1974).
- Lapides, J.R., 1981, Ph. D. Dissertation, University of Maryland.
- Lapides, J.R., Spergel, M.S., Lazareth, O.W., Levy, P.W., Reedy, R.C., and Trombka, J.I., 1980, *Abstracts Lunar and Planet. Sci. Conf. XI* (Houston, Texas: NASA, L.B. Johnson Space Center, 1980), p. 605.
- Lingenfelter, R.E., Canfield, E.H., and Hess, W.N., 1961, *J. Geophys. Res.*, **66**, 2665.
- Lingenfelter, R.E., Canfield, E.H., and Hampel, V.E., 1972, *Earth and Planetary Sci. Ltr.*, **16**, 355.
- Metzger, A.E., Anderson, E.C., Van Dilla, M.A., and Arnold, J.R., 1964, *Nature*, **204**, 766.
- Metzger, A.E., Trombka, J.I., Peterson, L.E., Reedy, R.C., and Arnold, J.R., 1973, *Science*, **179**, 800.
- Reedy, R.C., 1978, *Proc. Ninth Lunar Planet. Sci. Conf.*, 2961.

- Reedy, R.C., and Arnold, J.R., 1972, *J. Geophys. Res.*, **77**, 537.
- Reedy, R.C., Arnold, J.R., and Trombka, J.I., 1973, *J. Geophys. Res.*, **78**, 5847.
- Sjorgren, W.L., and Wollenhaupt, W.R., 1973, *Science*, **179**, 275.
- Spergel, M.S., Lazareth, O.W., Slatest, L.A., and Levy, P.W., 1980, *Abstracts Eleventh Lunar Planet. Sci. Conf.* (Houston, Texas: NASA, L. B. Johnson Space Center, 1980), p. 1069.
- Surkov, Y.A., 1977, *Proc. Eighth Lunar Planet. Sci. Conf.*, **3**, 2665.
- Surkov, Y.A., Moskalyova, L.P., Kirnozov, F.F., Khyarkukova, V.P., Manvelian, O.S., and Shchelov, O.P., 1976, *Space Research XVI* (Berlin: COSPAR Akademie-Verlag, 1976).
- Toburen, L.H., 1972, *Phys. Rev.*, **A5**, 2482.
- Trombka, J.I., Arnold, J.R., Reedy, R.C., Peterson, L.E., and Metzger, A.E., 1973, *Proc. Fourth Lunar Planet. Sci. Conf., Geochim Cosmochim Acta*, **3**, 2847.
- Trombka, J.I., Arnold, J.R., Adler, I., Metzger, A.E., and Reedy, R.C., 1977, *The Soviet American Conference on Cosmochemistry of the Moon and Planets*, ed. J.H. Pomeroy, and N.J. Hubbard, NASA SP-370, p. 153.
- Tucker, W.H., and Koren, M., 1971, *Ap. J.*, **168**, 283.
- Turkevich, A.L., Franzgrote, E.J., and Patterson, J.H., 1969, *Science*, **165**, 277.
- Vinogradov, A.P., Surkov, Y.A., Chernov, G.M., Kirnozov, F.F., and Nazarkina, G.B., 1966, *Geochemistry No. 8* (Moscow: Vernadsky Institute of Geochemistry and Analytical Chemistry, 1966), p. 891.

Vinogradov, A.P., Surkov, Y.A., Chernov, G.M., Kirnozov, F.F.,  
and Nazarkina, G.B., 1967, *Cosmic Res. USSR*, **5**, 741.

Woolum, D.S., Burnett, D.S., Furst, M., and Weiss, J.R., 1975,  
*The Moon*, **12**, 231.

## Chapter 4

# Solar Observations

### INTRODUCTION

Gamma ray astronomy, as applied to observations of the Sun, has the specific objective to investigate high energy processes that take place in the Sun's atmosphere and the relationship of these phenomena to the basic problems of solar activity. Gamma ray emission exhibits characteristics of the conditions in regions where accelerated high energy particles interact. A number of  $\gamma$ -ray production mechanisms, both particle field and particle matter, are of interest in such astrophysical considerations. The types of particle field interactions which are of specific interest are the Compton effect, magnetobremssstrahlung, and photomeson production yielding  $\pi^0 \rightarrow 2\gamma$ . Examples of particle-matter interactions of interest are as follows: bremsstrahlung;  $\pi^0$  meson production by proton-proton interaction or by proton-antiproton annihilation; nuclear deexcitation; fission; electron-positron annihilation; and neutral or charged particle radiative capture or inelastic scatter. In all cases the original  $\gamma$ -ray at the source can have its energy modified by Compton scattering and/or Doppler, gravitational, or cosmological shifts and broadening. Most of the interactions are considered in this book. However, not all such processes are of interest in the study of solar  $\gamma$ -ray emission as measured from spacecraft in Earth orbit. Background problems significantly limit the  $\gamma$ -ray flux that can be observed at energies greater than 100 keV; in fact with presently available  $\gamma$ -ray detection systems, solar  $\gamma$ -ray emission can be detected during periods

of solar flares only. The nature of the  $\gamma$ -ray background problems are considered in later chapters of this book.

To illustrate the nature of the information that can be obtained from  $\gamma$ -ray spectroscopic observations during solar flares, a few  $\gamma$ -ray emission mechanisms will be considered. The annihilation  $\gamma$ -ray line at 0.511 MeV in solar flares results either from the free annihilation of positrons with electrons or from the formation and decay of positronium. In the case of free annihilation, the formation of the 0.511-MeV line depends on the source of the positrons, on their propagation in the solar atmosphere, and on the density and temperature of the ambient medium in which they decelerate. Nuclear  $\gamma$ -ray line emission is evidence that a particular nuclear species with the corresponding nuclear excitation level has been excited by particles with energies above the excitation threshold. Moreover, the elemental composition of excited species can be inferred from the  $\gamma$ -ray line emission. Two or more lines from the same nuclear species provide information on the energy spectrum of the exciting particles. For example, the relative intensities of the 15.1-MeV and 4.4-MeV  $\gamma$ -ray lines from the excitation and subsequent deexcitation of the corresponding states of  $^{12}\text{C}$  can be used to determine the spectral distribution of the exciting energetic particles (Crannell et al., 1977). Doppler shifts in selected  $\gamma$ -ray lines can be used to study the anisotropic propagation of charged particles during solar flares. Protons with energies greater than 10 MeV will excite the 6.1-MeV  $\gamma$ -ray line of  $^{16}\text{O}$ . Because  $\gamma$ -rays are emitted in a time that is short compared with the slowing down time of the nucleus, any directional anisotropy in the primary exciting particles would cause a Doppler shift in the central energy of the observed lines (Lingenfelter and Ramaty, 1967; Ramaty and Crannell, 1976; and Ramaty et al., 1977). Finally, if the spectrum of energetic charged particles extends to hundreds of MeV per nucleon in solar flares, high energy  $\gamma$ -radiation will result from the production and decay of  $\pi^0$  mesons.

## INTERACTION PROCESSES

Various interaction processes occur during solar flares. High energy particle interaction producing positronium, solar  $\gamma$ -ray emission, continuum emission, and  $\pi^0$  mesons will be of major interest in terms of  $\gamma$ -ray observations.

## Positron Annihilation and Formation of Positronium

The production of positrons during solar flares is believed to be due to the decay of  $\pi^+$  mesons and of radioactive nuclei produced in nuclear reactions of flare-accelerated particles with constituents of the solar atmosphere (Lingenfelter and Ramaty, 1967; and Ramaty et al., 1975). Table 4-1 lists the principal positron emitters, their half-lives, and maximum positron energies (Ramaty et al., 1975).

**Table 4-1**  
**Principal Positron Emitters**

Nuclear Species	Half-Life	Maximum Positron Energy (MeV)	Production Mode	Reactive Threshold (MeV)
$\mu^+$	$1.5 \times 10^{-6}$ s	53	$p + {}^1\text{H} \rightarrow \pi^+ \dots$ $p + {}^4\text{He} \rightarrow \pi^+ \dots$ $\pi^+ \rightarrow \mu^+ + \nu$	292.3 185
${}^{10}\text{C}$	19s	1.9	$p + {}^{16}\text{O} \rightarrow {}^{10}\text{C} + \dots$ $p + {}^{14}\text{N} \rightarrow {}^{10}\text{C} + \dots$ $p + {}^{12}\text{C} \rightarrow {}^{10}\text{C} + \dots$	41.4 17.1 34.4
${}^{11}\text{C}$	20.5m	0.92	$p + {}^{16}\text{O} \rightarrow {}^{11}\text{C} + \dots$ $p + {}^{14}\text{N} \rightarrow {}^{11}\text{C} + \dots$ $p + {}^{12}\text{C} \rightarrow {}^{11}\text{C} + \dots$	27.5 3.1 17.9
${}^{12}\text{N}$	0.011s	16.4	$p + {}^{12}\text{C} \rightarrow {}^{12}\text{N} + n$	19.6
${}^{13}\text{N}$	10m	1.19	$p + {}^{16}\text{O} \rightarrow {}^{13}\text{N} + \dots$ $p + {}^{14}\text{N} \rightarrow {}^{13}\text{N} + \dots$	5.5 9.0
${}^{14}\text{O}$	71s	1.8 (99.4%) 4.1 (0.6%)	$p + {}^{16}\text{O} \rightarrow {}^{14}\text{O} + \dots$ $p + {}^{14}\text{N} \rightarrow {}^{14}\text{O} + n$	30.7 6.3
${}^{15}\text{O}$	2.06m	1.74	$p + {}^{16}\text{O} \rightarrow {}^{15}\text{O} + \dots$ $\alpha + {}^{12}\text{C} \rightarrow {}^{15}\text{O} + n$	14.3 2.8
${}^{19}\text{Ne}$	17.4s	2.2	$\alpha + {}^{16}\text{O} \rightarrow {}^{19}\text{Ne} + n$	3.75

**Note:** m = minutes, s = seconds.

**Source:** Ramaty et al. (1975).

As can be seen from Table 4-1 nuclear species produced during solar flares decay to produce positrons ranging in energy from several hundred keV to several hundred MeV. In Figure 4-1

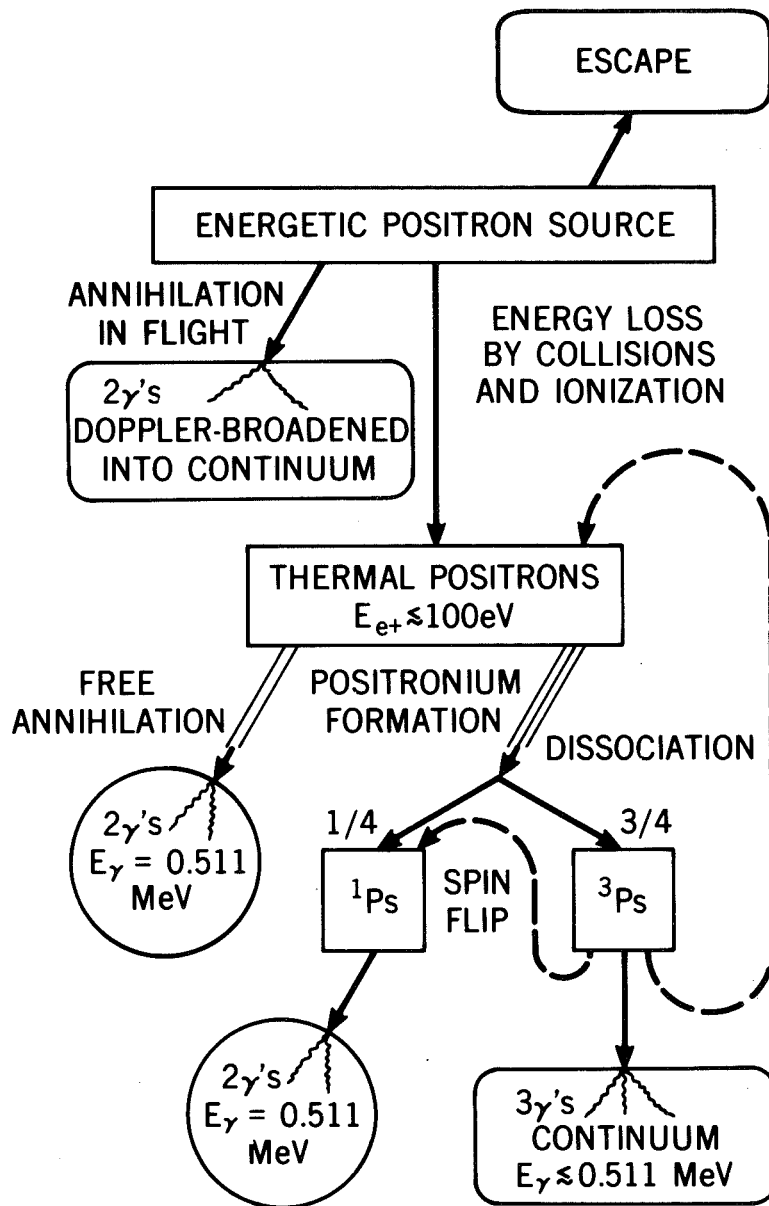


Figure 4-1. Possible methods of positron decay leading to  $\gamma$ -ray emission (Crannell et al., 1975).

an outline of the possible methods of positron decay leading to  $\gamma$ -ray emission is shown (Crannell et al., 1975). In the following discussion, Figure 4-1 can be used as a guide.

Relativistic positrons can annihilate in flight ( $\sim 10$  percent, e.g., Wang and Ramaty, 1975), escape from the Sun, or decelerate to thermal energies through interactions with ambient matter and magnetic fields. Those relativistic positrons which annihilate in flight produce 0.511-MeV line emission. Because of Doppler broadening, these annihilation lines are not observed at 0.511 MeV but appear as a  $\gamma$ -ray continuum.

Those positrons which do not escape from the Sun or annihilate in flight can lose energy by collision and ionization and thus be thermalized. The thermal positrons can then either annihilate freely or form positronium. Two 0.511 MeV  $\gamma$ -rays are produced per free annihilation. Because the annihilation occurs at thermal energies, there is very little Doppler broadening and these emissions can be observed as discrete  $\gamma$ -ray lines.

When a positron slows down in its passage through matter, it may join an electron to form a positron-electron system called positronium (Ps), which lasts for a measurable time before combining to produce annihilation radiation. Positronium can be thought of as an atom analogous to that of hydrogen in which an electron and a positron move in Bohr orbits about the center of mass, which is halfway between them. Of course, this is a rather peculiar atom since there is no nucleus. The lowest Bohr orbit of positronium is an S state. This state has fine structure because of the spins of the particles. The atom is in a  $^1S$  state when the two spins are oppositely directed. A  $^3S$  state can occur when the spins are parallel. The  $^3S$  state is a higher energy state than the  $^1S$  state. The triplet state is metastable and has an appreciably longer lifetime ( $1.4 \times 10^{-7}$  s) than the singlet state ( $1.2 \times 10^{-10}$  s). The annihilation radiation emitted by the combining of a positron-electron pair in a singlet state consists of two  $\gamma$ -ray photons emitted simultaneously with energies of 0.511 MeV each; but the annihilation radiation from the triplet state consists of three  $\gamma$ -ray photons emitted simultaneously each with energy less than 0.511 MeV. During positronium formation approximately 25 percent is formed in the singlet spin state and the other approximately 75 percent is formed in the triplet state. The energy threshold for positronium formation is 6.8 eV.

Depending on the state of ionization of the ambient medium, positronium production proceeds by radiation recombination with free electrons or by charge exchange with atoms and ions. The radiative recombination process can be considered to be that mechanism by which the positron approaches close enough to an electron to be captured and forms Ps, at the same time releasing energy of combination, that is



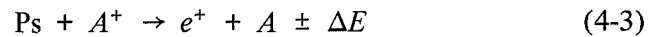
where  $\Delta E = 6.8$  eV is the energy discrepancy. An alternative mechanism is the three-body recombination process. These processes differ essentially in the method of disposal of the energy of recombination. The process indicated in Equation (4-1) seems to be the dominant mechanism for the case of interest in solar flares.

By charge exchange, the following interaction can be considered:



That is an interaction occurs between a positron  $e^+$  and a neutral atom  $A$  to form positronium, leaving atom  $A$  in an ionized state  $A^+$ . Again  $\Delta E$  is the energy discrepancy in the charge exchange interaction.

Two more processes of importance in positron interactions during solar flares must be considered in order to explain the spectral shape and flux magnitude of the  $\gamma$ -ray emission. Positron collisions with the ambient medium can produce spin flip transitions from the triplet  $^3\text{Ps}$  state to the singlet  $^1\text{Ps}$  state. Charge exchange with ions in the ambient medium can cause Ps dissociation; that is,



The  $\gamma$ -ray emission spectrum will depend on the fate of the positrons produced in a solar flare. The cross sections for the processes described above will depend on the temperature, density, and state of ionization of the solar flare environment. These cross sections have been considered in detail by Crannell et al. (1976). The results are summarized below.

For temperatures greater than  $10^6$  K, positron free annihilation dominates the decay process. For this case the width of the 0.511-MeV line is determined by the motion of the center of mass of the electron-positron pair, which is a function of the temperature of the medium. For temperatures just below  $10^6$  K, at which neutral hydrogen can be present, radiative recombination dominates over free annihilation. The relative importance of radiative recombination and charge exchange is determined by the residual neutral hydrogen abundance. For the fractional neutral densities characteristic of the quiescent solar atmosphere (Gabriel, 1971), charge exchange is expected to be the dominant process. At temperatures below a few times  $10^5$  K, positronium formation through charge exchange is a dominant reaction through which positrons annihilate. The relative rates of the competing processes of slowing down and of forming positronium depend primarily on the fractional ion density of the annihilation region.

When the ratio of the plasma density  $N_e$  to the neutral gas density  $N_n$  is greater than 0.5, most of the positrons first thermalize and then form positronium by charge exchange. This sequence of events could be maintained even if the mean energy of the ambient electrons were less than the 6.8 eV the threshold for positronium formation. When the positrons thermalize before forming positronium and the mean energy of the ambient electron is above 6.8 eV, the  $\gamma$ -ray line at 0.511 MeV will be broadened. When the mean energy is less than 6.8 eV, most of the positrons will form positronium at an energy just above the threshold. In this case the line will be broadened by only about 0.2 percent.

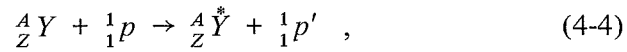
When the fraction of ions is low,  $N_e/N_n \leq 0.5$ , most of the positrons will form positronium before they are slowed below a kinetic energy of about 15 to 20 eV. The charge exchange cross section is a maximum in this energy domain. The rate of annihilation in this case is determined by charge exchange. It has been shown (Ramaty et al., 1975) that if the 2  $\gamma$ -ray decay occurs well before the positronium can thermalize, the Doppler broadening is determined by the mean kinetic energy of the positronium atom.

From the above discussion, it can be seen that the broadening of the line at 0.511 MeV and the ratio of the line intensity produced at 0.511 MeV to the continuum can be used to measure critical parameters relative to solar flare dynamics.

### **Charged and Neutral Particle Interactions**

Solar  $\gamma$ -ray emission can be stimulated by nuclear reactions between particles energized in solar flares and the abundant constituents of the ambient medium. The energetic particles include both primary charged particles and secondary particles which may be charged or neutral. Of particular interest for discrete  $\gamma$ -ray line production are those interactions involving protons,  $\alpha$ -particles, and neutrons. Capture, inelastic scattering, and spallation reaction are most important. Neutron prompt capture ( $n, \gamma$ ) and inelastic scatter ( $n, n'\gamma$ ) were considered in Chapter 3 for the case of remote elemental analysis of planetary surfaces.

There are a number of prompt discrete  $\gamma$ -ray lines produced during solar flares that should be observable by detector systems. The lines are primarily attributable to proton and  $\alpha$  particle interactions. The inelastic interactions of interest are outlined below.

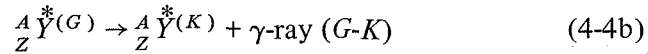


and, for example



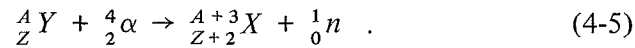
that is the excited nucleus decays to a ground state (g.s.).

The nucleus at excited level ( $G$ ) can also decay to a second excited state ( $K$ ) emitting a  $\gamma$ -ray of energy ( $G-K$ ). That is



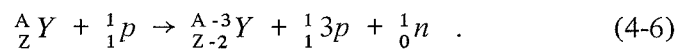
where  $Z$  is the atomic number,  $A$  is the atomic weight,  $Y$  is the nucleon, and  $p$  is a proton. The excited state can decay to a lower excited state and then further decay by  $\gamma$ -ray emission to a ground state. Multiple decay may be required before the final ground state is reached. The number of levels excited depends on the interaction cross section and energy of the particle.

Competing modes of decay are also possible. The proton interaction indicated in Equation (4-4) will be written as ( $p, p'$ ). In a similar way inelastic scattering  $\alpha$ -particle interactions will be noted as ( $\alpha, \alpha'$ ). Other interaction processes such as ( $\alpha, n$ ), ( $\alpha, p$ ) and ( $p, n$ ) will produce prompt  $\gamma$ -ray emission. For example, the ( $\alpha, n$ ) reaction can be written as follows:



In the interactions considered above the excited levels in nuclei were populated by direct excitation reactions. Another important reaction method is spallation. In this reaction protons or  $\alpha$ -particles break up heavier nuclei into lighter fragments that emerge from the reaction in excited states.

Examples of such interaction are ( $p, 2p$ ), ( $p, 2pn$ ), ( $p, pn$ ), ( $p, 3pn$ ), and ( $p, p\alpha$ ). The reaction ( $p, 3pn$ ) can be written, for example



Rather complex spallation reactions will be denoted by  $(p, -)$ . Table 4-2 lists some of the more prominent lines produced by such prompt  $\gamma$ -ray interaction (Ramaty et al., 1975). The relative intensity of the  $\gamma$ -ray lines for various solar flare conditions have been calculated and the results can be found in Ramaty et al. (1975).

It will be noted that only lines of  $\gamma$ -rays with energies less than 8 MeV have been indicated in Table 4-2. There are two principal methods by which  $\gamma$ -rays can be produced with energies 8 MeV or greater. First, in neutron capture ( $n, \gamma$ ),  $\gamma$ -ray energies corresponding to the binding energy per nucleon are obtained. Some of these interactions are shown in Table 3-4, Chapter 3. Because of the low concentration of the heavier elements in regions where solar flares are produced, these types of interactions should not produce significant fluxes of  $\gamma$ -rays with energies above 8 MeV regions. Second, high energy states can also be excited by the interaction of particles with sufficient energy to excite these levels. Most of the higher energy states are particle unstable and lead to little or no  $\gamma$ -ray emission. Such interactions have been studied (Crannell et al., 1979). The strength of  $\gamma$ -ray line emission is proportional to the product of three factors: Interaction cross section, branching ratio, and nuclear abundance. Gamma ray emission lines of possible interest with energies greater than 8 MeV are indicated in Table 4-3. Excitation due to both capture and high energy interactions are included.

The most promising solar flare  $\gamma$ -ray measurements for inferring energetic particle spectra are those of the decay of excited states of  $^{12}\text{C}$ . Except for the level at 15.11 MeV, excited states in the  $^{12}\text{C}$  nucleus with energies above the threshold for  $\alpha$ -emission at 7.367 MeV all decay predominately by direct particle emission and thus produce few nuclear  $\gamma$ -rays. The one exception is the energy state which is the analog ground state in  $^{12}\text{B}$  and  $^{12}\text{N}$ . This state lies 0.85 MeV below the lowest energy single particle emission threshold and thus is stable against neutron or proton emission.

The cross sections for production of the two nuclear states at 4.44-MeV and 15.11-MeV line production in  $^{12}\text{C}$  have different energy dependences, and thus the intensity of the 15.11-MeV line relative to that of the 4.44-MeV line depends on the functional form of the energy spectra of the incident protons and

**Table 4-2**  
**Prompt  $\gamma$ -Ray Lines of Interest in Solar Flares**

Energy MeV	Interaction Process	Decay Mode	Half (where applicable)
0.431	${}^4\text{He} (\alpha, n) {}^7\text{Be}^*$	${}^7\text{Be}^{*0.431} \rightarrow {}^7\text{Be} + \gamma\text{-Ray (0.431 MeV) to g.s.}$	
0.478	${}^4\text{He} (\alpha, p) {}^7\text{Li}^*$ ${}^4\text{He} {}^7 (\alpha, n) {}^7\text{Be}^*$	${}^7\text{Li}^{*0.478} \rightarrow {}^7\text{Li} + \gamma\text{-Ray (0.478) to g.s.}$ ${}^7\text{Be} \xrightarrow{12\%} \text{ECT } {}^7\text{Li}^{*0.478}$ ${}^7\text{Li}^{*0.478} \rightarrow {}^7\text{Li} + \gamma\text{-Ray (0.478) to g.s.}$	53.3d. ( ${}^7\text{Be}$ )
0.72	${}^{12}\text{C} (p, 2pn) {}^{10}\text{B}^*$ ${}^{16}\text{O} (p, -) {}^{10}\text{B}^*$	${}^{10}\text{B}^{*0.72} \rightarrow {}^{10}\text{B} + \gamma\text{-Ray (0.72) to g.s.}$ ${}^{10}\text{B}^{*0.72} \rightarrow {}^{10}\text{B} + \gamma\text{-Ray (0.72) to g.s.}$	
0.845	${}^{56}\text{Fe} (p, p') {}^{56}\text{Fe}^*$	${}^{56}\text{Fe}^{*0.845} \rightarrow {}^{56}\text{Fe} + \gamma\text{-Ray (0.845) to g.s.}$	
1.24	${}^{56}\text{Fe} (p, p') {}^{56}\text{Fe}^*$	${}^{56}\text{Fe}^{*2.08} \rightarrow {}^{56}\text{Fe}^{*0.845} + \gamma\text{-Ray (1.24)}$	
1.387	${}^{24}\text{Mg} (p, p') {}^{24}\text{Mg}^{*1.37}$	${}^{24}\text{Mg}^{*1.37} \rightarrow {}^{24}\text{Mg} + \gamma\text{-Ray (1.37) to g.s.}$	
1.63	${}^{20}\text{Ne} (p, p') {}^{20}\text{Ne}^*$ ${}^{14}\text{N} (p, p') {}^{14}\text{N}^*$ ${}^{16}\text{O} (p, 2pn) {}^{14}\text{N}^*$ ${}^{24}\text{Mg} (p, 2p) {}^{23}\text{Na}^*$	${}^{20}\text{Ne}^{*1.63} \rightarrow {}^{20}\text{Ne} + \gamma\text{-Ray (1.63) to g.s.}$ ${}^{14}\text{N}^{*3.94} \rightarrow {}^{14}\text{N}^{*2.31} + \gamma\text{-Ray (1.63)}$ ${}^{23}\text{Na}^{*2.07} \rightarrow {}^{23}\text{Na}^{*0.44} + \gamma\text{-Ray (1.63)}$	
1.78	${}^{28}\text{Si} (p, p') {}^{28}\text{Si}^*$	${}^{28}\text{Si}^{*1.78} \rightarrow {}^{28}\text{Si} + \gamma\text{-Ray (1.78) to g.s.}$	
1.99	${}^{12}\text{C} (n, pn) {}^{11}\text{C}^*$	${}^{11}\text{C}^{*1.99} \rightarrow {}^{11}\text{C} + \gamma\text{-Ray (1.99) to g.s.}$	
2.31	${}^{14}\text{N} (p, p') {}^{14}\text{N}^*$ ${}^{14}\text{N} (p, n) {}^{14}\text{O}$	${}^{14}\text{N}^{*3.94} \rightarrow {}^{14}\text{N}^{*2.31} + \gamma\text{-Ray (1.63)} \rightarrow {}^{14}\text{N} + \gamma\text{-Ray (2.31) to g.s.}$ ${}^{14}\text{O} \rightarrow {}^0_{+1}\text{e} + {}^{14}\text{N}^{*2.31}, \text{N}^{*2.31} \rightarrow {}^{14}\text{N} + \gamma\text{-Ray (2.31) to g.s.}$	70.59s ( ${}^{14}\text{O}$ )

Source: Ramaty et al. (1975).

Table 4-2 (continued)  
 Prompt  $\gamma$ -Ray Lines of Interest in Solar Flares

Energy MeV	Interaction Process	Decay Mode	Half (where applicable)
	$^{16}\text{O}(p, 2pn)^{14}\text{N}^*$	$^{14}\text{N}^*2.31 \rightarrow ^{14}\text{N} + \gamma\text{-Ray (2.31) to g.s.}$	
2.75	$^{16}\text{O}(p, p')^{16}\text{O}^*$	$^{16}\text{O}^*8.88 \rightarrow ^{16}\text{O}^*6.14 + \gamma\text{-Ray (2.75)}$	
~3.62	$^{16}\text{O}(p, 3pn)^{13}\text{C}^*$	$^{13}\text{C}^*3.68 \rightarrow ^{13}\text{C} + \gamma\text{-Ray (3.84) to g.s.}$	
	$^{12}\text{C}(p, -)^6\text{Li}^*$	$^6\text{Li}^*3.56 \rightarrow ^6\text{Li} + \gamma\text{-Ray (3.56) to g.s.}$	
3.84	$^{16}\text{O}(p, 3pn)^{13}\text{C}^*$	$^{13}\text{C}^*3.84 \rightarrow ^{13}\text{C} + \gamma\text{-Ray (3.84) to g.s.}$	
4.43	$^{12}\text{C}(p, p')^{12}\text{C}^*$		
	$^{12}\text{C}(\alpha, \alpha')^{12}\text{C}^*$	$^{12}\text{C}^*4.43 \rightarrow ^{12}\text{C} + \gamma\text{-Ray (4.43) to g.s.}$	
	$^{16}\text{O}(p, p\alpha)^{12}\text{C}^*$		
~5.3	$^{16}\text{O}(p, pn)^{15}\text{O}^*$	$^{15}\text{O}^*5.26 \rightarrow ^{15}\text{O} + \gamma\text{-Ray (5.26) to g.s.}$	
	$^{16}\text{O}(p, 2p)^{15}\text{N}^*$	$^{15}\text{N}^*5.28 \rightarrow ^{15}\text{N} + \gamma\text{-Ray (5.28) to g.s.}$	
	$^{16}\text{O}(p, 2p)^{15}\text{N}^*5.31$	$^{15}\text{N}^*5.31 \rightarrow ^{15}\text{N} + \gamma\text{-Ray (5.31) to g.s.}$	
6.14	$^{16}\text{O}(p, p, )^{16}\text{O}^*$	$^{16}\text{O}^*6.14 \rightarrow ^{16}\text{O} + \gamma\text{-Ray (6.14) to g.s.}$	
	$^{16}\text{O}(q, q, )^{16}\text{O}^*$		
6.33	$^{16}\text{O}(p, 2p)^{15}\text{N}^*6.33$	$^{15}\text{N}^*6.33 \rightarrow ^{15}\text{N} + \gamma\text{-Ray to g.s.}$	

Table 4-2 (continued)  
 Prompt  $\gamma$ -Ray Lines of Interest in Solar Flares

Energy MeV	Interaction Process	Decay Mode	Half (where applicable)
~6.7	$^{12}\text{C}(\rho, 2p)^{11}\text{B}^*$	$^{11}\text{B}^{*6.76} \rightarrow ^{11}\text{B} + \gamma\text{-Ray (6.76) to g.s.}$	
	$^{12}\text{C}(\rho, 2p)^{11}\text{B}^*$	$^{11}\text{B}^{*6.81} \rightarrow ^{11}\text{B} + \gamma\text{-Ray (6.81) to g.s.}$	
	$^{12}\text{C}(\rho, pn)^{11}\text{C}^*$	$^{11}\text{C}^{*6.50} \rightarrow ^{11}\text{C} \rightarrow \gamma\text{-Ray (6.50)}$	
7.12	$^{16}\text{O}(\rho, p')^{16}\text{O}^*$	$^{16}\text{O}^{*7.12} \rightarrow ^{16}\text{O} + \gamma\text{-Ray (7.12) to g.s.}$	

**Note:** g.s. = ground state, e.s. = excited state.

**Table 4-3**  
**Greater than 8 MeV  $\gamma$ -Ray Transitions of Interest in the Study of Solar Flares**

Excited Nuclide	Gamma Ray Energy in MeV	Interaction Process	Transition
$^{11}\text{B}$	8.56	$^{12}\text{C} (p, 2p)$	g.s.
$^{12}\text{C}$	10.67	$^{12}\text{C} (p, p')$ and $^{16}\text{O} (p, p')$	e.s.
	12.71		g.s.
	15.11		g.s.
$^{15}\text{N}$	8.31	$^{16}\text{O} (p, 2p)$	g.s.
	9.05		
	9.15		
	9.76		
	9.93		
	10.07		
$^{20}\text{Ne}$	8.32	$^{20}\text{Ne} (p, p')$	e.s.
$^{27}\text{Al}$	8.05	$^{28}\text{Si} (p, 2p)$	g.s.
$^{28}\text{Si}$	8.33	$^{28}\text{Si} (p, p')$	g.s.
	8.43		e.s.
	8.49		g.s.
	8.53		e.s.
	8.76		e.s.
	8.89		e.s.
	8.90		g.s.
	9.17		e.s.
	9.48		g.s.
	9.50		g.s.
	10.31		g.s.
	10.59		g.s.
	10.72		g.s.
	10.90		g.s.
	11.45		g.s.
$^{32}\text{S}$	8.13	$^{32}\text{S} (p, p')$	g.s.

**Source:** Crannell et al. (1979).

**Table 4-3 (continued)**  
**Greater than 8 MeV  $\gamma$ -Ray Transitions of Interest in the Study of Solar Flares**

Excited Nuclide	Gamma Ray Energy in MeV	Interaction Process	Transition
	8.59		e.s.
	10.63		e.s.
$^{23}\text{Na}$	11.23	$^{24}\text{Mg} (p, 2p)$	g.s.
	8.36		g.s.
	8.65		g.s.
$^{24}\text{Mg}$	8.67	$^{24}\text{Mg} (p, p')$	g.s.
	8.44		g.s.
	8.69		e.s.
	9.00		g.s.
	9.15		g.s.
	9.36		e.s.
	9.83		e.s.
	9.84		e.s.
	9.97		g.s.
	10.73		g.s.
	8.29		g.s.

**Note:** g.s. = ground state, e.s. = excited state.

$\alpha$ -particles. It may be possible therefore to obtain information concerning these particles' differential energy spectra from such ratios. One must be careful in such analyses because there are other reactions which might produce both the 4.44-MeV and the 15.11-MeV. The particular reaction of interest is the  $^{12}\text{C}(p, p')^{12}\text{C}^*$  (15.11). The other major interaction process that may compete in terms of  $\gamma$ -ray emission is  $^{16}\text{O}(p, p'\alpha)^{12}\text{C}^*$  (15.11-MeV lines). This cross section is being investigated (Lapides et al., 1978) and is significantly smaller than the  $^{12}\text{C}$  interaction, but because of the higher concentration of oxygen in the ambient medium it may contribute significantly to the emission of 15.11-MeV lines (Crannell et al., 1979). Other nuclides such as iron may also be of interest in determining proton energy spectra from discrete  $\gamma$ -ray line measurements (Lin and Ramaty, 1978).

In the discussion above, primary interactions by protons and  $\alpha$ -particles were considered. We shall now discuss secondary production of neutrons and interactions with nuclear species in the solar flare environment. Neutron production by accelerated charged particles has been studied in detail (Lingenfelter et al., 1965; and Lingenfelter and Ramaty, 1967). The most important neutron-producing reactions and their threshold energies are listed in Table 4-4 (Lingenfelter and Ramaty, 1967). Only the number of neutrons is indicated in some cases; the total interactions are not shown. The neutrons are born at high energies. Calculations of the distribution of neutrons released in the chromosphere or corona have yielded the following results (Lingenfelter and Ramaty, 1967). If the neutrons are released above the photosphere, any initially upward moving neutrons escape from the Sun. Some of the downward moving neutrons can also escape after being backscattered elastically by ambient protons, but most of these neutrons either are captured or decay at the Sun. Because the probability for elastic scattering is much larger than the capture probability, the majority of neutrons are thermalized before they are captured. The bulk of the thermal neutrons at the Sun are captured either in  $^1\text{H}$

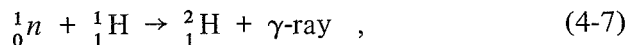


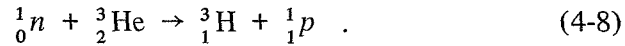
**Table 4-4**  
**Neutron Production Modes During Solar Flares**

Reaction	Threshold (MeV/nucleon)
1. $p + {}^1\text{H} \rightarrow n + p + \pi^+$	292.30
2. $p + {}^4\text{He} \rightarrow {}^3\text{He} + p + n + (\pi)$	25.70
$\rightarrow {}^2\text{H} + 2p + n + (\pi)$	32.60
$\rightarrow 3p + 2n + (\pi)$	35.40
3. $p + {}^{13}\text{C} \rightarrow n + \dots$	19.60
$p + {}^{13}\text{C} \rightarrow n + \dots$	3.20
4. $p + {}^{14}\text{N} \rightarrow n + \dots$	6.30
5. $p + {}^{16}\text{O} \rightarrow n + \dots$	16.60
$p + {}^{18}\text{O} \rightarrow n + \dots$	2.50
6. $p + {}^{20}\text{Ne} \rightarrow n + \dots$	15.90
7. $p + {}^{56}\text{Fe} \rightarrow n + \dots$	5.50
8. $\alpha + {}^4\text{He} \rightarrow {}^7\text{Be} + n$	9.50
9. $\alpha + {}^{12}\text{C} \rightarrow n + \dots$	2.80
$\alpha + {}^{13}\text{C} \rightarrow n + \dots$	-
10. $\alpha + {}^{14}\text{N} \rightarrow n + \dots$	1.50
11. $\alpha + {}^{16}\text{O} \rightarrow n + \dots$	3.80
$\alpha + {}^{18}\text{O} \rightarrow n + \dots$	0.21
12. $\alpha + {}^{20}\text{Ne} \rightarrow n + \dots$	2.16
$\alpha + {}^{22}\text{Ne} \rightarrow n + \dots$	0.15
13. $\alpha + {}^{56}\text{Fe} \rightarrow n + \dots$	1.37
14. $\alpha + {}^{25}\text{Mg} \rightarrow n + \dots$	-
$\alpha + {}^{26}\text{Mg} \rightarrow n + \dots$	-
15. $\alpha + {}^{29}\text{Si} \rightarrow n + \dots$	0.43

**Note:** (-) is exoergic

**Source:** Ramaty et al. (1975).

or on  ${}^3\text{He}$



The  $\gamma$ -ray energy produced during the interaction indicated by Equation (4-7) is 2.23 MeV. The reaction indicated in Equation (4-8) is radiation less. Thus, the magnitude of  $\gamma$ -ray emission at 2.23 MeV depends on the ratio  ${}^1\text{H}/{}^3\text{He}$  in the interacting medium.

As we have indicated above, the positrons and neutrons produced during a solar flare are thermalized by the ambient medium before they are captured or annihilated. Therefore, any information concerning directional anisotropies in the primary particles would be lost before the  $\gamma$ -rays at 0.511 MeV and 2.2 MeV are produced. On the other hand, the  ${}^{12}\text{C}$  and  ${}^{12}\text{O}$  nuclei, which emit the  $\gamma$ -ray lines at 4.4 MeV and 6.1 MeV, are excited by protons with energies of several tens of MeV which also impart kinetic energy to these nuclei. Because the  $\gamma$ -rays are subsequently emitted in a short time interval compared with the slowing down time of the nuclei, any directional anisotropy in the primary particles would cause a Doppler shift of the energies of the lines. It has been shown in Ramaty and Crannell (1976) that observable Doppler shifts result from particle anisotropies in solar flares. These lines can also be thermally broadened but the Doppler shift broadening caused by particle anisotropies would be expected to be an order of magnitude higher for the highest known temperature in the solar atmosphere.

### Continuum Emission

X-ray and  $\gamma$ -ray continuum emission can be produced by three major processes: bremsstrahlung, Compton scattering, and synchrotron radiation. In terms of  $\gamma$ -ray emission during solar flares, the latter two mechanisms are not important. However, they are important for other  $\gamma$ -ray astrophysical processes and will be considered in detail in later chapters of this book.

Bremsstrahlung processes will also be considered in detail later in this book. In the case of a solar flare in the nonrelativistic domain, most of the radiation is produced by the interaction of

accelerated electrons with ambient ions. The inverse process, in which accelerated protons interact with ambient electrons, can produce bremsstrahlung and the interaction is the electron-proton process when the accelerated protons have the same velocity as the accelerated electrons. Bremsstrahlung can also be produced in electron-electron interactions. This process is negligible in the nonrelativistic domain but becomes comparable to the electron-proton bremsstrahlung in the relativistic domain. Detailed calculations of bremsstrahlung produced during solar flares have been carried out by many authors (e.g., Ramaty et al., 1977).

### Decay of $\pi^0$ Mesons

The production of  $\pi^0$  mesons by the interaction of high energy particles such as



and



where  $n$  is the multiplicity which may become significant during solar flares. The decay of the  $\pi^0$  meson leads to  $\gamma$ -ray emission, that is



The  $\gamma$ -ray spectrum produced will be a broad continuum with a peak around 100 MeV. These  $\gamma$ -rays should dominate the very high energy portion of the spectrum. No discrete lines are visible; thus even detectors with poor energy resolution should be capable of detecting these emissions, though rather intense flares will be required for such observations. Details of the expected

emission have been given in Ramaty et al. (1975) for the case of solar flares. Details of  $\pi^0$  production will be considered in later chapters of this book.

## EXPERIMENTAL RESULTS

Gamma ray emission studies have been carried out on spacecraft that have been in Earth orbit. During quiet Sun periods, the  $\gamma$ -ray flux is too small to be observed by the detector systems flown in Earth orbit thus far. Gamma ray flux observations during periods of high solar activity have been reported. The  $\gamma$ -ray observation in 1972 by the seventh Orbiting Solar Observatory (OSO-7) was the most definitive measurement made up to that time (Chupp et al., 1975). A number of possible solar  $\gamma$ -ray events were reported earlier but no detailed spectral and temporal information was obtained (see, for example, Kondo and Nagase, 1969; Hirasima et al., 1969; and Koga et al., 1974). The Solar Maximum Mission (SMM) was launched on February 14, 1980. A  $\gamma$ -ray spectrometer aboard the spacecraft has been monitoring the Sun and it is expected to enable detailed observations of solar  $\gamma$ -ray emission. In the following two sections, the results from OSO-7 and preliminary results from SMM will be considered.

### OSO-7 Solar Flare Gamma Ray Observations

That solar  $\gamma$ -ray observations were indeed possible from Earth orbiting spacecraft was confirmed when  $\gamma$ -ray lines associated with solar emission were observed by OSO-7 during two flares in 1972 (Chupp et al., 1973a, 1973b). A  $7.6 \times 7.6$  cm NaI (Tl) detector was used to measure the  $\gamma$ -ray spectrum in the 0.3-MeV to 10-MeV region. The  $\gamma$ -ray spectrum was analyzed with a 377-channel pulse-height analyzer and stored in a memory on board the spacecraft. The  $\gamma$ -ray detector was surrounded by a cup-shaped active anticoincidence shield of CsI(Na) crystals. This shield is used to allow for directional measurement, reduction of background, and enhancement of the relative sensitivity for lines by the suppression of the Compton continuum. The  $\gamma$ -ray detector had an auxiliary X-ray detector consisting of NaI (Tl) crystal of 3.2 cm in diameter and 0.64 cm in thickness covered by a 10-mil thick Be foil. A 4-channel X-ray spectrum

could be obtained covering the energy range 7.5 to 120 keV. Details of the  $\gamma$ -ray spectrometer design have been given by Higbie et al. (1972). Operational characteristics of this type of detector and active shield system will be considered later in this book. The detector was mounted in the rotating wheel compartment of the OSO-7 spacecraft. Measurements of  $\gamma$ -ray flux during the flare and background were obtained.

Gamma rays associated with solar flares on August 4 and 7, 1972 were observed. The pulse-height spectrum obtained is shown in Figure 4-2. From this figure significant enhancement of 0.511 and 2.2-MeV emissions are evident. Line features at 4.4 and 6.1 MeV are also indicated. The lines at 1.17 and 1.33 MeV are caused by  $^{60}\text{Co}$  a calibration source which is part of the experiment. The August 4 flare activity was monitored and the following observations were made: A precursor flare in the X-ray region 0.5Å to 3Å was observed and continued for about an hour (Dere et al., 1973); after the first hour the main flare started in the X-ray energy region (7.5 keV to 15 keV) detected by the University of New Hampshire (UNH) system (Chupp et al., 1975); the main optical flare started 7 minutes later in the  $\text{H}\alpha$  region (Solar Geophysical Data UAG-12); and the excess  $\gamma$ -ray line and continuum emission were recorded about 7 minutes after the onset of the main optical flare (Chupp et al., 1973). Strong radio emission also accompanied this event (Castelli et al., 1973; and Croom and Harris, 1973). The temporal profile for the impulsive radio emission and the  $\gamma$ -ray emission for this event seem to correlate (Suri et al., 1975).

The August 7, 1970 event began when OSO-7 was behind the Earth. Forty minutes after the onset of the flare, the spacecraft emerged and rather limited observations were made. Enhancement of the 0.5-MeV and 2.2-MeV lines above background was observed.

Both discrete line and continuum  $\gamma$ -ray emission were observed; this is consistent with the processes considered earlier in this chapter. All the lines except the 2.2 MeV from deuterium formation are attributable to interaction with energetic protons and positron-electron interactions. The fact that the 2.2-MeV line was observed implies the presence of a significant thermal neutron flux, not absorbed by other processes. The  $\gamma$ -ray producing nuclear reactions begin in the first 200 seconds of a strong flare

with the hard X-rays and before the optical maximum. From the 0.511 MeV emission the density of region where electron-positron annihilation takes place is greater than  $10^{12}$  electrons  $\text{cm}^{-3}$ .

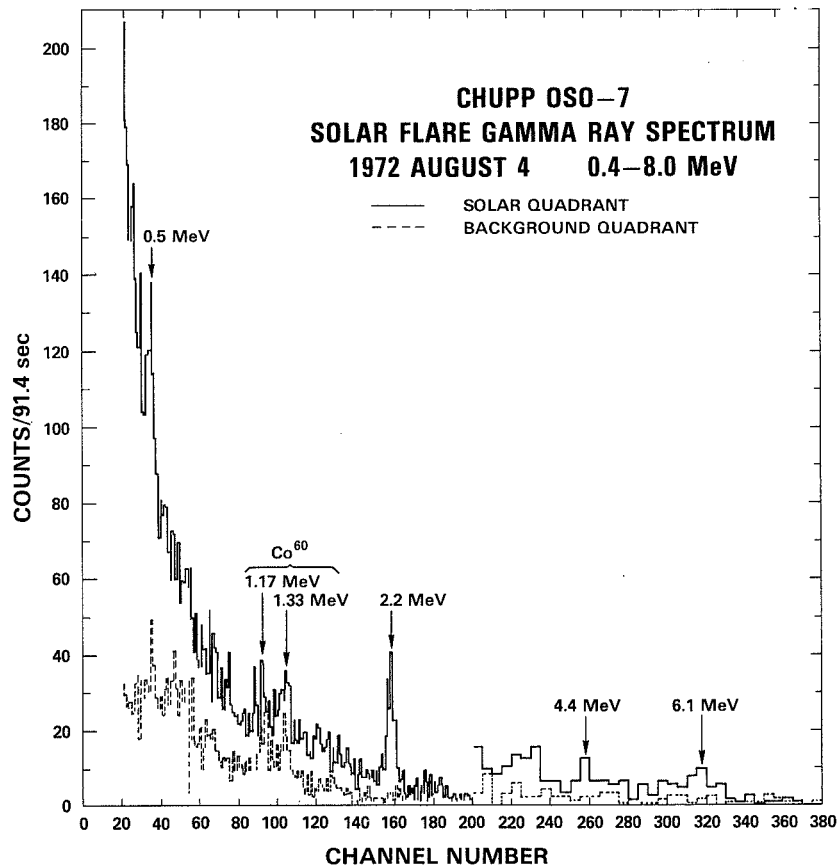


Figure 4-2. The pulse-height spectrum of the  $\gamma$ -ray emission associated with the August 4, 1972 solar flare is shown as a solid line. The spectrum was obtained with the University of New Hampshire (UNH)  $\gamma$ -ray spectrometer aboard OSO-7. The background is shown as a broken line. Reprinted with permission from the D. Reidel Publishing Co., Dordrecht, Holland (Chupp et al., 1975).

These observations have confirmed the importance of  $\gamma$ -ray astrophysical observations of the Sun, but because of the limited number of observations and the low sensitivity in terms of the counting statistics (both for temporal and energy spectral determination) only a limited understanding of the mechanisms producing these  $\gamma$ -ray emissions could be obtained.

### **Gamma Ray Observations on the Solar Maximum Mission (SMM)**

The next step in the observation of solar  $\gamma$ -ray emission was taken with the launch of the SMM satellite on February 14, 1980. The UNH group designed the system flown on SMM. The detector-spectrometer system consists of the following major components: the  $\gamma$ -ray spectrometer consists of seven high resolution 7.6 cm  $\times$  7.6 cm NaI(Tl) crystals with a 476-channel pulse-height analyzer. Spectra are accumulated every 16.38 seconds and cover the energy regions 0.3 MeV to 9 MeV. Two-second time resolution is available for three larger energy intervals between 3.5 MeV and 6.5 MeV. This allows for detailed study of the prompt  $\gamma$ -ray emission at 4.4 MeV (C) and 6.1 MeV (O). The higher energy (greater than 8 MeV) portion of the spectrum can be observed on command. In addition, a single channel analyzer covering the energy range 350 to 400 keV is read out every 64 ms for fast time resolution of bursts of hard X-rays. Another component, the active shield, completely surrounds the seven main NaI(Tl) crystals except in the solar direction. The active shield is constructed of 2.5 cm thick CsI(Na) elements which reject most direction charged particles and also suppress background  $\gamma$ -rays from all directions except the solar direction. High energy  $\gamma$ -ray detection can be achieved utilizing the complete group of seven NaI(Tl) detectors in addition to a large 25 cm  $\times$  7.6 cm CsI(Na) crystal behind the main detector system. Events in the  $\sim$  10 MeV to  $\sim$  100 MeV energy region occurring in any of the detector elements, individual or in combination, are analyzed by separate 4-channel pulse-height analyzers. Interactions in separate detectors or groups of detectors are accumulated in a 5  $\times$  5 matrix to yield positional information. Neutron events can be inferred from patterns derived from this position matrix. The X-ray detector system consists of two 8 cm<sup>2</sup>  $\times$  0.6 cm thick NaI detectors which are identical except for different filters in front of each detector. One filter is made of aluminum which allows 50 percent X-ray transmission at 10 keV and thus covers the energy region 10 to 80 keV. The second filter has an Al-Fe filter allowing 50 percent transmission at  $\sim$  35 keV. The second detector covers the energy range 25 to 140 keV. A 4-channel analyzer is used to obtain the pulse-height spectra from

each detector. Spectra are accumulated for 1.02 seconds. For further details see Forrest et al. (1980a).

A number of solar flares with associated  $\gamma$ -ray emission have been observed with the Gamma Ray Experiment (GRE) aboard SMM. Table 4-5 lists the major reported events in which both discrete line and continuum spectra have been measured. These measurements were made during the first year operation of SMM mission (Forrest et al., 1980b; Reppin et al., 1980; Ryan et al., 1980; Matz et al., 1980; Share et al., 1980; Chupp et al., 1981; Ryan et al., 1981).

**Table 4-5**  
**List of Solar Flares in Which Discrete Line and**  
**Continuum Emission were Observed During 1980**

Date	Heliographic Coordinates	Class	Time of Start in UT	
			Start Time of H $\alpha$ Solar Flare Observation	Start Time of GRE Observation
3/29/80		C9.6/	0918	~0918
3/29/80	N08W19	M1/58	0935	0955
6/7/80	N04W70	M7.3/5B	0309	0312
6/21/80	N020W90	X2.6/1B	0117	0118
6/29/80	S26W90	M4.2	1038	1042
7/1/80	S12W38	X25/1	1621	1627
11/6/80	S12E70	X9/18	0352	0345

In the following discussion, a few of the observations made during the June 7, 1980 and June 21, 1980 flares will be presented (Forrest et al., 1980; Reppin et al., 1980; Share et al., 1980; Chupp et al., 1981). These will indicate the nature of the results that have been made during the first year of observation on SMM.

As indicated above, discrete line emission was observed during the June 7 solar flare. The strongest  $\gamma$ -ray line observed occurred at an energy of 2.223 MeV.

The flux at the maximum observed intensity was  $\sim(7.1 + 1.2) \times 10^{-2}$  photons/cm $^2$ s $^{-1}$ . This line can be associated with the reaction  $^1\text{H}(n, \gamma) ^2\text{H}$ . Prompt  $\gamma$ -rays at 4.45 MeV and 6.13

MeV also were observed at flux levels  $\sim(2.7 \pm 1.3) \times 10^{-2}$  photons  $\text{cm}^{-2}\text{s}^{-1}$  and  $\sim(2.7 \pm 0.8) \times 10^{-2}$  photons  $\text{cm}^{-2}\text{s}^{-1}$ , respectively. These lines can be associated with interactions in  $^{12}\text{C}$  and  $^{16}\text{O}$ . The impulsive X- and  $\gamma$ -ray event lasted for greater than 50 s and temporal variations on a time scale of a few seconds were observed over the range of energies from 20 keV to 7 MeV (Forrest et al., 1980; Chupp et al., 1981). Analysis of the X- and  $\gamma$ -ray energy and time profiles suggest that both ions as well as electrons were accelerated on a similar time scale of a few seconds (Forrest et al., 1980; Ramaty et al., 1980; Chupp et al., 1981).

Fast neutrons produced by nuclear reactions are thermalized by interactions in the photosphere. The thermal neutrons can be removed by a number of interactions. The  $^1\text{H}$  capture reaction will lead to the emission of 2.223 MeV  $\gamma$ -ray. As was discussed earlier in the chapter, the yield of 2.223 MeV photons will depend on the  $^3\text{He}$  abundance and temporal distribution will depend on the regions of production of fast neutron and the microscopic loss rate of the neutrons. Assuming an isotropic emission of neutrons (from 0.5 MeV to greater than 50 MeV in energy at birth) a  $^3\text{He}/^1\text{H}$  ratio of  $5 \times 10^{-5}$ , and a total production of  $\sim 4 \times 10^{29}$  neutrons, results consistent with the observed rise and decay time and flux of the 2.223 MeV, can be obtained (Forrest et al., 1980; Ramaty et al., 1980; Chupp et al., 1981).

The June 21, 1980 flare produced  $\gamma$ -ray emission up to about 50 MeV. The hard X-rays (50 to 150 keV) and the high energy  $\gamma$ -ray emission (10-40 MeV) showed similar time structure down to the limit of time resolution on the high energy  $\gamma$ -ray channels although the high energy emission was delayed by a few seconds with respect to the hard X-ray. The 0.511 MeV line from positron-electron annihilation were rather strong and the 2.223 MeV line, as well a number of prompt  $\gamma$ -ray lines were observed (Reppin et al., 1980 and Share et al., 1980).

The results from the  $\gamma$ -ray experiment will shed new light on high energy astrophysical processes occurring during solar flares. Time will be required to assimilate the large amount of data that have been and will be collected over the next few years.

## REFERENCES

- Castelli, J. P., Barron, W. R., and Badillo, V. L., 1973, *World Data Center A, Report UAG-28*, part I, 183.
- Chupp, E. L., Forest, D. J., Higbie, P. R., Suri, A. N., Tsai, C., and Dunphy, P. P., 1973a, *Nature (London)*, **241**, 333.
- Chupp, E. L., Forrest, D. J., and Suri, A. N., 1973b, in R. Ramaty and R.G. Stone, eds., *High Energy Phenomena on the Sun*, NASA SP-342, p. 283.
- Chupp, E. L., Forrest, D. J., and Suri, A. N., 1975, in S. R. Kane, Ed., *Solar Gamma-, X-, and EUV Radiation*, IAU Symp. 68 (Dordrecht, Holland: D. Reidel Publishing Co., 1975), 341.
- Chupp, E. L., Forrest, D. J., Ryan, J. M., Cherry, M. L., Reppin, C., Kanbach, G., Rieger, E., Pinkau, K., Share, G. H., Kinzer, R. L., Strickman, M. S., Johnson, W. W., and Kurfess, J. D., 1981, *Ap. J. (Letters)*, **244**, L171.
- Crannell, C. J., Ramaty, R., and Werntz, C., 1975, *Positron Annihilation in Solar Flares*, NASA X-682-75-167 (Greenbelt, Md.: Goddard Space Flight Center, 1975).
- Crannell, C. J., Joyce, G., Ramaty, R., and Werntz, C., 1976, *Ap. J.*, **210**, 582.
- Crannell, C. J., Ramaty, R., and Crannell, H., 1977, *Proc. of the 12th ESLAB Symp.*, R. D. Wills and B. Battick, eds., ESA SP-124, European Space Agency, Noordwijk, Netherlands, Paris, France.
- Crannell, C. J., Crannell, H., and Ramaty, R., 1979, *Ap. J.*, **229**, 762.
- Croom, D. L., and Harris, L. D. J., 1973, *World Data Center A, Report UAG-28*, part I, 210.
- Dere, K. P., Horan, D. M., and Kreplin, R. W., 1973, *World Data Center A, Report UAG-28*, part II, 298.

- Forrest, D. J., Chupp, E. L., Ryan J. M., Cherry, M. L., Gleske, I. U., Reppin, C., Pinkau, K., Rieger, E., Kanbach, G., Kinzer, R. L., Share G., Johnson, W. W., and Kurfess, J. D., 1980a, *Solar Phys.*, **65**, 15.
- Forrest, D. J., Chupp, E. L., Ryan, J. M., Reppin, C., Rieger, E., Kanbach, G., Pinkau, K., Share, G., and Kinzer, R., 1980b, *Bul. Am. Astr. Soc.*, **12**, 890.
- Gabriel, A. H., 1971, *Solar Phys.*, **21**, 392.
- Higbie, P. R., Chupp, E. L., Forrest, D. J., and Gleske, I. U., 1972, *IEEE Trans. Nuc. Sci.*, *NS019*, no. 1, 606.
- Hirasima, Y., Okudaira, K., and Yamagami, T., 1969, *Acta Phys. Hungaria, Suppl. 2*, **39**, 683.
- Koga, R., Simnett, G. M., and White, R. S., 1974, in B. G. Taylor, ed., *Proc. of the 9th ESLAB Symp.*, ESRO SP-106, 31.
- Kondo, I., and Nagase, F., 1969, in C. Delager and Z. Švestka, eds., *Solar Flares and Space Research* (Amsterdam: North Holland Publishing Co., 1969), p. 114.
- Lapides, J. R., Crannell, C. J., Crannell, H., Hornyak, W. F., Seltzer, S. M., Trombka, J. I., and Wall, N. S., 1978, *Proc. Symp. on Gamma-Ray Spectroscopy in Astrophysics*, NASA TM-79619, 502.
- Lin, R. P., and Ramaty, R., 1978, *Gamma-Ray Spectroscopy in Astrophysics*, T. L. Cline and R. Ramaty, eds., NASA TM-79619, p. 76.
- Lingenfelter, R. E., Flamm, E. J., Canfield, E. H., and Kellman, S., 1965, *J. Geophys. Res.*, **70**, 4087.
- Lingenfelter, R. E., and Ramaty, R., 1967, *High-Energy Nuclear Reactions in Astrophysics*, Shen, B. S. P., Benjamin, W. A., eds. (New York: 1967), p. 99.

- Matz, S. M., Ryan, J. M., Chupp, E. L., Forest, D. J., Reppin, C., Rieger, E., Kanbach, G., Pinkau, K., Share, G., and Kinzer, R. L., 1980, *Bul. Am. Astr. Soc.*, **12**, 910.
- Ramaty, R., and Crannell, C. J., 1976, *Ap. J.*, **203**, 766.
- Ramaty, R., Kozlovsky, B., and Lingenfelter, R. E., 1975, *Space Sci. Rev.*, **18**, 341.
- Ramaty, R., Kozlovsky, B., and Suri, A. N., 1977, *Ap. J.*, **214**, 617.
- Ramaty, R., Kozlovsky, B., Chupp, E. L., and Forrest, D. J., 1980, *Bul. Am. Astr. Soc.*, **12**, 890.
- Reppin C., Rieger, E., Kanbach, G., Pinkau, K., Forrest, D. J., Chupp, E. L., Ryan, J. M., Share, G., and Kinzer, R. L., 1980, *Bul. Am. Astr. Soc.*, **12**, 891.
- Ryan, J. M., Chupp, E. L., Forrest, D. J., Reppin, C., Rieger, E., Kanbach, G., Pinkau, K., Share, G., and Kinzer, R. L., 1980, *Bul. Am. Astr. Soc.*, **12**, 891.
- Ryan, J. M., Forrest, D. J., Chupp, E. L., Cherry, M. L., Reppin, C., Rieger, E., Pinkau, K., Kanbach, G., Share, G., Kinzer, R. L., and Strickman M., 1981 *Ap. J. (Letters)*, **244**, L175.
- Share, G. H., Kinzer, R. L., Forrest, D. J., Chupp, E. L., Ryan, J. M., Rieger, E., Reppin, C., Kanbach, G., and Pinkau, K., 1980, *Bul. Am. Astr. Soc.*, **12**, 891.
- Suri, A. N., Chupp, E. L., Forest, D. J., and Reppin, C., 1975, *Solar Phys.*, **43**, 415.
- Wang, H. T., and Ramaty, R., 1975, *Ap. J.*, **202**, 532.

# **PART III**

# **THE GALAXY**

*Chapter 5*  
*The Interstellar Medium and Galactic Structure*

*Chapter 6*  
*Compact Objects*



## PART III

# THE GALAXY

*Gamma ray astronomy is providing astronomers with a valuable new tool for the exploration of our galaxy. Gamma ray sources of sufficient intensity to be detected at the Earth may be observed wherever they occur in the galaxy, since a high energy  $\gamma$ -ray can pass through the entire width of the galactic plane, even the central portion, with only about a one percent chance of being absorbed. The observed diffuse galactic high energy  $\gamma$ -radiation is generally agreed to be produced in interactions between the cosmic rays and the interstellar matter and photons. As more data become available, it should be possible to obtain a very detailed picture of the galactic cosmic ray distribution, and also a high contrast picture of the general structure of the galaxy since the present  $\gamma$ -ray data already suggest that the cosmic rays and matter are correlated. New insight into molecular clouds and the role cosmic rays play in their history is also possible. In addition to the diffuse emission, a number of galactic point sources have been established. Gamma rays, for example, have been seen from radio pulsars. For the known  $\gamma$ -ray pulsars, there is as much energy being released in the form of  $\gamma$ -rays,  $10^{34}$  to  $10^{35}$  ergs  $s^{-1}$ , as there is at all wavelengths for the Sun and substantially more energy than is being released in the radio region by the same pulsars. There are other galactic sources of high energy  $\gamma$ -rays including the interesting object Cygnus X-3. Black holes and supernovae have been predicted to be sources of  $\gamma$ -ray emission. Supernovae, for example, have long been postulated as the origin of nucleosynthesis, and  $\gamma$ -ray line radiation from the radioactive*

*decay of nuclei formed during nucleosynthesis should be present at levels detectable with future experiments. In the lowest energy portion of the  $\gamma$ -ray spectrum, there are unexplained low energy  $\gamma$ -ray bursts. The origin of these few second bursts of  $\gamma$ -rays with photon energies concentrated below one MeV remains a mystery, even though some source positions have recently been determined quite accurately by triangulation, using data from several widely spaced satellites.*

## Chapter 5

# The Interstellar Medium and Galactic Structure

### INTRODUCTION

Because there are many excellent photographs of other galaxies clearly showing their general structure, it is often forgotten that only a hazy picture of our own galaxy exists at present. This situation results from our Sun being located very near to the plane of the galactic disk and relatively far from the galactic center ( $\sim 10$  kpc). Because of absorption, optically it is only possible to see about 1 kpc in the disk, and even X-rays and radio waves suffer some absorption in trying to pass through the width of the disk. High energy  $\gamma$ -rays, however, suffer only negligible absorption for a typical path in the plane of the galaxy. Further, for quite some time high energy  $\gamma$ -rays have been recognized to be produced by the interaction of cosmic rays with the interstellar matter in our galaxy. By combining the  $\gamma$ -ray information with radio data in a manner to be described below, a picture of the galaxy not previously available, particularly with regard to the general structure and the effects of cosmic ray pressure, will be forthcoming.

### INTERACTION PROCESSES

Within the galaxy, cosmic rays may interact with matter, photons, and magnetic fields, in each case producing  $\gamma$ -rays. The cosmic ray nucleon interactions give rise to  $\gamma$ -rays primarily through the decay of  $\pi^0$  mesons. Cosmic ray electrons produce  $\gamma$ -rays through bremsstrahlung, but with a markedly different energy spectral

shape. In addition, the positrons left over as nuclear debris slow down and annihilate with electrons to form a pair of 0.511 MeV  $\gamma$ -rays. Cosmic ray electrons also interact with the interstellar starlight, optical and infrared, and the blackbody radiation through the Compton process. Finally, cosmic ray electrons can interact with magnetic fields giving rise to synchrotron or curvature radiation, but, as will be seen, these processes are much less important than the others previously mentioned. (A probable exception is the curvature radiation hypothesized to be emitted from pulsars which will be discussed in the next chapter.)

### Cosmic Ray Nucleon, Interstellar Matter Interactions

Of the many mesons produced in the interactions of the cosmic rays with interstellar matter, the most commonly produced are  $\pi$  mesons which can be either charged or neutral. The  $\pi^0$  mesons decay in about  $10^{-16}$  s into two  $\gamma$ -rays each with about 68 MeV in the rest frame. Many of the other mesons and hyperons also decay into  $\pi$  mesons, e.g.,  $\kappa^\pm \rightarrow \pi^\pm + \pi^0$ ,  $\kappa_1^0 \rightarrow 2\pi$ ,  $\kappa_2^0 \rightarrow 3\pi^0$ ,  $\kappa_2^0 \rightarrow \pi^+ + \pi^- + \pi^0$ , and  $\Lambda \rightarrow n + \pi^0$ . The detailed calculations leading to the predicted intensity and energy spectrum of the  $\gamma$ -rays (based on the average numbers of mesons formed in an interaction, their angular distribution, and the resulting energy spectrum) are quite lengthy. This is due to the need to study the many different products, to take into account the different cosmic ray species (protons, helium nuclei, and heavier particles) and interstellar nuclei in the correct proportions, follow their decay, integrate over all angles, and then integrate over the cosmic ray energy spectrum. These calculations have, however, been performed (see Carvalho and Gould, 1971; Stecker, 1971; Stecker, 1973, and the results with the more current parameters used by Kniffen et al., 1977). The resulting energy spectrum is shown in Figure 5-1. The total cosmic ray nucleon, matter interaction source function is estimated to be in the range (12 to 20)  $\times 10^{-26}$  photons ( $\geq 100$  MeV)  $\text{cm}^{-3} \text{s}^{-1}$  and (3.0 to 5.0)  $\times 10^{-26}$  photons ( $35 < E < 100$ )  $\text{cm}^{-3} \text{s}^{-1}$  in the local region of our galaxy assuming a helium-to-hydrogen ratio of 0.1, a heavy-nuclei-to-hydrogen ratio of 0.01 and a local hydrogen nucleus (atomic plus molecular) density of 1.0 to 1.7  $\text{cm}^{-3}$ .

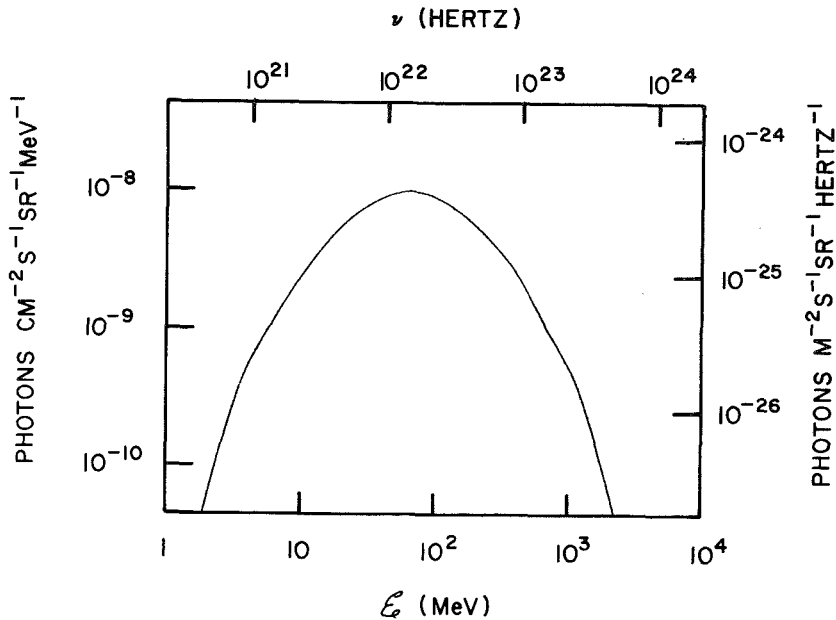


Figure 5-1. Typical differential spectrum expected from the decay of neutral pions produced in cosmic ray interactions with interstellar gas (adopted from Stecker, 1971). The curve is symmetric about  $\mathcal{E}^*$  since the abscissa is chosen to be  $\log \mathcal{E}$ .

The energy spectrum of the  $\gamma$ -rays resulting from  $\pi^0$  decay is quite different from that resulting from most other astrophysical processes, such as bremsstrahlung, synchrotron radiation, and the inverse Compton effect. The origin of the unique spectrum is the decay of the  $\pi^0$  into two massless particles of equal energy in the rest frame. The probability distribution of the  $\gamma$ -rays in the laboratory system can be shown (e.g., Fichtel and Kniffen, 1974) to be a constant from  $\mathcal{E}^* [(1-\beta)/(1+\beta)]^{1/2}$  to  $\mathcal{E}^* [(1+\beta)/(1-\beta)]^{1/2}$  and zero outside this range, where  $\mathcal{E}^*$  is the energy of the  $\pi^0$  decay  $\gamma$ -ray in the rest frame. Since this range always includes  $\mathcal{E}^*$  and the integral is performed over a distribution of  $\beta$ 's, it is seen at once that the distribution would have a peak at  $\mathcal{E}^*$  and be symmetrical when plotted against  $\ln \mathcal{E}$ , as seen in Figure 5-1.

## Cosmic Ray Electron Interactions

As cosmic ray electrons pass through the interstellar medium they produce photons over a wide range of energies. In the case of the energetic electrons, the resulting high energy photon spectrum reflects that of the electrons, at least qualitatively, in the sense that it is a monotonically decreasing function with increasing energy. The largest  $\gamma$ -ray intensity result from electrons probably comes from bremsstrahlung, the radiation from interactions of energetic electrons with matter. The calculation of the radiation from this mechanism in the region below  $10^2$  MeV is rather uncertain because the interstellar cosmic ray electron spectrum is not well known at low energies where the electron spectrum observed near the Earth has undergone strong solar modulation. This problem did not arise in the case of cosmic ray nucleon matter interactions because there the higher energy cosmic rays are most significant in the production of  $\gamma$ -rays, and their spectrum and general composition are well known and not affected markedly by solar modulation.

The cosmic ray electron, matter  $\gamma$ -ray production can be calculated using the bremsstrahlung cross-section formulas of Koch and Motz (1959). The calculations in general are very complex. However, to a good approximation, if the parent electron differential intensity has the form

$$j_e \equiv \frac{dJ_e}{dE_e} = K E_e^{-a} , \quad (5-1)$$

then the  $\gamma$ -ray source function is given by

$$q(\mathcal{E}) = \sum_s \frac{\rho_s}{X_0} \left( \frac{4\pi}{\mathcal{E}} \right) \int_{\mathcal{E}}^{\infty} j_e dE_e \quad (5-2)$$

where  $\rho_s$  is the mass density of the particular nuclear species and  $X_0$  is the radiation length. The sum is over all target species. Assuming the interstellar composition to be 10 percent He and 1 percent heavy nuclei, the result is

$$q(\mathcal{E}) \cong 4.7 \times 10^{-25} n_H \left( \frac{K\mathcal{E}^{-a}}{(a-1)} \right) \frac{\text{photons}}{\text{cm}^3 \text{ s MeV}} \quad (5-3)$$

where  $n_H$  is the number of protons per unit volume in both atomic and molecular form. This last equation includes the effect of the nuclei heavier than the proton as long as they are in the assumed proportions. Notice that the spectral index of the  $\gamma$ -ray differential source function is the same as that of the differential electron spectrum.

Considering the uncertainties in the molecular hydrogen density and in the electron spectrum, it seems possible only to give a range for the local source functions for bremsstrahlung, which are estimated as  $Q_b(\mathcal{E} > 100 \text{ MeV}) = (4 \text{ to } 8) \times 10^{-26} \text{ photons cm}^{-3} \text{ s}^{-1}$  and  $Q_b(35 < \mathcal{E} < 100 \text{ MeV}) = (6 \text{ to } 15) \times 10^{-26} \text{ photons cm}^{-3} \text{ s}^{-1}$  based on the work of Fichtel et al. (1978) and the earlier work referenced in that paper. Although this source function is smaller than the cosmic ray nucleon one above 100 MeV, it dominates at lower energies and, in fact, becomes increasingly important the lower the  $\gamma$ -ray energy.

Even for simple models, the cosmic ray electron spectrum is not expected to have exactly the same shape everywhere in the galaxy because more secondary electrons are produced in regions of greater matter density. Specific  $\gamma$ -ray spectral shapes will be discussed later in this chapter following a discussion of the galactic matter distribution and the current concepts of cosmic ray confinement and propagation.

Cosmic ray electrons also interact with starlight photons, for which both the optical and infrared ranges are important, and with the blackbody radiation to produce Compton  $\gamma$ -rays. The source functions of these interactions are much smaller in the galactic plane in the vicinity of the solar system. The total contribution to the galactic  $\gamma$ -radiation, however, is significant because

the cosmic ray and stellar photon scale heights above the galactic plane are much greater than those of the matter and, of course, the blackbody photon density is uniform. Hence, the integral intensity along a line of sight is closer to that of the bremsstrahlung than the source functions above would imply.

The calculations associated with the production of Compton  $\gamma$ -rays are quite complex; however, they have been performed in some detail for the cases of astrophysical interest by Ginzburg and Syrovatskii (1964). A power law in energy for the electron spectrum of the form given by Equation (5-1) will produce a power law  $\gamma$ -ray source function of the form

$$q(\mathcal{E}) \propto \mathcal{E}^{-(a+1)/2} \quad (5-4)$$

Whereas, in the case of bremsstrahlung, the astrophysical  $\gamma$ -rays come predominantly from electrons of energies similar to those of the  $\gamma$ -rays, or only a factor of several higher in energy, for the Compton case, the energy of the parent electron is given approximately by the equation

$$\mathcal{E}_\gamma \cong \left( \frac{E_e}{mc^2} \right)^2 \mathcal{E}_p \quad (5-5)$$

where  $\mathcal{E}_p$  is the photon energy before the electron interaction. Therefore, if the interaction is with starlight where the typical photon energy is a few eV, in order for the  $\gamma$ -ray to be about a hundred MeV,  $E_e$  must be several GeV. For the  $3^\circ$  blackbody radiation, the typical photon energy is about  $8 \times 10^{-4}$  eV; therefore, the parent electrons must be in the range of  $2 \times 10^5$  MeV to produce one hundred MeV  $\gamma$ -rays. In the energy range above a GeV, there is no serious uncertainty in the electron spectrum due to a lack of knowledge of the solar modulation. However, in the few GeV range, the electron energy spectrum changes shape; so the calculation must be performed carefully. At energies as high as a few hundred thousand MeV, the electron energy spectrum is less well known, and an increased uncertainty in the calculated  $\gamma$ -ray intensity is introduced.

Using the Compton scattering functions of Ginzburg and Syrovatskii (1964) and the calculations of Fichtel et al. (1978, and references therein), the local Compton source function is estimated to be  $S_{ec}$  ( $\epsilon > 100$  MeV) =  $(0.3 \text{ to } 0.6) \times 10^{-26}$  photons  $\text{cm}^{-3} \text{s}^{-1}$  and  $Q_c$  (35 MeV  $\epsilon > 100$  MeV) =  $(0.5 \text{ to } 1.0) \times 10^{-26}$  photons  $\text{cm}^{-3} \text{s}^{-1}$ . The range of values arises partially from uncertainties in the electron spectrum and partially from a lack of knowledge of the photon density.

The synchrotron radiation is quite small in the  $\gamma$ -ray region even though it is important in the radio region. The estimate for the synchrotron radiation source function is given in Table 5-1 as well as the other estimates that have been discussed. These source functions together with the associated knowledge of the spectral shape will be used later in this chapter to deduce the expected  $\gamma$ -ray intensities as a function of galactic coordinates after a discussion of the galactic matter and cosmic ray distributions.

**Table 5-1**  
**Source Functions in the Solar Vicinity**

Source Mechanism	Values of Source Functions ( $\text{cm}^{-3} \text{s}^{-1}$ )	
	$35 < \epsilon \text{ (MeV)} < 100$	$\epsilon \text{ (MeV)} > 100$
Cosmic Ray Nucleon, Matter Interactions	$(3.0 \text{ to } 5.0) \times 10^{-26}$	$(12 \text{ to } 20) \times 10^{-26}$
Electron Bremsstrahlung Compton Scattering,	$(6 \text{ to } 15) \times 10^{-26}$	$(4 \text{ to } 7) \times 10^{-26}$
Star Emission and 3 K	$(0.5 \text{ to } 1.0) \times 10^{-26}$	$(0.3 \text{ to } 0.6) \times 10^{-26}$
Synchrotron Radiation	$(0.3 \text{ to } 0.9) \times 10^{-30}$	$(0.2 \text{ to } 0.6) \times 10^{-30}$

### Gamma Ray Lines

In addition to the  $\gamma$ -ray continuum, existing in our galaxy it is possible for distinct  $\gamma$ -ray lines to be formed in the intergalactic medium. These lines may be created in several of the following ways: (1) the interaction of low energy cosmic rays with both interstellar gas and dust grains, leading to excited nuclei which

subsequently emit  $\gamma$ -rays through electromagnetic deexcitation of an excited state, (2) the annihilation of positrons which have been slowed down with interstellar electrons, and (3) the decay of nuclei which in turn emit  $\gamma$ -rays.

For case (1), the strength of the line radiation contains information about the composition and nuclear excitation conditions in the radiating gas. At least some of the dominant lines formed in this way should be the result of deexcitation of the lower levels of the most abundant nuclei. Table 5-2 (Fichtel et al., 1980) lists the first few of these nuclei with their abundance and the energy of the first excited state; a Population I composition is assumed. In general, the main nuclear lines from direct excitation lie in the energy range  $0.1 \text{ MeV} < E < 7 \text{ MeV}$ , where the lower range is affected by the contributions of higher excited states and less abundant nuclei. The lines from interstellar grains should be separable from those from the gas by their much narrower line widths allowing the two constituents to be studied separately. Unfortunately, the expected source strengths are below the observable level (Ramaty and Lingenfelter, 1979).

**Table 5-2**  
**Important Excited States of Abundant Nuclei**

Nucleus	$E$ (MeV)	Abundance (mass fraction)
H	-	$7.4 \times 10^{-1}$
He <sup>4</sup>	-	$2.4 \times 10^{-1}$
O <sup>16</sup>	6.14	$1.1 \times 10^{-2}$
C <sup>12</sup>	4.43	$4.5 \times 10^{-3}$
Fe <sup>56</sup>	0.847	$1.3 \times 10^{-3}$
Ne <sup>20</sup>	1.63	$1.2 \times 10^{-3}$
N <sup>14</sup>	2.31	$9.7 \times 10^{-4}$

Source: Fichtel et al. (1980).

Regarding case (2), positrons are produced in sizeable numbers through the interaction of the cosmic radiation with interstellar matter, both through the decay of  $\pi^+$  nuclei formed

in high energy cosmic ray interactions and as the result of low energy cosmic ray interactions. There has been an observation of the 0.511 MeV line from the galactic plane in the general direction of the galactic center at an intensity level of approximately  $1.0 \times 10^{-3}$  photons  $\text{cm}^{-2}\text{s}^{-1}$  (Levanthal, MacCallum, and Strong, 1978). This flux is almost two orders of magnitude greater than would be expected from cosmic ray interactions and may be from a single source at the galactic center. (Ramaty and Lingenfelter (1979) have proposed that positrons in large numbers may be coming either from black holes or from the decay of active nuclei produced in nucleosynthesis during supernovae explosions).

The subject of supernovae brings up case (3), the last of the three diffuse sources of  $\gamma$ -ray lines to be discussed. If the half-life of the unstable parent nuclei formed in a supernova, nova, or flare is very long compared to the typical time interval between production (nucleosynthesis) events in the volume of space observed, the abundance tends to build up to a steady-state value. Thus, in principle at least,  $\gamma$ -ray line astronomy provides a means for the study of cosmic explosions and nucleosynthesis events through their residue in interstellar space, as well as through direct observation of the explosion itself. The most promising line (for interstellar space as opposed to the supernova remnant itself) appears to be the 1.809 MeV line from the decay of  $^{26}\text{Al}$  whose intensity has been estimated to be  $5 \times 10^{-5}$  photons  $\text{cm}^{-2}\text{s}^{-1}\text{rad}^{-1}$  from the direction of the galactic center (Ramaty and Lingenfelter, 1979). In view of the long lifetime of the isotope (mean life =  $1.1 \times 10^6$  years), the emission would be expected to be steady.

## GALACTIC MATTER DISTRIBUTION

The relevant concern here is the galactic diffuse matter in the form of atoms, molecules, ions, and dust with which cosmic rays interact. The primary constituents are atomic and molecular hydrogen. Both are known to be confined to a narrow disk ( $\sim 0.1$  kpc in scale height for atomic hydrogen) with the molecular hydrogen distribution apparently narrower than that of the atomic hydrogen by a factor of two (e.g., Gordon and Burton, 1976; Solomon and Sanders, 1979). The radius of the disk does not have a sharp edge, but it is of the order of 15 to 18 kpc, with

the Sun about 10 kpc from the center and approximately in the middle of the disk.

Atomic hydrogen reveals its presence through the emission of the 21 cm line, which is produced by the hyperfine transition of this neutral atom. Observations of this line are usually expressed in terms of antenna or brightness temperature as a function of frequency Doppler shifted from the line's natural frequency. These measurements must then be converted to a density distribution using a rotational function for the galaxy and including corrections for partial saturation, where appropriate. Although the translation of the observations in to a galactic spatial distribution is difficult, on a broad scale the density profile is reasonably well known, even though details of arm structure are not always agreed on by all workers in the field. A general spiral pattern does appear to emerge. The distribution of continuum radiation (Landecker and Wielebinski, 1970; Price, 1974)  $\gamma$ -radiation (Bignami et al., 1975), HII regions (Georgelin and Georgelin, 1976), supernova remnants (Clark and Caswell, 1976), pulsars (Seiradakis, 1976), and infrared emission (Hayakawa et al., 1976) are all consistent with the existence of spiral structure in the galaxy. In pursuit of the galactic density pattern, Simonson (1976) and others have used the 21 cm measurements and the density wave theory to construct a model of the overall spiral pattern of our galaxy. The specific result obtained by Simonson (1976) is shown in Figure 5-2.

The density distribution of molecular hydrogen cannot be measured directly, but must be inferred from other measurements. At present, the best approach appears to be through the observations of the 2.6 mm spectral line of  $^{12}\text{CO}$ , which shows the distribution of cold interstellar material. The fact that  $^{12}\text{CO}$  and  $^{13}\text{CO}$  lines have the same general shape has been used to justify the belief that the  $^{12}\text{CO}$  lines are associated with optically thin regions and that a galactic distribution of CO may be derived accurately). The molecular hydrogen distribution is then deduced by relating the CO densities to those of  $\text{H}_2$  on the basis of solar abundances. The nature of this process makes the molecular hydrogen density distribution less certain than that of the atomic hydrogen. The average galactic radial distribution of molecular and atomic hydrogen deduced by Gordon and Burton (1976) shows that the molecular hydrogen to atomic hydrogen ratio is

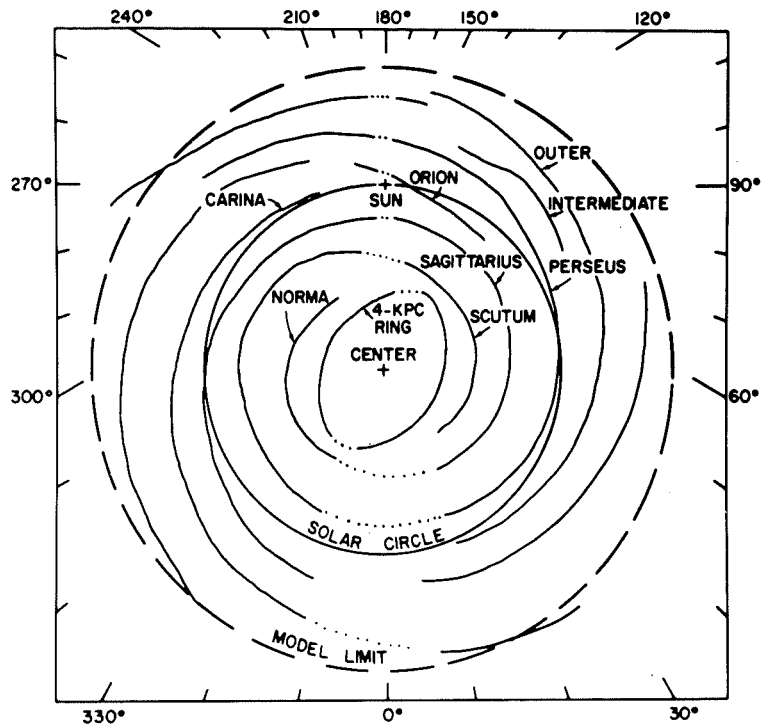


Figure 5-2. The spiral structure of our galaxy as determined by Simonson (1976; reprinted with permission). The specific figure shown here was supplied by Dr. C. Simonson and has not been published elsewhere. The lines represent the spiral arm density maxima.

much larger in the inner galaxy than it is in the outer galaxy. This is consistent with the concept that the density and clustering of matter is greater in the inner galaxy. The absolute intensity of molecular hydrogen is still quite uncertain, but Gordon and Burton (1976) estimated that the molecular hydrogen is dominant in the inner galaxy. From the Copernicus satellite data on the local interstellar gas densities, Savage et al. (1977) estimate the fraction of the gas in molecular form locally to be about 0.25 and possibly higher.

The CO observations indicate that the great majority of the molecular hydrogen is in clouds. There is also some evidence that atomic hydrogen tends to cluster on the peripheries of these clouds and in small clouds. The recent work of Solomon and Sanders (1980) has, in fact, suggested that the interstellar medium is dominated by massive cloud complexes, having a typical length of 40 pc, a mean  $H_2$  density of  $300 \text{ cm}^{-3}$ , and containing  $(10^5 \text{ to } 3 \times 10^6) M_{\odot}$ . They would then be the most massive objects in the galaxy.

Until recently it had not been clear whether molecular clouds were associated with spiral structure, because of the difficulty of the measurements and because data for the southern half of the galactic center region (the fourth quadrant) where the spiral arms appear most strongly in the 21 cm data did not yet exist. Now, on the basis of a high sample survey and observations in both the first and second quadrants of the galactic plane, Cohen et al. (1980) have shown the existence of the molecular counterparts of the five classical 21 cm spiral arms segments in these quadrants, namely the Perseus arm, the Local arm, the Sagittarius arm, the Scutum arm, and the 4 kpc arm.

Regarding the remaining material in the interstellar medium, it was noted earlier that the other constituents are small. Whereas ionized matter, grains, and dust are negligible from the standpoint of  $\gamma$ -ray production, except for the possibility of  $\gamma$ -ray lines from interstellar grains, helium and heavier nuclei do contribute small additions to the diffuse  $\gamma$ -ray intensity. Although they represent only about 10 percent and 1 percent of the hydrogen content, respectively, the cross sections for the  $\gamma$ -ray production are large. These factors were included in the production functions.

## GALACTIC COSMIC RAY DISTRIBUTION

The "cosmic rays" are the energetic nuclei and electrons that pervade interstellar space. The nuclei are the dominant component and have an average energy of several GeV, although nuclei with energies of over  $10^{20}$  eV have been detected. Protons constitute the majority of the nuclear component with helium nuclei making up to 10 percent of the total by number and heavy nuclei about 1 percent. In terms of energy per nucleon, the spectra are similar, at least to about  $10^{12}$  eV. There is some evidence for a

major change in composition at very high energies. Electrons of both positive and negative charges exist and their intensity is about 1 percent of that of the protons at the same energy. Found among the heavy nuclei are substantial numbers of secondary nuclei, such as lithium, beryllium, and boron, which are present only in very small quantities in normal cosmic abundances, but are produced in nuclear interactions of heavy nuclei. An analysis of these nuclei suggests that the cosmic rays have typically traveled through a few  $\text{g cm}^{-2}$ , although there is a distribution in path lengths, and that the higher energy ( $\sim 10^{11}$  eV) cosmic rays have passed through somewhat less material on the average than the lower energy ( $\sim 10^9$  eV) cosmic rays. Some secondaries, such as  $\text{Be}^7$ , are unstable and act as clocks giving an estimate of the age of the cosmic rays, now thought to be somewhat over  $10^7$  years. (For a general review of the detailed properties of cosmic rays, see the review papers of Meyer, 1969, and Waddington, 1977.)

Combining the lifetime of the nuclei, the velocity and the average amount of matter traversed shows that the average density of matter seen by the nuclear cosmic rays is about  $0.1 \text{ cm}^{-3}$ . Hence, on the basis of the discussion in the last paragraph, they do not spend most of their time in the thin matter disk where the density is about  $1 \text{ cm}^{-3}$ , but rather they must have a broader distribution relative to the galactic plane. The nonthermal continuum radio emission, which is generally attributed to the synchrotron radiation from cosmic ray electrons interacting with the galactic magnetic fields (e.g., Ginzburg and Syrovatskii, 1964, 1965), provides information about the high energy cosmic ray electrons. Baldwin (1967, 1976) estimates the equivalent disk thickness for synchrotron emission to be about 750 pc, and some analyses have suggested that it is even larger. Significant non-thermal emission is even seen as high as 2 kpc above the plane. If it is assumed that the electron density and magnetic field density both have the same distribution on the average and that it is Gaussian, then since the synchrotron radiation is proportional to the product of the two, the scale height of each individually is  $\sqrt{2} \times 0.75$  kpc, or just over 1 kpc. It seems reasonable to assume that cosmic ray electrons and protons and the magnetic fields, at least in our local region of the galaxy and probably elsewhere, all have a scale height of this order.

Little is known experimentally about the cosmic ray distribution in the plane of the galaxy. The high energy  $\gamma$ -ray data suggest that the cosmic ray density distribution is similar to that of the matter on a coarse scale in terms of the distribution in the galactic plane (e.g., Fichtel et al., 1975; Hartman et al., 1979). Further, the existing  $\gamma$ -ray data even support the concept of the cosmic ray density being greater in arm segments, including the strong interstellar matter feature about 5 kpc from the center.

Several fundamental theoretical considerations place constraints on the cosmic ray distribution. Under the now generally accepted assumption that the cosmic rays and magnetic fields are primarily galactic and not universal, these fields and cosmic rays can only be constrained to the galactic disk by the gravitational attraction of the matter (Biermann and Davis, 1960; Parker, 1966, 1969, and 1977). The local energy density of the cosmic rays ( $\sim 1 \text{ eV/cm}^3$ ) is about the same as the estimated energy density of the magnetic field and that of the kinetic motion of matter. Together the total expansive pressure of these three effects is estimated to be approximately equal to the maximum that the gravitational attraction can hold in equilibrium. Assuming the solar system is not at an unusual position in the galaxy, these features suggest that the cosmic ray density throughout the galaxy may generally be as large as could be contained under near-equilibrium conditions.

Further theoretical support is given to this concept by the calculated slow diffusion rate of cosmic rays in the magnetic fields of the galaxy and the small cosmic ray anisotropy. These considerations then lead to the hypothesis that the energy density of the cosmic ray is larger where the matter density is larger on a coarse scale such as that of the galactic arms. On a smaller scale, the pressures of the cosmic ray gas and magnetic fields cause the cosmic ray gas and field system to expand between the large clouds through which the magnetic fields thread. As noted earlier, the radio continuum measurements and cosmic ray results support the picture of the cosmic rays having a large scale height relative to the matter and spending only a relatively small amount of time passing through the dense cloud region. This large scale height is important in determining the Compton contribution to the diffuse emission, as will be seen later.

The picture that seems to emerge then is that cosmic rays, at least below  $10^{16}$  or  $10^{17}$  eV/nucleon, are bound to the lines of force and the field lines are closed (or else the cosmic rays would escape too quickly). The cosmic rays are constrained and not free to escape individually. Thus, if they do escape, it must be the result of cosmic ray group pressure inflating the magnetic field lines and pushing outward from the galaxy. All cosmic ray particles then, whether they have less than 1 GeV,  $10^2$  GeV, or over  $10^4$  GeV, escape with about equal ease. The modest variation in path length of the cosmic rays with energies supports this concept, and, in fact, there are theories which suggest that the path length variation which is seen could be largely the result of source location and local diffusion rather than escape.

The fact that the cosmic ray density is approximately as large as can be contained suggests a plentiful source. What is this source? At present most astrophysicists in the field feel that cosmic rays come from supernovae and flare stars and may or may not receive substantial subsequent acceleration. If supernovae were to supply the total cosmic ray energy, each supernova would have to produce between  $10^{49}$  and  $10^{50}$  ergs of cosmic rays, assuming a supernova rate of 1 every 30 years. This seems not a prohibitive amount of energy for a supernova to give to energetic particles provided a reasonable mechanism can be found and verified. Even if supernovae are not the primary initial source, they may supply an important part of the total energy of the cosmic rays by shock wave acceleration of existing cosmic rays (Blandford and Ostriker, 1980). One of the bright hopes for  $\gamma$ -ray astronomy is that it can identify the origins of the cosmic ray particles through their interactions with the local matter.

#### **CURRENT GAMMA RAY RESULTS AND THEIR INTERPRETATION**

The most intense celestial high energy  $\gamma$ -radiation observed is that from the galactic plane. This feature was observed first by the pioneering counter telescope flown on OSO-3 (Kraushaar et al., 1972), and the major features of this galactic radiation have now been defined by measurements made with the SAS-2 and COS-B satellites (Kniffen et al., 1973; Fichtel et al., 1975; Hartman et al., 1979; Bennett et al., 1977 and Mayer-Hasselwander et al.; 1980, respectively). The results from the SAS-2 satellite

shown in Figure 5-3 reveal that the galactic plane  $\gamma$ -radiation is strongly correlated with galactic structural features, especially when the known strong  $\gamma$ -ray sources were subtracted from the total radiation. The distribution of high energy ( $E > 100$  MeV)  $\gamma$ -ray intensity along the galactic plane summed over the latitude interval from  $-10^\circ$  to  $+10^\circ$  is shown in Figure 5-4 (Hartman et al., 1979) in bins which are  $2.5^\circ$  wide in latitude. Notice that the emission from the region  $310^\circ < l < 50^\circ$  is particularly intense relative to the remainder of the galactic plane. This contrast is much greater than that seen in other indicators of galactic structure such as the atomic hydrogen column density deduced from the 21 cm measurements, for example. The results of COS-B have confirmed these general features, as shown in Figure 5-5 (Mayer-Hasselwander et al., 1980).

When examined more closely, the longitudinal and latitudinal distributions appear generally correlated with galactic structural features, with maxima occurring at galactic longitudes of approximately  $215^\circ$ ,  $330-335^\circ$ ,  $340-345^\circ$ ,  $0^\circ$ , and  $25-35^\circ$  (Fichtel et al., 1975; and Hartman et al., 1979) in general agreement, for example, with the galactic center itself and the location of tangents to galactic arm segments (Simonson, 1976). These results and their theoretical interpretation have led to the hope that  $\gamma$ -ray astronomy, particularly with the high penetrating power of  $\gamma$ -rays may ultimately lead to a much improved picture of the galaxy.

Even at high latitudes ( $10^\circ < |b| < 90^\circ$ ) a major portion of the  $\gamma$ -radiation observed is now believed to be galactic on the basis of its correlation with the matter and synchrotron radiation (Fichtel et al., 1978). On a coarse scale, the high latitude  $\gamma$ -ray intensity is reasonably well represented by the expression

$$I_\gamma = C_1 + C_2/\sin|b| \quad (5-6)$$

When examined more closely, the correlation between the  $\gamma$ -ray emission and both the galactic matter distribution and the radio continuum radiation is quite good, as will be discussed in detail in Chapter 9.

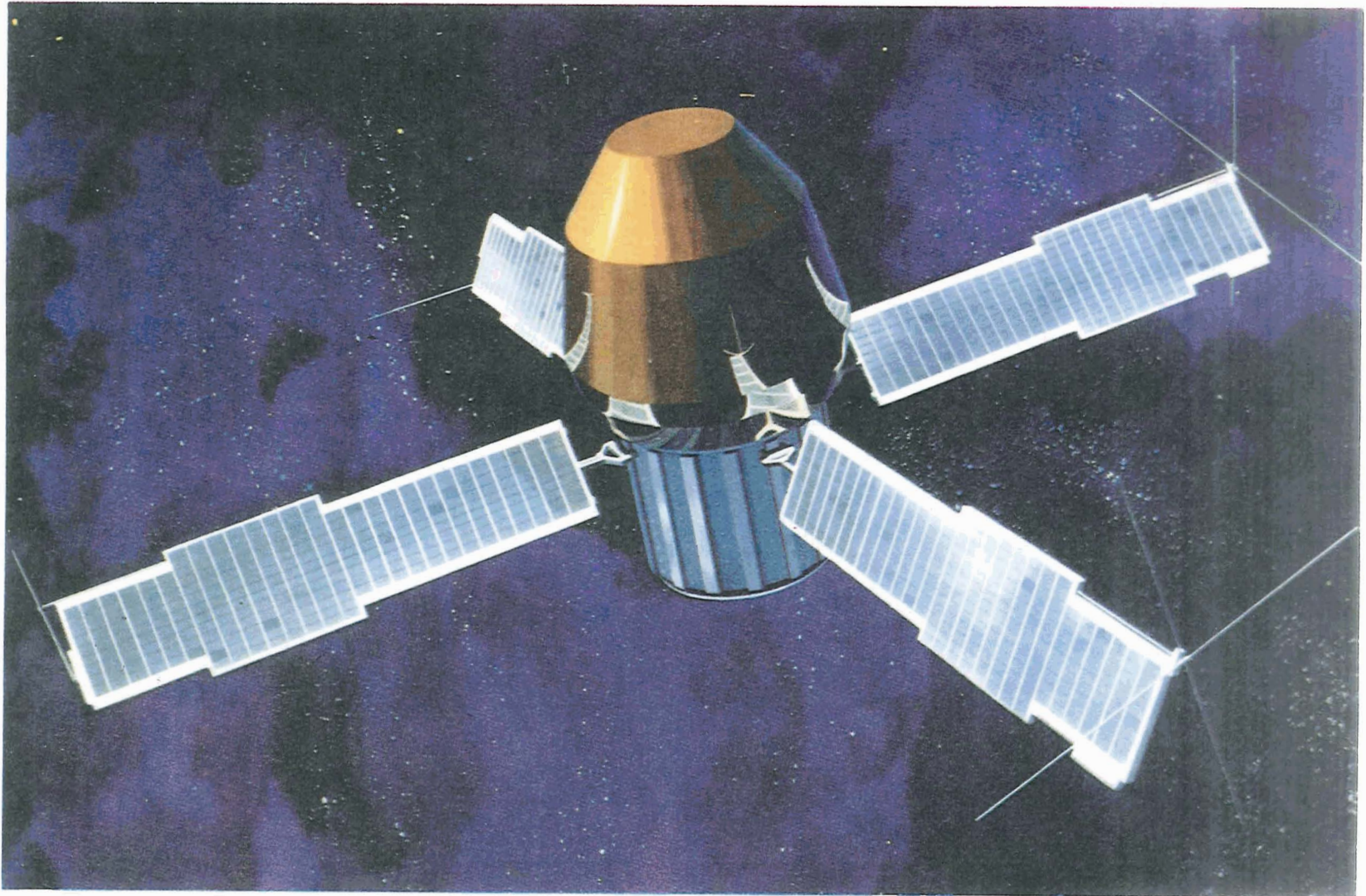


Figure 5-3. Artist's conception of the second Small Astronomy Satellite (SAS-2) in space. SAS-2, launched in November 1972, carried a high energy  $\gamma$ -ray telescope.

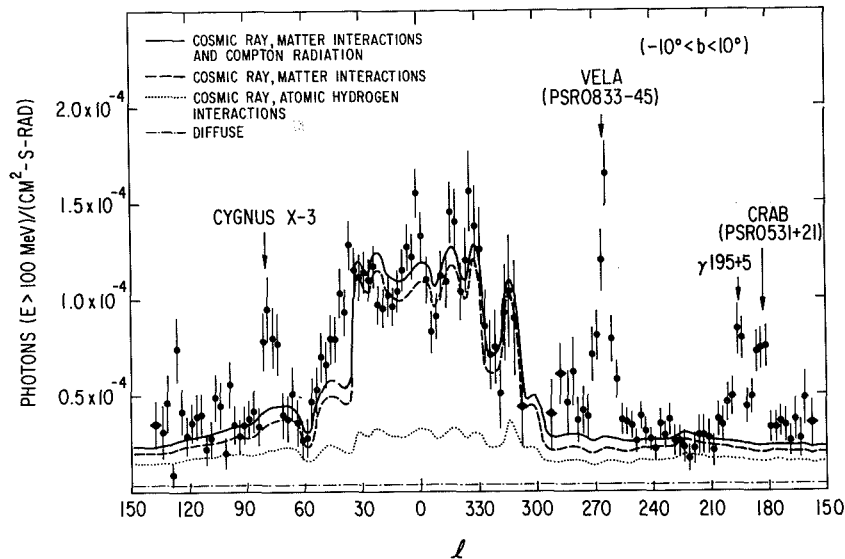


Figure 5-4. The longitude distribution of  $\gamma$ -rays with energy above 100 MeV from the SAS-2 results (Hartman et al., 1979). The curves calculated by these authors are based on the model of Kniffen et al., (1977), using updated values for the  $\gamma$ -ray source function and the local interstellar matter density as indicated by Fichtel et al. (1978) and Kniffen et al. (1978).

The distributions in galactic latitude for  $\gamma$ -rays above 70 MeV are given in Figure 5-5. The boundaries of the longitude intervals are such that the influence of the stronger discrete sources is avoided. In the range of galactic latitudes from  $330^\circ$  to  $30^\circ$  an enhancement is visible in the latitude range  $5^\circ < b < 20^\circ$  relative to the range  $-20^\circ < b < -5^\circ$  (Mayer-Hasselwander, 1980). This enhancement seen already in the early SAS-2 data taken together with the excess seen at negative latitudes in the galactic anticenter has been interpreted as  $\gamma$ -ray emission produced in the local concentration of clouds known as Gould's Belt (Fichtel et al., 1975; Thompson et al., 1977).

The latitude distributions for  $90^\circ < l < 150^\circ$  have a peak at about  $b = 2^\circ$ , while the distribution for  $250^\circ < l < 300^\circ$  has an excess at negative latitudes. This effect is seen in both the COS-B data shown in Figure 5-5 and the SAS-2 data (see, for example, Hartman et al., 1979). The offsets in the  $\gamma$ -ray data are qualitatively similar to the "hat brim" effect visible in the radio observations and due to the large-scale warping of the galactic disk (see, for example, the summary of Burton, 1976, based on the data of Weaver and Williams, 1973). The agreement is a further indication that the  $\gamma$ -ray emission is related to the large-scale structure of the galaxy.

The broad distribution in galactic latitude for the longitude intervals away from the galactic center provides strong evidence that the observed  $\gamma$ -rays in these directions are, for the most part, produced locally (within a few kpc, whereas the additional narrow distribution seen toward the inner parts of the galaxy implies that a large part of the emission comes from more distant ( $> 3$  kpc) features.

At present the existing measurements from SAS-2 and COS-B do not permit a determination of detailed energy spectra; however, important coarse features can be deduced.

Table 5-3 (Hartman et al., 1979) gives the power law exponents deduced from the SAS-2 data for seven different regions of the galactic plane and for all of these regions combined. The uncertainties associated with the exponents for individual regions are dominated by statistics; however, the uncertainty in the exponent for the combined data also reflects the systematic effects. The major systematic uncertainties are related to the inaccuracies in the energy resolution functions and the absolute average energy. Except for the four strong sources identified in Figure 5-4, there is no significant evidence for a variation of the energy spectrum along the galactic plane. Similar conclusions have been drawn from preliminary results of the COS-B satellite (Paul et al., 1978). The overall spectral index of  $1.70 \pm 0.14$  is consistent with the value deduced for the galactic component of the high altitude ( $|b| > 10^\circ$ ) radiation (Fichtel et al., 1978). The agreement, although of limited statistical weight, is important because there are no known local galactic sources contributing to the high latitude radiation. Figure 5-6 shows the spectrum of the galactic  $\gamma$ -radiation for a region near the galactic center ( $320^\circ < l < 40^\circ$ ).

Figure 5-5. Presentation in galactic coordinates of the structure of the galactic  $\gamma$ -ray emission as measured by COS-B (reprinted with permission from Mayer-Hasselwander et al., 1980). In the map the surface fitted to the data matrix is indicated by various colors. The latitude profiles show the data points with errors and the fitted surface (full line). The longitude ranges over which the data are averaged are indicated by brackets. In these profiles and in the map a background is subtracted; in the longitude profile the data points with errors averaged over  $+5^\circ$  are shown. The full line indicates a cross section through the fitted surface along the galactic equator. The background is indicated by the shaded area. The map and the profiles show the parameter "on-axis" counts,  $s^{-1}$ ,  $sr^{-1}$ . This figure is reprinted from the work of the Caravan collaboration consisting of Space Science Department, ESTEC, Noordwijk, The Netherlands; University of Leiden, The Netherlands; Centre d'Études Nucléaires de Saclay, France; University of Milan, Italy; University of Palermo, Italy; Max-Planck Institut für Extraterrestrische Physik, Garching, FRG; and it originally appeared in the *Annals of the New York Academy of Sciences* in the article referenced above and is reprinted here with their permission.



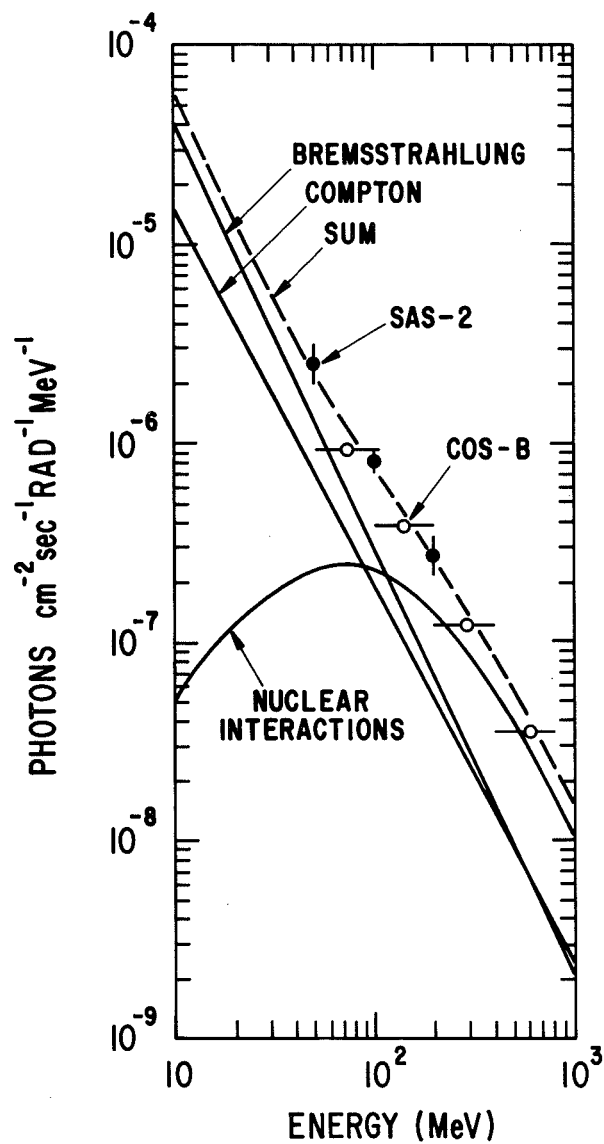


Figure 5-6. Energy spectrum of the galactic  $\gamma$ -radiation for a region near the galactic center (Kniffen and Fichtel, 1981). The calculated spectrum, shown by a dashed line in the figure is based on the work of Fichtel et al. (1976), but with an increase of a factor of two in the primary electron spectrum as suggested by the work of Fichtel et al. (1978) and Kniffen et al. (1978).

**Table 5-3**  
**Gamma Ray Spectral Index in the Galactic Plane**

Galactic Longitude Range	Spectral Index
350° - 10°	1.74 ± 0.15
10° - 40°	1.72 ± 0.15
40° - 70°*	1.79 ± 0.15
*90° - 175°**	1.68 ± 0.16
**205° - 255°***	1.62 ± 0.17
***275° - 320°	1.84 ± 0.22
320° - 350°	1.55 ± 0.15
All of Above	1.70 ± 0.14

\*Cygnus X-3 region was omitted.

\*\*Anticenter region near (PSR 0531+21) and (195,5) was omitted.

\*\*\* (PSR 0833-45) region was omitted.

**Source:** Hartman et al. (1979).

An estimate will now be made of the diffuse galactic  $\gamma$ -radiation to be expected from cosmic ray interactions with galactic matter and photons. It should be mentioned that there is probably also an unresolved point source contribution to the "diffuse" radiation measured by the SAS-2 and COS-B  $\gamma$ -ray instruments since the limited angular resolution of these instruments does not permit the separation of point sources. It is difficult to estimate this contribution; however, several factors suggest that point sources may not be a major contributor (see, for example, Cesarsky, 1980): these include the uniformity of the energy spectrum just discussed and, as will be seen, the  $\gamma$ -ray luminosity of the galaxy and its distribution being about what would be expected from the diffuse sources. In order to proceed now from the source functions to the estimated number of  $\gamma$ -rays to be seen in a given direction within a solid angle element,  $d\Omega$ , consider the following. The number of  $\gamma$ -rays per unit area and time within  $d\Omega$  falling on a surface a distance  $r$  from a volume element  $dV$  with a source strength of  $q$  is

$$\frac{1}{4\pi r^2} q(\mathfrak{E}, r) dV d\mathfrak{E} \quad . \quad (5-7)$$

Hence, the differential intensity is

$$j = \frac{dJ}{d\mathfrak{E}} = \frac{1}{4\pi} \int_0^\infty q(\mathfrak{E}, r) dr \quad , \quad (5-8)$$

where  $j$  is the number of photons per unit time, area, solid angle, and energy.

Considering first the interactions between cosmic rays and matter,

$$\begin{aligned} j(\mathfrak{E}_\gamma, l, b) = & \frac{1}{4\pi} \int dr [q_{\gamma_n}(\mathfrak{E}_\gamma, r=0) g_n(r, l, b) f_m(r, l, b)] \\ & + q_{\gamma_{e_p}}(\mathfrak{E}, r=0) g_e(r, l, b) f_m(r, l, b) \\ & + q_{\gamma_{e_s}}[(\mathfrak{E}, r=0) g_n(r, l, b) f_m^2(r, l, b)] \quad (5-9) \end{aligned}$$

where  $f_m$  is the ratio of the total interstellar gas density at a distance  $r$  from the Sun in the direction  $(l, b)$  to that at  $r = 0$ ,  $q_{\gamma_n}$  represents the number of rays produced per second per volume element per energy interval in interactions of nucleonic cosmic rays (with the intensity and spectral distribution in the solar vicinity) with the interstellar gas, and  $q_{\gamma_{e_p}}$  and  $q_{\gamma_{e_s}}$  are similar functions for primary and secondary cosmic ray electrons, respectively.  $g_n$  and  $g_e$  express the spatial variation with galactic

position of the ratio of the primary cosmic ray nucleon and electron components, respectively, to their interstellar value in the solar vicinity. Implicit in this approach is the assumption that the spectral shape of each component is unchanged throughout the galaxy. This assumption is reasonable as long as the source spectral shape in the solar vicinity is typical of that throughout the galaxy and energy losses remain within certain limits. The latter condition is true for the energy region and intensity levels relevant to the considerations here.

Equation (5-9) shows that if the cosmic ray primary electron component is proportional to the cosmic ray nucleon component, and if the secondary electron component is small compared to the primary electron component as the positron data suggest, the  $\gamma$ -ray intensity is approximately proportional to the integral over the product of the ratios of the cosmic ray intensity and matter density to their local values.

Similar expressions apply to the Compton radiation except that the  $f_m$  now refers to the photon density and the  $q$  refers to the Compton process. It is important to remember that, whereas Table 5-1 might suggest that the Compton radiation is relatively small, its contribution is, in fact, likely to be fairly important because of the large scale height thought to exist for the cosmic ray electrons and stellar photons relative to that for matter, coupled with the fact that the blackbody photon distribution is uniform. Estimates of the Compton radiation in fact suggest that it is comparable to the radiation from cosmic ray matter interactions at high latitudes; however, very close to the galactic plane  $|b| < 1^\circ$  the latter dominates very strongly.

It is not possible to proceed further without a specific model for the galactic matter distribution to be used in Equation (5-9). One test of any model, in addition to the data on which it was originally based, is whether it agrees with the  $\gamma$ -ray data. As might be expected, a substantial number of models currently exist in the literature which attempt to explain the  $\gamma$ -ray data, and the uncertainties in the results at present offer a fair degree of freedom of choice but one model of the diffuse galactic  $\gamma$ -ray emission, that of Kniffen et al. (1977), who also reviewed earlier work will be discussed. These authors assume that the cosmic rays are correlated with the galactic matter on the scale of galactic arms. The authors of several other papers (e.g., Bignami and

Fichtel, 1974; Paul et al., 1974; Schlickeiser and Thielheim, 1974; Bignami et al., 1975; Stecker et al., 1975; Puget et al., 1976; Paul et al., 1976) also come to the conclusion that the cosmic ray density is enhanced where the matter density is greatest, in agreement with the concept of coupling deduced from theoretical considerations by Parker (1966, 1969).

It is further assumed that the matter is preferentially concentrated in spiral arms in accordance with the model of Simonson (1976) which is based on 21 cm observations and the density wave theory. In addition to the 21 cm data, which shows that atomic hydrogen is primarily contained in spiral arms, the recent work of Cohen et al. (1980) demonstrates clearly that the molecular hydrogen is also strongly correlated with the same spiral arms. The radial dependence of the density of the atomic and molecular hydrogen was taken from the work of Gordon and Burton (1976), modulated to correspond to the spiral arm pattern. The scale height of the cosmic rays is about 1 kpc based on the equivalent disk thickness of the nonthermal continuum radio emission estimated by Baldwin (1967, 1976) and on the assumption that the scale heights for the cosmic rays and magnetic fields are the same. The exact arm-to-interarm matter density ratio is not critical as long as it is about 2:1 or greater. Figure 5-4 (Hartman et al., 1979) shows the  $\gamma$ -ray intensities predicted by this model, using updated parameters for the  $\gamma$ -ray production source function and the local interstellar matter density suggested by Fichtel et al. (1978). Also shown is the component due to Compton scattering. The electron interactions account for about one-third of the total  $\gamma$ -ray emission above 100 MeV. There is reasonable agreement with the experimental data, especially in view of the uncertainties in the knowledge of the mass distribution, particularly in the galactic center region, in the electron energy spectrum, and in the contribution of point sources.

A constant cosmic ray density, as might be predicted in a universal cosmic ray model, gives too small a ratio between the  $\gamma$ -ray intensity from the central region and that from the outer parts of the galaxy, and does not give rise to the significant peaks seen along galactic spiral arm features in the  $\gamma$ -ray data.

In Figure 5-6, the  $\gamma$ -ray spectrum predicted for the galactic center region is shown. The electron spectrum used to deduce this spectrum lies within the range appropriate for the values quoted in Table 5-1, but is on the high side of the range.

Instead of the approach discussed here, the existing  $\gamma$ -ray data might be used to deduce the galactic structure. Whereas this method is a potentially powerful means of determining galactic structure, at present several difficulties exist: (1) the large statistical uncertainty in the points which cause the deduced distribution to be far from unique in principal features; (2) the limited angular accuracy which makes seeing the fine features of a distribution impossible and makes seeing the principal ones even with a larger number of photons difficult; and (3) the remaining point source contributions which cannot be removed because the angular accuracy is not sufficient to resolve the individual point sources. A meaningful analysis of this type must, therefore, await data of better angular accuracy and statistical weight.

The future holds great promise that  $\gamma$ -ray astronomy will not only help in unraveling the general structure of the galaxy, especially in view of its apparent potential for giving a high contrast picture unaffected by absorption effects, but also in improving the understanding of galactic clouds, their relation to cosmic rays, and the origin and propagation of cosmic rays.

## REFERENCES

- Baldwin, J.E., 1967, in *Radio Astronomy and the Galactic System*, IAU Symp. 31, 337.
- Baldwin, J.E., 1976, in *The Structure and Content of the Galaxy and Galactic Gamma Rays*, NASA CP-002 (Washington, D.C.: NASA, 1976), p. 206.
- Bennett, K., Bignami, G. F., Buccheri, R., Hermsen, W., Kanbach, G., Lebrun, F., Mayer-Hasselwander, H.A., Paul, J.A., Piccinotti, G., Scarsi, L., Soroka, F., Swanenburg, B.N., and Wills, R.D., 1977, in *Recent Advances in Gamma Ray Astronomy*, ESA SP-124, p. 83.
- Biermann, L., and Davis, L., Jr., 1960, *Zs. F. Ap.*, **51**, 19.
- Bignami, G.F., and Fichtel, C.E., 1974, *Ap. J. (Letters)*, **189**, L65.
- Bignami, G.F., Fichtel, C.E., Kniffen, D.A., and Thompson, D.J., 1975, *Ap. J.*, **199**, 54.
- Blandford, R.D., and Ostriker, J.P., 1980, *Ap. J.*, **237**, 793.
- Burton, W.B., 1976, in *The Structure and Content of the Galaxy and Galactic Gamma Rays*, NASA CP-002 (Washington, D.C.: NASA, 1976), 163.
- Cavallo, G., and Gould, R.J., 1971, *Nuovo Cimento*, **2B**, 77.
- Cesarsky, C.J., 1980, *New York Academy of Sciences*, **336**, 223.
- Clark, D.H., and Caswell, J.L., 1976, *Mon. Not. Roy. Astr. Soc.*, **174**, 267.
- Cohen, R.S., Cong, H., Dame, T.M., and Thaddeus, P., 1980, *Ap. J. (Letters)*, **239**, L53.
- Fichtel, C.E., and Kniffen, D.A., 1974, in *High Energy Particles and Quanta in Astrophysics*, ed. McDonald and Fichtel (Cambridge, Mass.: The MIT Press, 1974), p. 428.

- Fichtel, C.E., Hartman, R.C., Kniffen, D.A., Thompson, D.J., Bignami, G.F., Ogelman, H., Ozel, M.E., and Tumer, T., 1975, *Ap. J.*, **198**, 163.
- Fichtel, C.E., Kniffen, D.A., Thompson, D.J., Bignami, G.F., and Cheung, C.Y., 1976, *Ap. J.*, **208**, 211.
- Fichtel, C.E., Simpson, G.A., and Thompson, D.J., 1978, *Ap. J.*, **222**, 833.
- Fichtel, C., Arnett, D., Grindlay, J., and Trombka, J., 1980, "Gamma Ray Astrophysics," in *Astrophysics from Spacelab*, ed. P.L. Bernacca and R. Ruffin (Dordrecht: D. Reidel Publ. Co., 1980), p. 145.
- Georgelin, Y.M., and Georgelin, Y.P., 1976, *Astron. Astrophys.*, **49**, 57.
- Ginzburg, V.L., and Syrovatskii, S.I., 1964, *The Origin of Cosmic Rays* (Oxford: Pergamon Press, 1964).
- Ginzburg, V.L., and Syrovatskii, S.I., 1965, *Ann. Rev. Astron.*, **3**, 297.
- Gordon, M.A., and Burton, W.B., 1976, *Ap. J.*, **208**, 346.
- Grindlay, J.E., Helmken, H.F., Brown, R.H., Davies, J., and Allen, L.R., 1975, *Ap. J. (Letters)*, **197**, L9.
- Hartman, R.C., Kniffen, D.A., Thompson, D.J., and Ozel, M.E., 1979, *Ap. J.*, **230**, 597.
- Hayakawa, S., Ito, K., Matsumoto, T., Ono, T., and Uyama, K., 1976, *Nature*, **261**, 29.
- Hewish, A., Bell, S.J., Pilkington, J.D., Scott, P.F., and Collins, R.A., 1968, *Nature*, **217**, 709.
- Klebesadel, R.W., Strong, I.B., and Olson, R.A., 1973, *Ap. J. (Letters)*, **182**, L85.

- Kniffen, D.A., and Fichtel, C.E., 1981, *Ap. J.*, **249**, to be published.
- Kniffen, D.A., Fichtel, C.E., and Thompson, D.J., 1977, *Ap. J.*, **215**, 765.
- Kniffen, D.A., Hartman, R.C., Thompson, D.J., and Fichtel, C.E., 1973, *Ap. J. (Letters)*, **186**, L105.
- Kniffen, D.A., Bertsch, D.L., Morris, D.J., Palmeira, R.A.R., and Rao, K.R., 1978, *Ap. J.*, **225**, 591.
- Koch, H.W., and Motz, J.W., 1959, *Rev. Mod. Phys.*, **31**, 920.
- Kraushaar, W.L., Clark, G.W., Garmire, G.P., Borken, R., Higbie, P., Leong, C., Thorsos, T., 1972, *Ap. J.*, **177**, 341.
- Lamb, R.C., Fichtel, C.E., Hartman, R.C., Kniffen, D.A., and Thompson, D.J., 1977, *Ap. J.*, **212**, L63.
- Landecker, T.L., and Wielebinski, R., 1970, *Aust. J. Phys. Suppl.*, **16**, 1.
- Levanthal, M., McCallum, C.J., Strong, P.D., 1978, *Ap. J. (Letters)*, **225**, L11.
- Mayer-Hasselwander, H.A., Bennett, K., Bignami, G.F., Buccheri, R., D'Amico, N., Hermsen, W., Kanbach, G., Lebrun, F., Lichti, G.G., Masnou, J.L., Paul, J.A., Pinkau, K., Scarsi, L., Swanenburg, B.N., Wills, R.D., 1980, *Annals of the New York Academy of Sciences, Proc. of the 9th Texas Symp.*, ed. J. Ehlers, J.J. Perry, and M. Walker, **336**, 211.
- Meyer, P., 1969, *Ann. Rev. of Astron. and Astrophys.*, **7**, 1.
- Parker, E.N., 1966, *Ap. J.*, **145**, 811.
- Parker, E.N., 1969, *Space Sci. Rev.*, **9**, 651.

- Parker, E.N., 1977, "Cosmic Ray Propagation and Containment," in *The Structure and Content of the Galaxy and Galactic Gamma Rays*, NASA CP-002 (Washington, D.C.: Government Printing Office, 1977), p. 283.
- Paul, J., Casse, M., and Cesarsky, C.J., 1974, *Proc. of the 9th ESLAB Symp.*, ESRO SP-106, 249.
- Paul, J., Casse, M., and Cesarsky, C.J., 1976, *Ap. J.*, **207**, 62.
- Paul, J.A., Bennett, K., Bignami, G.F., Buccheri, R., Caraveo, P., Hermsen, W., Kanbach, G., Mayer-Hasselwander, H.A., Scarsi, L., Swanenburg, B.N., and Wills, R.D., 1978, *Astron. Astrophys.*, **63**, L31.
- Price, R.M., 1974, *Astron. Astrophys.*, **33**, 33.
- Puget, J.L., Ryter, C., Serra, G., and Bignami, G., 1976, *Astron. Astrophys.*, **50**, 247.
- Ramaty, R., and Lingenfelter, R.E., 1979, *Nature*, **278**, 127.
- Savage, B.D., Bohlin, R.C., Drake, J.F., and Budich, W., 1977, *A Survey of Interstellar Molecular Hydrogen*, Wisconsin Astrophysics Preprint no. 46.
- Schlickeiser, R., and Thielheim, K.O., 1974, *Astron. Astrophys.*, **34**, 167.
- Seiradakis, J., 1976, in *The Structure and Content of the Galaxy and Galactic Gamma Rays*, NASA CP-002 (Washington, D.C.: Government Printing Office, 1974), p. 265.
- Simonson, S.C., 1976, *Astron. Astrophys.*, **46**, 261.
- Solomon, P.M., and Sanders, D.B., 1980, "Giant Molecular Clouds as the Dominant Component of Interstellar Matter in the Galaxy," in *Molecular Clouds in the Galaxy*, ed. P.M. Solomon and M. Edmunds (Oxford: Pergamon Press, 1980), p. 41.

- Stecker, F.W., 1971, *Cosmic Gamma Rays* (Baltimore, Md.: Mono Book Corp., 1971).
- Stecker, F.W., 1973, *Ap. J.*, **185**, 499.
- Stecker, F.W., Solomon, P.M., Scoville, N.Z., and Ryter, C.E., 1975, *Ap. J.*, **201**, 90.
- Thompson, D.J., Fichtel, C.E., Hartman, R.C., Kniffen, D.A., and Lamb, R.C., 1977, *Ap. J.*, **213**, 252.
- Waddington, C.J., 1977, *Fundamentals of Cosmic Physics*, 3 (New York: Gordon and Breach Science Publishers Ltd., 1977), p. 1.
- Weaver, H., and Williams, D.R.W., 1973, *Astron. Astrophys. Suppl.*, **8**, 1.

## Chapter 6

# Compact Objects

The emergence of  $\gamma$ -ray astronomy as an observational science has stimulated an impressive number of theoretical studies related to celestial compact objects. This high level of activity is justified by the importance of  $\gamma$ -ray astronomy in comprehending the most energetic processes occurring in association with astrophysical objects. The  $\gamma$ -ray observations thus far have been limited by the angular resolution of the detector systems, for which even in the high energy region, above 100 MeV, the accuracy has been only of the order of  $2^\circ$  to  $2\frac{1}{2}^\circ$  for individual photons and  $\frac{1}{2}^\circ$  to  $1^\circ$  for the localized excesses that have been identified. It is hoped that in the latter half of the 1980's instruments with angular resolution of 5 to 10 arcmin will be flying on satellites, since the technology for these instruments already exists.

Even with the existing data, it has been possible to identify some high energy  $\gamma$ -ray emission as emanating from compact objects by correlating observed time variations with those seen at other wavelengths. The pulsars are a notable case. Some of the very low energy  $\gamma$ -ray bursts have had their origins determined relatively precisely by using the time profiles from several satellites and triangulation methods. Many of the more than two dozen localized high energy  $\gamma$ -ray excesses still to be identified are probably associated with compact objects; others are likely to be localized regions such as the large molecular clouds discussed in Chapter 5.

In the following sections, various types of objects and phenomena and their significance in high energy astrophysics will

be discussed. The current concepts of the nature of the objects and the mechanisms generating high energy electromagnetic radiation will be discussed and current observational data will be presented where appropriate.

## NEUTRON STARS AND PULSARS

The discovery of radio pulsars by Hewish et al. (1968) initiated an extensive search for these objects. This investigation has led to the detection of over 300 radio pulsars whose periods range from 33 milliseconds to several seconds. However, in spite of extensive searches only two have been seen in the optical region (one of these after its  $\gamma$ -ray identification), and only one has been detected in the X-ray region. It was quite unexpected that at this early stage in the development of  $\gamma$ -ray astronomy  $\gamma$ -ray pulsars ( $E > 30$  MeV) with radio counterparts would already be identified. Clearly, this result implies that pulsars must be particularly efficient in accelerating high energy particles. Indeed for the known pulsars, there is much more energy being released in the form of  $\gamma$ -rays,  $10^{34}$  to  $10^{35}$  ergs  $s^{-1}$ , than in the radio region, which is typically  $10^{31}$  ergs  $s^{-1}$  for the pulsars also seen in the  $\gamma$ -ray region.

Almost immediately after their discovery, pulsars were proposed to be associated with neutron stars (Gold, 1968, 1969), and this relationship is now generally accepted. The large release of energy, the very fast period, and the remarkably small variation of the period seemed to dictate that the pulsed radiation must be from a massive object of small size. The very short length of the individual pulses indicates that the size of the emitting region is associated with something substantially smaller than normal stellar dimensions. On the other hand, the periods in general are constant to one part in  $10^8$  or greater indicating a massive object rather than a plasma phenomenon. If the period of the pulse is associated with a rotating body, then the object must be a neutron star rather than a normal stellar object because the surface cannot move faster than the speed of light. Further, the period is probably too short to be associated with an oscillating phenomenon.

Long before the observation of pulsars, theoreticians had predicted the existence of neutron stars. It was, and still is,

believed that neutron stars form from the violent collapse of the inner core of a star in a supernova explosion, wherein the outer part of the star is ejected. Neutron stars are believed to have masses somewhat larger than one  $M_{\odot}$ , radii of about 10 km, and a mean density of  $10^{14}$  gm cm<sup>-3</sup>. The observed association of the fastest pulsars with known supernovae remnants provided further evidence to support the identification of these objects as neutron stars.

It is now generally agreed that the ultimate source of the radiated energy is the rotational energy of the neutron star, which would be about  $10^{49}$  ergs for the fastest observed pulsar, PSR 0531+21 in the Crab Nebula. As energy is radiated and lost in other ways, the pulsar must slow down, and, indeed, the radio pulsars generally seem to have periods increasing with time, although the rate of change is very small. For PSR 0531+21, the change in rotational energy based on the pulsar period change is about  $-2 \times 10^{38}$  ergs s<sup>-1</sup>. In general slower pulsars have smaller rates of change. Another generally accepted idea is that as the neutron star was formed, its surface magnetic field strength became about  $10^{12}$  gauss on the basis of calculations associated with the collapse of a body of  $1 M_{\odot}$  having an initial surface field similar to that of an ordinary star. Hence, the picture that has evolved for a pulsar is a rapidly rotating neutron star with a high surface magnetic field configured such that there is beaming of the radiation.

No consensus yet exists with regard to the exact model for the pulsed radiation, although ideas are plentiful. Many theoretical models involve either synchrotron or curvature radiation in the high magnetic fields, often in association with the polar regions to give the beaming effect. There is still, however, a great variety of opinions regarding the details of the model, including the specific manner and location of the relativistic particle acceleration.

The highest intensity pulsar as observed at the Earth in the  $\gamma$ -ray region is the one in Vela, PSR 0833-45, for which  $(1.2 \pm 0.2) \times 10^{-5}$  photons ( $E > 100$  MeV) cm<sup>-2</sup> s<sup>-2</sup> are seen (Thompson et al., 1977). This pulsar, which is the third fastest radio pulsar seen thus far, is shown in Figure 6-1. The two most striking features are the two  $\gamma$ -ray pulses as opposed to one in the radio region, and the fact that neither  $\gamma$ -ray pulse is in phase

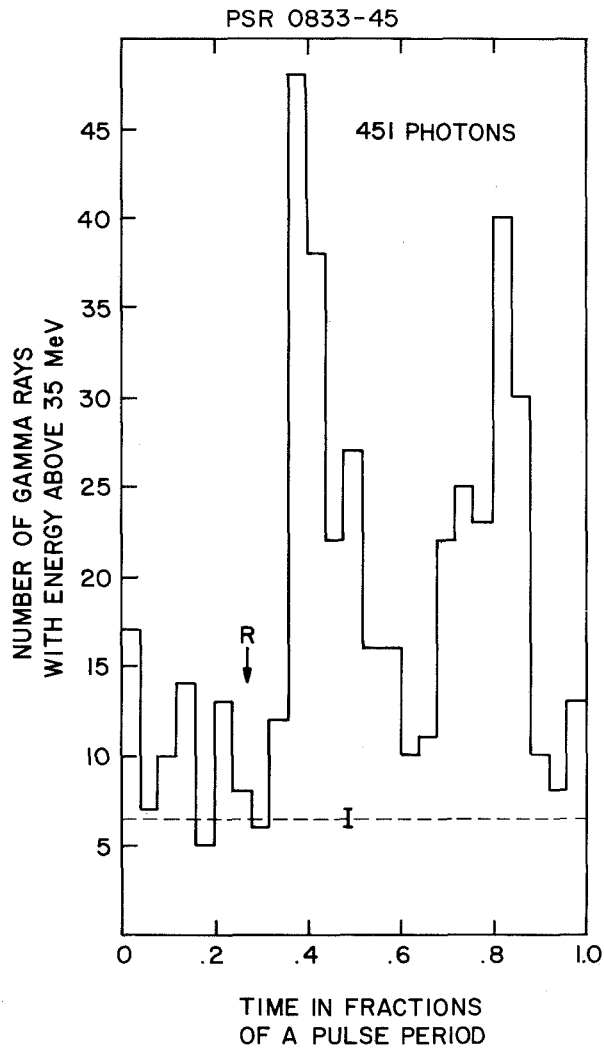


Figure 6-1. Distribution of  $\gamma$ -ray arrival times in fractions of a radio pulse period for  $\gamma$ -rays above 35 MeV from the direction of PSR 0833-45, as seen by the SAS-2 satellite. Arrow R marks the position of the radio pulse. The dashed line shows the  $\gamma$ -ray level expected from galactic and diffused radiation if no localized source were present (Thompson et al., 1977). Later data from PSR 0833-45 obtained with COS-B are shown in Figure 6-2.

with the radio pulse. These features were confirmed by the data obtained later from the COS-B satellite  $\gamma$ -ray telescope (Buccheri et al., 1978). They determined that the first  $\gamma$ -ray pulse followed the radio pulse (e.g., Komesaroff et al., 1972) by  $11.2 \pm 0.4$  ms. The period is 89 ms, and the time between the pulses is 38 ms. If this result was not enough to complicate attempts to find a satisfactory theoretical model, following the detection of PSR 0833-45 in  $\gamma$ -rays two peaks were found in the optical region by Wallace et al. (1977), neither one of which was in phase with either the  $\gamma$ -ray or the radio peaks as shown in Figure 6-2. In spite of many attempts to obtain a certain detection of pulsation in the X-ray wavelength range, none has yet been made.

The observational picture for the second strongest  $\gamma$ -ray pulsar PSR 0531+21 in the Crab nebula is much simpler to describe. This pulsar, which is the fastest radio pulsar yet detected and was the first  $\gamma$ -ray pulsar reported (Browning et al., 1971), even though it is not the strongest, is seen with the double pulsed structure in the radio, optical, X-ray, and  $\gamma$ -ray regions, and the pulses in each wavelength are in phase as shown in Figure 6-2. PSR 0531+21 has even been detected at  $10^{11}$  eV by Helmken et al. (1975) (see also Grindlay et al., 1976) using the ground based 10 m reflector on Mt. Hopkins. The common in-phase double peak feature suggests the same mechanism for the radiation at all wavelengths for PSR 0531+21, which is perhaps to be expected for the pulsar which is the youngest known,  $10^3$  years old. The older Vela pulsar, PSR 0833-45 apparently then has a dominant high energy component. In fact, whereas the pulsed luminosity ratio,  $L(\text{PSR } 053+21)/L(\text{PSR } 0833-45)$ , is about 5 above 100 MeV, it is almost  $10^4$  in the optical range. The Crab nebula also has strong constant emission, and the constant is compared to the pulsed components in Figure 6-3. The ratio of the pulsed to unpulsed emission appears to increase monotonically with energy until in the high energy  $\gamma$ -ray region the pulsed emission dominates.

Other radio pulsars have been reported to be possible  $\gamma$ -ray emitters, but confirmation is required because the statistical level of the observations is low. Most likely several of the radio pulsars will be revealed as  $\gamma$ -ray emitters.

In some pulsar models (e.g., Ostriker and Gunn, 1969; Ruderman and Sutherland, 1975), the current value of  $P/(2\dot{P})$  is representative of the pulsar age, where  $P$  is the pulsar period. For

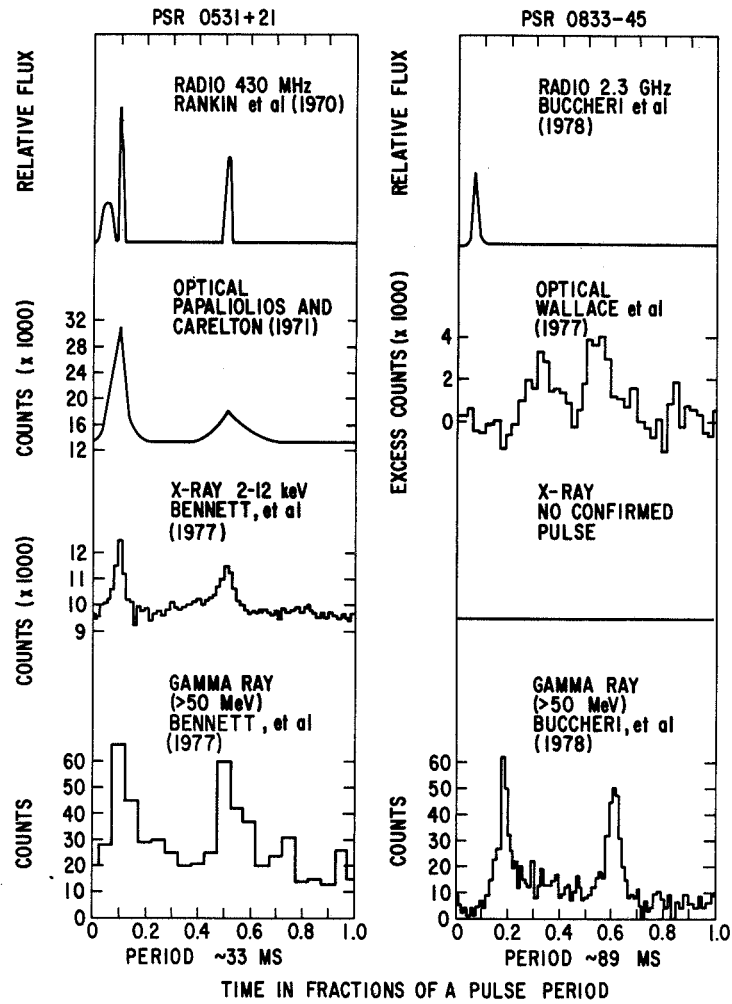


Figure 6-2. Comparison of the pulse structure and phase at radio, optical, X-ray, and  $\gamma$ -ray energies for PSR 0531+21 and PSR 0833-45, taken from Fichtel et al. (1979). References to the work are given in the figure.

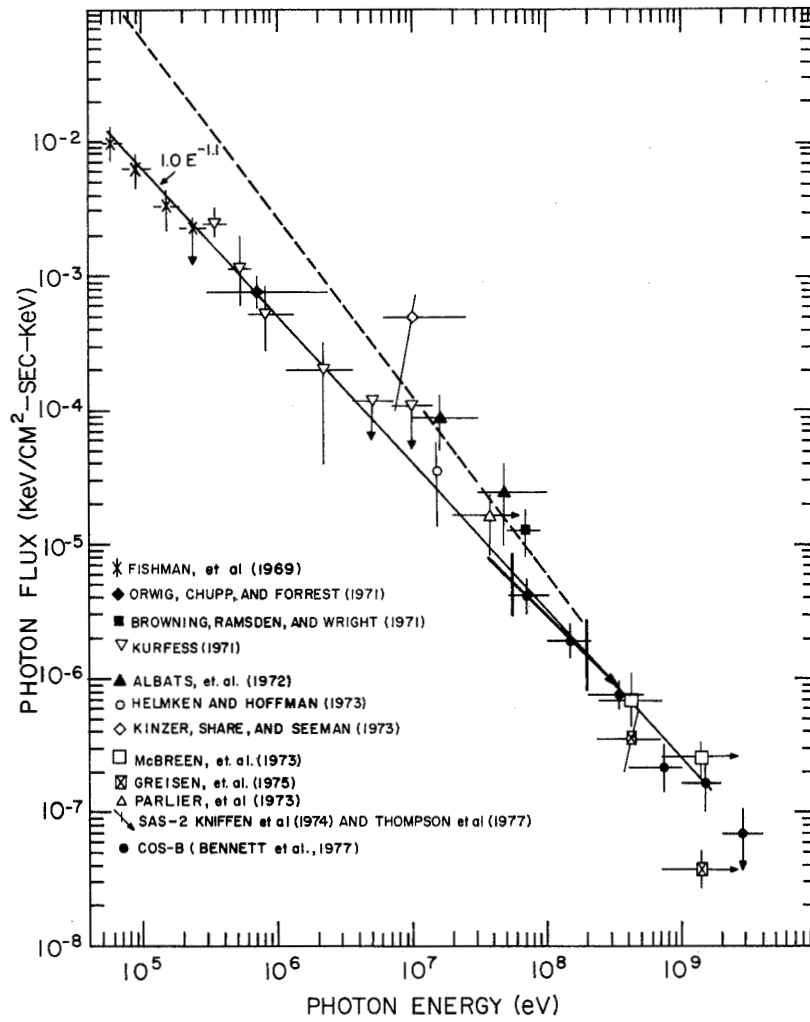


Figure 6-3. Energy spectrum of the pulsed  $\gamma$ -ray emission from PSR 0531+21, compared to the unpulsed flux shown by a dashed line. The dashed line for the total flux is based on X-ray data and the results at high energy. The solid line connects the pulsed X-ray results near 10 keV with the pulsed results near 100 MeV.

the Crab pulsar, this apparent age is reasonably consistent with the known age of the pulsar. Although consistency between apparent and true age may not hold for pulsars with  $P/(2\dot{P})$  greater than  $10^6$  years (Lyne et al., 1975), and some sudden changes in pulsar period have been observed, it still seems worth examining the pulsed  $\gamma$ -ray luminosities and upper limits as a function of this parameter. In Figure 6-4, the  $\gamma$ -ray intensity or upper limit is shown as a function of the apparent age in years; there is the hint that a threshold for detection has just been approached by the SAS-2 and COS-B  $\gamma$ -ray instruments.

The radio luminosity of pulsars older than  $10^6$  years appears to decrease relatively rapidly, and various theoretical reasons for this turnoff have been suggested (Gunn and Ostriker, 1970; Ruderman and Sutherland, 1975; Lyne et al., 1975). The data of Figure 6-4 suggest that a similar pattern may exist for  $\gamma$ -ray pulsars. The upper limits for many pulsars with apparent ages greater than  $10^6$  years are inconsistent with  $\gamma$ -ray luminosities comparable to the positive results, while no such statement can be made for pulsars with apparent ages less than  $10^6$  years.

Assuming that the observed pulsar radiation comes from the rotational energy, and that the term containing the change in the moment of inertia is negligible compared to the term containing the period change, the rotational energy loss is given by the expression

$$\frac{dE_R}{dt} \cong I \Omega \dot{\Omega} = \left( \frac{4\pi^2 I}{P^3} \right) \dot{P} \quad (6-1)$$

where  $I$  is the pulsar moment of inertia and  $\Omega$  is the angular frequency of the pulsar. Attempts to correlate this expression with observed radio periods, period derivatives, and luminosity have been ambiguous, but there may be many reasons for this (see for example Lyne et al., 1975; Ogelman et al., 1976). Using the measured values of  $P$  and  $\dot{P}$  and a value for  $I$  of  $10^{45}$  g cm<sup>2</sup> (Taylor and Manchester, 1975), an estimate of the values of  $(dE_R/dt)$  can be made. The values of the rotational energy loss thus calculated are upper limits for the  $\gamma$ -radiation assuming that all the energy that is lost comes from the rotational energy. For

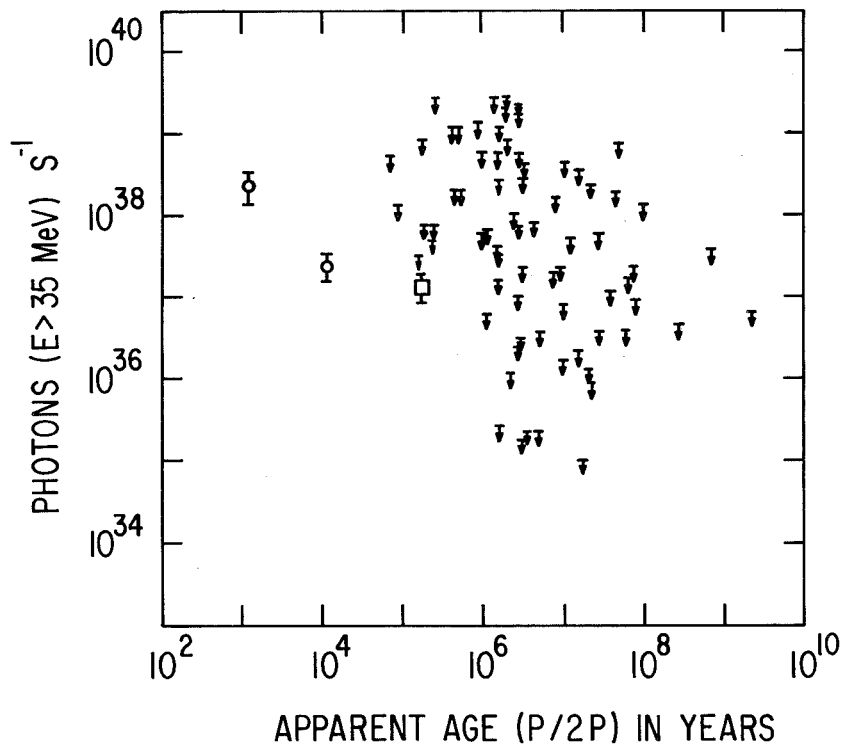


Figure 6-4. Observed  $\gamma$ -ray luminosities and upper limits to luminosity above 35 MeV as a function of pulsar apparent age (apparent age  $P/2\dot{P}$ ). The  $\gamma$ -ray luminosities are calculated using the distance estimates of Taylor and Manchester (1975) and taking the solid angle of emission for each pulsar to be 1 sr. The error bars shown reflect only the uncertainties in the  $\gamma$ -ray flux measurements. Reading from left to right, the points using the symbol "o" are for PSR 0531+21 and PSR 0833-45, and the one using "□" is for PSR 1747-46. The points and limits are those derived from SAS-2 data (Ogelman et al., 1976).

the Crab pulsar,  $4\pi^2 I \dot{P}/P^3$  is calculated to be  $5 \times 10^{38}$  ergs  $s^{-1}$ , and the pulsed  $\gamma$ -ray emission above 100 MeV is  $3 \times 10^{34}$  ergs  $s^{-1}$ , assuming the radiation is emitted into one-tenth of  $4\pi$ . The  $\gamma$ -ray luminosities and the computed  $(dE_R/dt)$  values are all uncertain by an order of magnitude or more because of uncertainties in the value for  $I$ , in the distance estimates, and in the solid

angle of emission of  $\gamma$ -rays. Based on only three positive observations, there is an indication that a larger fraction of the pulsar energy loss goes into  $\gamma$ -rays as the pulsar gets older.

It seems likely that future  $\gamma$ -ray observations with more sensitive telescopes will make a major contribution to the understanding of the pulsar phenomenon. At present, it can be said that radio pulsars have been seen in the  $\gamma$ -ray range, emitting very large amounts of energy and displaying properties that, at a minimum, are intriguing.

## SUPERNOVAE

Supernovae, the most spectacular of stellar events, have received much deserved attention by optical astronomy and were among the first objects considered by  $\gamma$ -ray theorists. They are thought to be the source of nucleosynthesis of the heavy elements, and many feel they are the origin of most of the energy in cosmic rays. If nucleosynthesis has occurred during the explosive phase, specific  $\gamma$ -ray lines with known energies and lifetimes will be emitted by unstable heavy nuclei. The cosmic rays would reveal themselves through the emission of  $\gamma$ -rays produced in the interaction of cosmic rays with the surrounding material.

Exactly what occurs just before and during a supernova explosion is still unknown. It is generally agreed that the temperature inside massive stars reaches the point at which nucleosynthesis occurs, and, after a number of steps, an "Fe" core is formed. There is then a sudden, implosive collapse of the core. It is now thought to be more likely that the shock wave and ejection of matter result from an elastic bounce (see, for example, Bruenn et al., 1977; Arnett, 1977b; Van Riper, 1978) rather than from the deposition of neutrino energy in the outer layers. Most astrophysicists in this field would, however, agree that a completely satisfactory theoretical model of the process does not yet exist. For smaller stellar masses, the core remaining behind resulting from the collapse of the rotating, magnetic stellar interior is the neutron star, now generally accepted as giving rise to the pulsar radiation discussed in the last section.

As the shock moves outward in the star, rapid nucleosynthesis occurs in the intermediate layers as a result of the shock heating. Following the early work of Fowler and Hoyle (1964),

the abundances to be expected in the thermonuclear burning were calculated in substantial depth (e.g., Bodansky et al., 1968). During the explosive phase the creation in great numbers of many nuclear species which are unstable to beta decay, followed by a nuclear  $\gamma$ -ray emission (Clayton et al., 1969), provides a unique opportunity for  $\gamma$ -ray astronomy to determine if supernovae are the sites of nucleosynthesis at the level required to supply the observed quantities of some of the heavier elements.

Hydrodynamic calculations of these shocks have been performed and the nucleosynthesis predicted in the matter to be ejected has been determined. The result for one of these assessments is shown in Table 6-1. Several points should be noted. The iron, cobalt, and nickel group might appear to be the most likely to be detected because of the relatively large number of atoms predicted. The decay times are relatively fast, however, and a typical supernova, because of the overlying layers, may not become transparent to these  $\gamma$ -rays for several months. Nevertheless, the characteristic lines of this group are certainly ones to search for, perhaps especially the 0.847 MeV line associated with

**Table 6-1**  
Gamma Line Prospects for a "Typical" Supernova

Nucleus	$X_{\odot}$	Progenitor	$\tau_{1/2}$	Atoms/SN
$^{56}\text{Fe}$	$1.3 \times 10^{-3}$	$^{56}\text{Co}$	77d	$3.0 \times 10^{54}$
$^{56}\text{Co}$	$1.3 \times 10^{-3}$	$^{56}\text{Ni}$	6.1d	$3.0 \times 10^{54}$
$^{48}\text{Ti}$	$2.3 \times 10^{-6}$	$(^{48}\text{Cr}) ^{48}\text{V}$	16d	$6.2 \times 10^{51}$
$^{22}\text{Ne}$	$1.2 \times 10^{-4}$	$^{22}\text{Na}$	2.6 yr	(?)*
$^{44}\text{Ca}$	$1.9 \times 10^{-6}$	$(^{44}\text{Ti}) ^{44}\text{Sc}$	48 yr	$5.6 \times 10^{51}$
$^{60}\text{Ni}$	$2.0 \times 10^{-5}$	$^{60}\text{Fe}$	$3 \times 10^5$ yr	$4.4 \times 10^{52}$
		$^{60}\text{Co}$	5.26 yr	
$^{26}\text{Mg}$	$8.6 \times 10^{-5}$	$^{26}\text{Al}$	$7.3 \times 10^5$ yr	$4.5 \times 10^{50}$
$^{238}\text{U}$	$1.3 \times 10^{-10}$	(r-process)	$4.5 \times 10^9$ yr	$1.3 \times 10^{47}$
(example)				

\*Not well determined.

Source: Fichtel et al. (1980).

the  $^{56}\text{Co}$  to  $^{56}\text{Fe}$  decay. Although an adequate abundance of  $^{44}\text{Ca}$  gas appears to be formed as  $^{44}\text{Ti}$  in constant temperature quasi-equilibrium calculations, better analysis (including freeze-out) suggests that they are destroyed before ejection. The mechanism for production of the observed  $^{60}\text{Ni}$  is an open question. If explosive carbon burning had a large neutron flux,  $^{60}\text{Fe}$  could be made, giving a  $\gamma$ -line prospect. However, actual stellar hydrodynamic calculations suggest that (1) the neutron flux during carbon burning is too small, and (2) most  $^{60}\text{Ni}$  is made as  $^{60}\text{Zn}$ . The latter decays take less than one half-hour, so the  $\gamma$ -rays are not likely to escape the star. Formed in both hydrostatic and explosive carbon burning (Arnett, 1969),  $^{26}\text{Al}$  which decays to  $^{26}\text{Mg}$ , is one of the best prospects for  $\gamma$ -ray line emission (Arnett, 1977a; Ramaty and Lingenfelter, 1977). An excess of  $^{26}\text{Mg}$  in the Ca-Al rich inclusion in the carbonaceous meteorite Allende has been interpreted as strong evidence for  $^{26}\text{Al}$  in primitive solar system matter (Lee et al., 1977). In young supernova remnants, the large velocities smear the line; however, in older remnants better signal to noise ratios might be obtained with higher energy resolution.

In addition to the  $\gamma$ -ray lines, it has long been thought possible that a  $\gamma$ -ray continuum with the appropriate energy spectrum might be produced by the interaction of cosmic rays, created in association with the supernova, with the surrounding material. The origin of the cosmic rays is a problem which has attracted attention for decades. Since it is generally believed that the cosmic rays are galactic, and since supernovae appear to be the most energetic events occurring in the galaxy, interest developed in supernovae as the primary sources of cosmic rays. An early concept was that the cosmic rays were actually the outermost thin layer of a supernova which was accelerated to cosmic ray energies (Colgate and Johnson, 1960); more recently, however, hydrodynamic calculations make this possibility less certain, although Colgate (1974) argues that it is still a viable alternative for Type I supernovae. One aspect of the shock theory of cosmic ray acceleration is the prediction of a short (tens of nanoseconds), intense burst of  $\gamma$ -rays (Colgate, 1968). The details of the calculation of the pulse width of the burst are given, for example, by Fichtel and Kniffen (1974). Also, the possibility exists that the cosmic rays are accelerated in the shock and turbulence following the actual supernova explosion.

A continuum emission from the Crab supernova remnant has been observed ranging upward to at least the hard X-ray region, as shown in Figure 6-3, suggesting synchrotron radiation from relativistic electrons. Other supernovae have not been seen to have this type of radiation, but it may be only a question of sensitivity. A further important test of whether cosmic rays are accelerated by supernovae would be the observation of a continuum  $\gamma$ -radiation resulting from cosmic ray-matter interactions. Thus far, although pulsed radiation has been observed from the Crab and Vela pulsars, there is no clear identification of a continuum of high energy  $\gamma$ -ray emission associated with a supernova remnant, except possibly in the case of the Crab.

In fact, except in a region of abnormally high density,  $\gamma$ -rays from cosmic ray interactions would not be expected to be seen from a supernova with present experiments. Approximately a few times  $10^{49}$  ergs per supernova in the form of relativistic particles are required if they are to be the source of cosmic rays. A straightforward calculation using the source functions in the previous section and a density the same as that locally gives an intensity of about  $10^{-7}$  photons ( $E > 100$  MeV)  $\text{cm}^{-2} \text{s}^{-1}$  for a supernova 1 kpc away. This level would be detectable with future experiments. For the Vela supernova remnant, which is closer but in a possibly less dense region, a larger number might be predicted, making it a candidate for future study. Also, supernovae in high density regions would be logical objects to search for high energy  $\gamma$ -rays (Montmerle, 1979).

## BLACK HOLES

The intriguing theoretical prediction of the possible existence of black holes has excited astronomers and laymen alike. Masses ranging from just over one solar mass (the upper limit for a white dwarf is  $1.4 M_{\odot}$ ) to over a billion solar masses could be created in the universe as it exists today, and mini black holes might have been created during the big bang. To pursue the discussion of the last section, the following is one way in which a black hole may form: If the outward shock following the collapse of a stellar core is not adequate to create an explosion blowing off the outer shells, the core will continue to accrete matter from the surrounding envelope, ultimately evolving into a black hole. It is

worth noting that the formation of a black hole in this manner does not lead to a spectacular visible explosion, and, hence, does not leave an outstanding signature to be read by astronomers. Such objects would continue to collect matter which comes too close. However, the very massive black holes that are speculated upon are associated with the centers of galaxies.

Theorists originally believed that once a black hole formed it remained, and there was no chance of observing it. Now there are thought to be several ways the presence of a black hole might be revealed, although in some cases the observation of the radiation would not uniquely establish its source as a black hole. Much of the predicted radiation falls in the range of  $\gamma$ -rays. Thus, black holes are a very appropriate subject for discussion here, and several possible mechanisms for the emission of high energy electromagnetic radiation from black holes will be described below.

At present, the most interesting evidence suggesting the possible existence of a black hole comes from optical and X-ray observations. A black hole in a binary system might pull gas off its companion in sufficient quantity that the X-rays emitted as the gas was heated while falling into the black hole would be detectable. To be certain that the emission is from a binary with a black hole rather than a neutron star or a white dwarf, the unseen companion must be proven to have a mass clearly in excess of three solar masses. After a careful search in which several candidates were eliminated, Cygnus X-1 remained as the best candidate—having a mass which appeared to be large enough, gas flowing from the visible supergiant star to its unseen companion as revealed by optical observation, an aperiodic motion, a periodically varying Doppler shift, and strong X-ray emission. (For a detailed discussion, see Thorne, 1974; Oda, 1977.) Two other X-ray sources, Cir X-1 (Toor, 1977) and GX339-4 (Samimi et al., 1979), appear to have similar X-ray properties and, hence, are also black hole candidates, although mass estimates do not exist. Other viable models for these objects have been proposed; so the case for their being black holes cannot be considered to be conclusive.

Gamma rays would also be expected from black holes, although they are yet to be observed from a likely candidate. Maraschi and Treves (1977) have noted that, if the accretion flow onto the black hole is turbulent and dissipation maintains ap-

proximate equipartition among the different forms of energy, electrons can be accelerated by the induced electric fields. The resulting synchrotron energy spectrum is quite flat to about 20 MeV, above which it falls steeply. There would also be a Compton contribution. Under the right conditions, observable  $\gamma$ -ray fluxes would be generated. Collins (1979) has pointed out that matter falling onto a rotating black hole will be heated sufficiently that proton-proton collisions will produce mesons, including neutral pions which decay into two  $\gamma$ -rays. For massive ( $> 10^3 M_{\odot}$ ) black holes, such as might exist in the galactic center, the resulting  $\gamma$ -ray luminosity may exceed  $10^{36}$  ergs  $s^{-1}$ , which would give rise to over  $3 \times 10^{-6}$   $\gamma$ -rays per second at the Earth for a source at the galactic center. The energy spectrum would have a peak near 20 MeV. Emission from black holes through the Penrose process is another mechanism, but it is most appropriately discussed in relation to very large black holes which may exist at the centers of active galaxies (Chapter 7).

One of the most intriguing predictions of  $\gamma$ -ray emission from black holes is that of bursts with a very unique signature from mini black holes left from the big bang (e.g., Page and Hawking, 1976; Hawking, 1977). These mini holes, whose masses are only a very small fraction of that of the Sun, cannot be created in the universe as it exists today because the necessary compressional forces do not exist. Hawking (1974) was the first to show that black holes could indeed emit particles, contrary to the belief at the time that black holes could not emit anything. The strong gravitational fields around the black holes cause particle creation, and, as a result, all species of particles are emitted thermally with a temperature of about  $1.2 \times 10^2 M^{-1}$  K, where  $M$  is the mass in grams of the black hole. Although it is not practical to detect particle emission from black holes of stellar mass because the temperature would be less than 10 K, primordial black holes, which would by now have decayed to a mass of about  $5 \times 10^{14}$  g, would have a temperature of about  $2.5 \times 10^{11}$  K, or 20 MeV. Such a black hole would radiate energy at the rate of about  $2.5 \times 10^{17}$  ergs  $s^{-1}$  with about 1 percent in gravitons, 45 percent in neutrinos, 45 percent in  $e^+$  and  $e^-$ , and 9 percent in photons (Page, 1976). The photons would have a spectrum peaking at about 120 MeV. These photons may contribute to the diffuse background which will be discussed in Chapter 9.

As the black hole continues to lose mass, its temperature rises, and it begins to emit particles of higher rest mass, until finally it ejects all its remaining rest mass in a very short time. The heavy hadrons emitted in this final release would decay very rapidly, giving about 10 to 30 percent of their energy ( $\sim 10^{34}$  ergs) into a short burst (about  $10^{-7}$  s) of hard  $\gamma$ -rays between  $10^2$  and  $10^3$  MeV, peaking around 250 MeV.

An observation of a  $\gamma$ -ray burst with these very distinctive characteristics would not only be a very strong piece of experimental evidence in support of general relativity and quantum theory, but also provide information on the early universe and strong interactions at high energies.

### OTHER HIGH ENERGY GAMMA RAY SOURCES

As indicated in the beginning of this chapter, the angular resolution of  $\gamma$ -ray telescopes flown thus far is not adequate to identify a localized source as a point source unless there is other information such as a well-known periodicity which may be used to identify the  $\gamma$ -radiation with that seen at other wavelengths. Besides the pulsars there is only one other  $\gamma$ -ray point source whose identification has been established, namely Cygnus X-3, although there are many localized excesses which have been identified—some of which are good candidates for point sources.

Energetic ( $E > 35$  MeV)  $\gamma$ -rays from Cygnus X-3 were observed with the SAS-2  $\gamma$ -ray telescope by Lamb et al. (1977), as shown in Figure 6-5. They were modulated at the 4.8<sup>h</sup> period observed in the X-ray and infrared regions, and within the statistical error are in phase with this emission. The flux above 100 MeV has an average value of  $(4.4 \pm 1.1) \times 10^{-6}$  photons  $\text{cm}^{-2} \text{s}^{-1}$ . Earlier, Galper et al. (1975) reported an excess above 40 MeV from Cygnus X-3 also with a 4.8 period at a higher intensity, but with a lower statistical weight ( $3.6 \sigma$ ). If the distance to Cygnus X-3 is 10 kpc, the flux reported by SAS-2 implies a luminosity of more than  $10^{37}$  ergs  $\text{s}^{-1}$  if the radiation is isotropic and about  $10^{36}$  ergs  $\text{s}^{-1}$  if the radiation is restricted to a cone of one steradian, as it might be in a pulsar. At that luminosity level, during the time of the SAS-2 observation, Cygnus X-3 was the most luminous  $\gamma$ -ray source. However, since it is quite distant its flux as observed at the Earth is only a few times the threshold for

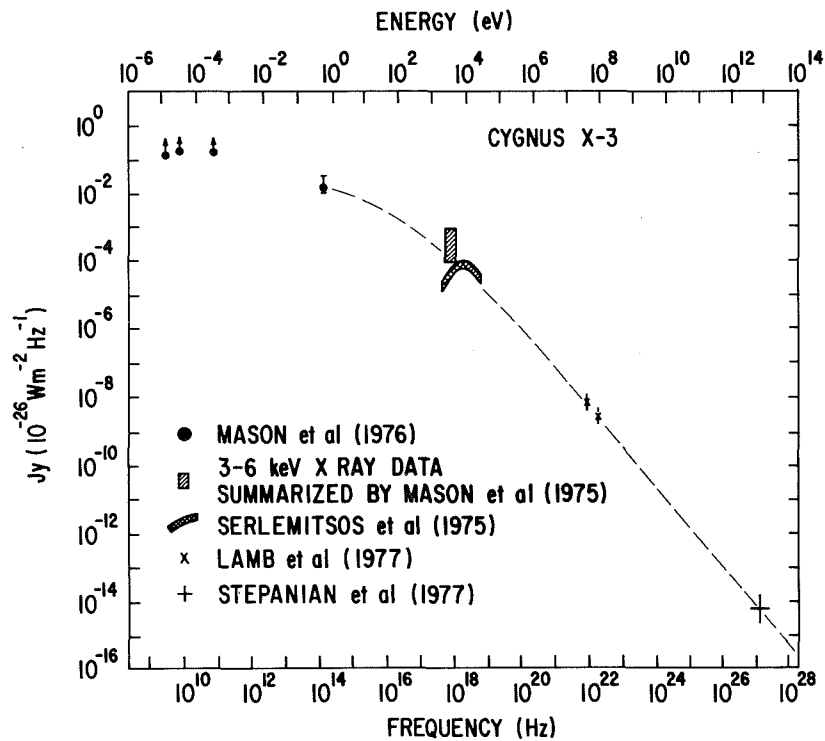


Figure 6-5. The differential photon energy flux spectrum observed for Cygnus X-3. Upward pointing arrows on the fluxes indicate that flaring sometimes increases these fluxes by over an order of magnitude. The X-ray intensities are represented by crosshatched regions which bracket the reported values. The radio observations show no indication of the  $4.8^{\text{h}}$  periodicity; however, at higher frequencies there is a periodic component which apparently increases relative to the constant component as a function of energy.

detection by SAS-2 or COS-B. When COS-B searched for radiation in later years (the SAS-2 observed it in 1972) no  $\gamma$ -radiation was detected (Bennett et al., 1977), but observations in the X-ray range showed that Cygnus X-3 was in a low state at that time. Reports of  $\gamma$ -ray emission from Cygnus X-3 also have been made at very high energies ( $\approx > 10^{11}$  eV) (Vladimirsky et al., 1975; Stepanian et al., 1977).

One of the four strongest high energy  $\gamma$ -ray localized excesses seen is that at galactic coordinates  $l = 195, b = +5$ . It has been seen by both the SAS-2 (Fichtel et al., 1975; Thompson et al., 1977) and COS-B (Masnou et al., 1977)  $\gamma$ -ray telescopes. Because it is in a region of the galactic plane with a relatively low diffuse flux and no known large clouds, it seems to be a promising candidate for a point source; however, there is no object at other wavelengths within the solid angle of uncertainty of source position which appears to be a strong possibility for a counterpart of the  $\gamma$ -ray sources. Both the SAS-2 (Thompson et al., 1977) and COS-B (Masnou et al., 1977) results indicate a possible 59 s modulation in the intensity of this source. Maraschi and Treves (1977) have speculated that this source may be either a slowly rotating, accreting neutron star surrounded by a cloud thick to X-rays or a freely precessing neutron star.

Over two dozen other localized high energy  $\gamma$ -ray excesses have been reported by Hermsen et al. (1977), Mayer-Hasselwander et al. (1980) and Wills et al. (1980) from COS-B observations. With three exceptions, they are all within six degrees of the galactic plane, suggesting that they are indeed largely galactic. Further, they are generally associated with concentrations of matter in arms, and, hence, also supernova remnants and young stars. It is not yet clear whether they are mostly point sources or emission from localized regions, such as clouds or galactic arm tangents. Future observations of these regions should determine which are actually point sources. Correlated radio measurements should help to determine if some of them are pulsars. Other possibilities for  $\gamma$ -ray sources of marginal statistical significance have been reported in literature, but have not been confirmed.

In summary, present indications are that the future for  $\gamma$ -ray point source astronomy should be very bright, with even the possibility of new classes of astronomical objects being discovered.

## **LOW ENERGY GAMMA RAY BURSTS**

The nature of the  $\gamma$ -ray burst sources discovered by Klebesadel et al. (1973) remains an unsolved puzzle. These bursts are short, typically observable for a few seconds to tens of seconds, and have energies concentrated in the low energy  $\gamma$ -ray region. Their differential energy spectra have slopes of the order of -1 in the

region below 100 keV, and this slope steepens to approximately  $-2.5$  above several hundred keV. The spectra of all observed events are very similar, implying a common production mechanism for these bursts. One of the best measured energy spectra is shown in Figure 6-6. The events typically have quite irregular features as a function of time such as the one shown in Figure 6-7, which is based on data gained in the trans-Earth portion of the Apollo 16 mission on April 27, 1972, by Metzger et al. (1974).

From matching pulse profiles, which show significant structure on short time scales such as that shown in Figure 6-7, relative arrival times can be determined, from which loci of possible arrival directions have been established from multiple satellite observations over long baselines. The arrival directions inferred in this way from some of the original burst data have relatively large uncertainties because of limitations in timing accuracy. More recent determinations for several bursts using the detectors on the Helios-2 spacecraft and others aboard Vela-5A, Vela-6A, and Ariel-5 with from 1 to 2 AU separation from Helios-2 have yielded bands of position about an arcmin wide, though many degrees long (Cline et al., 1979). No known X-ray or  $\gamma$ -ray "steady" sources are included in these positions, nor any other known example of exceptional classes of astronomical objects, such as a pulsar or a new supernova. Positions determined by Helios-2, Earth orbiting satellites, and the Venus probes have now provided source positions as small as 1 arcmin<sup>2</sup> with still no truly exceptional object in the region of uncertainty.

The distribution of the number of events as a function of the observed flux for the  $\gamma$ -bursts now recorded shows some indication for a power index for the flux of  $\alpha < 3/2$ , or perhaps  $\alpha \sim 1$ , as would be expected for a galactic distribution of the sources. However, the small number of the smallest ( $\sim 10^6$  ergs cm<sup>-2</sup>) bursts so far detected, as well as the large uncertainties in the total burst energy flux (given the often limited energy information), preclude a firm conclusion that the  $\gamma$ -burst sources are not isotropic (Cline and Schmidt, 1977; White et al., 1978). Also, there is no indication that the  $\gamma$ -ray bursts tend to occur preferentially in the galactic plane.

The speculation on the origin of these bursts has been abundant. There is, however, no generally accepted leading can-

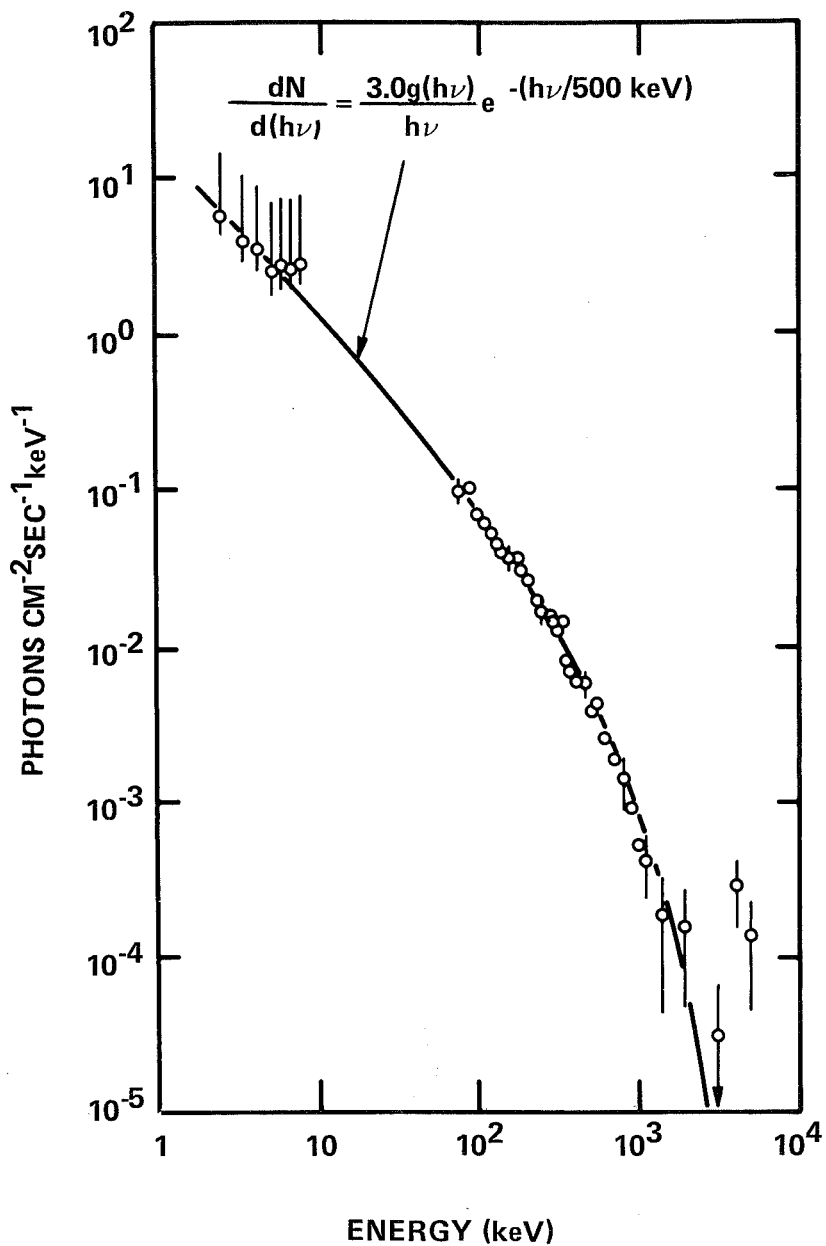


Figure 6-6. Average spectrum of the Apollo  $\gamma$ -ray burst (Gilman et al., 1980). The points in the X-ray have a relatively large uncertainty because of lack of definite knowledge of the direction of the source relative to the detector axis. (Trombka et al., 1974) Also shown is a thermal bremsstrahlung fit with  $KT = 500$  keV.

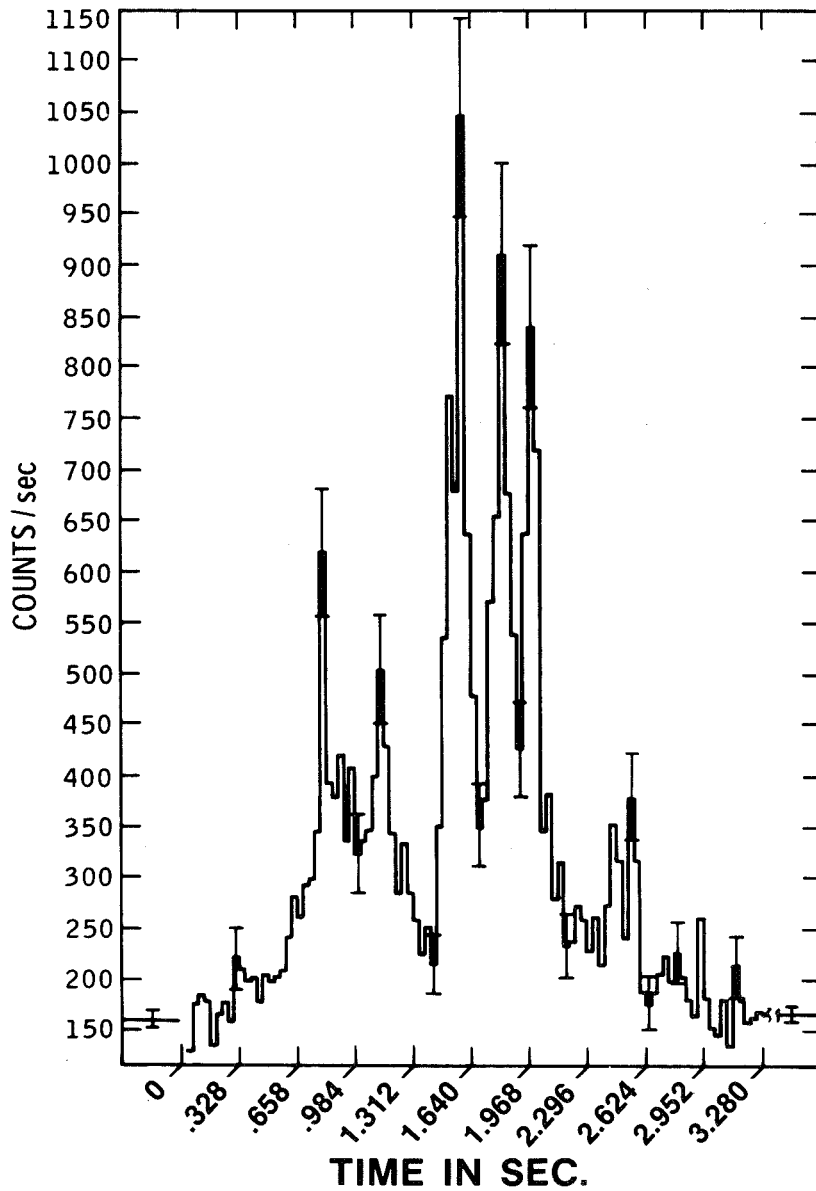


Figure 6-7. Measured time profile of intensity of the  $\gamma$ -ray burst observed during Apollo 16 trans-Earth mission on April 27, 1972 (Metzger et al., 1974).

didate for their origin. It is generally felt now that identification of the objects with observations at other wavelengths will probably be required before significant progress can be made in determining their origin.

A  $\gamma$ -ray burst which was markedly different than all the others occurred on March 5, 1979 (Barat et al., 1979; Cline et al., 1980; Evans et al., 1980; Terrell et al., 1980). The most remarkable aspect was a periodicity of about 8 seconds in the burst intensity which apparently lasted for at least 22 periods. It was also unique in having a very fast rise time of  $< 0.25$  ms to a very high initial peak. The initial peak also had a full width at half maximum of only 120 ms, which is unusual, but not unique. It thus appears to result from an astrophysical phenomenon quite different from the other  $\gamma$ -ray bursts, which show neither evidence for periodicity nor such a sharp rise. An accurate source location exists for this source, which is consistent with that of the N49 supernova remnant associated with the Large Magellanic Cloud. Caution in making this identification seems appropriate both because of the large distance and because of the lack of any observed correlated emission at other wavelengths.

The subject of  $\gamma$ -ray bursts, as well as the study of neutron stars, supernovae, black holes, and high energy  $\gamma$ -ray sources, should advance markedly with observations made during the 1980's since exploration of these fields is just beginning.

## REFERENCES

- Albats, P., Frye, G.M., Jr., Zych, A.D., Mace, O.B., Hopper, V.D., and Thomas, J.A., 1972, *Nature*, **240**, 221.
- Arnett, W.D., 1969, *Ap. J.*, **157**, 1369.
- Arnett, W.D., 1977a, *Annals of the New York Academy of Sciences, Proc. of the 8th Texas Sym.*, ed., M.D. Papagiannis, **302**, 90.
- Arnett, W.D., 1977b, *Ap. J.*, **218**, 815.
- Barat, C., Chambon, G., Hurley, K., Niel, M., Vedrenne, G., Estulin, I.V., Kurt, V.G., and Zenchenko, V.M., 1979, *Astron. Astrophys.*, **79**, L24.
- Bennett, K., Bignami, G.F., Boella, G., Buccheri, R., Hermsen, W., Kanbach, G., Lichti, G.G., Masnou, J.L., Mayer-Hasselwander, H.A., Paul, J.A., Scarsi, L., Swanenburg, B.N., Taylor, B.G., and Wills, R.D., 1977, *Astron. Astrophys.*, **61**, 279.
- Bennett, K., Bignami, G., Hermsen, W., Mayer-Hasselwander, H.A., Paul, J.A., and Scarsi, L., 1977, *Astron. Astrophys.*, **59**, 273.
- Bodansky, D., Clayton, D.D., and Fowler, W.A., 1968, *Ap. J., Suppl.*, **16**, 299.
- Browning, R., Ramsden, D., and Wright, P.J., 1971, *Nature*, **232**, 99.
- Bruenn, S.W., Arnett, W.D., and Schramm, D.N., 1977, *Ap. J.*, **213**, 213.
- Buccheri, R., Caraveo, P., D'Amico, N., Hermsen, J.L., Wills, R.D., Manchester, R.N., and Newton, M., 1978, *Astron. Astrophys.*, **69**, 141.
- Clayton, D.D., Colgate, S.A., Fishman, G.J., 1969, *Ap. J.*, **155**, 75.

- Cline, T.L., Desai, U.D., Pizzichini, G., Spizzichino, A., Trainor, J., Klebesadel, R., Ricketts, M., and Helmken, H., 1979, *Ap. J.*, **229**, L47.
- Cline, T.L., Desai, U.D., Pizzichini, G., Teegarden, B.J., Evans, W.D., Klebesadel, R.W., Laros, J.G., Hurley, R., Niel, M., Vedrenne, G., Estoulin, I.V., Kouznetsov, A.V., Zenchenko, V.M., Hovestadt, D., and Gloeckler, G., 1980, *Ap. J. (Letters)*, **237**, L1.
- Cline, T.L., and Schmidt, W.K.H., 1977, *Nature*, **266**, 749.
- Colgate, S.A., 1968, *Can. J. Phys.*, **46**, S476.
- Colgate, S.A., 1974, *Phys. Rev. Letters*, **34**, 1177.
- Colgate, S.A., and Johnson, M.H., 1960, *Phys. Rev. Letters*, **5**, 235.
- Collins, M.S., 1979, *Astron. Astrophys.*, **74**, 108.
- Evans, W.D., Klebesadel, R.W., Laros, J.G., Cline, T.L., Desai, U.D., Hurley, K., Niel, M., Vedrenne, G., Estoulin, I.V., Kouznetsov, A.V., and Zenchenko, V.M., 1980, *Ap. J. (Letters)*, **237**, L7.
- Fichtel, C.E., and Kniffen, D.A., 1974, "Gamma Ray Astronomy" in *High Energy Particles and Quanta in Astrophysics*, ed., F.B. McDonald and C.E. Fichtel (Cambridge Mass.: MIT Press, 1974), p. 428.
- Fichtel, C.E., Hartman, R.C., Kniffen, D.A., Thompson, D.J., Bignami, G.F., Ogelman, H., Ozel, M.E., and Tumer, R., 1975, *Ap. J.*, **198**, 163.
- Fichtel, C.E., Arnett, D., Grindlay, J., and Trombka, J., 1980, "Gamma Ray Astrophysics" in *Astrophysics from Spacelab*, P.L. Bernacca and R. Ruffini, eds. (Dordrecht: D. Reidel Publishing Co., 1980).

- Fishman, G.J., Harnden, F.R., Jr., Johnson, W.N., III, and Haymes, R.C., 1969, *Ap. J. (Letters)*, **158**, L61.
- Fowler, W.A., and Hoyle, F., 1964, *Ap. J., Suppl.*, **9**, 201.
- Galper, A.M., Kirillov-Uguryumov, V.G., Kurochkin, A.V., Leikov, N.G., Luchkov, B.I., and Yurkin, Yu. T., 1975, *Proc. of the 14th Int. Cosmic Ray Conf.*, **1**, 95.
- Gilman, D., Metzger, A.E., Parker, R.H., Evans, L.G., and Trombka, J.I., 1980, *Ap. J.*, **236**, 951.
- Gold, T., 1968, *Nature*, **218**, 731.
- Gold, T., 1969, *Nature*, **221**, 25.
- Greisen, K., Ball, S.E., Jr., Campbell, M., Gilman, D., and Strickman, M., 1975, *Ap. J.*, **197**, 471.
- Grindlay, J.E., Helmken, H.F., and Weekes, T.C., 1976, *Ap. J.*, **209**, 592.
- Gunn, J.E., and Ostriker, J. P., 1970, *Ap. J.*, **160**, 979.
- Hawking, S.W., 1974, *Nature*, **248**, 30.
- Hawking, S.W., 1977, *Scientific American*, **236**, 34.
- Helmken, H., and Hoffman, J., 1973, *Proc. of the 13th Int. Cosmic Ray Conf.*, **1**, 31.
- Helmken, H.F., Grindlay, J.E., and Weekes, T.C., 1975, *Proc. of the 14th Int. Cosmic Ray Conf.*, **1**, 123.
- Hermesen, W., Bennett, K., Bignami, G.F., Boella, G., Buccheri, R., Higdon, J.C., Kanbach, G., Lichti, G.G., Masnou, J.L., Mayer-Hasselwander, H.A., Paul, J.A., Scarsi, L., Swanenburg, B.N., Taylor, B.G., and Wills, R.D., 1977, *Nature*, **269**, 494.

- Hewish, A., Bell, S.J., Pilkington, J.D., Scott, P.F., and Collins, R.A., 1968, *Nature*, **217**, 709.
- Kinzer, R.L., Share, G.H., and Seeman, N., 1973, *Ap. J.*, **180**, 547.
- Klebesadel, R.W., Strong, I.B., and Olson, R.A., 1973, *Ap. J. (Letters)*, **182**, L85.
- Kniffen, D.A., Hartman, R.C., Thompson, D.J., Bignami, G.F., Fichtel, C.E., Ogelman, H., and Tumer, T., 1974, *Nature*, **251**, 397.
- Komesaroff, M.M., Hamilton, P.A., and Ables, J.G., 1972, *Aust. J. Phys.*, **25**, 759.
- Kurfess, J.D., 1971, *Ap. J. (Letters)*, **168**, L39.
- Lamb, R.C., Fichtel, C.E., Hartman, R.C., Kniffen, D.A., and Thompson, D.J., 1977, *Ap. J.*, **212**, L63.
- Lee, T., Papanastassiou, D.A., and Wasserburg, G.J., 1977, *Ap. J. (Letters)*, **211**, L107.
- Lyne, A.G., Ritchings, R.T., and Smith, F.G., 1975, *Mon. Not. Roy. Ast. Soc.*, **171**, 579.
- Maraschi, L., and Treves, A., 1977, *Ap. J. (Letters)*, **218**, L113.
- Masnou, J.L., Bennett, K., Bignami, G.F., Buccheri, R., Caraveo, P., D'Amico, N., Hermsen, W., Kanbach, G., Lichti, G.G., Mayer-Hasselwander, H.A., Paul, J.A., Swanenburg, B.N., and Wills, R.D., 1977, in *Recent Advances in Gamma Ray Astronomy*, ESA SP-124, 33.
- Mason, K.O., Sanford, P., Ives, J., 1975, *Proc. GSFC X-Ray Binary Symposium*, NASA SP-389, p. 255.

- Mason, K.O., Becklin, E.E., Blankenship, L., Brown, R.L., Elias, J., Hjellming, R.M., Matthews, K., Murdin, P.G., Neugebauer, G., Sanford, P.W., and Willner, S.P., 1976, *Ap. J.*, **207**, 78.
- Mayer-Hasselwander, H.A., Bennett, K., Bignami, G.F., Buccheri, R., D'Amico, N., Hermsen, W., Kanbach, G., Lebrun, F., Lichti, G.G., Masnou, J.L., Paul, J.A., Pinkau, K., Scarsi, L., Swanenburg, B.N., and Wills, R.D., 1980, *Annals of the New York Academy of Sciences, Proc. of the 9th Texas Symp.*, **336**, 211.
- McBreen, B., Ball, S.E., Jr., Campbell, M., Greisen, K., and Koch, D., 1973, *Ap. J.*, **184**, 571.
- Metzger, A.E., Parker, R.E., Gilman, D., Peterson, L.E., and Trombka, J.I., 1974, *Ap. J.*, **194**, L19.
- Montemerle, T., 1979, *Ap. J.*, **231**, 95.
- Oda, M., 1977, *Space Sci. Rev.*, **20**, 757.
- Ogelman, H.B., Fichtel, C.E., Kniffen, D.A., and Thompson, D.J., 1976, *Ap. J.*, **209**, 584.
- Orwig, L.E., Chupp, E.L., and Forrest, D.J., 1971, *Nature Phys. Sci.*, **231**, 191.
- Ostriker, J.P., and Gunn, J.E., 1969, *Ap. J.*, **157**, 1395.
- Page, D.N., 1976, *Phys. Rev. D.*, **14**, 3260.
- Page, D.N., and Hawking, S.W., 1976, *Ap. J.*, **205**, 1.
- Papaliolios, C., and Carleton, N.P., 1971, *The Crab Nebula*, ed. R.D. Davis and E.G. Smith (Dordrecht: Reidel, 1977), p. 142.
- Parlier, B., Agrinier, B., Forichon, M., Leray, J.P., Boella, G., Maraschi, L., Buccheri, R., Robba, N.R., and Scarsi, L., 1973, *Nature, Phys. Sci.*, **242**, 117.

- Ramaty, R., and Lingenfelter, R.E., 1977, *Ap. J.*, **213**, L5.
- Rankin, J.M., Comella, J.M., Craft, H.D., Jr., Richards, D.W., Campbell, D.B., and Counselman, C.C., III, 1970, *Ap. J.*, **162**, 707.
- Ruderman, M.A., and Sutherland, P.G., 1975, *Ap. J.*, **196**, 51.
- Samimi, J., Share, G.H., Wood, K., Yentis, D., Meekins, J., Evans, W.D., Shulman, S., Byram, E.T., Chupp, T.A., and Friedman, H., 1979, *Nature*, **278**, 434.
- Serlemitsos, P.J., Boldt, E.A., Holt, S.S., Rothschild, R.E., and Saba, J.L.R., 1975, *Ap. J. (Letters)*, **201**, L9.
- Stepanian, A.A., Vladimirovsky, B.M., Neshpor, Yu. I., 1977, *Proc. of the 15th Int. Cosmic Ray Conf.*, **1**, 135.
- Taylor, J.H., and Manchester, R.N., 1975, *Astron. Jour.*, **80**, 794.
- Terrell, J., Evans, W.D., Klebesadel, R.W., Laros, J.G., 1980, *Nature*, **285**, 383.
- Thompson, D.J., Fichtel, C.E., Kniffen, D.A., and Ogelman, H.B., 1975, *Ap. J.*, **200**, L79.
- Thompson, D.J., Fichtel, C.E., Hartman, R.C., Kniffen, D.A., and Lamb, R.C., 1977a, *Ap. J.*, **213**, 252.
- Thompson, D.J., Fichtel, C.E., Kniffen, D.A., Ogelman, H.B., 1977b, *Ap. J. (Letters)*, **214**, L17.
- Thorne, K.S., 1974, *Scientific American*, **231**, 32.
- Toor, A., 1977, *Ap. J. (Letters)*, **215**, L57.
- Trombka, J.I., Dyer, C.S., Evans, L.G., Bielefeld, M.J., Seltzer, S.M., and Metzger, A.E., 1977, *Ap. J.*, **212**, 925.
- Van Riper, K.A., 1978, *Ap. J.*, **221**, 304.

- Vladimirsky, B.M., Neshpor, Yu. I., Stepanian, A.A., and Fomin, V.P., 1975, *Proc. of the 14th Int. Cosmic Ray Conf.*, 1, 118.
- Wallace, P.T., Peterson, B.A., Murdin, P.G., Danziger, I.J., Manchester, R.N., Lyne, A.G., Goss, W.M., Smith, F.G., Disney, M.J., Hartley, K.F., Jones, D.H.P., and Wellgate, G.W., 1977, *Nature*, 266, 692.
- White, R.S., Ryan, J.M., Wilson, R.B., and Zych, A.D., 1978, *Nature*, 271, 635.
- Wills, R.D., Bennett, K., Bignami, G.F., Buccheri, R., Caraveo, P., D'Amico, N., Hermsen, W., Kanbach, G., Lichti, G.G., Masnou, J.L., Mayer-Hasselwander, H.A., Paul, J.A., Sacco, B., Swanenburg, B.N., 1980, *Advances in Space Exploration*, 7, Non-Solar Gamma Rays (COSPAR), ed. R. Cowsik and R.D. Wills (New York and Oxford: Pergamon Press, 1980), p. 43.

Vertical line of text on the left side of the page.

Horizontal line of text at the top right of the page.

Horizontal line of text at the bottom of the page.

Vertical line of text on the right side of the page.

**PART IV**  
**EXTRAGALACTIC**  
**RADIATION**

*Chapter 7*  
*Galaxies*

*Chapter 8*  
*Cosmology*

*Chapter 9*  
*Diffuse Radiation*



## PART IV

# EXTRAGALACTIC RADIATION

*As our attention turns to celestial objects beyond those of our own galaxy, even less familiar phenomena than those encountered in our galaxy appear. Several types of galaxies such as BL Lacertae objects, Seyfert galaxies, and quasars appear to emit more energy by orders of magnitude than our own galaxy and the many other galaxies similar to it. The existence of these very energetic galaxies and their proposed explanations which seem inevitably to involve very high energy phenomena, suggest that  $\gamma$ -ray astronomy should ultimately make a very important contribution to the understanding of other galaxies. Although  $\gamma$ -ray astronomy has moved only a modest way below the threshold for detection of sources, several active galaxies, including NGC 4151, 3C 273, and Centaurus-A have already been observed. Also extragalactic diffuse  $\gamma$ -radiation has been seen and current thinking suggests that this radiation, whose origin has been the subject of much theoretical study and debate, is likely to have a substantial cosmological significance.*

*In the next three chapters the celestial realm beyond our own galaxy will be discussed in terms of  $\gamma$ -ray astronomy. In Chapter 7, the more common galaxies such as our own and the less familiar exotic ones will be considered. In Chapter 8, a short discussion of cosmology will be presented as a background for the treatment of the high energy diffuse  $\gamma$ -radiation to be given in Chapter 9.*



## Chapter 7

### Galaxies

#### NORMAL GALAXIES

In the context of the discussion here, normal galaxies compose a very broad category which includes most galaxies and, in particular, elliptical galaxies, normal spirals, barred spirals, and all their variations. It specifically excludes those galaxies which are of an exceptional nature in luminosity or variability in at least one wavelength region, such as Seyfert galaxies, quasars, BL Lacertae objects, and intense radio galaxies.

As discussed in Chapter 5, our galaxy seems to be a typical spiral galaxy, belonging to a small local group of about 20 galaxies, most of which have masses smaller than our own. The distribution of galaxies in the universe on a fine scale is irregular. Galaxies generally exist in small groups which, in turn, are part of large clusters, the biggest of which may contain a thousand members or more. There is now even some evidence to suggest that the clusters of galaxies are not uniformly spaced, but tend to be grouped into superclusters of galaxies.

Normal galaxies have been studied in great depth in the optical range, and many have now been seen in the X-ray range. As yet none have been seen in  $\gamma$ -rays. A straightforward calculation can be performed to show that no other normal galaxy would have been expected to be seen in  $\gamma$ -rays if they are assumed to be like our own. Gamma ray instruments flown to date did not have enough sensitivity to see the closest galaxies at the level of emission expected on the basis of the one known example, namely our own galaxy.

To determine the intensity of  $\gamma$ -ray emission that might be expected from another galaxy similar to our own, first it is necessary to determine the luminosity of our own galaxy and then to estimate how the galactic luminosity might vary with mass. Chapter 5 showed that the galactic  $\gamma$ -ray intensity observed at the Earth could be explained in terms of models of  $\gamma$ -ray emission throughout the galaxy. It further develops that the  $\gamma$ -ray luminosity calculated for the galaxy is not very sensitive to the particular model. Calculations of Bignami et al. (1975), Strong and Worrall (1976), Kniffen et al. (1977), and Caraveo and Paul (1979) give estimates in the range  $(0.9 \text{ to } 1.3) \times 10^{42}$  photons  $\text{s}^{-1}$  for the luminosity of our galaxy above 100 MeV. Thus, unless our concept of the galaxy is quite wrong, a value of  $1.0 \times 10^{42}$  photons ( $\text{E} > 100 \text{ MeV}$ )  $\text{s}^{-1}$  should have a reasonable probability of being within a factor of two of the  $\gamma$ -ray luminosity of the galaxy. The corresponding energy emission for  $\text{E} > 100 \text{ MeV}$  is  $\sim 5 \times 10^{38}$  ergs  $\text{s}^{-1}$  which is similar to that in the radio and X-ray regions, but several orders of magnitude smaller than that in the optical band.

Since it is assumed that the production processes involved are the same in other galaxies, the energy spectrum in other normal galaxies are expected to be similar to that in our own. However, estimating the luminosity of another galaxy requires a bit more caution and probably should not be attempted for galaxies differing from our own in interstellar mass by a very large factor. As Chapter 5 described, the high energy  $\gamma$ -radiation arises both from interactions of cosmic rays with matter and photons and from point sources, with the former seeming, at present, to be the larger contributor. If another galaxy is a flat disk with the same matter density as ours, has cosmic rays like ours, and is simply bigger or smaller, the  $\gamma$ -ray luminosity would most likely just scale as the mass of the diffuse matter since it is the local emitting density which determines the local cosmic ray density. However, if the other galaxy were as big as ours and had a flat disk like ours, but its matter density were very different, the cosmic rays would be proportional to the density since they can ultimately be held by gravitational attraction only, and the intensity everywhere, and, hence, the luminosity would scale as the square of the mass. Since less massive galaxies are generally smaller, the first example seems closer to

the typical case and appears to be a less extreme assumption. The question of the number of  $\gamma$ -ray point sources as a function of galactic mass is clearly speculative, and, depending on the theories of their formation, many conclusions could be reached. For simplicity, it will be assumed that the number of point sources is proportional to the mass of the galaxy to the first power or a bit larger. It is also possible that another type of galaxy such as an ellipsoidal one might have few sources of cosmic rays. Answers to these and other questions await future experimental study.

A few of the closest galaxies will be considered below.

### The Large Magellanic Cloud

This is the closest galaxy to our own and it is estimated to be about 55 kpc away. It is just under  $8^\circ$  in extent and, hence, about 7 kpc in diameter, one-quarter the diameter of our galactic disk. The mass of neutral hydrogen is estimated to be about  $1.1 \times 10^{42}$  g (Bok, 1966) approximately one-quarter of our own. Assuming the  $\gamma$ -ray luminosity is proportional to a number between the ratio of the masses of the interstellar hydrogen of the Large Magellanic Cloud and our galaxy and the square of the masses, the  $\gamma$ -ray intensity observed at the Earth would be

$$(1/4 \text{ to } 1/16) 1.0 \times 10^{42} \frac{1}{4\pi (55 \times 3 \times 10^{21})^2} =$$

$$(2 \text{ to } 7) \times 10^{-7} \text{ photons } (\epsilon > 100 \text{ MeV}) \text{ cm}^{-2} \text{ s}^{-1}.$$

This intensity is slightly below the capability of detection for satellite instruments that have been flown thus far, but is well within the capability of the next generation of high energy  $\gamma$ -ray instruments.

The Large Magellanic Cloud is of particular interest because it is close enough that the general structure of the  $\gamma$ -ray emission can be studied. A comparison of the matter distribution deduced from radio measurements and the  $\gamma$ -ray radiation observations will be of great interest in determining the high energy spatial content and distribution and, hence, potentially determining the effect of the cosmic ray pressure on the dynamics of the galaxy.

### The Small Magellanic Cloud

The Small Magellanic Cloud is not only close to its larger companion, but it is also very similar, since it is only slightly more distant from us, about 63 kpc away, and has somewhat less mass (Bok, 1966). The predicted intensity as observed in the solar system is about half that of the Large Magellanic Cloud. It is still close enough and large enough in extent that the  $\gamma$ -ray structure could be studied.

### Great Galaxy in Andromeda (M31, NGC 224)

This galaxy is the closest galaxy that is similar to our own. It is slightly larger, about 50 kpc in diameter, and is estimated to have significantly more neutral hydrogen. It has a flat disk with a well-defined spiral structure. The spiral arms as defined by  $H_I$  are generally in quite good agreement with those defined optically (Guibert, 1974). Following the same analysis as that for the Large Magellanic Cloud, the  $\gamma$ -ray intensity of this galaxy as viewed from the solar system would be expected to be  $(0.5 \text{ to } 1.0) \times 10^{-7}$  photons ( $\geq 100$  MeV)  $\text{cm}^{-2} \text{s}^{-1}$ , a level within the range of future experiments.

The apparent similarity in structure and size to our own galaxy combined with its proximity has made M31 an attractive object for study. Since it is about  $4^\circ$  in diameter, obtaining information on its  $\gamma$ -ray structure will be possible along with studying the cosmic ray distribution and pressure effects.

A few other galaxies in our local group are likely to be detectable, but either their size or distance prohibits hope of any structural studies.

## INTRODUCTION TO ACTIVE GALAXIES

Active galaxies, including Seyfert galaxies, radio galaxies, quasars, and BL Lacertae objects are far less common than ordinary galaxies, but have a far greater luminosity. There is certainly no general agreement regarding how similar or different they are. It has sometimes been suggested that all have massive (of the order of  $10^8 M_\odot$ ) black holes at their centers. Alternatively, it has been postulated that, whereas quasars and BL Lacertae

objects may be similar with the latter being less luminous and possibly less numerous, Seyfert and radio galaxies may be very different, not only at present, but even in terms of their number density in the past. In terms of the energy release from active galaxies,  $\gamma$ -rays may be very important. For the three active galaxies for which  $\gamma$ -ray data exist (Centaurus-A, NGC 4151, and 3C 273), as much or more energy is emitted in the  $\gamma$ -ray region ( $E > 0.1$  MeV) than in the radio, optical, or X-ray range.

Before discussing separately the individual classes of active galaxies, it is advantageous to examine first some of the general mechanisms which might be producing  $\gamma$ -rays in at least some types of active galaxies. Clearly, with the greater energy involved, it would seem reasonable that even greater numbers of high energy particles should be produced than in a normal galaxy and that they would interact with the galactic matter producing  $\gamma$ -rays (see Chapter 5). Several other processes which are discussed below are also likely to be important.

In general, active galaxies are expected to have very large magnetic fields and larger photon densities than are seen in our galaxy. In these conditions synchrotron radiation and Compton radiation could become quite important, and the radiation from the synchrotron process itself might even create enough photons for the Compton process to become important between the parent electrons and the secondary photons (e.g., Grindlay, 1975; Shapiro and Salpeter, 1975; Mushotzky, 1976; and Maraschi and Treves, 1977). These Compton-synchrotron models predict a break in the energy spectrum between the X-ray and  $\gamma$ -ray energy ranges, based on the observation of a break in the synchrotron spectrum between the radio and optical energy ranges for many active galaxies. In addition,  $\gamma$ -radiation in the 100 MeV region might be expected from second-order Compton scattering (Bergeron and Salpeter, 1971).

High energy photon-photon interactions might become important near the center of active galaxies, depleting the number of high energy  $\gamma$ -rays. The astrophysical significance of high energy  $\gamma$ -ray absorption in dense photon regions associated with active galaxies was first noted by Jelley (1966), and developed by others such as Herterich (1974), primarily for stellar objects, and Rees (1978). In a region with a high electron and hard X-ray photon density, X-rays and  $\gamma$ -rays are created through Compton

radiation and possibly bremsstrahlung in great numbers. The photon density then could become such that  $\gamma$ -rays with energies much above  $mc^2$  interact frequently with X-rays leading to pair production. The resulting electrons and positrons lose energy through Compton interactions which enhance the X-ray, and even the hard X-ray component. The positrons ultimately combine with electrons annihilate each other, creating photons near 1/2 MeV. Assuming that there is a sufficiently hard X-ray photon density in the beginning, a marked increase in spectral slope will result near 1 MeV and there will be a relative dearth of very high energy photons. The photon region just below an MeV could actually be enhanced. There is some evidence to suggest that just this type of spectrum, i.e., one which is relatively flat in the hard X-ray region and dramatically steeper in the  $\gamma$ -ray region, may exist at least for some active galaxies.

The massive ( $\geq 10^8 M_{\odot}$ ) black holes postulated to exist at the centers of active galaxies may lead to  $\gamma$ -ray emission in still another way. Leiter and Kafatos (1978) and Kafatos and Leiter (1979) note that large energy releases may occur as the result of Penrose quantum processes occurring in the ergosphere of a massive black hole. In this model, hard X-ray and  $\gamma$ -rays fall toward the massive black hole gaining a very substantial amount of energy. They then interact with electrons and protons moving tangentially in what is sometimes called an accretion layer. When the blueshifted  $\gamma$ -ray has an energy of from tens of MeV to tens of GeV, it may scatter off a proton and produce electron-positron pairs that subsequently escape with energies as high as  $\sim 4 mc^2$ . This process is called "Penrose pair production." The high energy electrons may then produce  $\gamma$ -rays through the processes already discussed. Alternately, a low energy infalling  $\gamma$ -ray may scatter off an electron ("Penrose-Compton Scattering"), inject the electron into the black hole, and escape as a blueshifted  $\gamma$ -ray with an energy as large as  $\sim 4 mc^2$ . If there is a spread in energies, as there would be in an astrophysical situation, the resulting energy spectrum would have a marked increase in spectral slope near a few  $mc^2$ .

The positrons generated in these processes as they come to rest and annihilate with electrons could be the origin of a strong source of half MeV  $\gamma$ -rays. Since these  $\gamma$ -ray pairs may be created within the strong gravitational environment of the

massive black hole, their energy as seen in the solar system could be strongly redshifted, and there would very likely not be a sharp line.

The following sections describe specific types of active galaxies.

## SEYFERT GALAXIES

Seyfert galaxies have very bright nuclei with strong and broad emission lines in their spectra. Their energy release typically far exceeds that of a normal galaxy. Through a telescope, a Seyfert galaxy appears as a bright star surrounded by a faint envelope. In addition to their high luminosity, the broad emission lines are also an indication of an exceptionally high level of activity. Seyfert galaxies have been found to range from ordinary to barred spirals, but there seem to be few ellipticals.

It has been suggested that a combination of at least three different radiation mechanisms, stars, nonthermal radiation, and reradiation have to be combined to explain the intense Seyfert continua (Neugebauer et al., 1976). One of the most striking aspects of Seyfert galaxies is the variability in their luminosity. The small radiating volume implied by this variability combined with the high luminosity places severe constraints on theoretical models for the radiation and is the basis for the current popularity of various black hole models. A list of Seyfert galaxies and their properties as well as a general discussion of these objects has been given by Weedman (1977).

Turning now to the high energy photon emission, a substantial number of Seyfert galaxies have now been observed to be emitting X-rays (e.g., Elvis et al., 1978; Tananbaum et al., 1978; Dower et al., 1980). On the basis of their X-ray luminosity function and their relatively hard spectra, the Type I Seyferts appear to be the most likely to be observable as  $\gamma$ -ray sources. (Type I Seyfert galaxies have broad hydrogen lines, but narrower forbidden lines relative to Type II.)

Perotti et al. (1979) have reported  $\gamma$ -ray emission from NGC 4151, a Type I Seyfert, in the 0.2 to  $\sim 5$  MeV region, while Bignami et al. (1979) have reported a rather severe upper limit above 35 MeV. These results and relevant X-ray data for NGC 4151 are shown in Figure 7-1. At a later time than the

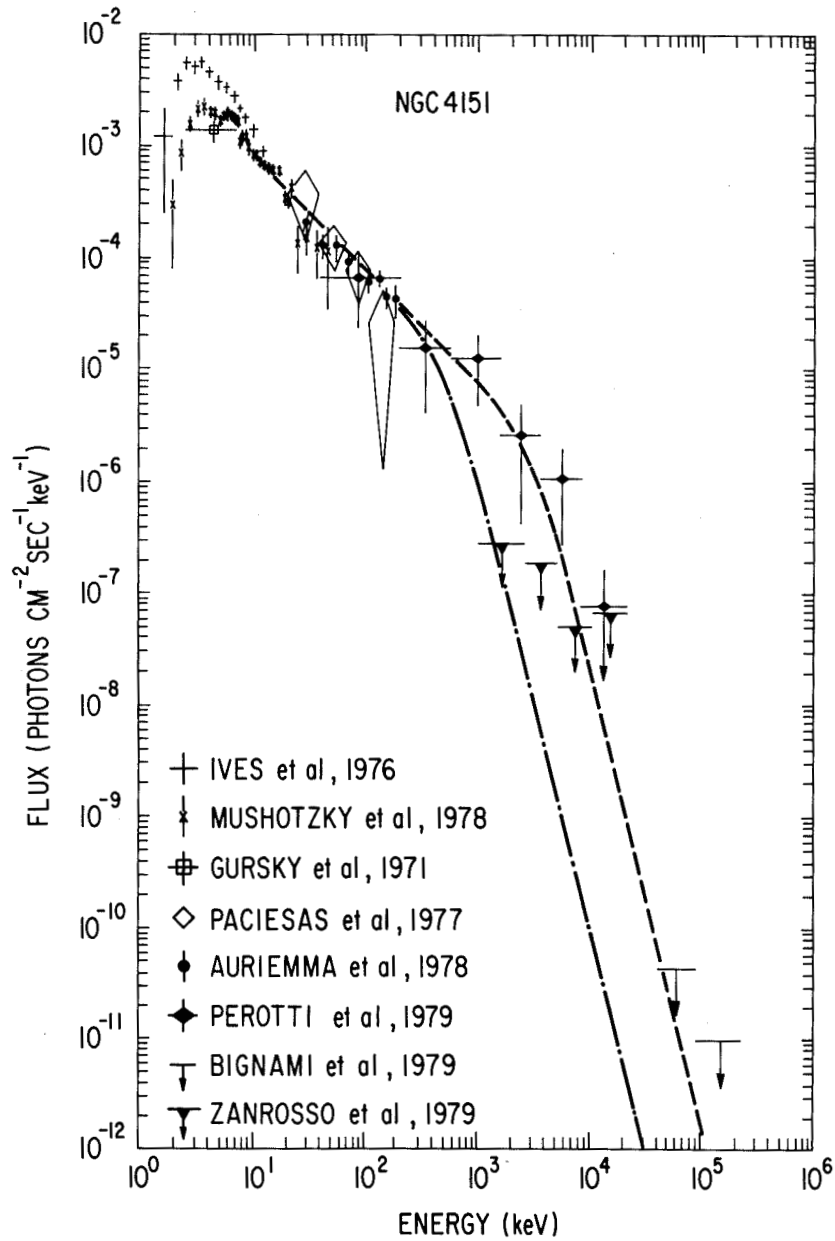


Figure 7-1. The differential high energy photon spectral results from several experiments as a function of energy for NGC 4151. The dashed curve is given by the equation  $\phi = 0.8 \times 10^{-2} / \epsilon^{1.0} [1 + (\epsilon/3 \times 10^3)^{3.0}]$  photons  $\text{cm}^{-2} \text{s}^{-1} \text{keV}^{-1}$  with  $\epsilon$  in keV.

measurements of Perotti et al. (1979), Zanzosso et al. (1979) reported only upper limits to the flux from NGC 4151 in the 1 to 20 MeV range. In particular, the upper limit in the 1 to 3 MeV range lies lower by about a factor of ten, as seen in Figure 7-1. These two results both seem reliable, suggesting the possibility of time variability in the  $\gamma$ -ray range as well as the X-ray range, especially in view of the fact that the result of Perotti et al. (1979) was made only two days after a major increase in the X-ray flux.

For five other Seyferts (and also several other emission line galaxies) upper limits derived from the SAS-2  $\gamma$ -ray data (Bignami et al., 1979) are substantially (more than an order of magnitude) below an extrapolation of the power law X-ray spectra (Mushotzky et al., 1979), suggesting that a sharp spectral change in the low-energy  $\gamma$ -ray region may be a general feature of these galaxies.

The spectral shape of NGC 4151 is consistent with the model involving a large Kerr black hole and the Penrose processes. Leiter (1980) has applied this model to this particular galaxy and has shown that it not only provides an explanation of the spectral shape, but also the temporal behavior of the radiation observed at energies ranging from the soft X-ray ( $< 10$  keV) to the  $\gamma$ -ray region.

## RADIO GALAXIES

There is a class of galaxies comprising particularly strong radio emitters without having exceptional optical properties. The majority of the identified radio galaxies are extended and show little evidence of self-absorption of the radio emission. The source of the radio emission is often thought to be synchrotron radiation. Associated with this radiation is self-Compton radiation wherein the electrons interact with photons emitted in the synchrotron process and Compton scatter off the microwave background radiation. These latter radiations are in the higher frequency realm of X-ray and even  $\gamma$ -ray astronomy (e.g., Burbidge et al., 1974).

Centaurus-A (NGC 5128), generally believed to be the closest radio galaxy, has been detected in all frequency bands from radio through low energy  $\gamma$ -rays (e.g., Hall et al., 1976)

and, although  $\gamma$ -ray emission is not seen in the 30 to  $10^3$  MeV region (Bignami et al., 1979), a strong indication of very high energy ( $\epsilon > 3 \times 10^{11}$  eV)  $\gamma$ -ray emission has been found (Grindlay et al., 1975). Centaurus-A (CEN-A) demonstrates considerable intensity variations in the radio region; in the moderate and hard X-ray range, its variation has been over nearly an order of magnitude and may be accompanied by substantial changes in spectral shape (Beall et al., 1978; Mushotzky et al., 1978a). Using the radio luminosity given by Kellermann (1974), the Seyfert galaxy space density and the radio luminosity function given by Schmidt (1978), the space density of galaxies with radio luminosities similar to that of CEN-A is seen to be comparable to that of the Seyferts. However, the X-ray luminosity of CEN-A (Mushotzky et al., 1978a) is comparable only to that of the weakest identified X-ray Seyfert galaxy, and no other radio galaxies similar to CEN-A have been identified in the X-ray region.

As seen in Figure 7-2, the existing results for CEN-A suggest a rather complex spectrum. However, it is consistent with the two-component Compton-synchrotron model of Grindlay (1975), shown in Figure 7-2, which even explains the  $10^{12}$  eV  $\gamma$ -radiation mentioned above, or the Compton self-synchrotron model of Mushotzky (1976) and Beall et al. (1978). It will be interesting to see if other radio galaxies are found to have this complex emission at high energies.

## QUASARS

Quasars were discovered in the early 1960's and immediately received wide attention because of the apparently large red shift of spectral lines, implying large distances and, hence, extraordinary power. Quasars are now generally accepted as being especially active nuclei of distant galaxies. Present theories are usually built around a massive region of  $10^7$  to  $10^9 M_{\odot}$  in a small volume at the center of a galaxy. The mass is generally assumed to be in the form of a dense star cluster, a massive star, or a black hole. As Rees (1978) has noted, once this massive region has reached the point where its power output becomes large enough to be visible at cosmological distances, it is difficult to envisage an evolutionary endpoint other than a

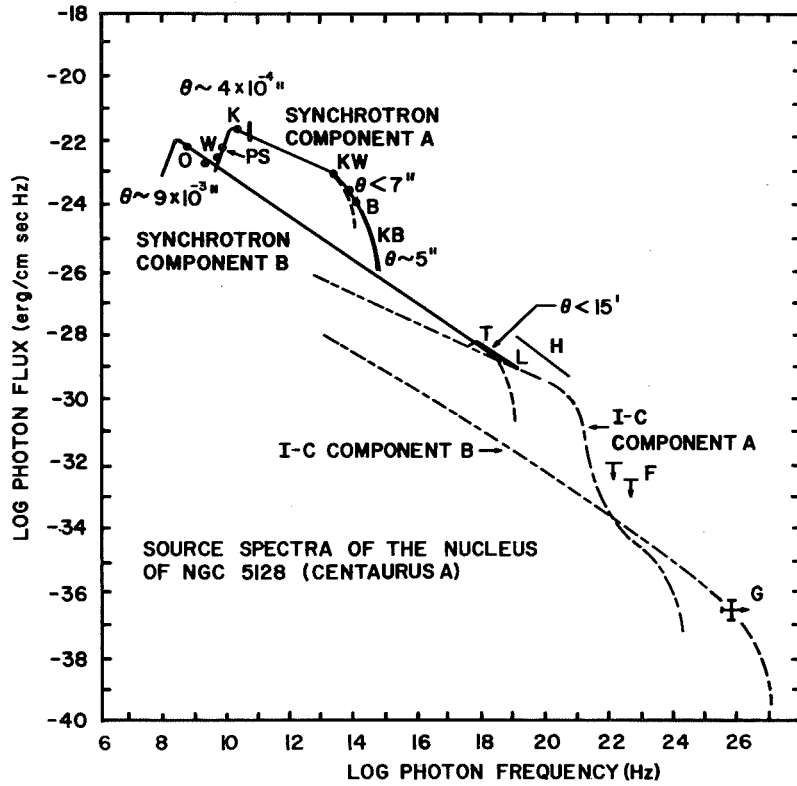


Figure 7-2. Observed spectral data and inferred connecting spectra for the nucleus of NGC 5128 (CEN-A). The references to the data are as follows: O—O'Sullivan (1975, private communication to Grindlay); W (two points)—Wade et al. (1971); PS—Price and Stull (1973); K (two points, where the vertical line connects the flux observed on 1974, March 27 and 28)—Kellermann (1974); KW—Kleinmann and Wright (1974); B (two points)—Becklin et al. (1971); KB (heavy curve)—Kunkel and Bradt (1971); T and L (connecting heavy curve)—Tucker et al. (1973) and Lampton et al. (1972); H—Hall et al. (1975); F—Fichtel et al. (1975); and G—Grindlay et al. (1975). Available data for the source angular diameter  $\theta$  are given. The data up through X-ray spectrum are well-described by the sum of two synchrotron spectra A and B with assumed cutoffs (dashed curves) at  $\sim 10^{14}$  Hz and  $\sim 3 \times 10^{18}$  Hz, respectively, as described by Grindlay (1975). The source component angular diameters shown are appropriate to synchrotron self-absorption at the turnover frequencies 30 GHz (a) and  $\sim 600$  MHz (b) and the calculated inverse Compton (I-C) spectra from each component, which are shown by the dot-dashed curves.

complete collapse of at least a part of the matter involved. Hence, it is likely that a massive black hole is the ultimate result even if one of the other models describes an earlier state. Since the black hole is also potentially a more efficient power source, it seems reasonable to attribute the radiation from quasars primarily to processes associated with a black hole.

The general mechanism which seems most attractive for the production of the radiation within the framework of a massive black hole model is accretion. Studies of galaxies show that the necessary infall of material can be supplied by the galaxy, although it has also been suggested that a significant part of the mass might be supplied by the disruption of stars in the dense region near the central black hole. If this concept is accepted, the processes for producing high energy electromagnetic radiation in the vicinity of a black hole become relevant.

A very large number of quasars have been detected in the soft X-ray region with the HEAO-2 satellite (Tananbaum et al., 1979), and a few in the hard X-ray region including 3C 273 (Bowyer et al., 1970), 2S 0241+622 (Apparao et al., 1978) and 2S 2251-179 (Ricker et al., 1978). The latter two were identified as quasars after being recognized as X-ray sources. Of these three quasars, 3C 273 is optically the brightest and by far the most luminous. It is the only quasar which has been clearly identified as a source of high energy ( $> 100$  MeV)  $\gamma$ -rays (Swanenburg et al., 1978). The spectrum of 3C 273 steepens sharply from the X-ray range to the  $\gamma$ -ray region, as shown in Figure 7-3, with the slope of the differential energy spectrum changing from 1.4 in the hard X-ray region to 2.7 in the high energy  $\gamma$ -ray region. The upper limits measured in the low energy  $\gamma$ -ray range suggest that either the spectrum is complex or the emission is time varying. The upper limit in the very high energy  $\gamma$ -ray interval of  $3 \times 10^8$  to  $3 \times 10^9$  keV, also shown in the figure, is consistent with the steep spectrum continuing to these energies. Thus, unlike CEN-A, at least for the present, there is no evidence in the case of 3C 273 for an additional hard component at very high energies.

The change in spectral shape between the hard X-ray and  $\gamma$ -ray region seen for 3C 273 is similar to that suggested for the Seyfert galaxies for which data existed. This spectrum, although as yet poorly defined, is consistent with several of the massive

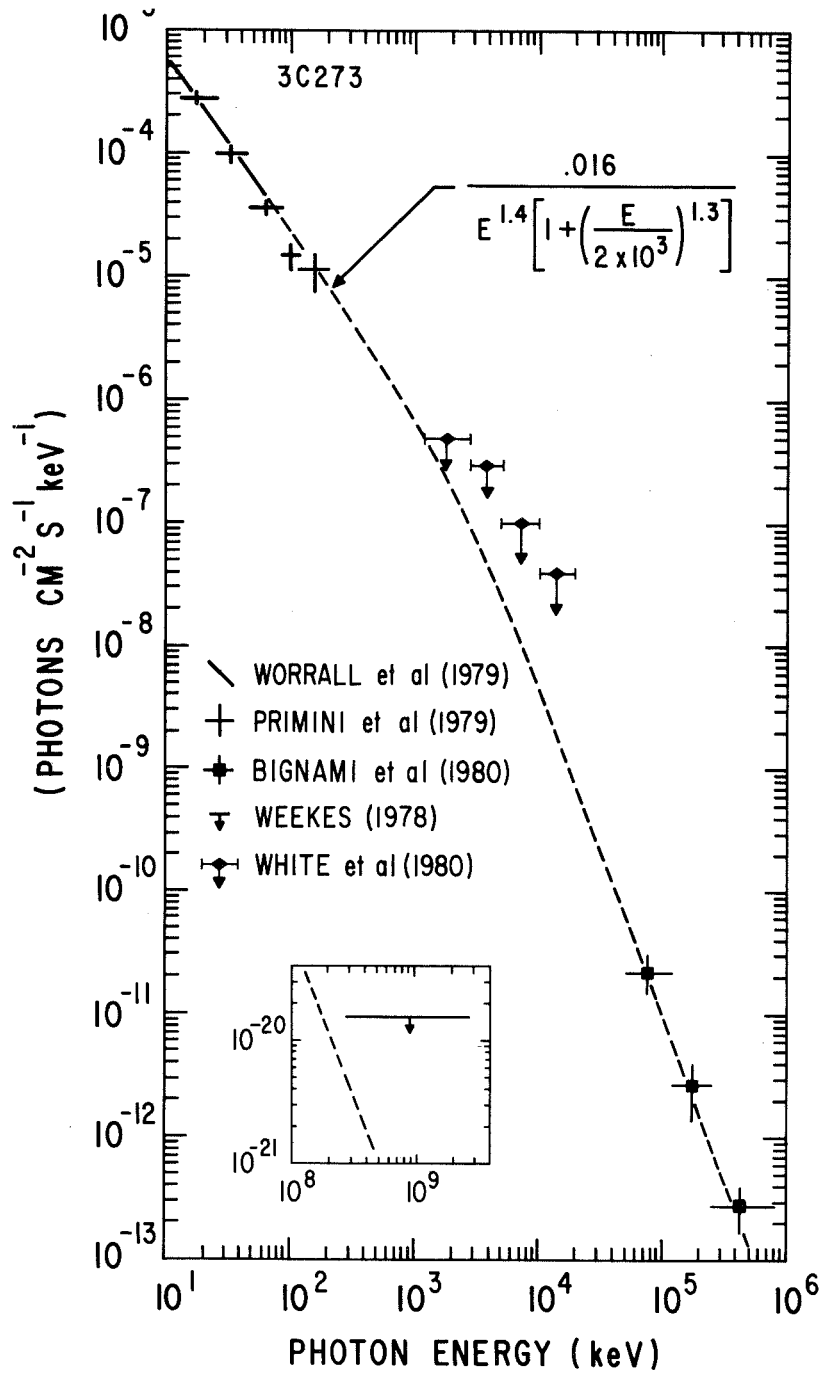


Figure 7-3. The differential high energy photon spectral results from several experiments as a function of energy for 3C 273. The dashed curve is given by the equation shown in the figure.

black hole models discussed earlier. Clearly, it would be very desirable to have data in the low energy  $\gamma$ -ray region for 3C 273 and other quasars to compare the whole spectrum with theoretical predictions.

The closest known quasar is 2S 0241+622, but it is very close to the galactic plane ( $b \simeq 2^\circ$ ). The error box of the COS-B  $\gamma$ -ray source CG 135+1 (Hermsen et al., 1977) contains the position of 2S 0241+622, and the possible association has been pointed out by Apparao et al. (1978). Because of the large area of the  $\gamma$ -ray error box as well as the alternative explanation of a  $\gamma$ -ray source within the galaxy, this identification must be considered tentative.

### BL LACERTAE OBJECTS

BL Lacertae objects derive their name from the first of these objects studied in detail, namely the peculiar "variable star" BL Lacertae, which is also the unusual radio source VRO 42.22.01. These objects are now generally accepted to be galaxies possibly similar to, but less intense than, quasars. They generally have the following characteristics: (1) rapid variability at radio, infrared, and visual wavelengths, (2) absence of strong emission lines in the core, (3) strong and variable polarization, and (4) a nonthermal continuum with most of the luminosity in the infrared range. A review of the properties of these objects is given by Stein et al. (1976).

Of the objects in this class, two galaxies, Markarian 421 and 501, have been clearly identified as X-ray sources (Schwartz et al., 1978; Marshall and Jernigan, 1978), and 1912+30.5 and 0548-32.2 have tentative identifications as X-ray emitters. X-ray spectra of Mk 421 and Mk 501 show no absorption, and have photon power law spectral indexes of  $0.9 \pm 0.5$  and  $1.2 \pm 0.2$ , respectively (Mushotzky et al., 1978a). Even if the steepest allowable spectrum (index  $\sim 1.4$ ) is used, extrapolation of the 100 MeV range predicts intensities roughly an order of magnitude above the upper limits reported by Bignami et al. (1979) for these two objects, as shown for Mk 501 in Figure 7-4. Thus their spectra must also have a significant steepening somewhere between 50 keV and 35 MeV. The six-fold reduction in intensity observed for Mk 421 over a period of 6 months (Mushotzky et al., 1979)

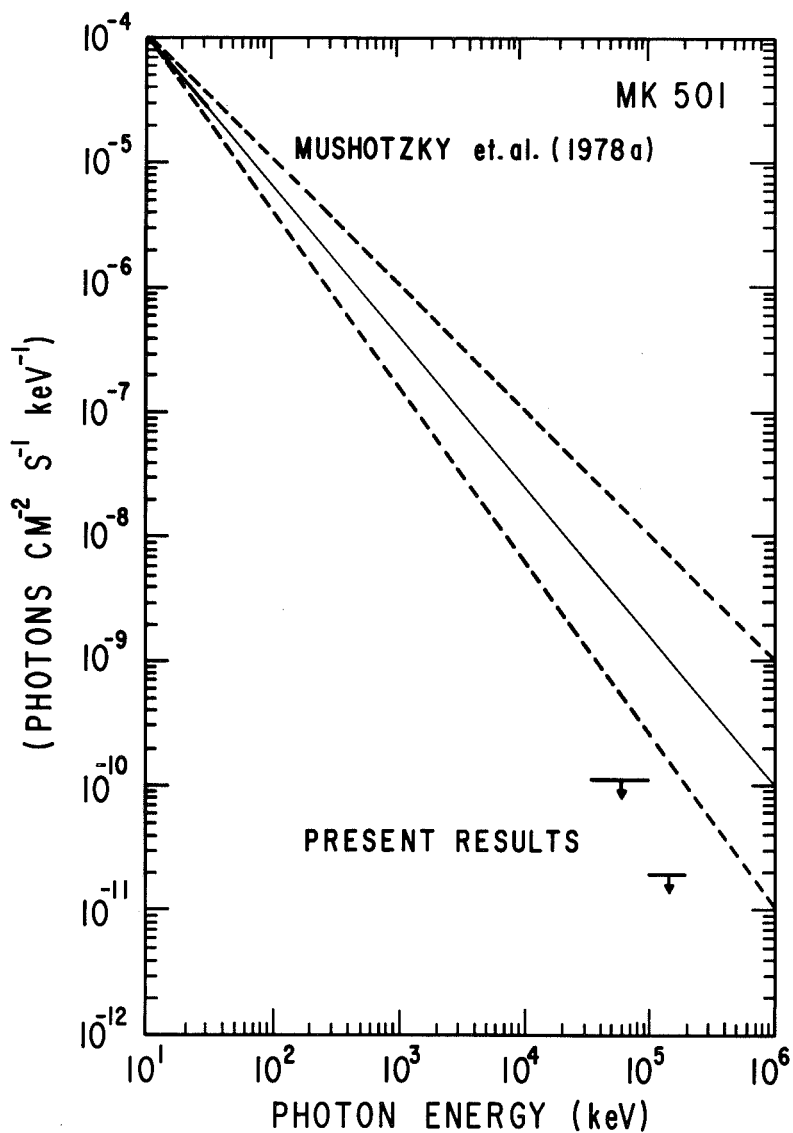


Figure 7-4. The high energy spectrum of the BL Lacertae object Mk 501. Solid line: X-ray spectrum of Mushotzky et al. (1978b), measured up to 30 keV and extrapolated above that energy. Dashed lines: upper and lower limits on the extrapolation of the power law X-ray spectrum. The 35 to 100 MeV upper limit was derived directly from SAS-2 observations. The SAS-2 upper limit between 100 MeV and 200 MeV was derived from an integral upper limit for energies above 100 MeV assuming a differential photon intensity power law spectrum with an index of 2 (Bignami et al., 1979). The BL Lacertae object HO 548-322 has a similar X-ray spectrum (Mushotzky et al., 1978b) and similar upper limits from SAS-2.

could, however, affect this conclusion significantly. Even so, at present it seems that BL Lacertae objects also have a marked change in spectral slope between the hard X-ray and the higher energy  $\gamma$ -ray region.

#### CONCLUDING REMARKS

The presentations in the last sections have shown that at present little is known experimentally about external galaxies in the high energy region. However, both the significance of  $\gamma$ -rays to the understanding of galaxies and the experimental data which do exist suggest that experiments are close to many significant results and that  $\gamma$ -ray astronomy should make a major contribution to the understanding of both normal and active galaxies in the next decade.

## REFERENCES

- Apparao, K. M. V., Maraschi, L., Bignami, G., Helmken, H., Margon, B., Hjellming, R., Bradt, H. V., and Dower, R. G., 1978, *Nature*, **273**, 450.
- Beall, J. H., Rose, W. K., Graf, W., Price, K. M., Dent, W. A., Hobbs, R. W., Conklin, E. K., Ulich, B. L., Dennis, B. R., Crannel, C. J., Dolan, J. F., Frost, K. J., and Orwig, L. E., 1978, *Ap. J.*, **219**, 836.
- Becklin, E. E., Frogel, J. A., Kleinmann, D. E., Neugebauer, G., Ney, E. P., and Strecker, D. W., 1971, *Ap. J. (Letters)*, **170**, L15.
- Bergeron, J., and Salpeter, E. E., 1971, *Astrophys. Letters*, **9**, 121.
- Bignami, G. F., Fichtel, C. E., Kniffen, D. A., and Thompson, D. J., 1975, *Ap. J.*, **199**, 54.
- Bignami, G. F., Fichtel, C. E., Hartman, R. C., and Thompson, D. J., 1979, *Ap. J.*, **232**, 649.
- Bignami, G. F., Bennett, K., Buccheri, R., Caraveo, P. A., Hermesen, W., Kanbach, G., Lichti, G. G., Masnou, J. L., Mayer-Hasselwander, H. H., Paul, J. A., Sacco, B., Scarsi, L., Swanenburg, B. N., and Wills, R. D., 1980, *Astron. Astrophys.*, in press.
- Bok, B. J., 1966, *Ann. Rev. Astron. Astrophys.*, **4**, 95.
- Bowyer, C. S., Lampton, M., Mack, J., and de Mondonca, F., 1970, *Ap. J. (Letters)*, **161**, L1.
- Burbidge, G. R., Jones, T. W., and O'Dell, S. L., 1974, *Ap. J.*, **193**, 43.
- Caraveo, P., and Paul, J. A., 1979, *Astron. Astrophys.*, **75**, 340.

- Dower, R. G., Griffiths, R. E., Bradt, H. V., Doxsey, R. E., and Johnston, M. D., 1980, *Ap. J.*, **235**, 355.
- Elvis, M., Maccacaro, T., Wilson, A. S., Ward, M. J., Penston, M. V., Fosbury, R. A. E., and Perola, G. C., 1978, *Mon. Not. Roy. Ast. Soc.*, **183**, 129.
- Fichtel, C. E., Hartman, R. C., Kniffen, D. A., Thompson, D. J., Bignami, G. F., Ogelman, H. B., Ozel, M. E., and Tumer, T., 1975, *Ap. J.*, **198**, 163.
- Grindlay, J. E., 1975, *Ap. J.*, **199**, 49.
- Grindlay, J. E., Helmken, H. F., Brown, R. H., Davis, J., and Allen, L. R., 1975, *Ap. J. (Letters)*, **197**, L9.
- Guibert, J., 1974, *Astron. Astrophys.*, **30**, 353.
- Hall, R. D., Meegan, C. A., Walraven, G. D., Djuth, F. T., Shelton, D. H., and Haymes, R. C., 1975, *Proc. of the 14th Int. Cosmic Ray Conf.*, **1**, 84.
- Hall, R. D., Meegan, C. A., Walraven, G. D., Djuth, F. T., and Haymes, R. C., 1976, *Ap. J.*, **210**, 631.
- Hermesen, W., Swanenburg, B. N., Bignami, G. F., Boella, G., Buccheri, R., Scarsi, L., Kanbach, G., Mayer-Hasselwander, H. A., Masnou, J. L., Paul, J. A., Bennett, K., Higdon, J. C., Lichti, G. G., Taylor, B. G., Wills, R. D., 1977, *Nature*, **269**, 494.
- Herterich, K., 1974, *Nature*, **250**, 311.
- Ives, J. C., Sanford, P. W., and Penston, M. V., 1976, *Ap. J. (Letters)*, **207**, L159.
- Jelley, T. V., 1966, *Nature*, **211**, 472.
- Kafatos, M., and Leiter, D., 1979, *Ap. J.*, **229**, 46.
- Kellermann, K. I., 1974, *Ap. J. (Letters)*, **194**, L135.
- 182 GAMMA RAY ASTROPHYSICS

- Kleinmann, D. E., and Wright, E. L., 1974, *Ap. J. (Letters)*, **191**, L19.
- Kniffen, D. A., Fichtel, C. E., and Thompson, D. J., 1977, *Ap. J.*, **215**, 765.
- Kunkel, W. E., and Bradt, H. V., 1971, *Ap. J. (Letters)*, **170**, L7.
- Lampton, M., Margon, B., Bowyer, S., Mahoney, W., and Anderson, K., 1972, *Ap. J. (Letters)*, **171**, L45.
- Leiter, D., 1980, *Astron. Astrophys.*, **89**, 370.
- Leiter, D., and Kafatos, M., 1978, *Ap. J.*, **226**, 32.
- Maraschi, L., and Treves, A., 1977, *Ap. J. (Letters)*, **218**, L113.
- Marshall, F. J., and Jernigan, J. G., 1978, *IAU Circular #3224*.
- Mushotzky, R. F., 1976, Ph.D. Thesis, University of California, San Diego.
- Mushotzky, R. F., Serlemitsos, P. J., Becker, R. H., Boldt, E. A., and Holt, S. S., 1978a, *Ap. J.*, **220**, 790.
- Mushotzky, R. F., Boldt, E. A., Holt, S. S., Pravdo, S. H., Serlemitsos, P. J., Swank, J. H., and Rothschild, R. H., 1978b, *Ap. J. (Letters)*, **226**, L65.
- Mushotzky, R. F., Boldt, E. A., Holt, S. S., and Serlemitsos, P. J., 1979, *Ap. J.*, **232**, L17.
- Neugebauer, G., Becklin, E. E., Oke, J. B., Searle, L., 1976, *Ap. J.*, **205**, 29.
- Perotti, F., Della Ventura, A., Sechi, G., Villa, G., DiCocco, G., Baker, R. E., Butler, R. C., Dean, A. J., Martin, S. J., and Ramsden, D., 1979, *Nature*, **282**, 484.
- Price, K. M., and Stull, M. A., 1973, *Nature, Phys. Sci.*, **245**, 83.

- Primini, F. A., Cooke, B. A., Dobson, C. A., Howe, S. K., Scheepmaker, A., Wheaton, W. A., Lewin, W. H. G., Baity, W. A., Gruber, D. E., Matteson, J. L., and Peterson, L. E., 1979, *Nature*, **278**, 234.
- Rees, M. J., 1978, *Physica Scripta*, **17**, 193.
- Ricker, G. R., Clarke, G. W., Doxsey, R. E., Dower, R. G., Jernigan, J. G., Delvaille, J. P., MacAlpine, G. M., and Hjelling, R. M., 1978, *Nature*, **271**, 35.
- Schmidt, M., 1978, *Physica Scripta*, **17**, 135.
- Schwartz, D. A., Bradt, H., Doxsey, R. E., Griffiths, R., Gursky, H., Johnston, M., and Schwarz, J., 1978, *Ap. J.*, **224**, L103.
- Shapiro, S. L., and Salpeter, E. E., 1975, *Ap. J.*, **198**, 671.
- Stein, W. A., O'Dell, S. L., and Strittmatter, P. A., 1976, *Ann. Rev. Astron. Astrophys.*, **14**, 173.
- Strong, A. W., and Worrall, D. M., 1976, *Jour. Phys. Astron.: Math. Gen.*, **9**, 823.
- Swanenburg, B. N., Bennett, K., Bignami, G. F., Caraveo, P., Hermsen, W., Kanbach, G., Masnou, J. L., Mayer-Hasselwander, H. A., Paul, J. A., Sacco, B., Scarsi, L., and Wills, R. D., 1978, *Nature*, **275**, 298.
- Tananbaum, H., Peters, G., Forman, W., Giacconi, R., and Jones, C., 1978, *Ap. J.*, **223**, 74.
- Tananbaum, H., Avni, Y., Branduardi, G., Elvis, M., Fabbiano, G., Feigelson, E., Giacconi, R., Henry, J. P., Pye, J. P., Soltan, A., and Zamorani, G., 1979, *Ap. J. (Letters)*, **234**, L9.
- Tucker, W., Kellogg, E., Gursky, H., Giacconi, R., and Tananbaum, H., 1973, *Ap. J.*, **180**, 715.

- Wade, C. M., Hjellming, R. M., Kellermann, K. I., and Wardle, J. F. C., 1971, *Ap. J. (Letters)*, **170**, L11.
- Weedman, D. W., 1977, *Ann. Rev. Astron. Astrophys.*, **15**, 69.
- Weekes, T. C., 1979, *Proc. of the 1978 DUMAND Summer Workshop*, **2**, ed. A. Roberts (LaJolla: Scripps Institution of Oceanography, 1979), p. 313.
- White, R. S., Dayton, B., Gibbons, R., Long, J. L., Zanzosso, E. M., Zych, A. D., 1980, *Nature*, **284**, 608.
- Worrall, D. M., Mushotzky, R. F., Boldt, E. A., Holt, S. S., and Serlemitsos, P. J., 1979, *Ap. J.*, **232**, 683.
- Zanzosso, E. M., Long, J. L., Zych, A. D., Gibbons, R., White, R. S., and Dayton, B., 1979, *Proc. of the 16th Int. Cosmic Ray Conf.*, **1**, 112a.



## Chapter 8

# Cosmology

### INTRODUCTION

The study of extragalactic  $\gamma$ -ray astrophysics cannot proceed further without a discussion of cosmology. Hence, a very brief summary of the current view of the universe, the equations used to describe it, and the means of interpreting the diffuse  $\gamma$ -radiation which might result from phenomena which occurred in the distant past are described below.

The current concept of our universe probably had its beginning about a half century ago when Hubble first concluded that there was an approximately linear relationship between the distances to galaxies and their red shifts. Over the intervening half century the data have improved remarkably, but the result is still basically the same, that is galaxies appear to be moving apart at velocities proportional to their separations. Hence, the obvious conclusion is that at some time in the past, estimated now to be about  $15 \times 10^9$  years ago, they must have all been close together.

In 1922, Alexandre Friedmann found the general homogeneous and isotropic solution to the equations that Einstein had developed in his theory of general relativity for the whole universe. This "Friedmann model" forms the basis of what is now considered to be modern standard cosmology, and the next section of this chapter will explore the equations of this model.

One aspect of the model which has received much attention is that, depending on the energy density, the universe is either

open or closed. If it is open, it will continue to expand forever, and, if it is closed, its present expansion will ultimately stop and a contraction will begin. The detailed theory shows that whether it is open or closed depends only on the average energy density. The critical density,  $\rho_c$ , is about  $10^{-29}$  g cm<sup>-3</sup>, or more specifically

$$\rho_c = 0.7 \times 10^{-29} (H_0/60 \text{ km s}^{-1} \text{ Mpc}^{-1})^2 \text{ g cm}^{-3}, \quad (8-1)$$

where  $H_0$  is the present best value for the Hubble parameter. Since at present matter is the major contributor to the energy density, if the matter density is less than this value the universe is open, and, if not, it is closed. Currently, it appears that  $\rho$  is substantially less than  $\rho_c$ , but there may be unseen mass; so the question of whether  $\rho$  is greater or less than  $\rho_c$  remains open for the moment.

The other major discovery related to our current view of cosmology was that of the diffuse cosmic 3 K microwave radiation by Penzias and Wilson (1965). As Dicke, Peebles, Roll, and Wilkinson (1965) explained, this radiation is exactly what is expected in a universe which has expanded from a time when it was very hot and dense and the scattering of free electrons and photons maintained matter and radiation in thermal equilibrium. As the universe expanded and cooled from this early state, a temperature ( $\sim 3 \times 10^3$  K) was reached when the electrons combined with nuclei to form atoms. The photons were no longer coupled thermally, and the photon radiation thereafter simply expanded freely. The density and temperature then decreased, but continued to have a spectral shape described by the Planck blackbody equation. The microwave radiation mentioned above has been found to have the spectrum appropriate for that of 3 K blackbody radiation, and, hence, this observation gives strong support to the theory of the expanding universe, or the "big bang."

Knowing the present temperature of the blackbody radiation, it is possible to calculate the production of complex nuclei in the early stages of the universe. One result of these calculations is that about 27 percent by mass of the nucleons should have fused into He<sup>4</sup> (Weinberg, 1972). This prediction is in agreement with the range of values allowed by current measurements and, hence, provides additional support for the model.

There is also the question of whether the universe as a whole is symmetric with regard to matter and antimatter. Gamma ray astronomy has already made an important contribution in this area by showing that the steady-state theory, wherein matter and antimatter were continually created (Hoyle, 1948; Bondi and Gold, 1948) throughout the universe, was inconsistent with the level of diffuse  $\gamma$ -radiation by several orders of magnitude. There remains the question of whether superclusters of galaxies of matter and antimatter might exist and how they might have come into being.

For a general review of cosmology see Peebles (1971) and Weinberg (1972).

### DIFFUSE RADIATION

In order to consider the diffuse emission that is being observed, it is necessary to look as far back in time as necessary to include all the emission that might be reaching the observer at the present time. In proceeding, it is not only necessary to take into account properly spatial considerations, but also to remember that a frequency,  $\nu_o$ , or energy,  $\mathcal{E}_o$ , observed now had a larger value in the past. (The subscript "o" will be used in this section to refer to the time of observations.) The universe being considered here is isotropic and homogeneous; all the sources will be assumed to emit radiation isotropically and to be distributed isotropically (or at least to be so on a coarse scale so that such an assumption is an adequate representation of the real world).

The number density of photons per energy interval at any time  $t$  which at time  $t_o$  have an energy between  $\mathcal{E}_o$  and  $\mathcal{E}_o + d\mathcal{E}_o$  is  $N(\mathcal{E}_o, t)$ . The rate of change of the number of photons in a proper volume  $R^3(t)$  and an energy interval  $d\mathcal{E}_o$  at time  $t_o$  is

$$\begin{aligned} \frac{d}{dt} [N(\mathcal{E}_o, t) R^3(t)] &= \Gamma \left( \mathcal{E}_o \frac{R(t_o)}{R(t)}, t \right) R^3(t) \left( \frac{R(t_o)}{R(t)} \right) \\ &- A \left( \mathcal{E}_o \frac{R(t_o)}{R(t)}, t \right) N(\mathcal{E}_o, t) R^3(t) , \end{aligned} \quad (8-2)$$

where  $\Gamma$  is the rate of emission per unit volume in the energy interval  $d\epsilon_0$  and  $A$  is the absorption rate (see Weinberg, 1972).

Consider first the case for which the second term is negligible. This case is appropriate for  $\gamma$ -ray astronomy for all but the lowest energy  $\gamma$ -rays and the earliest times, when the density was much higher. To obtain a coarse idea that this statement is correct, consider a  $\gamma$ -ray traveling for  $15 \times 10^9$  years through a medium with a density even as high as that needed to close the universe  $\sim 0.7 \times 10^{-29}$  g cm $^{-3}$ . Its total path length is 0.2 g cm $^{-2}$ , which for  $\gamma$ -rays above a few MeV is only about one-thousandth of an interaction mean free path, and even for  $\gamma$ -rays in the 0.1 to 1 MeV range it is small. Although the density in the past was larger, the  $0.7 \times 10^{-29}$  g cm $^{-3}$  figure is probably significantly larger than the actual value. For  $A = 0$  Equation (8-2) becomes

$$d[N(\epsilon_0, t) R^3(t)] = \Gamma \left( \epsilon_0 \frac{R(t_0)}{R(t)} \right) R^3(t) \left( \frac{R(t_0)}{R(t)} \right) dt \quad (8-3)$$

Using the following expression, which is valid for the standard universe in the matter dominated era (i.e., the matter energy density  $\gg$  the radiation energy density) which began long before galaxies were formed,

$$dt = \frac{dR}{R} = \frac{dR(t)}{R(t_0)H_0} \left[ 1 - 2q_0 + 2q_0 \left( \frac{R(t_0)}{R(t)} \right) \right]^{-1/2}, \quad (8-4)$$

where  $H_0$  is the present value of the Hubble parameter, and  $q_0$  is the deceleration parameter. Since

$$\frac{R(t_0)}{R(t)} = (z + 1), \quad (8-5)$$

equation (8-4) may be rewritten as

$$dt = \frac{dz}{(1+z)^2} \left( \frac{(1+2q_0 z)^{-1/2}}{H_0} \right). \quad (8-6)$$

Using Equations (8-5) and (8-6), Equation (8-3) becomes

$$d[N(\mathfrak{E}_0, t) R^3(t)] = \Gamma(\mathfrak{E}_0, (1+z), z) \frac{R^3(z=0) dz}{H_0 (1+z)^4 (1+2q_0 z)^{1/2}}. \quad (8-7)$$

Hence,

$$N(\mathfrak{E}_0, t_0) = \frac{1}{H_0} \int_0^{z_{\max}} \Gamma(\mathfrak{E}_0, (1+z), z) \frac{dz}{(1+z)^4 (1+2q_0 z)^{1/2}} \quad (8-8)$$

under the assumption that at the beginning of the time of interest  $N(\mathfrak{E}_0, t_i) R^3(t_i)$  is zero or negligible compared to  $N(\mathfrak{E}_0, t_0) \times R^3(t_0)$ .

The differential intensity associated with this differential density is

$$j \equiv \frac{dJ}{dE} = \frac{c}{4\pi H_0} \int_0^{z_{\max}} \Gamma(\mathfrak{E}_0, (1+z), z) \left( \frac{dz}{(1+z)^4 (1+2q_0 z)^{1/2}} \right). \quad (8-9)$$

To proceed further it is necessary to make a specific assumption about  $(\mathcal{E}_o (1+z), z)$ . Two specific cases will be considered here in preparation for the next chapter. First, consider the case wherein the diffuse background is due to active galaxies. Then,  $\Gamma$  may be written as

$$\Gamma_{I,i}(\mathcal{E}_o (1+z), z) = n_i (1+z) Q_i(\mathcal{E}_o (1+z), z) \quad , \quad (8-10)$$

where  $n(1+z)$  is the number density of galaxies of type  $i$ , and  $Q_i(z)$  is the average source strength. If it is assumed that the number of galaxies remains constant, then the number density is proportional to  $(1+z)^3$ . It will also be assumed that  $Q_i(z)$  may be written as  $Q_i(\mathcal{E}_o (1+z)) f(z)$ , i.e., that intensity evolution is separable and that the spectral form does not change. Equation (8-10) then becomes

$$\Gamma_{I,i}(\mathcal{E}_o (1+z), z) = n_i(o) (1+z)^3 Q_i(\mathcal{E}_o (1+z)) f(z) \quad , \quad (8-11)$$

and Equation (8-9) becomes

$$j_I = \frac{c n_i(o)}{4\pi H_o} \int_0^{z_{\max}} \frac{Q_i(\mathcal{E}_o (1+z)) f(z) dz}{(1+z) (1+2q_o z)^{1/2}} \quad (8-12)$$

Another case of interest concerns any photon creating interaction between two species, such as cosmic rays and matter or cosmic ray electrons and photons. Here, the densities of both species would be proportional to  $(1+z)^3$ , and, if neither species were being created during the period of interest and their losses were negligible, then  $\Gamma(\mathcal{E}_o (1+z), z)$  would be

$$\Gamma_{II,i,j}(\mathcal{E}_o (1+z), z) = n_i(o) n_j(o) (1+z)^6 F_{ij}(\mathcal{E}_o (1+z)) \quad , \quad (8-13)$$

and Equation (8-8) would become

$$j_{II} = \frac{cn_i(o)n_j(o)}{4\pi H_o} \int_0^{z_{\max}} \frac{(1+z)^2 F_{ij}(\mathcal{E}_o(1+z)) dz}{(1+2q_o z)^{1/2}} . \quad (8-14)$$

If one or both of the interacting species changes in number with time (e.g., cosmic rays being created in galaxies and leaking into intergalactic space), then  $n_i$  could be written as

$$n_i = (1+z)^3 n_i(o) f_i(z) , \quad (8-15)$$

and then Equation (8-9) would be

$$J_{III} = \frac{cn_i(o)n_j(o)}{4\pi H_o} \int_0^{z_{\max}} \frac{(1+z)^2 f_i(z) f_j(z) F_{ij}(\mathcal{E}_o(1+z)) dz}{(1+2q_o z)^{1/2}} . \quad (8-16)$$

Normally these integrals have to be solved by numerical integration. However, there is an interesting simple case which can be used as an example. Consider the case represented by Equation (8-12) and assume that  $q_o$  is near enough to zero to be neglected over the presently estimated age of the existence of galaxies i.e.,  $z_{\max} = (3 \text{ to } 4)$ . Further assume that  $Q_i$  at the present time is a power law in energy so that

$$Q_i(\mathcal{E}_o(1+z)) = C_i \mathcal{E}_o^{-a_i} (1+z)^{-a_i} , \quad (8-17)$$

with  $a_i > 2$ . Also assume that

$$f(z) = (1+z)^{b_i} \quad (8-18)$$

Then,

$$j_I = \frac{cn_i(o)}{4\pi H_o} \int_0^{z_{\max}} \frac{C_i dz}{\mathcal{E}_o^{a_i} (1+z)^{a_i+1-b_i}} \quad (8-19)$$

For  $a_i - b_i \neq 1$ , Equation (8-19) becomes

$$j_I = \left[ \frac{cn_i(o)}{4\pi H_o} \left( \frac{C_i}{\mathcal{E}_o^{a_i}} \right) \frac{(1+z)^{b_i-a_i}}{(b_i-a_i)} \right] \Big|_0^{z_{\max}} \quad (8-20)$$

Hence, individual sources with power law spectra of a given slope will yield a power law of the same slope. This aspect of the result (i.e., a power law yields a power law of the same slope) is true even if  $q_o$  is not zero; however, the integral over  $z$  to obtain the multiplying factor is not as simple.

Return to Equation (8-2), and consider the case where  $\Gamma = 0$  for the entire time of the integration; that is the one in which all photons of interest were created before some point in time. Equation (8-2) then becomes

$$\frac{d}{dt} [N(\mathcal{E}_o, t) R^3(t)] = -A \left( \mathcal{E}_o \frac{R(t_o)}{R(t)}, t \right) N(\mathcal{E}_o, t) R^3(t), \quad (8-21)$$

which may be integrated at once to give

$$N(\mathbb{E}_o, t_o) R^3(t_o) = N(\mathbb{E}_o, t_i) R^3(t_i) \times \exp \left[ - \int_{t_i}^{t_o} A \left( \mathbb{E}_o \frac{R(t_o)}{R(t)}, t \right) dt \right]. \quad (8-22)$$

Using Equation (8-4), this equation becomes

$$N(\mathbb{E}_o, t_o) R^3(t_o) = N(\mathbb{E}_o, t_i) \frac{1}{(1+z)^3} \times \exp \left[ - \int_{t_i}^{t_o} A \left( \mathbb{E}_o \frac{R(t_o)}{R(t)}, t \right) dt \right]. \quad (8-23)$$

Thus, the density is decreased with time by both the  $(1+z)^{-3}$  factor and an exponential absorption term.

### THE VALUES OF $H_o$ AND $q_o$

In the equations developed in the last section, in addition to the parameters related to the creation and absorption of the radiation, there are the fundamental parameters  $H_o$  and  $q_o$ . There has been a long effort to determine  $H_o$  well, and there is still a fairly wide range of uncertainty. Current estimates range from 40 to 100  $\text{km s}^{-1} \text{Mpc}^{-1}$  (e.g., Sandage and Tammann, 1976; Bottinelli and Gouguenheim, 1976; Tulley and Fisher, 1977; Branch, 1979; DeVaucouleurs and Bollinger, 1979).

The determination of  $q_o$  is a matter of substantial debate at present. Under the assumption that the cosmological constant,

$\Lambda$ , is zero (Friedmann model),  $q_0$  equals  $\Omega/2$ , where  $\Omega$  is the density parameter defined as  $\rho/\rho_c$  and  $\rho_c$  in turn is the critical density. A number of types of evidence (for example, Tinsley, 1977) combined with recent theoretical work of Schramm and Wagoner (1977) and Young et al. (1979) lead to the conclusion that  $\Omega$  is most likely constrained to the range 0.04 to 0.20 and hence  $0.02 < q_0 < 0.1$ , although some (e.g., Stecker, 1980) believe it could be significantly larger.

One of the stronger arguments in favor of a low density is the current value determined for the deuterium abundance. Of the several approaches for obtaining an estimate of the deuterium abundance, the best one at present is probably that based on the ultraviolet observations obtained with the ultraviolet telescope on the OAO-3 (Copernicus) satellite. Results reported by Rogerson and York (1973), and other, more recent ones, give a deuterium abundance of  $2 \times 10^{-5}$  of hydrogen by weight based on the relative strength of the Lyman absorption lines of interstellar atomic hydrogen and deuterium. If other sources have not contributed significantly to the present deuterium abundance, then this figure represents a lower limit to the primordial (pregalactic) abundance of deuterium relative to hydrogen, and, in turn, leads to a ratio of photons to nuclear particles of  $\gtrsim 1.1 \times 10^9$  in the framework of the standard universe theory. Hence, on the basis of there being about  $5.5 \times 10^5$  photons per liter at present, a nuclear particle density of  $\lesssim 5 \times 10^{-4}$  nuclei per liter is predicted. This number, or an equivalent  $0.8 \times 10^{-30}$  g cm $^{-3}$ , is about an order of magnitude less than the energy density needed to close the universe, since

$$\Omega = \frac{\rho}{\rho_c} = \frac{0.8 \times 10^{-30}}{0.7 \times 10^{-29} (H_0/60)^2} \cong 0.11 \left( \frac{60}{H_0} \right)^2, \quad (8-24)$$

with  $H_0$  in km s $^{-1}$ Mpc $^{-1}$ . Although no one has yet thought of a likely explanation for deuterium production in large quantities other than its being primordial, if it could be generated in significant amounts by other means, then  $\Omega$  could be larger. There is also the possibility that if neutrinos have a finite mass they may make a considerable contribution. However, for the present, it will be assumed that  $\Omega$  does not significantly exceed the value

given in Equation (8-24). It is also worth mentioning that the galactic contribution to  $\Omega$ , generally felt to be the major one, has been estimated by Gott and Turner (1977) to have a best value of about 0.06.

Gott et al. (1974) found that when they combined all the observational constraints within the assumption that  $\Lambda = 0$ , a consistent value of  $\Omega \sim 0.1$  was obtained, together with a value of  $H_0 \sim 60 \text{ km s}^{-1} \text{ Mpc}^{-1}$ . This leads to an age of the universe of  $16 \times 10^9$  years. These values, together with a value for  $q_0$  of 0.05 deduced from the value for  $\Omega$  unless otherwise stated, will be used henceforth.

### MATTER-ANTIMATTER SYMMETRY OR ASYMMETRY

A particularly intriguing question is whether the universe is symmetric in matter and antimatter or whether it is mostly matter. It was noted in the introduction to this chapter that  $\gamma$ -ray astronomy played an important part in showing that matter and antimatter could not be continually created throughout the universe. It also seems very plausible that a galaxy, and probably even clusters of galaxies, should be made entirely of either matter or antimatter. This position is supported by the absence of antimatter in cosmic rays except for the very small amount expected from interstellar interactions.

In the standard big bang cosmology, the matter in the universe consists of the relatively small amount remaining after the early annihilation of much larger amounts of matter and antimatter. There are at least two possible points of view. One is that there is a small asymmetry and the matter that remains represents this asymmetry. The other view is that the universe is symmetric and the matter and antimatter separate at an early stage into what later become clusters, or more likely super-clusters, of galaxies.

The first point of view leads to a rather straightforward conventional development once it is accepted that an excess of matter over antimatter may remain. There is then no major difficulty with physical laws in following the expansion of the universe to its present state. Nonetheless, the initial asymmetry had seemed disturbing to some. Now, however, with the new elementary particle theories involving baryon-nonconserving forces

in grand unified field theories such as SU(5), the baryon symmetry is broken at an early stage in the universe by leptoquark interactions (e.g., Dimopoulos and Susskind, 1978; Ignatiev et al., 1978; Weinberg, 1979), and the observed baryon excess could be a natural consequence.

On the other hand, it is at least aesthetically pleasing to think of an inherently symmetric big bang theory. In this earlier concept of a baryon-symmetric big bang model (Harrison, 1967; Omnes, 1969), while the universe is still above the critical density and temperature, domains containing mostly matter and domains containing mostly antimatter are created. These domains coalesce and ultimately become superclusters of galaxies, having only matter or antimatter since all but the excess annihilates. One of the most significant aspects of this theory is that it predicts an observable diffuse  $\gamma$ -ray emission resulting from matter-antimatter annihilation at the boundaries. When a proton and an antiproton interact, on the average, about five  $\pi$  mesons are formed, of which a third are neutral. The  $\gamma$ -rays resulting from the  $\pi^0$  decays have the typical  $\pi^0$  spectrum with a maximum at 68 MeV and an upper limit of about 1 GeV set by energy conservation. The integrated spectrum can be obtained using Equation (8-14) with the appropriate emission function (Stecker et al., 1971). Since the peak is increasingly redshifted with increasing  $z$  and also increases in intensity with  $z$ , the net result is a spectrum smoothly decreasing with energy above  $\sim 1$  MeV. There is a decrease in the annihilation spectrum below about  $\frac{1}{2}$  MeV caused by absorption and scattering of the  $\gamma$ -rays in interactions with the interstellar medium at early times. The exact spectrum has been calculated by Stecker et al. (1971) and will be seen in Chapter 9 to be in agreement with the experimental data. Electrons and positrons will also annihilate, but the predicted spectrum falls well below the observed hard X-ray diffuse radiation which is believed to result from other sources.

Clearly the agreement between theory and experiment is attractive, but as the next chapter will show, there is also at least one other plausible explanation of the diffuse radiation. Further, whereas the calculation of the  $\gamma$ -ray spectrum is straightforward in the baryon-symmetric big bang theory, there is substantial doubt that the required separation into regions of matter and antimatter which ultimately become superclusters can occur

(see for example, Steigman, 1974). The major problem appears to be that there is too much annihilation leading to too little remaining matter by many orders of magnitude. Even if it is assumed that strong interactions can cause a phase transition in which the nucleons and antinucleons are separated, it appears that the remixing is so efficient that there will still be much too much annihilation.

The baryon-nonconserving forces in the grand unified field theories mentioned earlier represent a way of obtaining a baryon-symmetric universe with superclusters of galaxies of matter and antimatter which may avoid the difficulty described in the last paragraph. As Brown and Stecker (1979) have shown, grand unified field theories lead naturally to a global baryon-symmetric big bang cosmology with a domain structure. The symmetry is then broken at random in casually independent domains, favoring neither a baryon nor an antibaryon excess on a universal scale. It is unclear whether the domains could be large enough to become superclusters of galaxies. The predicted  $\gamma$ -ray spectrum is the same. A piece of evidence favoring this domain-type symmetric cosmology would be the determination that the already observed extragalactic  $\gamma$ -radiation is diffuse on the appropriately fine scale and indeed has the specific predicted energy spectrum.

## REFERENCES

- Bondi, H., and Gold, T., 1948, *Mon. Not. Roy. Ast. Soc.*, **108**, 252.
- Bottinelli, L., and Gouguenheim, L., 1976, *Astron. Astrophys.*, **51**, 275.
- Branch, D., 1979, *Mon. Not. Roy. Ast. Soc.*, **186**, 609.
- Brown, R. W., and Stecker, F. W., 1979, *Phys. Rev. Letters*, **43**, 315.
- Dicke, R. H., Peebles, P. J. E., Roll, P. G., and Wilkinson, D. T., 1975, *Ap. J.*, **142**, 414.
- DeVaucouleurs, G., and Bollinger, G., 1979, *Ap. J.*, **233**, 433.
- Dimopoulos, S., and Susskind, L., 1978, *Phys. Rev.*, **D18**, 4500.
- Gott, J. R., and Turner, E. L., 1977, *Ap. J.*, **213**, 309.
- Gott, J. R., III, Gunn, J. E., Schramm, D. N., and Tinsley, B. M., 1974, *Ap. J.*, **194**, 543.
- Harrison, E. R., 1967, *Phys. Rev. Letters*, **18**, 1011.
- Hoyle, F., 1948, *Mon. Not. Roy. Ast. Soc.*, **108**, 372.
- Ignatiev, A. Yu., Krosnikov, N. V., Kuzmin, V. A., and Tavkhelidze, A. N., 1978, *Phys. Lett.*, **76B**, 436.
- Omnes, R., 1969, *Phys. Rev. Letters*, **23**, 38.
- Peebles, P. J. E., 1971, *Physical Cosmology* (Princeton: Princeton University Press, 1971).
- Penzias, A. A., and Wilson, R. W., 1965, *Ap. J.*, **142**, 1149.

- Rogerson, J. B., Jr., and York, D. G., 1973, *Ap. J. (Letters)*, **186**, L95.
- Sandage, A., and Tammann, G. A., 1976, *Ap. J.*, **210**, 7.
- Schramm, D. N., and Wagoner, R. V., 1977, *Ann. Rev. Nucl. Sci.*, **27**, 37.
- Stecker, F. W., 1980, *Phys. Rev. Letters*, **44**, 1237.
- Stecker, F. W., Morgan, D. L., Jr., and Bredekamp, J., 1971, *Phys. Rev. Letters*, **27**, 1469.
- Steigman, G., 1974, in *Confrontation of Cosmological Theories with Observational Data*, ed. M. S., Longair, IAU Symp. 63 (Dordrecht: Reidel, 1974), p. 347.
- Tinsley, B. M., 1977, *Annals of the New York Academy of Sciences*, **302**, 423.
- Tull, R. B., and Fisher, J. R., 1977, *Astron. Astrophys.*, **54**, 661.
- Weinberg, S., 1972, *Gravitation and Cosmology* (New York: John Wiley and Sons, 1972), p. 469.
- Weinberg, S., 1979, *Phys. Rev. Letters*, **42**, 850.
- Yang, J., Schramm, D. N., Steigman, G., and Rood, R. T., 1979, *Ap. J.*, **277**, 697.



## Chapter 9

# Diffuse Radiation

### INTRODUCTION

A diffuse celestial radiation, which is isotropic at least on a coarse scale, has been measured from the soft X-ray region to about 150 MeV, at which energy the intensity falls below that of the galactic emission for most galactic latitudes. The spectral shape, the intensity, and the established degree of isotropy of this diffuse radiation already place severe constraints on the possible explanations for this radiation. For example, these considerations make a galactic halo model interpretation very unlikely.

Among the extragalactic theories, the more promising explanations of the isotropic diffuse emission appear to be radiation from exceptional galaxies (e.g., Strong et al., 1976; Bignami et al., 1979) or the  $\gamma$ -ray emission (Stecker et al., 1971; Stecker, 1978) from matter-antimatter annihilation at the boundaries of superclusters of galaxies of matter and antimatter in baryon-symmetric big bang models (Harrison, 1967; Omnes, 1969; Brown and Stecker, 1979). Other possible sources for extragalactic diffuse  $\gamma$ -radiation include normal galaxies, clusters of galaxies, primordial cosmic rays interacting with intergalactic matter, primordial black holes, and cosmic ray leakage from galaxies.

### OBSERVATIONS

The first indication that diffuse celestial radiation extended from the X-ray region into at least the low energy  $\gamma$ -ray ( $\sim 1$  MeV)

portion of the spectrum was reported by Arnold et al. (1962). Detectors on the Ranger 3 and Ranger 5 Moon probes saw an apparent flattening of the spectrum between about 1 and 2.5 MeV, the highest energy recorded. This result was also the first indication that significant structure might be present in the spectrum. At energies above 50 MeV, the first measurements were those of Kraushaar and Clark (1962), whose upper limits from Explorer 11 provided an experimental refutation of the steady-state theory of cosmology. Several other upper limits were reported from early balloon experiments, but the first suggestion of a diffuse high energy flux came from the OSO-3 satellite experiment (Clark, Garmire, and Kraushaar, 1968; Kraushaar et al., 1972). The final result of the SAS-2 high energy ( $> 35$  MeV)  $\gamma$ -ray experiment clearly established a high energy extension of the diffuse radiation with a steep energy spectrum above 35 MeV.

The most controversial energy region has been from about 1/2 to 10 MeV, where there is a substantial background, resulting from cosmic ray interactions leading to excited nuclei. The analyses of Trombka et al. (1977) and Daniel and Lavakare (1975) have indicated that many of the early reported results in this energy range were too high because of the failure to eliminate all the background from the measurements. At present, the final results from the Apollo 15 and 16  $\gamma$ -ray detectors (Trombka et al., 1977), which were on a boom of variable length, are generally accepted as a good representation of the diffuse energy spectrum in the intermediate energy range. Although lower in intensity than the earlier reported spectra, it still shows the "hump" in the spectrum near 2 MeV.

The high energy ( $> 35$  MeV) region also deserves special mention not because of the significant detector or locally produced background, which can be very small, but because of the need to separate the galactic diffuse radiation from the general diffuse radiation being discussed here. It has been noted in Chapter 5 that the total diffuse radiation could be separated into two components, by observing it as a function of galactic latitude. Fichtel et al. (1978) have done a much more detailed analysis wherein other galactic radiation such as the 21 cm line and the 150 MHz brightness temperature were compared with the  $\gamma$ -radiation as a function of  $\gamma$ -ray energy for several different galactic longitude regions. There is a good linear correlation among all these radiations. Since the 21 cm radiation which is directly

interpretable in terms of atomic hydrogen column density is known to be almost entirely galactic, an extrapolation of a straight line, relating  $\gamma$ -ray intensity to the 21 cm column density, to zero 21 cm column density gives a measure of the excess  $\gamma$ -ray emission over that related to the galaxy. Figure 9-1 shows that correlation for the highest energy region studied where the residual is at its least, yet it is still clearly there. Moreover, the straight line shown on each subfigure is the same, namely the least squares fit to the combined observations from all the sky intervals with  $|b| \geq 12.8^\circ$ . In this figure the low column density points correspond to high galactic latitudes. Similar results at lower energies showed a larger residual, which within errors was again the same in the several regions of the sky examined. This result implied that the energy spectrum is uniform within uncertainties supporting the concept of a uniform diffuse component. More important, this spectrum is quite different from the galactic spectrum being markedly steeper.

The experimental results for the diffuse  $\gamma$ -emission are shown together in Figure 9-2. The 2 MeV "hump" is obvious. Notice that the high energy isotropic diffuse radiation is much steeper than that associated with the galaxy. The galactic component spectrum shown in the figure is representative of fairly high latitudes; hence, it is unlikely that it will be possible to measure the diffuse radiation above about 200 MeV unless the spectral slope of the isotropic diffuse radiation should become much smaller again at very high energies.

Although the diffuse spectral measurements are reasonably self-consistent, the degree of spatial isotropy is not well known. The X-ray spectrum through about 100 keV is known (cf., Schwartz and Gursky, 1973) to be isotropic to within about 5 percent. At low  $\gamma$ -ray energies ( $\sim 1$  MeV), Trombka et al. (1977) estimate that the anisotropic component from galactic sources does not exceed 20 percent of the total flux. At high energies (35 to 100 MeV), the center-to-anticenter ratio for radiation with  $20^\circ < |b| < 40^\circ$  was measured to be  $1.10 \pm 0.19$  and the perpendicular to the galactic plane intensity to that in the  $20^\circ < |b| < 40^\circ$  region was measured to be  $0.87 \pm 0.09$ ; each of these results is consistent with isotropy to within errors (Fichtel et al., 1978). Although much more precise measures of the isotropy are clearly desired, no evidence for a major anisotropy

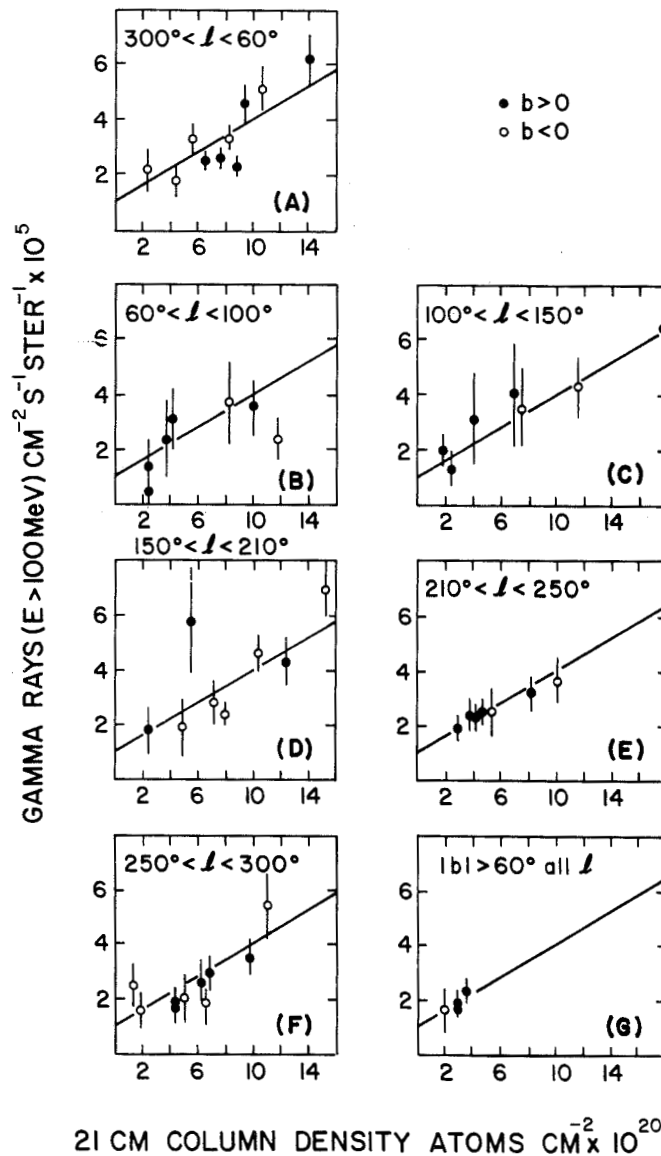


Figure 9-1. Distribution of  $\gamma$ -ray ( $E \geq 100 \text{ MeV}$ ) intensity as a function of atomic hydrogen column density deduced from 21 cm radio data for  $|b| > 12.8^\circ$  for the indicated longitude and latitude intervals. Error bars shown on the  $\gamma$ -ray intensities are statistical. An uncertainty of approximately 10 percent should be attached to the 21 cm column densities. The solid line is the best fit to all the data points shown (Fichtel et al., 1978).

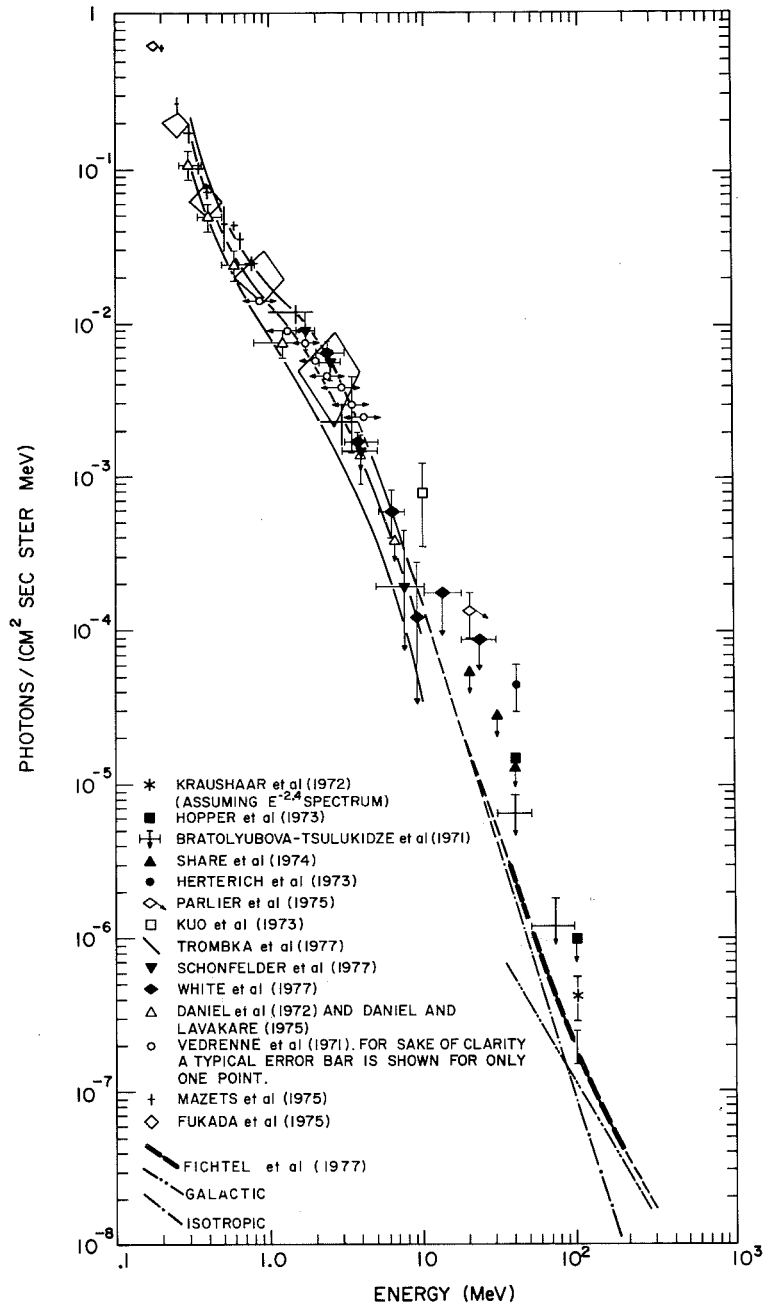


Figure 9-2. Experimental results on the energy spectrum of the general diffuse  $\gamma$ -radiation.

exists. In particular, the high energy  $\gamma$ -ray results just quoted eliminate a spherical galactic halo origin for the radiation in view of the Sun's great distance from the galactic center. In the future trying to establish the level of isotropy, or deviations there from, on both a coarse scale and a fine scale will be important. Some of the possible fine scale deviations will be apparent in the following discussion of possible sources.

## POSSIBLE CONTRIBUTORS TO THE DIFFUSE RADIATION

A wide variety of explanations for the diffuse radiation have been proposed. The last section showed that the galactic halo model of the origin was eliminated by the already existing measurements on spatial uniformity. The intensity and energy spectrum are also important constraints for any potential explanation of this radiation. Two currently attractive proposed origins are the baryon-symmetric big bang model, discussed in Chapter 8, and active galaxies, which were described in Chapter 7. These and several other possibilities will be considered below.

### Baryon-Symmetric Big Bang

The concept of baryon-nonconserving forces in the grand unified field theory has created new interest in the possibility of a baryon-symmetric universe, containing superclusters of galaxies of matter and others of antimatter. The annihilation of nucleons and antinucleons at the boundaries leads the  $\gamma$ -ray spectrum shown in Figure 9-3, taken from the work of Stecker et al. (1971). The shape of the spectrum is determined by the interaction process and the cosmological integration as was explained in Chapter 8. Whereas the normalization was selected to have the curve agree with the data, it is consistent with the currently accepted possible range of densities between clusters.

Generally, this theoretical model predicts a smooth distribution over the sky; however, a test of this theory (in addition to a precise measure of the energy spectrum) would be the detection of fairly small enhancements in the  $\gamma$ -radiation in the direction of boundaries between close superclusters of galaxies. The diffuse  $\gamma$ -radiation associated with these particular boundaries would be at the higher energies where the diffuse radiation inten-

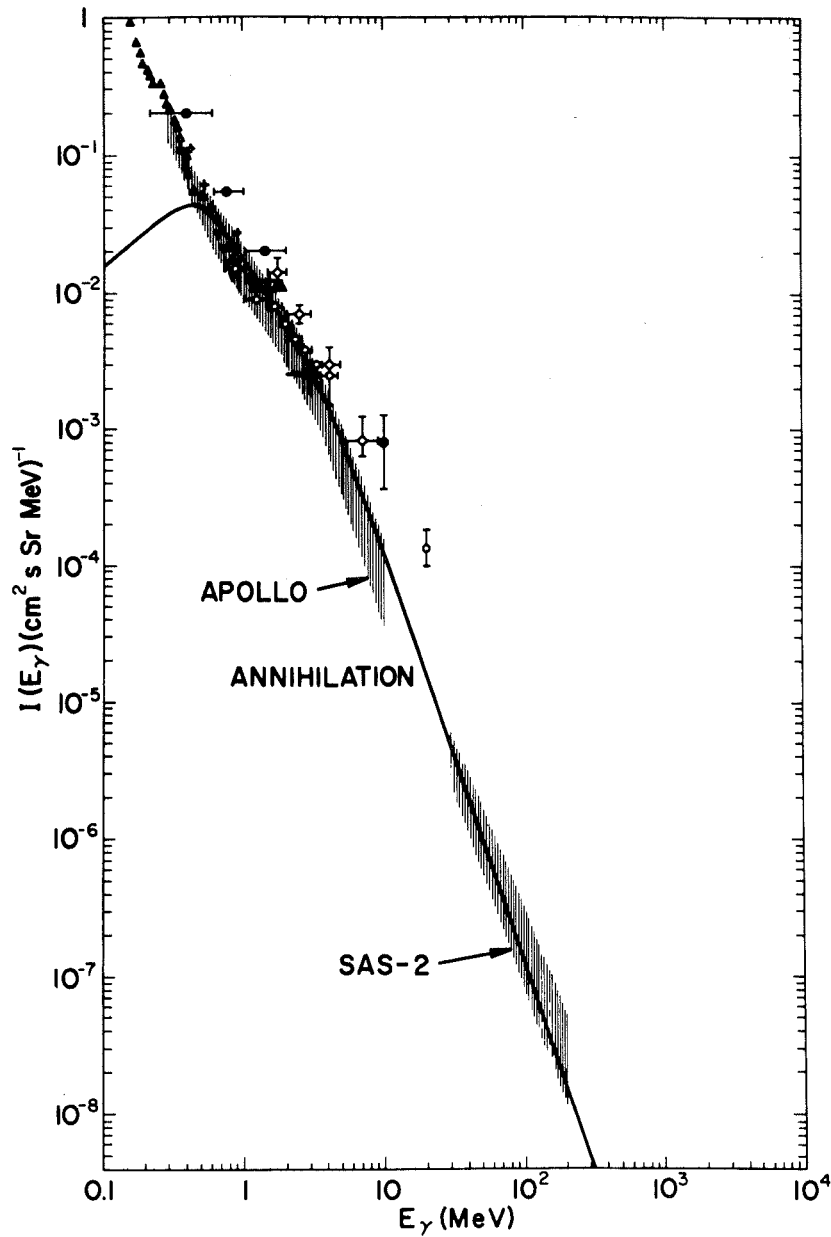


Figure 9-3. The diffuse  $\gamma$ -ray energy spectrum calculated to be produced by the annihilation of nucleons and antinucleons at the boundaries of superclusters of galaxies in the baryon-symmetric big bang cosmology (Stecker et al., 1971). The experimental data are largely the same as those in Figure 9-2 (many upper limits are not shown in this case). See text for a discussion of the theoretical curve.

sity begins to fall below that of the galactic radiation, even at high latitudes. Calculations show, however, that with future high sensitivity  $\gamma$ -ray telescopes there is reasonable hope of seeing these ridges if they exist. The search for these ridges is important in relation to clarifying the current picture of cosmology, since there are so few possible tests of whether our universe is baryon-symmetric or not on this scale.

### Seyfert Galaxies

Seyfert galaxies are the first of several active galaxies which will be discussed here as possible contributors to the diffuse  $\gamma$ -radiation. As was noted in Chapter 7, a typical X-ray spectrum seems not to exist for Seyfert galaxies, but the data at  $\gamma$ -ray energies other than that from NGC 4151 is restricted to upper limits. Nonetheless, all the data are at least consistent with a change in spectral shape in the low energy  $\gamma$ -ray region. Some theoretical reasons exist for believing that a sharp change in spectral shape might occur in this energy range. Further, the other two active galaxies for which there are data, CEN-A and 3C 273, also show this type of spectral change. To anticipate the later conclusions, in the 1 to 50 keV region, active galaxies cannot account for the unresolved diffuse emission by approximately an order of magnitude at 10 keV, as has been shown previously, for example, by Elvis et al. (1978) and Boldt (1978). Yet, if the spectral slope were to remain constant to higher energies, the predicted diffuse radiation would equal that which is observed at a few MeV and exceed it above that energy. Hence, a major spectral slope change is implied.

With this discussion in mind, it seems worth pursuing the question of the possible importance of the contribution of Seyfert galaxies to the  $\gamma$ -ray diffuse radiation a little further, in spite of the very limited data. Employing the general approach of Bignami et al. (1979), although differing in a few numerical values, the following analytical function for the spectrum which is selected describes one power law changing smoothly to another:

$$Q_i(E) = \frac{A_i}{E^{a_i} \left[ 1 - (E/E_{oi})^{b_i - a_i} \right]} \quad (9-1)$$

At this stage of development there is not enough  $\gamma$ -ray information to develop a luminosity function so “ $A_i$ ” and “ $a_i$ ” are determined from the X-ray luminosity (2 to 10 keV) and spectral shape, respectively. For Seyfert galaxies they will be estimated as  $3.9 \times 10^{46}$  photons  $\text{keV}^{-1} \text{s}^{-1} \text{source}^{-1}$  (based on a 2 to 10 keV X-ray luminosity of  $2 \times 10^{43}$  ergs  $\text{s}^{-1}$ ) and 1.7, respectively. At present  $E_{oi}$  is chosen to be in the range 0.5 to 3 MeV, and  $b_i$  is chosen to be 4.0 to give the high energy slope discussed for NGC 4151 in Chapter 7. (NGC 4151 has a relatively flat energy spectrum in the X-ray range.)

Equation (8-12) may now be used to estimate the contribution of Seyfert galaxies to the diffuse  $\gamma$ -radiation. For Seyferts,  $N_i$  is taken to be  $1 \times 10^{-5} \text{Mpc}^{-3}$  (Elvis et al., 1978; Schmidt, 1978). Following the discussion in Chapter 8,  $z_{\text{max}}$  will be estimated to be 4,  $H_0$  to be  $60 \text{ km s}^{-1}$ , and  $q_0$  to be 0.05. Figure 9-4 shows the result of the cosmological integration for  $f(z) = 1$ , that is no evolution. If the assumptions are valid, there clearly cannot have been a large evolutionary factor, since, below 1 MeV, these active galaxies are predicted to be making a notable contribution even with no evolution. In the  $\gamma$ -ray region, the situation is uncertain, and must remain so until further information becomes available.

### Quasars

As was noted in Chapter 7, the extraordinary power radiated by quasars makes them of very special interest; however, the data which exist for quasars is very limited not only in the  $\gamma$ -ray field, but also in the hard X-ray regime. Matters are further complicated by the variability in the X-ray emission observed at least for 3C 273. It is, nonetheless, worth considering the possible contribution of these unique objects to the diffuse background. It was seen in Chapter 7 that the quasar 3C 273 had a spectral shape that was consistent with the expression represented in Equation (9-1) with  $a_q = 1.4$ ,  $b_q = 2.7$ , and  $A_q = 2 \times 10^{51}$  photons  $\text{s}^{-1} \text{keV}^{-1} \text{source}^{-1}$ . The value of  $A_q$  is based on a 2 to 10 keV luminosity which is half the maximum emission of 3C 273, or  $5 \times 10^{45}$  ergs  $\text{s}^{-1}$ .

Particularly considering the recent HEAO-2 soft X-ray results (Tananbaum et al., 1979), which show that quasars have

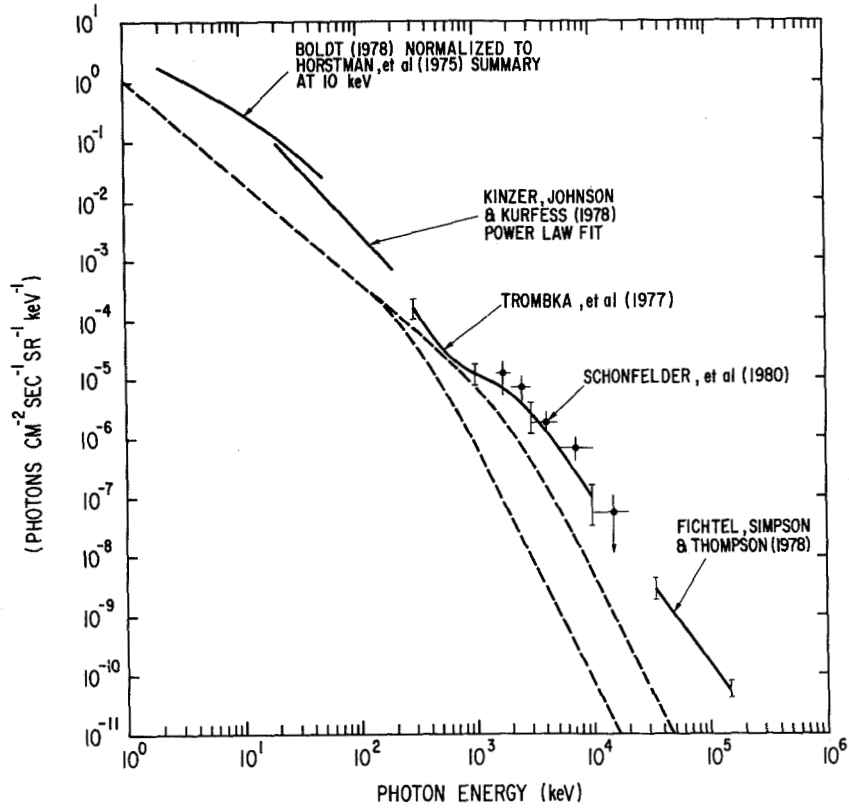


Figure 9-4. The diffuse  $\gamma$ -ray energy spectrum estimate for Seyfert galaxies under the assumptions described in the text, compared to some of the more recent experimental data.

been observed back to  $z = 3.2$ , and that there is a general correlation between X-ray and optical luminosity, it seems reasonable to apply an evolutionary function consistent with the optical, X-ray, and radio data to the study of the contribution of quasars to the high energy diffuse radiation. Wills and Lynds (1978) have shown that a number density law for quasars which provides an acceptable fit to the experimental data, that is largely associated with a value of  $z$  from about  $1/2$  to  $2$ , is as follows:

$$\rho = \rho_0 \exp(\beta\tau) \quad , \quad (9-2)$$

where  $\tau$  is the look-back time expressed as a fraction of the age of the universe. Following the work of Schmidt (1978)  $\beta$  will be estimated as 10 and  $\rho_0$  will be estimated as  $0.1 \text{ Gpc}^{-3}$ , on the basis of the spatial densities that he gives for quasars with flat radio spectra of  $0.05 \text{ Gpc}^{-3}$  for those with more than  $10^{47}$  ergs  $\text{s}^{-1}$  and  $0.3 \text{ Gpc}^{-3}$  for those with more than  $10^{46}$  ergs  $\text{s}^{-1}$ . These values lead to a low energy X-ray flux consistent with the observations mentioned previously. It should be mentioned that the density law  $\rho = \rho_0 (1+z)^n$ , which has often been used in the past particularly with  $n = 6$ , does not now appear to agree well with the data, as has been noted for example by Wills and Lynds (1978).  $\rho/\rho_0$  is the  $f(z)$  of Equation (8-12). The relationship between  $\tau$  and  $z$  is complex, and the reader is referred to the work of Weinberg (1972).

Using these values and functions in Equations (8-12), the estimated contribution of quasars to the diffuse radiation is calculated and shown in Figure 9-5. It is seen that within the present relatively large uncertainties, when evolution is considered in the framework of standard cosmology, quasars may account for a major part, if not most, of the diffuse  $\gamma$ -radiation ( $E > \text{few MeV}$ ). In the X-ray region it seems more likely that another, more important component exists.

Unfortunately, data to provide a clear picture of the importance of the  $\gamma$ -ray contribution to this universal radiation are not expected until the later half of the 1980's. It is at least conceivable that their contribution may be dominant, and it will be possible to ask in a meaningful way the question, "What evolutionary factor is compatible with the observations and the above assumptions?"

### Other Active Galaxies

Three other types of active galaxies deserve to be mentioned. These are BL Lacertae objects, emission line galaxies, and radio galaxies not included in one of the other categories already discussed. BL Lacertae objects are thought possibly to be similar to quasars. Their spatial density, however, appears to be only 1 to 10 percent that of quasars (Schmidt, 1978), although very

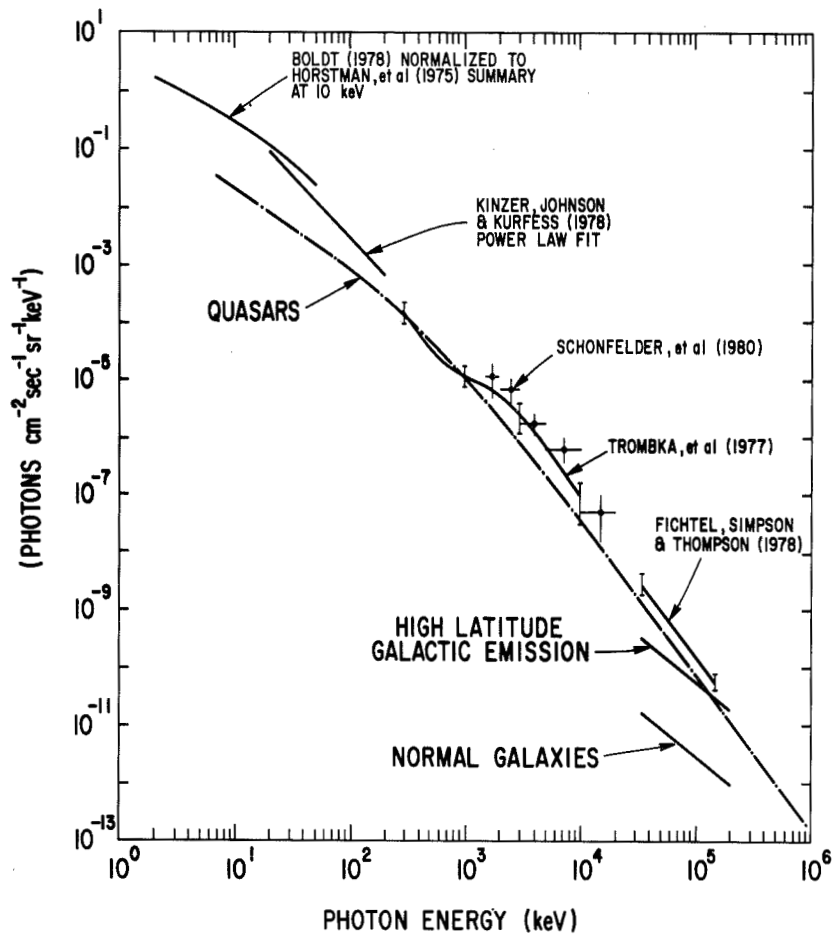


Figure 9-5. The diffuse  $\gamma$ -ray energy spectra estimated for quasars and normal galaxies under the assumptions described in the text, compared to some of the more recent experimental data.

limited X-ray data suggest that they may be more numerous relative to the corresponding quasars than is allowed by this range (Schwartz et al., 1978). Their luminosity in the X-ray region, based on a very small sample, seems to be only 1 to 10 percent that of quasars. They seem to be quite variable in the X-ray region (Mushotzky et al., 1978a), but the sample is small. There have been no  $\gamma$ -ray observations of BL Lacertae objects, and Bignami et al. (1979) report several significant upper limits. For the present, at least, the limited data suggest BL Lacertae objects probably make a much smaller contribution than quasars. Similar considerations suggest that other radio galaxies and emission line galaxies also make a small contribution.

### Normal Galaxies

The attempt to determine the contribution of normal galaxies to the diffuse radiation is complicated by the fact that whereas a good estimate exists for the  $\gamma$ -ray luminosity for one galaxy, our own, only upper limits exist for any others. As discussed earlier, the upper limits are consistent with the intensities that would be predicted on the basis of the emission from our galaxy, as estimated from the  $\gamma$ -ray measurements obtained with the SAS-2 satellite (Fichtel et al., 1975; Kniffen et al., 1977). Normal galaxies also represent a possibility to be considered because they are very numerous compared to active galaxies.

In order to proceed, it will be assumed that the  $\gamma$ -ray luminosity of our galaxy discussed in Chapter 7 is typical in terms of both intensity and energy spectrum. The density of galaxies at the present time is taken to be  $2 \times 10^{-2} \text{ Mpc}^{-3}$ . Several more sophisticated approaches have been used, including some which assume that the optical luminosity and  $\gamma$ -ray luminosity are proportional; however, because of the present limited knowledge and because these other approaches give very similar results, the simple approach mentioned above seems appropriate here. A more difficult problem is the determination of the evolution function. If the galaxies have remained much as they are now from birth,  $f(z)$  is approximately 1, but not quite since the blackbody radiation was more intense in the past. However, since the blackbody Compton radiation is presently a small part of the total, and  $z_{\text{max}}$  is only about four, this effort does not cause a

a major increase. If galaxies had more diffuse matter in the past and correspondingly stronger magnetic fields, they could hold more cosmic rays and the  $\gamma$ -ray luminosity from cosmic ray matter interactions could have been larger. Also, there could have been more or less  $\gamma$ -ray point sources in the past. Mostly because there is no compelling argument to do otherwise,  $f(z)$  will be chosen to be 1.

Using these values in Equation (8-12) the estimated contribution of normal galaxies to the diffuse radiation is calculated and shown in Figure 9-5. This result is very similar to those obtained previously by several authors (e.g., Kraushaar et al., 1972; Strong et al., 1976; Lichti et al., 1978; and Fichtel et al., 1978). Notice that the predicted intensity falls about an order of magnitude below the observed high latitude radiation that is attributed to galactic radiation alone. The predicted spectral shape is, of course, similar because the origin was assumed to be the same. An upper limit to the contribution would probably be about one-third of the radiation now believed to be galactic in view of the latter's good correlation with matter and galactic latitude. It is more likely that normal galaxies do not make a detectable contribution to the diffuse  $\gamma$ -radiation even at high energies where they might be contributing more than active galaxies. It should be remembered, however, that active galaxies may have a high energy component about which nothing is known at present.

### Clusters of Galaxies

This possible contribution deserves attention primarily because of results obtained in the X-ray domain, since there is no evidence yet for  $\gamma$ -ray emission from clusters of galaxies. Clusters of galaxies have been identified as strong sources of large scale X-ray emission (e.g., Gursky et al., 1971; Cash et al., 1976; Gorenstein et al., 1977; Mushotzky et al., 1978b) with the intensity in some cases being as much as two orders of magnitude greater than would be expected on the bases of the number of galaxies in the cluster, and X-ray emission from each galaxy being similar to our own. It is also now thought that the X-ray emission of our galaxy is larger than the average. The size of the emission region seems to be consistent with the dimensions of the clusters of galaxies, and the energy spectra are in good agreement with a

thermal origin for the radiation (e.g., Mushotzky et al., 1978b). The Perseus cluster, which is the brightest X-ray source, for example, has a spectrum which is characteristic of a plasma at a temperature of about 80 million degree. Pravdo et al. (1979) have found that the optically richest clusters of galaxies are not exceptional in the X-ray region. When the contribution of these clusters to the diffuse X-ray background is considered, it is estimated that they would contribute only a few percent; and, further, the calculated spectrum is quite different from the observed diffuse spectrum.

With regard to the  $\gamma$ -ray region, the steeply falling spectrum in the hard X-ray region, the relatively small estimated contribution to the diffuse background in the X-ray region, and the nature of the radiation implied by the spectral shape give no reason to believe that there will be a significant contribution to the diffuse background in the  $\gamma$ -ray region from clusters of galaxies.

### Galactic Cosmic Ray Leakage

When early measurements of the diffuse X-ray and  $\gamma$ -ray spectrum suggested a single power law description, several proposals were forthcoming to explain the spectrum on the basis of cosmic ray interactions in intergalactic space. An inverse Compton model was one of these wherein the cosmic ray electrons interacted with the newly discovered  $2.7^\circ$  blackbody radiation. However, now this concept is not thought to be very likely, both on energetic grounds, since the required electron number could arise from normal galaxies only if galactic trapping times are very low, and from the point of view that rapid leakage of the electrons through galactic magnetic fields would seem unrealistic and inconsistent with the now-known age of cosmic rays, at least in the local region of our galaxy.

Nonthermal bremsstrahlung of electrons interacting with low density intergalactic gas has also been proposed, but this model would require a large ad hoc intensity of subrelativistic intergalactic cosmic rays produced in a burst at  $z \simeq 10$ . These and other early models for the low energy spectrum are reviewed by Silk (1970). The spectral shape, as it now appears to be, causes further difficulties for galactic cosmic ray leakage models, although some attempts have been made to explain the spectral shape.

### Primordial Cosmic Rays

Another early attempt to explain the diffuse  $\gamma$ -ray emission, but not the X-ray region, involved cosmic ray nucleon interactions with intergalactic matter. Because of the high intensity required, the cosmic ray nucleons would almost certainly have to be primordial. The 1 MeV feature in this model results from  $\pi^0$  decay  $\gamma$ -rays from intergalactic cosmic rays interacting with the intergalactic gas integrated back to  $z_{\text{max}} \simeq 100$ . The major problems with this picture, in addition to the fact that the required cosmological cosmic ray density is very high, are that  $z_{\text{max}}$  is an arbitrary factor, and the spectral shape seems to be not quite correct, although the latter is not yet a serious disagreement.

### Primordial Black Holes

The primordial black holes postulated by Page and Hawking (1976) can evaporate via a particle tunneling process at an accelerating rate that ends in an explosive  $\gamma$ -ray burst. The time at which this burst occurs is inversely proportional to the black hole mass. A  $10^{15}$  gram primordial black hole formed at the time of the big bang would just now be exploding with a burst of  $\gamma$ -rays whose average energy and duration are about 100 MeV and about  $10^{-7}$  s respectively, although these numbers are somewhat model dependent. These events are predicted to be significantly harder and faster than the low energy  $\gamma$ -ray bursts observed (e.g., Klebesadel et al., 1973). The primordial black hole bursts, should they occur, when integrated over all  $z$  could produce the diffuse background, and the spectral shape would then place constraints on the primordial black hole mass spectrum and the evaporation process. The observed spectral shape does appear to create some difficulty; however, the most significant test of this model and upper limit for the local density of primordial black holes thus far has been the optical light flash and atmospheric Cerenkov experiment of Porter and Weekes (1977). This experiment limited the density of objects providing bursts at  $\geq 200$  MeV and durations  $< 10^{-7}$  s to  $\leq 10^9$   $\text{pc}^{-3}$ , and, for the assumed burst parameters, would seem to eliminate primordial black holes as being a significant source of the diffuse radiation. However, in view of the uncertain mass spectrum and burst characteristics to be

expected for these objects, they cannot yet be eliminated with complete certainty.

### SUMMARY

Whereas the general intensity level of the diffuse  $\gamma$ -radiation, its approximate spectral shape, and its isotropy on a very coarse scale appear established, it would be very desirable to have better measurement of the energy spectrum particularly in the 0.5 to 20 MeV range, and to determine the degree of isotropy on a fine scale.

At present, two general models appear most promising. These are the model of  $\gamma$ -ray emission from matter-antimatter interactions in the baryon-symmetric big bang picture, and the model involving  $\gamma$ -radiation from active galaxies integrated back to their formation. Improved knowledge of the degree of isotropy and future measurements of the  $\gamma$ -radiation from active galaxies can clearly differentiate between these two models. It is hoped that the needed observation will be forthcoming in the second half of the 1980's with the Space Shuttle generation of experiments.

## REFERENCES

- Arnold, J. R., Metzger, A. E., Anderson, E. C., and VanDilla, M. A., 1962, *J. Geophys. Res.*, **67**, 4878.
- Bignami, G. F., Fichtel, C. E., Hartman, R. C., and Thompson, D. J., 1979, *Ap. J.*, **232**, 649.
- Boldt, E. A., 1978, NASA TM-78106, *The Diffuse Component of the Cosmic X-Radiation*.
- Bratolyubova-Tsulukidze, L. E., Grigorov, N. L., Kalinkin, L. F., Melioransky, A. S., Pryakhin, Ye. A., Savenko, I. A., Yufarkin, V. Ya., 1971, *Geomagnetism and Aeronomy (Soviet)*, **11**, 585.
- Brown, R. W., and Stecker, F. W., 1979, *Phys. Rev. Letters*, **43**, 315.
- Cash, W. C., Maline, R. F., and Wolff, R. S., 1976, *Ap J. (Letters)*, **209**, L111.
- Clark, G. W., Garmire, G. P., and Kraushaar, W. L., 1968, *Ap. J. (Letters)*, **153**, L203.
- Daniel, R. R., and Lavakare, P. J., 1975, *Proc. of the 14th Int. Cosmic Ray Conf.*, **1**, 23.
- Daniel, R. R., Joseph, G., and Lavakare, P. J., 1972, *Ap. and Space Science*, **18**, 462.
- Elvis, M., Maccacaro, T., Wilson, A. S., Ward, M. J., Penston, M. V., Fosbury, P. A. E., and Perola, G. C., 1978, *Mon. Not. Roy. Ast. Soc.*, **183**, 129.
- Fichtel, C. E., Hartman, R. C., Kniffen, D. A., Thompson, D. J., Bignami, G. F., Ogelmen, H. B., Ozel, M. E., and Tumer, T., 1975, *Ap. J.*, **198**, 163.
- Fichtel, C. E., Simpson, G. A., and Thompson, D. J., 1978, *Ap. J.*, **222**, 833.

- Fukada, Y., Hayakawa, S., Kasahara, I., Mokine, F., and Tanaka, Y., 1975, *Nature*, **254**, 398.
- Gorenstein, P., Fabricant, D., Topka, K., Tucker, W., and Harnden, F. R., Jr., 1977, *Ap. J. (Letters)*, **216**, L95.
- Gursky, H., Kellogg, E., Murray, S., Leong, C., Tananbaum, H., and Giacconi, R., 1971, *Ap. J. (Letters)*, **167**, L81.
- Harrison, E. R., 1967, *Phys. Rev. Letters*, **18**, 1011.
- Herterich, W., Pinkau, K., Rothermel, H., and Sommer, M., 1973, *Proc. of the 13th Int. Cosmic Ray Conf.*, **1**, 21.
- Hopper, V. D., Mace, O. B., Thomas, J. A., Albats, P., Frye, G. M., Jr., Thomson, G. B., and Staib, J. A., 1973, *Ap. J. (Letters)*, **186**, L55.
- Klebesadel, R. W., Strong, I. B., and Olsen, R. A., 1973, *Ap. J. (Letters)*, **182**, L85.
- Kniffen, D. A., Fichtel, C. E., and Thompson, D. J., 1977, *Ap. J.*, **213**, 765.
- Kraushaar, W. L., and Clark, G. W., 1962, *Phys. Rev. Letters*, **8**, 106.
- Kraushaar, W. L., Clark, G. W., Garmire, G. P., Borken, R., Higbie, R., Leong, C., and Thorsos, T., 1972, *Ap. J.*, **177**, 341.
- Kuo, F., Frye, G. M., Jr., and Zych, A. D., 1973, *Ap. J. (Letters)*, **186**, L51.
- Lichti, G. G., Bignami, G. F., and Paul, J. A., 1978, *Astrophys. and Sp. Sci.*, **56**, 403.
- Mazets, E. P., Golenetskii, S. V., Il'inskii, V. N., Gur'yan, Yu. A., and Kharitonova, T. V., 1975, *Astrophys. and Sp. Sci.*, **33**, 347.

- Mushotzky, R. F., Boldt, E. A., Holt, S. S., Pravdo, S. H., Serlemitsos, P. J., Swank, J. H., and Rothschild, R. H., 1978a, *Ap. J. (Letters)*, **226**, L65.
- Mushotzky, R. F., Serlemitsos, P. J., Smith, B. W., Boldt, E. A., and Holt, S. S., 1978b, *Ap. J.*, **225**, 21.
- Omnes, R., 1969, *Phys. Rev. Letters*, **23**, 38.
- Page, D. N., and Hawking, S. W., 1976, *Ap. J.*, **206**, 1.
- Parlier, B., Forichon, M., Montmerle, T., Agrinier, B., Boella, G., Scarsi, L., Mel, M., and Palmeira, R., 1975, *Proc. of the 14th Int. Cosmic Ray Conf.*, **1**, 14.
- Porter, N., and Weekes, T., 1977, *Ap. J.*, **212**, 224.
- Pravdo, S. H., Boldt, E. A., Marshall, F. E., McKee, J., Mushotzky, R. F., Smith, B. W., and Reichert, G., 1979, *Ap. J.*, **234**, 1.
- Schmidt, M., 1978, *Physica Scripta*, **17**, 135.
- Schönfelder, V., Graser, U., and Daugherty, J., 1977, *Ap. J.*, **217**, 306.
- Schönfelder, V., Graml, F., and Penningsfeld, F. P., 1980, *Ap. J.*, **240**, 350.
- Schwartz, D. A., and Gursky, H., 1973, *Gamma Ray Astrophysics*, ed. F. W. Stecker and J. I. Trombka, NASA SP-339.
- Schwartz, D. A., Bradt, H., Doxsey, R., Griffiths, R., Gursky, H., 1978, *Ap. J. (Letters)*, **224**, L103.
- Share, G. H., Kinzer, R. L., and Seeman, N., 1974, *Ap. J.*, **187**, 511.
- Silk, J., 1970, *Space Sci. Rev.*, **11**, 671.
- Stecker, F. W., 1978, *Nature*, **273**, 493.

- Stecker, F. W., Morgan, D. L., Bredekamp, J., 1971, *Phys. Rev. Letters*, **27**, 1469.
- Strong, A. W., Wolfendale, A. W., and Worrall, D. M., 1976, *J. Phys. A: Math Gen.*, **9**, 1553.
- Tananbaum, H., Avni, Y., Branduardi, G., Elvis, M., Fabbiano, G., Feigelson, E., Giacconi, R., Henry, J. P., Pye, J. P., Soltan, A., and Zamorani, G., 1979, *Ap. J. (Letters)*, **234**, L9.
- Trombka, J. I., Dyer, C. S., Evans, L. G., Bielefeld, M. J., Seltzer, S. M., and Metzger, A. E., 1977, *Ap. J.*, **212**, 925.
- Vedrenne, G., Albernhe, F., Martin, I., and Talon, R., 1971, *Astron. Astrophys.*, **15**, 50.
- Weinberg, S., 1972, *Gravitation and Cosmology* (New York: John Wiley and Sons, 1972), p. 469.
- White, R. S., Daton, B., Moon, S. H., Ryan, J. M., Wilson, R. B., Zych, A. D., 1977, *Ap. J.*, **218**, 920.
- Wills, D., and Lynds, R., 1978, *Ap. J., Supp.*, **36**, 317.
- Zanrosso, E. M., Long, J. L., Zych, A. D., Gibbons, R., White, R. S., and Dayton, B., 1979, *Proc of the 15th Int. Cosmic Ray Conf.*, **1**, 112a.



# **PART V**

# **INSTRUMENTATION**

*Chapter 10*  
*Gamma Ray Interaction Processes*

*Chapter 11*  
*Detectors for Energies Less Than 10 MeV*

*Chapter 12*  
*Detectors for Energies Greater Than 10 MeV*

*Chapter 13*  
*Analysis of Observational Spectra*

---



## PART V

# INSTRUMENTATION

*The astrophysical information which is discussed in this book and is needed for the interpretation relative to various theoretical models depends on the proper analysis of observations of the  $\gamma$ -ray photon energy spectra, intensity, and angular distribution obtained with  $\gamma$ -ray telescopes with spectroscopic capability. In understanding the data obtained from these  $\gamma$ -ray instruments, it is important to know the relationship between the energy loss spectrum and the estimates of the photon energies, the efficiency as a function of energy, the accuracy of the estimate of the photons arrival direction, and the interrelationship between all these factors. Especially in the low energy region, the methods of conversion from energy loss space to photon energy and direction space can only be developed by understanding in detail the interactions of  $\gamma$ -rays with the detector materials as both a function of the photon energy and of the angular distribution of the incident photon flux. Furthermore, the  $\gamma$ -ray fluxes of interest in low energy  $\gamma$ -ray astrophysics are rather small relative to the background produced by charged and neutral particles and unwanted  $\gamma$ -rays. Spectrometer design will be further influenced by attempting to obtain systems with optimum sensitivity.*

*In Chapter 10, the major interaction processes of importance in the construction of  $\gamma$ -ray spectrometers are considered. Detector materials and designs are dependent on the energy domain of interest. Thus two chapters are devoted to the detector systems, Chapter 11 for detector systems used in the energy domain less than about 10 MeV and Chapter 12 for detector*

*systems used in the energy domain greater than about 10 MeV. There has been no attempt to evaluate all the spectrometer systems either flown or proposed for spaceflight. A number of flight systems are considered which we believe demonstrates general principles used in spectrometer design. Finally, in Chapter 13 a number of methods for deriving photon spectra from energy loss spectra are presented and the problem of background interferences in the spaceflight environment is considered.*

## Chapter 10

# Gamma Ray Interaction Processes

### INTRODUCTION

Gamma ray detection in the energy region above 1 keV involves measurements of the energy exchange or energy loss between the  $\gamma$ -rays and the mass of the detector. In most cases of interest, it is the kinetic energy imparted to charged particles by the  $\gamma$ -ray which is lost in the detector and measured in order to obtain spectral knowledge of the incident  $\gamma$ -ray flux. Furthermore, the angular relationship between the incident  $\gamma$ -ray photon and the direction of the secondary particles contains important energy information.

We begin by considering the interaction  $\gamma$ -ray removal processes in matter. This interaction removal process is characterized by the fact that each  $\gamma$ -ray photon is removed individually from the incident beam. By removal we mean either total absorption or removal from the energy group. The number of photons removed in this manner is proportional to the thickness of matter traversed. In the one dimensional case then

$$I = -\mu I_0 \Delta X \quad , \quad (10-1)$$

where  $\mu$  is a constant,

$\Delta X$  is the distance traversed in matter,

$I_0$  is the number flux for the incident beam, and

$I$  is the number flux after the beam has traversed a distance  $X$ .

Upon integration, one obtains of course

$$I = I_0 e^{-\mu x} . \quad (10-2)$$

The product  $\mu x$  is dimensionless. With this in mind a number of removal cross sections or coefficients can be defined. If the dimension term  $X$  is expressed in cm then  $\mu$  is expressed in  $\text{cm}^{-1}$ , the linear absorption coefficient is numerically equal to the fractional number of photons removed per cm of absorber. Now the dimension unit can also be expressed as  $x\rho^{-1}$  where  $\rho$  is the density of the material; the dimension of the product is then  $\text{gm cm}^{-2}$ . The mass absorption coefficient  $\mu\rho^{-1}$  has the dimensions  $\text{cm}^2 \text{ gm}^{-1}$ . The mass absorption coefficient is equal to the fractional reduction in photon intensity produced by 1 cm of absorber. An electronic absorption coefficient can also be defined as  $\mu(\rho N_0)^{-1}$  with units  $\text{cm}^2/\text{electron}$ .  $N_0$  is Avagadro's number.

Another term of interest in the attenuation of  $\gamma$ -rays is the range. Regarding the number flux, this term can be considered equal to the inverse of the mass absorption coefficient and is thus expressed in terms of  $\text{gm cm}^{-2}$ ; hence, this term reflects the photon range which reduces the flux by a factor of  $e^{-1}$ .

The change in the number flux has been considered above. In the energy region being considered here, there are basically three processes by which  $\gamma$ -rays may interact with matter and be removed from the incident beam: the photoelectric effect, Compton scattering, and pair production. These processes act independently of each other and thus the total interaction cross section can be separated into three parts; the photoelectric effect cross section,  $\tau$ ; the Compton scattering cross section,  $\sigma$ ; and the pair production cross section,  $\chi$ . Thus

$$\mu = \tau + \sigma + \chi . \quad (10-3)$$

The removal processes have just been considered but what is important in considering  $\gamma$ -ray detectors is the amount of  $\gamma$ -ray energy lost in the detector. Some of the more important loss mechanisms will be discussed in this chapter. These processes

will be considered in terms of the three major interaction processes. Detailed considerations of the interaction and processes and cross sections have been given by Bethe and Ashkin (1953), Heitler (1954), Rossi (1956), Davisson (1968), Hubbell (1969), Hubbell (1977), and Hubbell et al. (1980).

Table 10-1 lists briefly the most important energy loss processes of  $\gamma$ -ray detectors. In the following sections an outline only of the mechanisms will be presented in order to provide the background needed to understand the analysis and the operations of the detector systems which will be discussed in the following two chapters.

**Table 10-1**  
**Gamma Ray Energy Loss Processes of Importance with Respect to**  
**the Detection of Gamma Rays in the  $> 1$  keV Energy Domain**

- 
- I. Principal energy loss processes
    - 1. Photoelectric effect
    - 2. Pair production
    - 3. Compton scattering
  
  - II. Important secondary energy loss processes
    - 1. Fluorescence radiation
    - 2. Annihilation radiation
    - 3. Electron leakage or escape
    - 4. Bremsstrahlung
- 

By single or multiple interaction processes mentioned above, either all or part of the  $\gamma$ -ray energy can be absorbed by matter. One can find methods for calculating this energy loss mechanism (e.g., Rossi, 1956; Goldstein, 1959). Two further terms, relative to the absorption of  $\gamma$ -ray energy need to be presented. The energy absorption coefficient  $\mu_a$  is given by

$$\mu_a = (\bar{\epsilon}/\epsilon) \mu \quad (10-4)$$

where  $\bar{\epsilon}$  is the average energy loss of photons per collision and  $\epsilon$  is the initial energy of interacting photons.

Second, the radiation length  $X_0$  is defined by

$$\frac{1}{X_0} = 4\alpha \left( \frac{N_0}{A} \right) Z^2 r_e^2 \ln(183Z^{-1/3}) \quad , \quad (10-5)$$

where  $Z$  and  $A$  are the charge and mass number of material traversed,  $N_0$  is Avagadro's number,  $r_e$  is the classical radius of the electron, and  $\alpha = e^2/hc = 1/137$ . This term comes from the quantum mechanical calculation of photon energy loss. In the description of certain radiation phenomena, there is only a slight dependence of a number of parameters on the atomic number when thicknesses are measured in radiation lengths. An example of such an effect will be presented in the section on pair production. A more detailed discussion on radiation lengths can be found in Rossi (1956). Detailed compilations of  $\gamma$ -ray cross sections in the energy region of interest can be found in Hubbell (1969), Hubbell (1977), and Hubbell et al. (1979).

### PHOTOELECTRIC EFFECT AND FLUORESCENCE RADIATION

Photoelectric absorption results from the interaction of  $\gamma$ -rays with bound electrons of the detector crystal. All of the energy of the  $\gamma$ -ray is lost in this interaction, but not all of the energy is imparted to secondary electrons as kinetic energy; some of it is required to overcome the binding energy of the electron. However, after the photoelectric absorption, X-rays are produced with energies almost equal to this binding energy. The absorption of these X-rays and their conversion to kinetic energy of secondary electrons will then reclaim, in a sense, the lost energy. In principle, some of the excess photon energy goes into the kinetic energy of the recoiling atom, but this is a negligible fraction. On the other hand, the excess momentum carried off by the recoiling atom is important, for it can be shown that momentum cannot be converted in the photoelectric effect with a free electron. Therefore, the binding of the electron to the atom is all-important for this phenomena (Heitler, 1954).

For photon energies very large compared with the ionization energy, the electron appears to be only lightly bound and the photoelectric effect becomes relatively improbable. Hence,

as the photon energy increases, the cross section for photoelectric emission decreases rapidly from its maximum value at the binding energy. In the low  $Z$ -elements, the binding of even the innermost  $K$ -electrons is quite weak, and the photoelectric effect is correspondingly small for photon energies of interest here. As  $Z$  increases, the binding energy increases rapidly and thus the photoelectric effect becomes more prominent. The increase of the cross section with atomic number goes roughly between  $Z^4$  and  $Z^5$ . The  $K$ -shell electrons contribute the most to the photoelectric effect, since they are the most tightly bound electrons. For photon energies below the  $K$  ionization energy, however, only the  $L$ - and higher shell electrons can be ejected by the photon, and they provide the entire photoelectric effect. Thus, going down in energy, the photoelectric effect drops almost discontinuously at the  $K$  ionization energy to the much lower values characteristic of the  $L$ -shell cross sections. Figures 10-1, 10-2, 10-3, 10-4, 10-5, and 10-6 show photoelectric mass absorption coefficient as a function of energy for plastic, Na I, Cs I, Ge, Fe, and Al. The pair production Compton scattering and total mass absorption coefficients are also shown.

## PAIR PRODUCTION AND ANNIHILATION RADIATION

In the pair production process, the incident  $\gamma$ -ray is annihilated in the field of the nucleus, producing an electron-positron pair. The excess of the  $\gamma$ -ray's energy above that required to produce an electron-positron pair at rest is imparted as kinetic energy to the electron and positron. This kinetic energy is then available to produce scintillations, for example. The positron later annihilates with an electron, usually producing two 0.51 MeV  $\gamma$ -rays. These can lose all or part of their energy by Compton scattering and/or photoelectron absorption in the detector crystal. Thus, the original incident  $\gamma$ -ray interacting through the pair production process may eventually lose any amount of its energy between its total energy and its total energy minus 1.02 MeV to secondary electrons.

Pair production has a threshold at  $2mc^2 = 1.022$  MeV, below which it cannot take place. Like the photoelectric effect, pair production cannot take place in free space; to conserve momentum it can occur only in the electric field of a particle

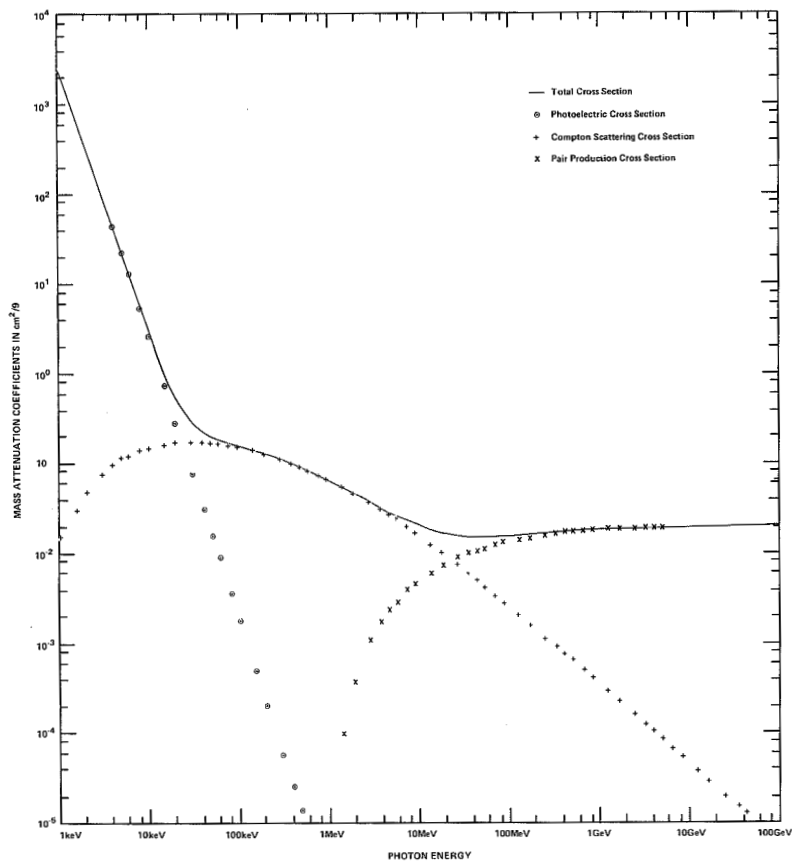


Figure 10-1. The photoelectric, Compton scattering, pair production, and total mass absorption coefficient for plastic scintillator plotted flows (from Hubbell, 1969, 1977, and Hubbell et al., 1979).

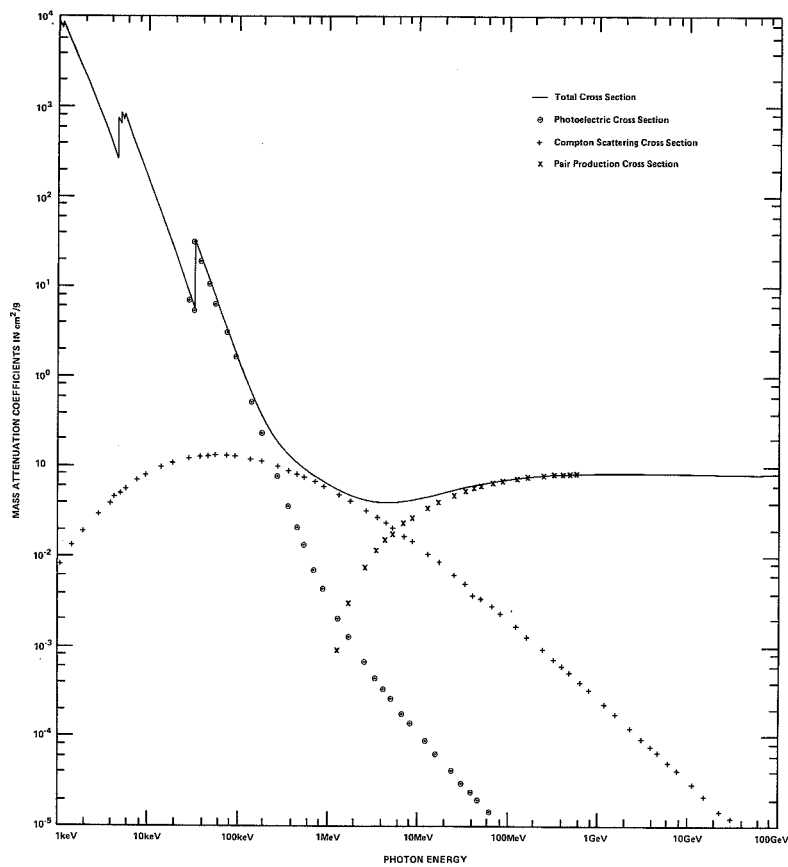


Figure 10-2. The photoelectric, Compton scattering, pair production, and total mass absorption coefficient for Na I (from Hubbell, 1969, 1977, and Hubbell et al., 1979).

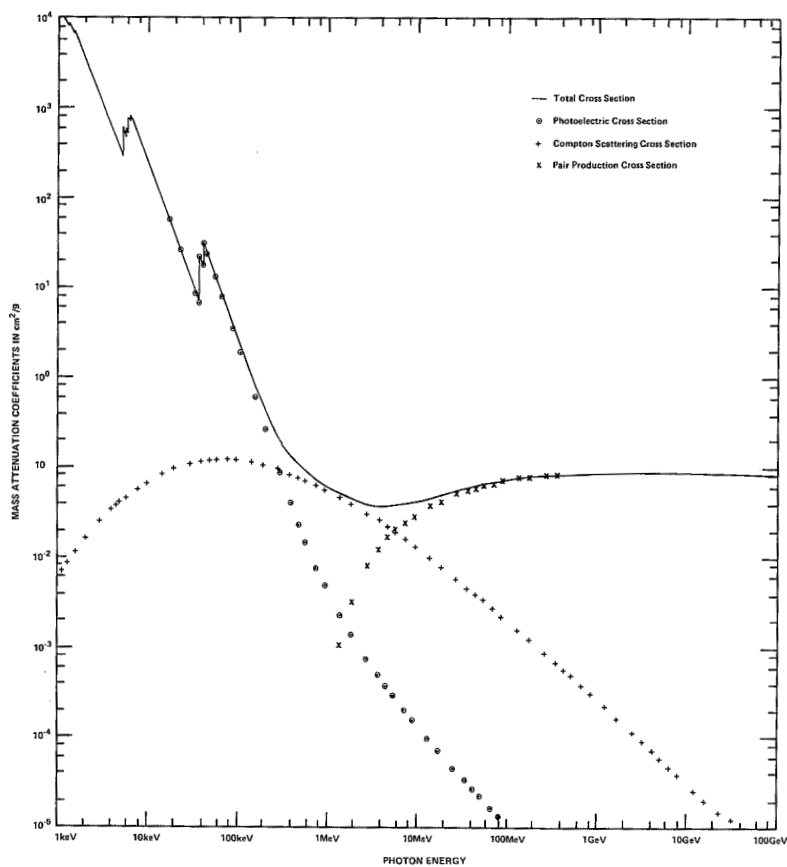


Figure 10-3. The photoelectric, Compton scattering, pair production, and total mass absorption coefficient for Cs I (from Hubbell, 1969, 1977, and Hubbell et al., 1979).

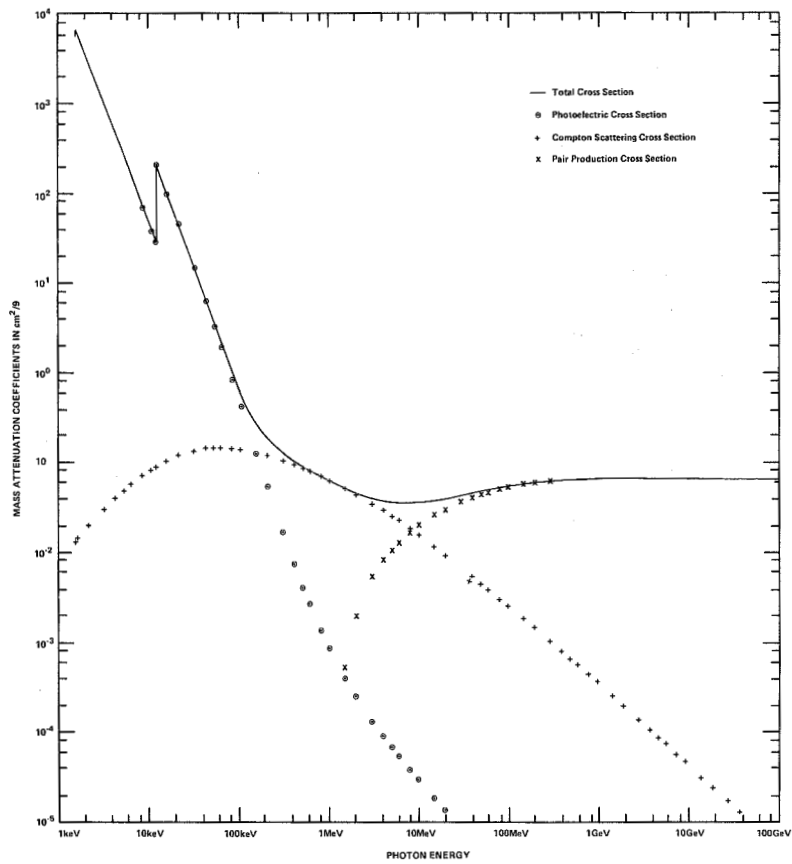


Figure 10-4. The photoelectric, Compton scattering, pair production, and total mass absorption coefficient for Ge (from Hubbell, 1969, 1977, and Hubbell et al., 1979).

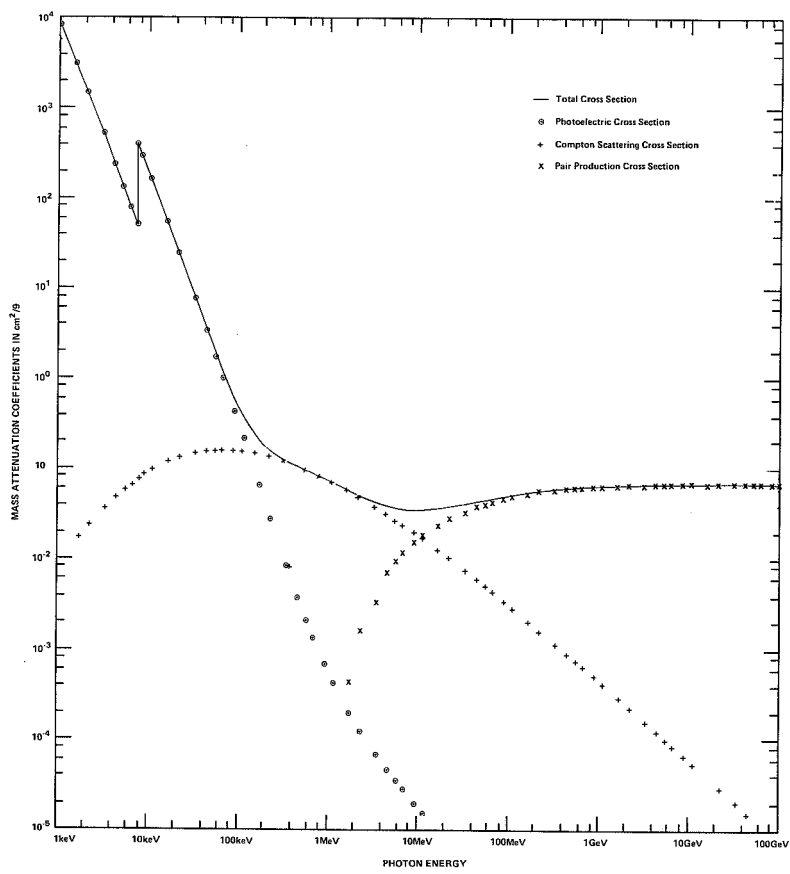


Figure 10-5. The photoelectric, Compton scattering, pair production, and total mass absorption coefficient for Fe (from Hubbell, 1969, 1977, and Hubbell et al., 1979).

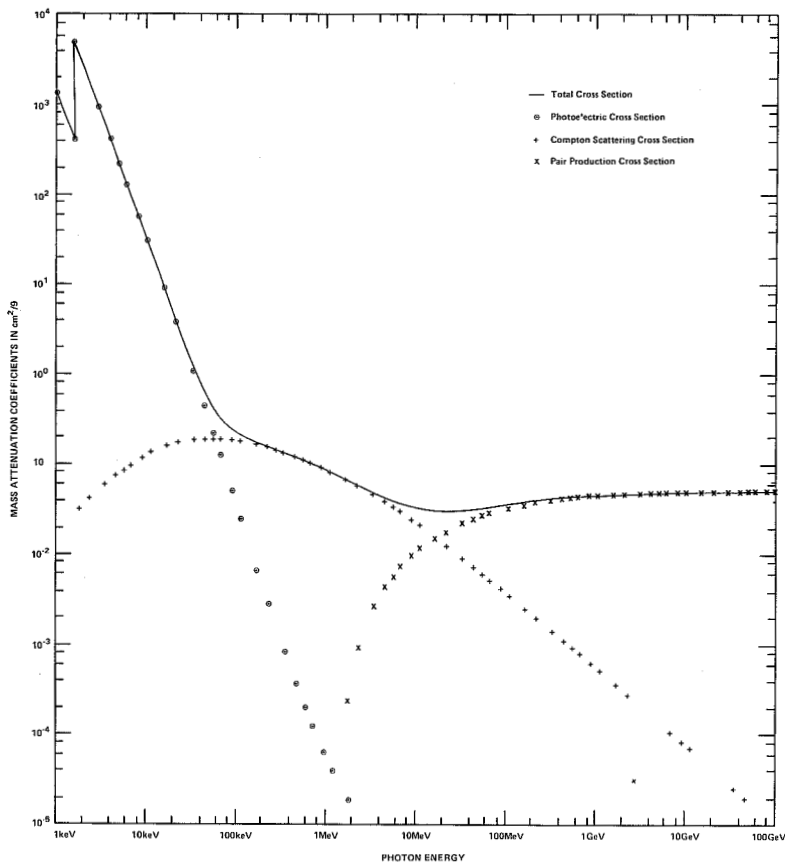


Figure 10-6. The photoelectric, Compton scattering, pair production, and total mass absorption coefficient for Al (from Hubbell, 1969, 1977, and Hubbell et al., 1979).

which can carry away some of the momentum in the recoil. Either the atomic electrons or the charge on the nucleus can provide this field. Where the pair production involves an electron, the energy of recoil is quite large and the threshold for such a process is, in fact, doubled. The amount of pair production caused by the atomic electrons goes as  $Z$ , whereas in the energy range of interest the pair production in the field of the nucleus goes as  $Z^2$ . Since the pair production cross section is proportional to the square of the particle's charge, for the detectors under consideration, most interactions are with the nucleus rather than one of the atomic electrons. For high energy photons, a good approximation is simply to add  $Z$  to  $Z^2$  in the cross section to include the effect of the atomic electrons. At low energies near the threshold for this process the approximation is not valid because the threshold for pair production in the field of an electron occurs at a higher energy.

The probability per radiation length for pair production is shown in Chapter 12, Figure 12-4. As was mentioned in this chapter for the case of radiation processes, the probability of interaction per radiation length depends only very slightly on atomic number, or  $Z$ , particularly at high energies. As Figure 12-4 shows, the interaction probability rises quickly with energy above a few MeV and then levels to a plateau value of  $7/9$  at very high energies. The energy at which this process dominates over the Compton scattering process, to be discussed in the next section, depends on the material in which the interaction occurs (see also Figures 10-2 through 10-6). This is an important feature to be kept in mind in the design of a detector.

Since most of the photon's energy goes into the electrons, it is readily understandable that the electrons have a fairly good memory of the arrival direction of the parent  $\gamma$ -ray. The root mean square angle between the trajectory of a secondary electron of energy  $E$  and that of the primary photon of energy  $\epsilon$  is given by the equation

$$\langle \epsilon^2 \rangle^{1/2} = q(\epsilon, E, Z) \frac{mc^2}{\epsilon} \ln \left( \frac{\epsilon}{mc^2} \right), \quad (10-6)$$

where  $q$  varies between about 0.6 and 3.5 as  $(E + mc^2)/\hbar$  varies between 0.9 and 0.1 (Stearns, 1949). Averaging over energy, this angle is found to vary from  $4^\circ$  at 30 MeV to  $1.5^\circ$  at  $10^2$  MeV to  $0.2^\circ$  at  $10^3$  MeV, showing the value of higher energy  $\gamma$ -rays for source location. Unfortunately, the higher energy  $\gamma$ -rays are much less numerous, as we have seen in the previous chapters.

It is, of course, in general not possible to measure the electrons at the instant they interact or without disturbing them. Hence, it is important to consider what happens to the secondary electrons. An electron undergoes a large number of Coulomb collisions as it passes through matter most of which produce very small angular deflections. If the layer is very thin so that energy loss is negligible, and if there is not a very improbable bremsstrahlung interaction in which a significant amount of energy is imparted to a secondary photon, the root mean square angle of scattering is given to a good approximation by

$$\langle \theta \rangle = \left( \frac{E_0}{\beta cp} \right)^2 \frac{x}{x_0} \quad (10-7)$$

where  $x_0$  is the radiation length,  $x$  is the distance traversed in radiation lengths, and  $E_0$  is approximately 21 MeV (Rossi, 1956). In any particle detector the scattering which occurs before the electron trajectories can be determined increases the uncertainty in the arrival direction of the  $\gamma$ -ray.

In attempting to measure the total energy of the photon by stopping the electron in an absorber such as a scintillator of some type, it is important to remember that not only the electron and positron must be absorbed, in addition, if an accurate energy estimate is to be obtained, the secondary bremsstrahlung radiation and particularly at low energies, the two  $1/2$  MeV photons formed when the positron comes to rest and annihilates with an electron in the material must be also absorbed. An alternative method for estimating the energy is to measure the average Coulomb scattering angle of the electrons.

## COMPTON SCATTERING

In the Compton scattering process, the electron is treated as unbound, or free, and must conserve energy and momentum. The  $\gamma$ -ray can be scattered through an angle, with a diminution of energy, and all the energy lost in scattering will be given up to secondary electrons as kinetic energy. Furthermore, the  $\gamma$ -ray may suffer one or a number of Compton scatterings. As the energy is degraded, the probability of photoelectric absorption increases. Thus, the  $\gamma$ -ray may lose only part of its energy (through Compton scattering only) or it may lose its total energy (through Compton scattering followed by photoelectric absorption) to the crystal.

Since the scattering electrons are taken as free, without interactions among themselves, the effect is strictly additive. The characteristics of the phenomenon can therefore be discussed for a single electron, and the cross sections multiplied by  $Z$  to obtain the atomic cross section.

The formulas describing the Compton scattering effects take particularly simple form if the photon wavelength,  $\lambda$ , and the energy,  $\mathcal{E}$ , are expressed in units of the Compton wavelength,  $h/mc = 0.02426 \text{ \AA}$ , and the electron rest mass energy,  $mc^2 = 0.511 \text{ MeV}$ , respectively. In these units the relation between the change in photon wavelengths and the angle of scattering is simply

$$\lambda' - \lambda = 1 - \cos\theta \quad (10-8)$$

where  $\lambda'$  is the final wavelength,  $\lambda$  is the initial wavelength, and  $\theta$  is the angle of scattering. Expressed in terms of energy, Equation (10-8) appears as

$$\mathcal{E}' = \frac{\mathcal{E}}{1 + \mathcal{E}(1 - \cos\theta)} \quad (10-9)$$

The maximum energy loss occurs for backward scattering (i.e.,  $\theta = 180^\circ$ ), at which the scattered energy is

$$\xi' = \frac{\xi}{1 + 2\xi} \quad (10-9a)$$

For  $E \gg 1$  (i.e.,  $\gg 0.511$  MeV) the final energy is never far from  $1/2$  (i.e.,  $0.255$  MeV), independent of the initial energy. Also, it should be noted that the photon can never lose all of its energy in any single Compton interaction.

In discussing the total cross section for the Compton effect it is convenient to introduce the Thomson unit

$$1 \text{ Thomson unit} = \frac{8\pi}{3} \left( \frac{e^2}{mc^2} \right) = 0.665 \text{ barns.} \quad (10-10)$$

In terms of this unit, the total cross section per electron is

$$\begin{aligned} \sigma_e(E) = \frac{3}{4} \left\{ \frac{1+E}{E^2} \left[ \frac{2E(1+E)}{1+2E} - \ln(1+2E) \right] \right. \\ \left. + \frac{1}{2E} \ln(1+2E) - \left( \frac{1+3E}{(1+2E)^2} \right) \right\} \quad (10-11) \end{aligned}$$

For small electron energies,  $E \ll 1$ ,  $\sigma_e$  is equal to unity in terms of the Thomson unit. In the limit of large energy,  $E \gg 1$ , the formula simplifies to

$$\sigma_e(E) \sim \frac{3}{8E} (\ln 2E + 1/2) \quad E \gg 1. \quad (10-12)$$

The total Compton scattering cross section thus decreases relatively slowly with increasing energy. Figure 10-1 through 10-6 show the energy-dependent cross sections for a number of elements and materials.

The Compton effect as shown above is independent of  $Z$  and is calculated per electron, thus when the mass absorption coefficient is considered, this cross section is nearly constant and is almost independent of the  $Z$  of the material in which the  $\gamma$ -rays interact.

Another important cross section of interest in detector design is the differential angular cross section,  $\sigma(\theta)$ , the cross section for scattering into a given angle per unit solid angle. This cross section is given by the Klein-Nishina formula, using Thomson units as

$$\sigma(\theta) d\Omega = \left(\frac{3}{16\pi}\right) \frac{\mathfrak{E}'^2}{\mathfrak{E}^2} \left(\frac{\mathfrak{E}}{\mathfrak{E}'} + \frac{\mathfrak{E}'}{\mathfrak{E}} - \sin^2\theta\right) d\Omega \quad (10-13)$$

where  $d\Omega$  is the differential of solid angle, and remembering the  $\theta$  and  $E$  are related by Equation (10-9).

For very low values of  $E$ , that is as  $E$  approaches 0, the Compton scattering cross section is symmetric and varies by a factor of 2 with angle, and having a maximum value at 0 and 180° and a minimum at 90°. As the energy increases the cross section becomes peaked in the forward direction. By 10 MeV, the cross section falls to half of its initial value at about 12° and drops to about 1 percent of the initial value for 180° or back-scattering.

## ELECTRON LEAKAGE AND BREMSSTRAHLUNG

These effects will only be briefly considered in terms of their effect on energy loss.

Electron leakage or escape complicates our understanding of the amount of energy deposited by the  $\gamma$ -ray in the detector. If enough energy is imparted to secondary electrons so that these electrons can escape the detector mass without losing all their kinetic energy, then the resolution of the detector will be affected and the knowledge of the incident  $\gamma$ -ray energy will be degraded.

Loss of electron energy by the bremsstrahlung processes can also degrade the knowledge of the incident energy unless the photoradiation produced is absorbed by the detector mass and produces a measurable energy loss in the detector. These processes will be considered in more detail later when detector response functions are considered.

## REFERENCES

- Bethe, H. A., and Askin, J., 1953, in Segre, ed., *Experimental Nuclear Physics*, 1 (New York: John Wiley and Sons, Inc., 1953), pp. 305-349.
- Davisson, C. M., 1968, in Siegbahn, ed., *Alpha-, Beta- and Gamma-Ray Spectroscopy*, vol. 1, Chapter 2 (Amsterdam: North-Holland Publishing Company, 1968), pp. 37-78.
- Goldstein, H., 1959, *Fundamental Aspects of Reactor Shielding* (New York: Addison-Wesley Publishing Co., Inc., 1959).
- Heitler, W., 1954, *Quantum Theory of Radiation*, 3rd ed. (New York: Oxford University Press, 1954).
- Hubbell, J. H., 1969, *Photon Cross Sections, Attenuation Coefficients from 10 keV to 100 GeV*, NSRDS-NBS29 (Washington D.C.: U.S. Government Printing Office, 1969).
- Hubbell, J. H., 1977, *Radiation Research*, **70**, 58.
- Hubbell, J. H., Gimm, H. A., and Overbo, I., 1980, *Jour. of Phys. Chem. Ref. Data*, **9**, 1023.
- Rossi, B., 1956, *High Energy Particles* (Englewood Cliffs, N.J.: Prentice Hall, Inc., 1956), pp. 10-90.
- Stearns, M., 1949, *Phys. Rev.*, **76**, 836.

# Chapter 11

## Detectors for Energies Less Than 10 MeV

### INTRODUCTION

In the energy domain 100 keV to 10 MeV, both crystal scintillators and semiconductors are widely used for  $\gamma$ -ray detectors in spectrometer systems. These detectors' operation depend on the fact that  $\gamma$ -rays lose energy by ionization in these materials and electrons and holes are produced. In the case of semiconductors, these electrons and holes are collected by an electric field, and they provide an electric signal that is a direct measure of the energy lost by the  $\gamma$ -ray in the material. Scintillation detectors depend on a further conversion of the energy lost in electron-hole pair production to the production of photons. A photomultiplier tube measures the intensity of the photon flux, and an electrical pulse proportional to the photon intensity is produced at the photomultiplier output. The electrical pulses appearing at the solid state or scintillation detector output can be analyzed as the number of events in terms of the magnitude of the electrical output either as a current or a voltage pulse. The resulting spectrum, called a pulse-height spectrum, is a measure of the energy loss spectrum in the detector material.

An important characteristic of any such detection system is that the number of carriers produced and in the case of scintillation detectors the number of photons produced be linearly related to the  $\gamma$ -ray energy lost to the detector. The best materials require only a small amount of energy to produce an electron-hole pair; thus, a large number of carriers produced for a given

energy absorption, and the statistical fluctuations are small when expressed as a percentage of the total number. This factor significantly affects the energy resolution of the spectrometer system.

## PROPERTIES OF DETECTORS

Gamma ray energy can be lost to the detector through a variety of processes such as photoelectric effect, Compton scattering, and pair production. These processes involve both total and partial energy loss, thus the energy loss spectrum is not necessarily in a one-to-one correspondence with the incident photon spectrum. High  $Z$  materials are used to optimize the total absorption process, and anticoincidence systems can reduce the contribution of the partial absorption events to degrading the shape of the pulse-height spectrum with respect to the incident flux. The measured pulse-height spectrum is further smeared out by the finite energy resolution of a real  $\gamma$ -ray spectrometer system. The incident photon spectrum can be used to infer the astrophysical properties of interest in  $\gamma$ -ray astronomy. Thus, an understanding of the detector interaction processes is essential to infer the true incident photon spectrum from a measurement of the energy loss or pulse-height spectrum. The methods of transformation from pulse-height space to energy space will be discussed in detail in Chapter 13.

Semiconductor detectors can be significantly damaged by the space radiation environment. This effect can be greatly reduced by proper design of detectors. Here we shall consider the problem of radiation damage in semiconductors and its effect in degrading detector performance.

### NaI (Tl) Crystal Scintillators

A number of scintillators are of interest in  $\gamma$ -ray spectroscopy—e.g., NaI(Tl), CsI(Tl), CsI(Na), and plastic—but for the purpose of this discussion we will consider the NaI(Tl) scintillation detector.

In Chapter 10, we considered the various mechanisms by which  $\gamma$ -rays interact with matter to produce high energy electrons. The photoelectric effect, Compton scattering, and pair production are the dominant interaction processes. By any of

these processes, or combinations thereof, the  $\gamma$ -ray loses all or part of its energy to the crystal. After having converted this energy to high energy electrons, the crystal experiences ionization due to the energy loss  $dE/dx$  of the electron in moving through the crystal. This process is similar to the ionization of a gas by a charged particle. In the case of the crystal however, one deals with a solid insulator in which the band theory is applicable (Sietz, 1940; Kittel, 1953).

Band theory values of energy for bound electrons in a perfect NaI crystal belong to allowed intervals of energy (the valence and conduction bands) which are separated by "unallowed" intervals (the forbidden bands). Passage of a high energy electron through the crystal excites electron-hole formation in the valence band. The energy gap  $E_g$  (i.e., the interval between the valence and conduction band) for NaI is about 30 eV.

The NaI(Tl) crystal is not perfect, and, because of the presence of thallos ions and lattice defects, localized allowed electron levels exist in the normally forbidden interval between the conduction band and the valence band. Some of these levels are in regions called "trapping centers," which are due largely to lattice imperfections, but partly to the presence of impurity ions. Still other allowed levels that exist between the bands are called "luminescence-center levels." The mechanisms of light emission (scintillations) are attributed to the existence of these centers. An energy level diagram is shown in Figure 11-1 (Mott, 1958; Price, 1958).

It is believed that the luminescence centers consist of pairs of thallos ions which have some of the properties of ordinary diatomic molecules. The energy,  $E$ , of those electrons within the effective radius of a pair of thallos ions, as a function of the interior separation,  $r$ , is function of the type shown in Figure 11-1 above the words "luminescence-center levels." The lower curve,  $A$ , is for the electronic ground state, and the upper curve,  $B$ , is for an excited electronic state.  $A$  and  $B$  have shapes that allow the thallos ion to vibrate along  $r$ . Some of the vibrational levels are excited at room temperatures. By the Frank-Condon principle (Mott, 1952), changes in electronic energy are represented by vertical lines at the extremes of the ion vibration locus on the energy diagrams, whereas in the classical picture the ions are instantaneously stationary. In the transition of the electron

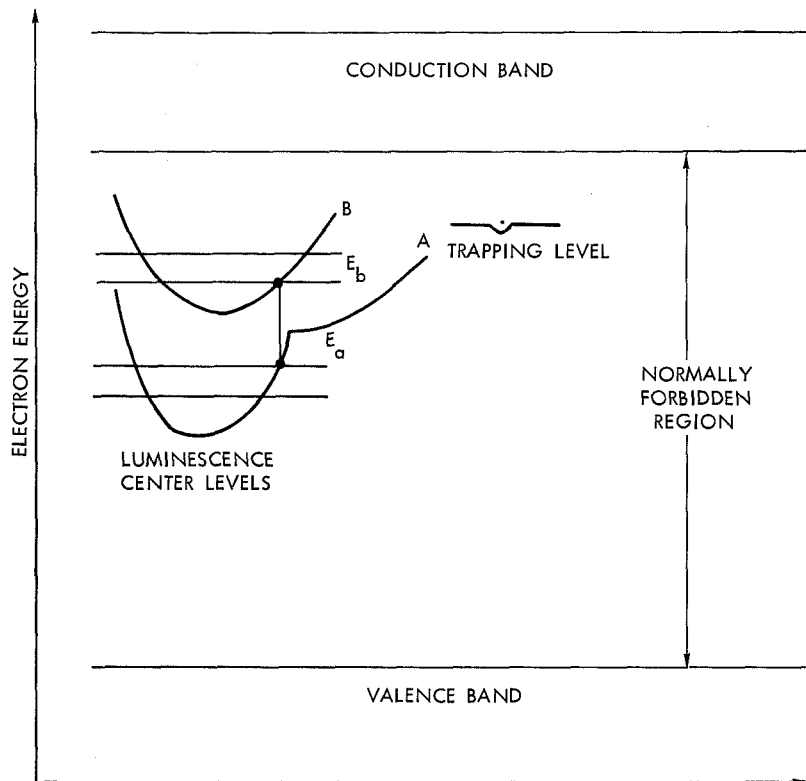


Figure 11-1. Energy level scheme for NaI(Tl) detector.

from  $E_b$  to  $E_a$ , a photon of energy  $E_b$  to  $E_a$  is emitted. Since transition may occur at the extremes of these ion vibrations, one obtains photons whose wavelengths lie in a rather broad band about energies corresponding to 3 eV or 4100 Å (Mott and Sutton, 1958).

Electrons excited to the conduction band can fall to the valence band through the trapping level and the luminescence-center levels. Transitions via the luminescence-center levels result in the emission of light: the scintillations of interest in the detection process. Transitions via other levels do not produce detectable scintillations. NaI(Tl) has the property that the intensity of scintillation, or total light energy produced, is proportional to the energy lost by the  $\gamma$ -rays or fast particles that produced it.

This is the property of NaI(Tl) that makes it useful in  $\gamma$ -ray spectrometry. Figure 11-2 shows the NaI(Tl) emission spectrum and the absolute efficiency of the conversion of electron excitation energy into emitted light (Bird, 1956). The total light energy produced,  $\mathcal{E}_l$ , given an initial electron excitation energy,  $E_e$ , is

$$\mathcal{E}_l = E_e \int_0^{\infty} C_{np}(\lambda) d\lambda \quad (11-1)$$

where  $C_{np}(\lambda)$  is the conversion efficiency as a function of the wavelength of the photons produced in the scintillation process.  $C_{np}(\lambda)$  does not depend upon the initial electron excitation energy (Bird, 1956; Price, 1958). Thus, there is a linear relation between  $\mathcal{E}_l$  and  $E_e$ .

Other NaI(Tl) properties of interest in detector design (Heath et al., 1965) are its transparency to its own luminescence, its high light yield relative to other scintillators, the 0.25 s decay constant of its scintillation, and the fact that it is very hygroscopic.

### Photomultiplier Tube

The intensity of the scintillations induced in the NaI(Tl) crystal by the absorption and scattering of  $\gamma$ -rays is measured very accurately. The light from the crystal passes through the glass envelope of the photomultiplier tube and ejects electrons from the photocathode. The photosensitive materials used in the photocathode (e.g., Cs Sb) are chosen because of their good photoelectric yield at the wavelength of the luminescent emission from scintillation crystal. The photocathode absorption spectrum is shown in Figure 11-2. The photoelectrons are electrically accelerated to the first dynode, where they eject secondary electrons. The process is cascaded in ten stages, so that the charge of the cascade ejected from the tenth dynode and collected on the anode is about  $6 \times 10^5$  times the original charge from the cathode (where the potential difference per stage is 105 V) (Mott and

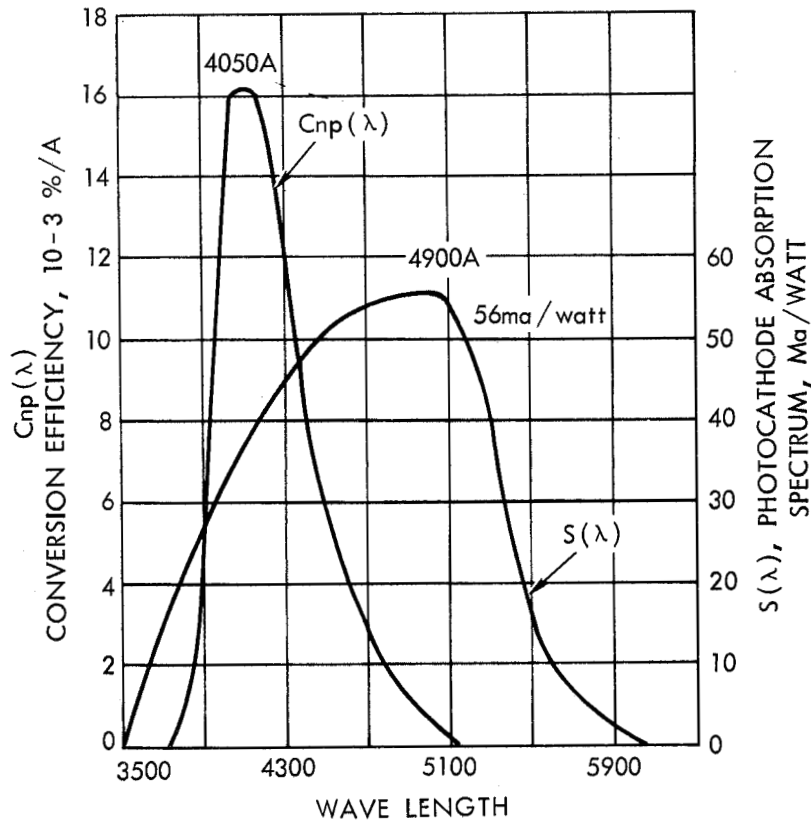


Figure 11-2. Emission spectrum, absolute conversions efficiency spectrum, and photocathode "absorption" spectrum for NaI(Tl) crystal and end window (Sb Cs<sub>3</sub>) photocathode multiplier tubes.

Sutton, 1958). The fraction of the photon energy which strikes the photocathode surface is  $\epsilon_1(T_p, F_p)$ , where  $T_p$  is the transparency both of the crystal and of the phototube optical seal, and  $F_p$  is the nonescape probability. For a well-reflected crystal, both  $T_p$  and  $F_p$  should be nearly unity. A fraction of this energy will be absorbed in the photocathode, resulting in the release of a number,  $n_e$ , of low energy photoelectrons inside the photo-

tube. The efficiency of this conversion from photons to electrons depends on the absorption spectrum of  $\text{Sb Cs}_3$  and on the electronic stopping power of the photocathode; it is measured by the sensitivity factor  $S(\lambda)$ , shown also in Figure 11-2.

Now,  $dn_e/d\mathcal{E} = S(\lambda)$  can be written  $dn_e = S(\lambda) d\mathcal{E}$ , but from Equation (11-1) above

$$d\mathcal{E} = d\mathcal{E}_1 = E_e C_{np}(\lambda) d\lambda$$

and

$$dn_e = E_e C_{np}(\lambda) S(\lambda) d\lambda ,$$

or the number of photoelectrons ejected,  $n_e$ , depends on the product of the spectra of Figure 11-2

$$n_e = E_e \int_0^{\infty} C_{np}(\lambda) S(\lambda) d\lambda . \quad (11-2)$$

If  $F_c$  is defined as the fraction of such electrons striking the first dynode and if the subsequent phototube multiplication is  $M$ , the total charge  $q$  produced at the anode as a result of a single original  $\gamma$ -ray interaction is

$$q = n_e e M F_c = V_0 / C , \quad (11-3)$$

where  $e$  is electronic charge and  $q$  is the charge collected on the input capacitance  $C$  of an amplifier and measured as a voltage pulse  $V_0$ . Thus, it is seen that the pulse height is proportional to the initial electron excitation energy  $E_e$ . However, because of the

statistical fluctuation in  $dE/dx$ ,  $n_e$ ,  $M$ , and  $F_c$ , a distribution of voltage pulse heights about some mean value  $V_0$  will be observed, rather than a constant pulse height as implied by Equation (11-3).

### Factors Affecting Resolution

The  $\gamma$ -ray dissipates its energy in the phosphor, thus, producing high energy photoelectrons which produce pulses with varying magnitudes at the output of a scintillation counter. A number of experimental and theoretical studies (e.g., Wright, 1954; Kelley et al., 1956) have been made of the widths of the generated pulse-height spectra.

**Emission of Photons by the Phosphor.** There is a statistical fluctuation in the number of photons per scintillation. There are other statistical variations that may be attributed to local variations in luminescent efficiency of the phosphor caused by possible nonuniform distribution of activity ions by the fact that: successive particles lose different amounts of energy to the phosphor through interaction, edge, and scattering effects; and also by the luminescence process itself (i.e., the ratio of absorbed energy to photon energy fluctuates for successive particles).

**Collection of Emitted Photons by the Photocathode.** Successive scintillations never occur at exactly the same position in the crystal; thus, the photon collection efficiency of the photocathode depends on the position where the scintillation is produced. Optical flaws in the crystal and at the various optical seals further spreads the distribution.

**Emission of Photoelectrons  $n_e$  by the Photocathode.** There is a statistical fluctuation of the number of photoelectrons released from the photocathode per scintillation. Further, there is a point-to-point variation of photocathode response; also, a random emission of thermal electrons by the photocathode also adds to a variation in the pulse-height distribution.

**Collection of Photoelectrons by the First Dynode  $F_c$  and Multiplication  $M$  by the Successive Stages.** The variance due to the multiplication process can be shown to be fundamentally statis-

tical in nature (Gamble, 1955). In addition, losses can be attributed to the variations in the fraction of photoelectrons collected by the first dynode, in the collection efficiencies of subsequent dynodes, and in dynode response.

Other processes affecting the pulse-height resolution of scintillation detectors have also been considered, such as the statistical variation in  $dE/dx$ ; they have been found to be negligible compared with those mentioned above. For further details see Swank and Buch (1952), Wright (1954), and Mott and Sutton (1958). Also it is shown in those references that the effects considered in the first two processes are small compared with those of the third and fourth processes. Therefore, the theoretical calculation of energy resolution usually considers only the statistical fluctuation in the third and fourth processes (Swank and Buch, 1952; Gamble, 1955; Kelley et al., 1956; Mott and Sutton, 1958). The statistical variation in the number of photoelectrons  $n_e$  produced at the photocathode can be considered to be Gaussian. If  $V = V_0$  is the mean value of the pulse height produced by the absorption of the  $\gamma$ -ray energy  $\mathcal{E}_0$  in the phosphor of the anode, then the probability  $P_1$  that a pulse of height  $V_1$  is produced at the phototube anode because of statistical fluctuation in  $n_e$  is

$$P_1 = \frac{n_e(V_0)}{n_e(V_1)} = \exp - \left[ \frac{(V_1 - V_0)^2}{2\sigma_n^2} \right], \quad (11-4)$$

where  $\sigma_n^2$  is the photoelectron dispersion. Here we have only considered the variance in  $n_e$ .

Now consider the effect of the variance in the multiplication,  $M$ . A Gaussian distribution of statistical fluctuation is assumed (Gamble, 1955; Kelly et al., 1956). Therefore, the probability that the phototube multiplication of  $n_e(V_1)$  produces a pulse corresponding to height of  $V_2$  is

$$P_2 = \frac{M(V_2)}{M(V_1)} = \exp - \left[ \frac{(V_2 - V_1)^2}{2\sigma_m^2} \right], \quad (11-4a)$$

where  $\sigma_m^2$  is the dispersion due to the statistical variation in the multiplication. The probability  $P_3$  of obtaining a pulse of height  $V_2$  from the complete absorption of energy  $\mathcal{E}_0$  is the product of  $P_1$  and  $P_2$  integrated over all  $V_1$

$$P_2 = \int_{-0}^{+\infty} \exp \left[ \frac{-(V_1 - V_0)^2}{2\sigma_n^2} \right] \exp \left[ \frac{-(V_2 - V_1)^2}{2\sigma_m^2} \right] dV_1 \quad (11-4b)$$

Letting  $\alpha = (V_2 - V_0)$  and  $\sigma^2 = \sigma_n^2 + \sigma_m^2$ ,  $P_3$  reduces to

$$P_3 = K \exp - \left[ \frac{\alpha^2}{2\sigma^2} \right], \quad (11-5)$$

where  $\sigma^2$  is the dispersion of the photoelectron rate and subsequent multiplication rate, and  $K$  is a constant.

Analysis has shown (Swank and Buck, 1952; Gamble, 1955) that

$$\sigma_n^2 \sim \bar{n}_e = K_1 \mathcal{E}_0 = K_1' V_0 \quad ,$$

and

$$\sigma_m^2 \sim \bar{n}_e f(M) = K_2 \mathcal{E}_0 = K_2' V_0 \quad ,$$

where  $f(M)$  is a function of the multiplication, and is constant for a fixed  $M$ . Also,

$$\sigma^2 = K_3 \mathcal{E}_0 = K_3' V_0 \quad (11-6)$$

It has been found experimentally that Equation (11-6) is true for limited energy ranges (Kelley et al., 1956).

The Gaussian form given in Equation (11-5) describes the pulse-height distribution generally; however, one cannot use Equation (11-6) to determine  $\sigma^2$  in general. It has been found that over a limited energy range the relation

$$\sigma = K\mathcal{E}_0^n = K'V_0^n \quad , \quad (11-7)$$

where  $n$  is determined experimentally, can be used more generally.

The detector resolution can be defined as the ratio of  $V_{1/2}$  the full width at half maximum (FWHM) in pulse-height units, or  $\mathcal{E}_{1/2}$  the FWHM in energy units to the position  $V_0$  or  $\mathcal{E}_0$ . That is

$$R = \frac{\Delta V_{1/2}}{V_0} = \frac{\Delta \mathcal{E}_{1/2}}{\mathcal{E}_0} \quad (11-8)$$

and  $\Delta V_{1/2} = 2(\ln 2)^{1/2} \sigma_V$  (in pulse units), and similarly  $\Delta \mathcal{E}_{1/2} = 2(\ln 2)^{1/2} \sigma_{\mathcal{E}}$  (in energy units).

The standard measure of the operation of a scintillation detector is the resolution obtained for the photopeak or total absorption of the 0.662 MeV  $\gamma$ -ray line (the monoenergetic  $\gamma$ -ray line emitted by  $^{137}\text{Cs}$ ). An extremely good detector would have a resolution of about 7 percent. This would yield a  $\Delta \mathcal{E}_{1/2}$  of 46 keV.

Details of the properties other scintillator of interest in  $\gamma$ -ray spectroscopy can be found in Neiler and Bell (1968), and in Adams and Dams (1970).

### Semiconductor Detectors

Semiconductor  $\gamma$ -ray detectors materials such as Si(Li), Ge(Li), and high purity Ge [Ge(HP)] are extremely attractive for use in X-ray and  $\gamma$ -ray spectroscopy because of their improved energy resolution compared with gas proportional counters and scintilla-

tion counters in the energy domain above 6 keV and extending up to about 20 MeV. As described above for the case of scintillation detectors, charged particles or  $\gamma$ -rays lose energy to the detector material, and in so doing, lift electrons from the valence band or deeper conduction band to higher energy bands. An electron-hole pair is produced. The high energy electron produced, for example, by photoelectric absorption, Compton scattering, and pair production, rapidly loses energy to other electrons and after about  $10^{-12}$  s a stationary situation is achieved when the electrons reside in the conduction band. Single  $\gamma$ -ray interactions are then detected by applying an electric field to the detector and sweeping the electron-hole pair through the material so that an electrical pulse is measured at the detector output. This differs from the scintillation detector technique in that further signal amplification devices such as photomultiplier tubes are not used.

At this point one of the reasons for the improved energy resolution can be indicated. About 3 eV is required to produce an electron-hole pair which is finally detected at the output of a Ge semiconductor detector as compared with about 300 eV needed to create one photoelectron at the photocathode in the case of a NaI(Tl) scintillation detector.

**Band Theory.** A number of compound semiconductor materials are being studied as possible detectors for X-ray and  $\gamma$ -ray spectrometers. Such materials as CdTe, GaAs, HgI<sub>2</sub>, Ge(Li), Si(Li), and Ge(HP) and Si(HP). Up to this time Ge(Li), Si(Li) and Ge(HP) show the greatest promise for performing such measurements. Of these detectors, those containing Ge have the highest  $Z$  and density and, thus, are most appropriate for  $\gamma$ -ray measurements. In the following discussions we will consider Ge-type detectors in their application to  $\gamma$ -ray spectroscopy.

The same band theory used to describe the properties of scintillators can also be used to describe the properties of semiconductor detectors. The energy gap separating the valence and conduction bands in Ge is 0.764 keV at absolute zero. In a perfect crystal at absolute zero, the conduction band is vacant and the valence band filled. Electron-hole pairs can be produced as the temperature increases by thermal excitation of electrons from the top of the valence band to the bottom of the conduction band. The inverse process can also occur when carriers of

the opposite sign collide and annihilate. The creation of one electron-hole pair in the energy band model corresponds to thermal breaking of one covalent bond between the atoms of the material. The thermally generated electrons and holes give rise to electrical conduction.

The charge carriers are influenced by electric fields present in the lattice and these fields give a random motion to these charges when an external field is applied. The electrons and holes drift. In pure materials the mobility of the electrons and holes is governed by lattice scattering, and increases rapidly as the temperature is reduced. In pure semiconductor materials such as Ge, the mobility of both carriers is nearly the same. A maximum mobility for a given material is achieved as a result of the decrease in the mean free path between successive collisions as the average carrier energy is increased by an electric field. The production of electron-hole pairs and their behavior as described above is called intrinsic semiconduction and is characterized by an equilibrium concentration of free electrons and holes in the crystal.

The electrical properties of semiconductors can be modified by the presence of various types of imperfections. These imperfections can be attributed to chemical impurities and structural defects. Chemical impurities in substitutional or interstitial sites introduce transition levels in the forbidden energy band (cf., the consideration of scintillation materials with the introduction of thallous atoms).

Of course, all real crystal will contain various imperfections which change their electrical properties. The semiconductor, in such cases, is said to be extrinsic. Ge is a group IV element. A diamond lattice characterizes the structural form: each atom of one sublattice is tetrahedrally surrounded by four atoms of the other sublattice and gives one electron to each of the four atoms to form covalent bonds. If a small concentration of an element from group V is present, for example, this element might replace a Ge atom at a number of sites in the crystal lattice. In this case, four of the valence electrons are used for the covalent bands in the lattice and the fifth electron is loosely bound (a level in the forbidden band) to the impurity atom. This loosely bound electron can easily be thermally excited to the conduction band and a fixed positive charge results in the lattice. This type of impurity behaves as an electron donor and is denoted as an

*n*-type material. On the other hand, if a group III element is a replacement in the Ge lattice position, it constitutes a fixed negative charge and a positive hole occurs in the valence band. An electron acceptor denoted as a *p*-type material is produced. A group I type material such as lithium can occur interstitially in the semiconductor material and behave as an electron donor.

In all the cases mentioned above, the energy required to ionize these extrinsic materials is less than the energy gap because of the localized energy levels introduced in the forbidden energy region. Further, in an extrinsic semiconductor the equality does not hold between electron density and hole density. Also, the mobility of electrons and holes in an extrinsic detector differs from that in intrinsic material. This is especially important at low temperatures. In extrinsic materials, the mobilities are controlled by Coulomb attraction at the impurities sites rather than by lattice scattering as in intrinsic materials.

With the above factors in mind, let us consider these effects with respect to ionization produced by  $\gamma$ -radiation incident upon such detectors. At a given temperature the equilibrium distribution is disturbed by the introduction of a number of excess carriers due to  $\gamma$ -rays being absorbed in the crystal. In intrinsic semiconductor material, the recombination time is very long (i.e., seconds, because the direct recombination of an electron with positive holes is not a highly probable process). In extrinsic materials, the recombination is much shorter (i.e., one millisecond or less). Localized energy levels due to impurities or structural defects have significant capture cross sections for the drifting electrons or holes. The electrons or holes can be either lost or reexcited (recombination) or trapped for a time and then can be restored to the conduction band if an electron or to the valence band if a hole. These properties significantly affect the use of these materials in  $\gamma$ -ray detectors. Details of the properties discussed above can be found in a number of texts. A rather complete description is given in Bertolini and Coche (1968).

**Total Volume Sensitive Detector.** As mentioned above, the most suitable semiconductor for use in the  $\gamma$ -ray energy region (about 10 keV to about 20 MeV) is Ge. Such detectors must operate at low temperature (e.g., cooled by liquid nitrogen) to avoid the large leakage current produced at room temperature. Thermal

generation of electron-hole pairs at room temperature is large because of the 0.7 eV band gap in this type of material.

Now consider the problem of a volumetric detector with electrodes connected to opposite sides of the detector. The utilization of such contract electrodes may cause large currents to flow through the detector because there may be a free exchange of holes and electrons between the semiconductor and the electrodes. If this is the case, a current will flow upon the application of high voltage across the detector. It has been found that "blocking contacts" can be used to overcome this problem (Pehl et al., 1968; Pehl and Goulding, 1970; Pehl, 1977). Blocking contacts have the property that the positive contact does not inject holes and the negative contact does not inject electrons. The two approaches that have been used to achieve these properties are as follows: careful choice of metals used for the contacts or forming contacts with heavily doped  $n$  and  $p$  regions by either high temperature diffusion or by ion implantation into the detector surface.

Surface leakage currents can also cause difficulties in signal detection. This surface leakage problem can be attributed to, among other things, the absorption of various chemical species on the detector surface, which by modifying its electrical properties, results in severe leakage and breakdown problems. Thus, during the production of the detector proper chemical treatment of the surface is required and proper protection of the surface is required during operation.

**Detector Resolution.** Gamma ray interactions in the sensitive volume of the detector create highly energetic electrons which can lose energy by the creation of electron-hole pairs or by interactions with the crystal lattice. Considering these loss processes,  $k$  is defined as the mean energy per ion pair (about 3 eV for Ge); then the mean number,  $N$ , of electron-hole pairs produced is

$$\bar{N} = \left( \frac{E}{k} \right) , \quad (11-9)$$

where  $E$  is the energy absorbed. There is a statistical function in the production of the electron-hole pairs given by the standard deviation  $\sigma_n$

$$\sigma_n = (\bar{N})^{1/2} = \left(\frac{E}{k}\right)^{1/2} \quad (11-10)$$

The actual experimentally determined  $\sigma_n$  has been found to be smaller than that shown in Equation (11-10). A Fano factor,  $F$ , similar to an equivalent situation in gaseous detectors has been used to explain the difference (Pehl et al., 1968) when calculating the variance  $\sigma_n^2$ ,

$$\sigma_n^2 = F\bar{N} = F\left(\frac{E}{k}\right) \quad (11-11)$$

One can consider the Fano factor,  $F$ , to be approximately equal to the ratio of the energy imparted to the detector lattice by non-electron-hole production processes, to the total energy imparted to the crystal by the slowing down of the  $\gamma$ -ray produced high energy electrons. If almost all the energy loss produced electron-hole pairs,  $F$  would approach zero and there would be "no" statistical variance, while if the probability of electron-hole creation was very low,  $F$  would approach unity. For large germanium detectors the Fano factor seems to be near 0.13.

The measured detector resolution can be understood in terms of the statistical variance related to electron-hole pair production  $\sigma_n^2$  and the increase in the electronic noise produced variance  $\sigma_e^2$ . The total variance  $\sigma_T^2$  is then

$$\begin{aligned} \sigma_T^2 &= \sigma_e^2 + \sigma_n^2 \\ &= \sigma_e^2 + F\left(\frac{E}{k}\right) \end{aligned} \quad (11-12)$$

For a given spectrometer/detector system,  $\sigma_e^2$  should be constant. For scintillation detectors  $\sigma_e^2$  is small compared to  $\sigma_n^2$  and, thus, was ignored; for semiconductor devices such as Ge detectors these factors are comparable and, thus,  $\sigma_e^2$  cannot be ignored. With the formulation shown in Equations (11-7) and (11-8), the resolution becomes

$$R = \frac{\Delta \mathcal{E}_{1/2}}{\mathcal{E}} = \frac{2\sqrt{\ln 2} \sigma_T}{\mathcal{E}} = \frac{2\sqrt{\ln 2}}{\mathcal{E}} \sqrt{\sigma_e^2 + \frac{FE}{k}}$$

$$= \sqrt{\frac{A}{\mathcal{E}^2} + \frac{B}{\mathcal{E}}}, \quad (11-13)$$

where  $A$  and  $B$  are constants for a given detector spectrometer system. The resolution of the 1.33 MeV ( $^{60}\text{Co}$ ) line with a Ge detector of volume about 120 cm<sup>3</sup> can be about 0.2 percent as compared with a good NaI(Tl) detector with resolution about 4.7 percent.

**Ge(Li) and Ge(HP) Detectors.** A major problem with Ge semiconductors is the presence of the trapping centers discussed earlier. A carrier “trapped” by one of these centers can be released or “detrapped” by thermal excitation. The “detrapping time” is defined as the average time a carrier remains trapped. Trapped carriers affect energy resolution. These carriers can be regained, in a sense, if the detrapping time in the detector is very short compared with the pulse collection time of the external electronics. Because the location of the initial carrier charge production changes and because of the variations in the concentration of traps at different points in the detector, the loss of signal can be different from one event to another, and thus, there is a further fluctuation in the output signal.

Early in the development of Ge detectors, the high impurity concentration in the available Ge required that “Lithium drifting” be used to reduce the problems introduced by the presence of acceptor impurities. Lithium acts as an interstitial donor. In

this way Ge detectors could be produced with rather large volumes of material exhibiting low net impurity properties. This process required that the detector be kept constantly at cryogenic temperature; at elevated temperatures the lithium becomes mobile and the impurity properties are destroyed. The lithium-drifted detectors are made by evaporating lithium onto a *p*-type germanium block and drifting the lithium into the block at higher temperatures. Ge lithium drifted (Ge(Li)) detectors with large volumes have been produced by means of coaxial drift techniques. The lithium is drifted from the outer surface of a cylindrical block of Ge toward the center, and the drift process is stopped when a small core of *p*-type Ge remains. This core is the *p*-contact for the detector.

More recently, higher purity germanium Ge(HP) detectors have become available. These detectors do not require lithium compensation; the low impurity concentration does not significantly affect the resolution. These Ge properties are still extrinsic in nature and both *p*-type and *n*-type material can be produced. This property is extremely important in radiation damage considerations. These detectors will not be ruined by elevated temperatures, although they must be operated at low temperatures.

Both planar and coaxial geometries can be used for Ge(HP) and Ge(Li) detectors. However, in terms of the coaxial Ge(HP) detector, the equivalent of the undrifted central core as in Ge(Li) material does not exist. Consequently, a central core of material must be removed and a contact put on the inside surface of the Ge. Detectors of both the *n*-type and *p*-type have been manufactured in this coaxial configuration.

## DETECTOR RESPONSE TO MONOENERGETIC RADIATION

The pulse-height spectrum obtained when monoenergetic  $\gamma$ -rays are detected by a scintillation or semiconductor detector is never a line, but is of a shape determined by  $\gamma$ -ray energy and the source detector configuration. These shapes are determined by (1) the relative magnitude of the photoelectric, Compton, and pair-production cross sections and (2) the losses and statistical fluctuation that characterize the detector system. The latter

consideration was discussed in a previous section, and it was indicated that one could describe to a first approximation this spreading for a given energy  $\mathcal{E}_0$  by Gaussian

$$y = A_m \exp - \left[ \frac{(\mathcal{E} - \mathcal{E}_0)^2}{\alpha^2 \mathcal{E}_0^n} \right], \quad (11-14)$$

where  $y$  is the count rate at energy  $\mathcal{E}$  or pulse height  $V$ , and  $A_m$  is a constant. Modifications of the approximation will be considered in Chapter 13.

We first consider the shape of the response of a detector to monoenergetic  $\gamma$ -rays at lower energies when photoelectric absorption predominates and Compton scattering and pair production can be considered negligible. The kinetic energy imparted to a secondary electron is equal to the energy of the  $\gamma$ -ray minus the electron binding energy. This binding energy can be reclaimed in a sense by the absorption of the X-rays produced by photoelectric absorption. There is also the possibility that the X-rays may escape the crystal without being absorbed. The pulse-height distribution caused by photoelectric absorption is characterized by two regions: (1) the region of total absorption (the photopeak) and (2) the region of total absorption minus X-ray escape energy (the escape peak). This distribution spreading, plus the Gaussian spreading discussed above yields a pulse-height spectrum similar to that shown in Figure 11-3.

When Compton scattering becomes an important energy-loss mechanism, another region is observed in the pulse-height spectrum, the so-called Compton continuum. All the energy lost in scattering will be given up to the electron as kinetic energy. The  $\gamma$ -ray may lose part of its energy to the detector; furthermore, after suffering one or more Compton collisions, it may then undergo a photoelectric absorption, losing its remaining energy. Thus, the  $\gamma$ -ray either loses all or part of its energy in the crystal, or escapes the crystal at a diminished energy. See Figure 11-4 for a NaI(Tl) pulse-height spectrum and Figure 11-5 for a pulse-height spectrum measured with a Ge(HP) detector. The improvement in energy resolution can be easily noted.

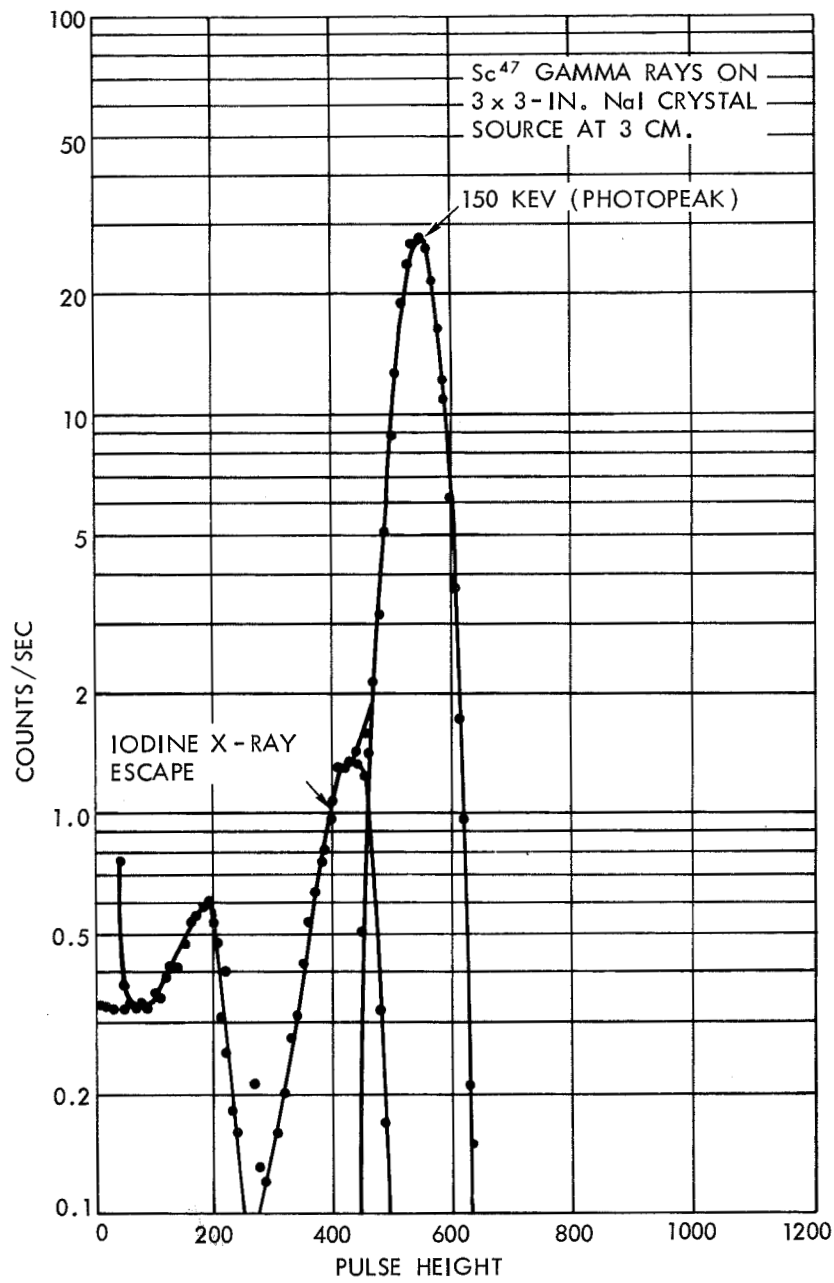


Figure 11-3. <sup>47</sup>Sc  $\gamma$ -rays on 3 x 3 in. NaI(Tl) crystal. Source at 3 cm; energy scale 0.42 keV/PHU.

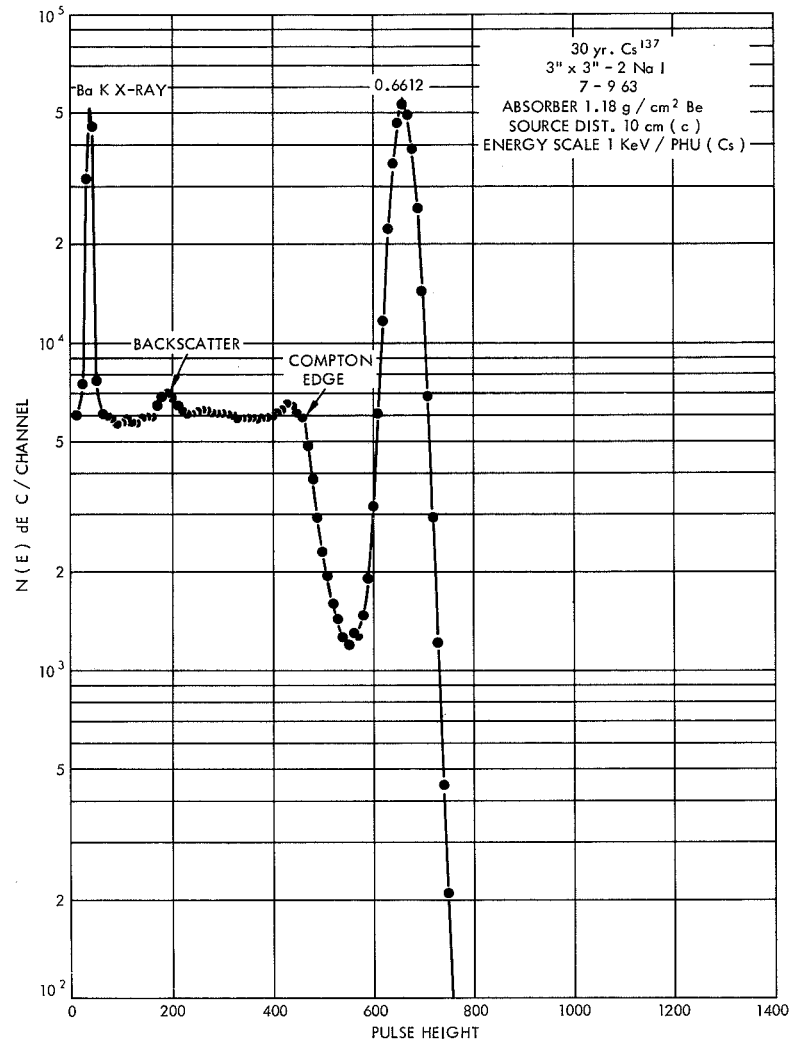


Figure 11-4. <sup>137</sup>Cs  $\gamma$ -rays on 3  $\times$  3 in. NaI(Tl) crystal. Source at 10 cm; energy scale, 1 keV/PHU.

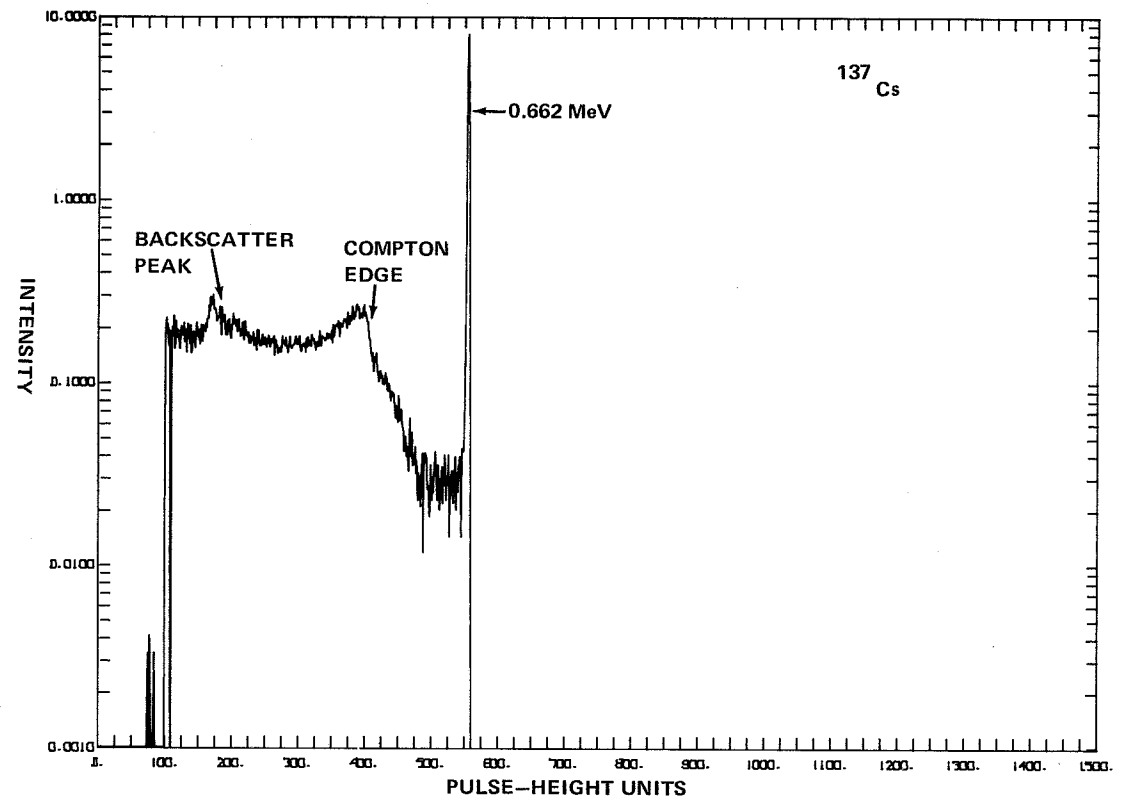


Figure 11-5.  $^{137}\text{Cs}$   $\gamma$ -rays on 120 cc Ge(HP) detector. Source at 25 cm.

At  $\gamma$ -ray energies higher than 2 MeV, pair production becomes appreciable. Two false photopeaks are then observed. Figure 11-6 is the pulse-height spectrum obtained using  $^{24}\text{Na}$  source. The  $\gamma$ -ray energies emitted by  $^{24}\text{Na}$  are 2.76 MeV and 1.38 MeV. The three peaks of greatest height are caused, in order of increasing pulse height, by (1) pair production with escape of both annihilation quanta, (2) by pair production with the absorption of one annihilation quantum, and (3) by pair production

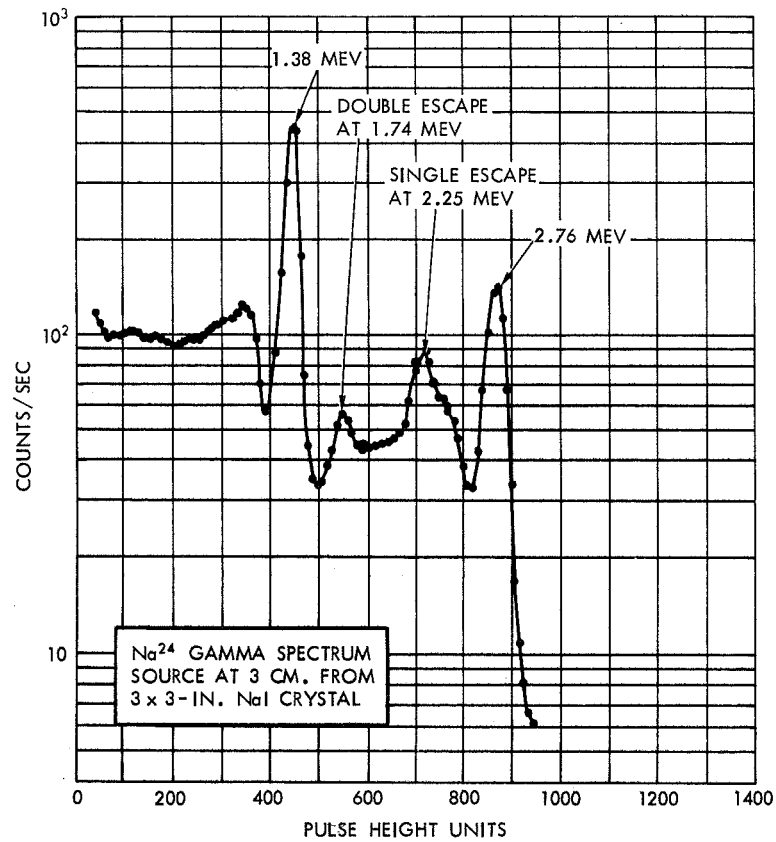


Figure 11-6.  $^{24}\text{Na}$   $\gamma$ -rays on  $3 \times 3$  in.  $\text{NaI(Tl)}$  crystal. Source at 3 cm; scale about 3.1 keV/PHU.

with absorption of both annihilation quanta and total absorption by the photoelectric effect or any combination of other effects leading to total absorption.

In addition to the photopeak, the iodine X-ray escape peak, the Compton continuum, and the pair-escape peaks, there are several other regions characteristic of experimentally determined pulse-height spectra of monoenergetic  $\gamma$ -rays:

1. Multiple Compton scattering region. Because of multiple Compton scattering from materials surrounding the source and crystal, which degrades the primary  $\gamma$ -ray energy, there is a continuous distribution of  $\gamma$ -ray incidents upon the crystal with energies less than the initial  $\gamma$ -ray energy. This tends to spread out the true Compton continuum produced by  $\gamma$ -rays of undegraded energy scattering in the crystal.
2. Annihilation radiation from the surroundings. If there is position emission, they may annihilate in surrounding material. Some of the 0.511 MeV  $\gamma$ -rays thus produced reach the crystal, and a pulse-height spectrum characteristic of 0.511 MeV  $\gamma$ -rays is superimposed on the monoenergetic pulse-height spectrum (see Figure 11-7).
3. Coincidence distribution. If two  $\gamma$ -rays interact with the detector during a time which is shorter than the decay time of the light in a scintillator or the electron-hole/collection time in a semiconductor, a pulse will appear whose height is proportional to the sum of the energies lost to the crystal by both interacting  $\gamma$ -ray (see Figure 11-8 for NaI(Tl)). Figure 11-9 shows the pulse-height spectrum using Ge(HP). The sum peak is not shown in this later figure. A single gamma interacting with the crystal produces only one pulse; whose height is affected by the type and number of interactions by the given  $\gamma$ -ray. If these coincidence effects are negligible, the measured monoenergetic pulse-height spectrum can be considered as a distribution of the probability of energy loss as a function of energy for the given  $\gamma$ -ray energy and source detector geometry.

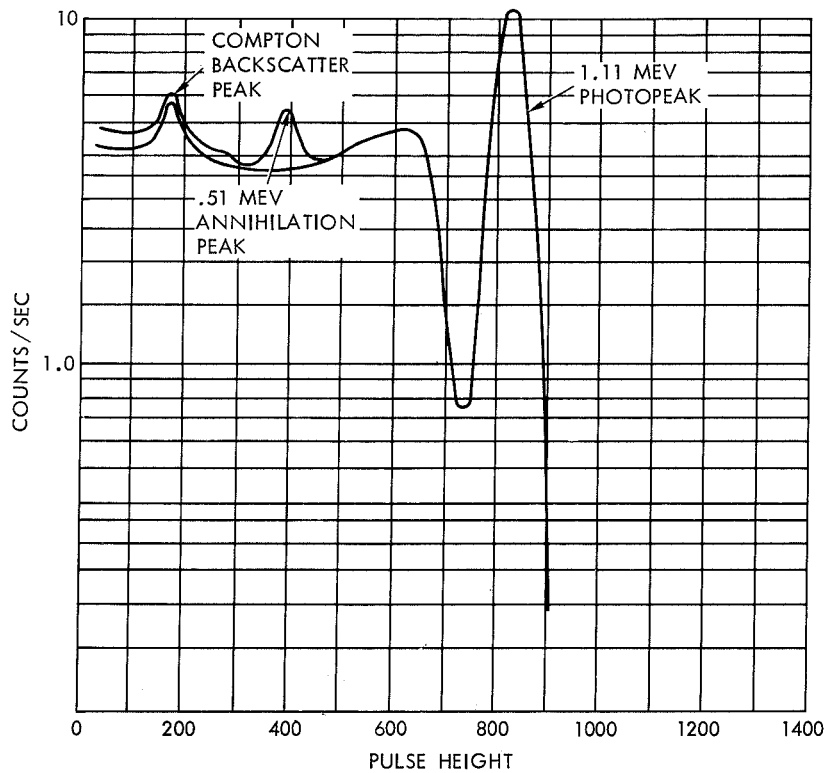


Figure 11-7.  $^{65}\text{Zn}$  at 0.24 cm from  $3 \times 3$  in.  $\text{NaI(Tl)}$  crystal. Scale about 1.3 keV/PHU.

4. Escape of high energy electrons. When very high energy (greater than about 10 MeV)  $\gamma$ -rays interact, the kinetic energy of the electrons may be great enough so that some of the electrons escape the detector without losing their total energy to the detector material. This tends to smear out the pulse-height spectrum and at high energies (greater than 15 MeV) the photopeak and the first and second escape peak merge.

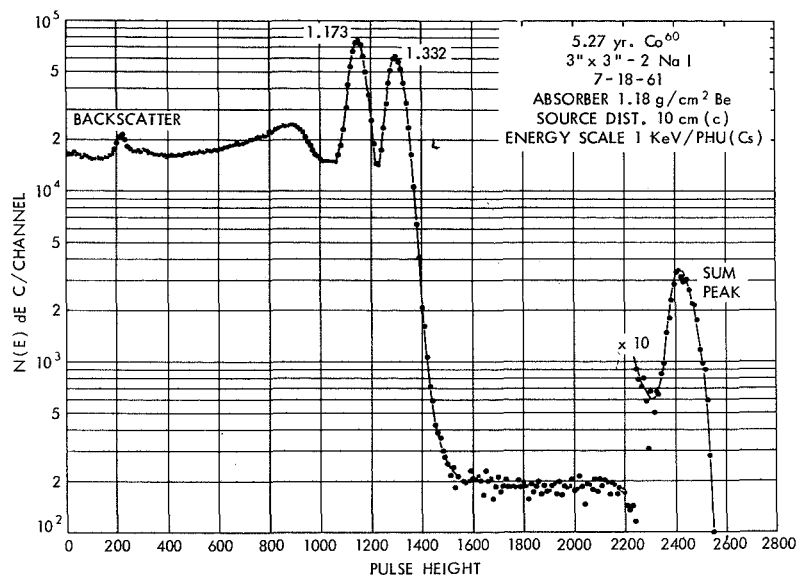


Figure 11-8.  $^{60}\text{Co}$   $\gamma$ -rays on  $3 \times 3$  in.  $\text{NaI(Tl)}$  crystal. Source at 10 cm; energy scale 1 keV/PHU (Cs).

If coincidence losses are negligible, the pulse-height distribution caused by a polyenergetic gamma flux will be a summation of the pulse spectra associated with the various monoenergetic components in the polyenergetic gamma flux. A simple example is shown in Figure 11-10. The pulse-height spectrum caused by a source that was a mixture of  $^{137}\text{Cs}$  (0.661 MeV) and  $^{51}\text{Cr}$  (0.320 MeV) was measured (Figure 11-10a). The pulse-height spectra of  $^{137}\text{Cs}$  and  $^{51}\text{Cr}$  were also measured separately obtaining the pulse-height spectra in Figure 11-10b. The sum of the monoenergetic spectra is also shown in Figure 11-10b, and is the same as the spectrum obtained in Figure 11-10a. The source strength of  $^{137}\text{Cs}$  and  $^{51}\text{Cr}$  were the same in both measurements. Theoretical calculation of detector response functions for  $\text{NaI(Tl)}$  crystals can be found in Seltzer (1975).

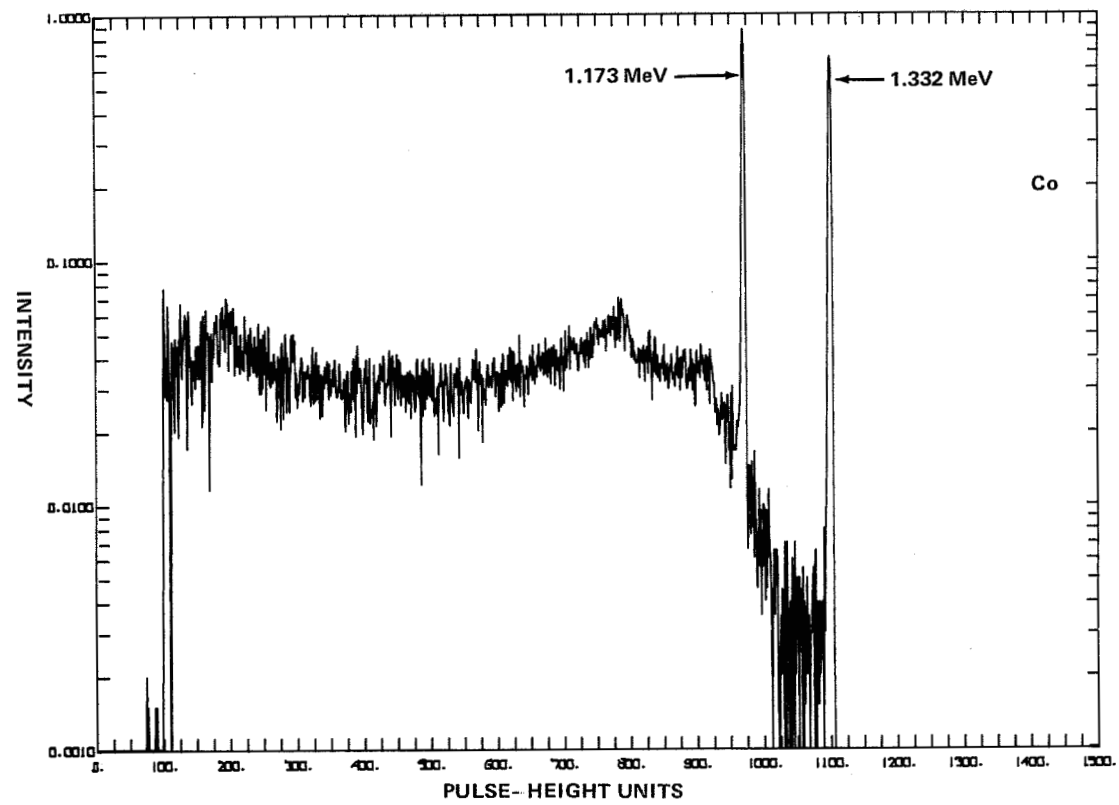


Figure 11-9.  $^{60}\text{Co}$  on 120 cc Ge (HP) detector. Source at 25 cm above a Ge(HP) detector.

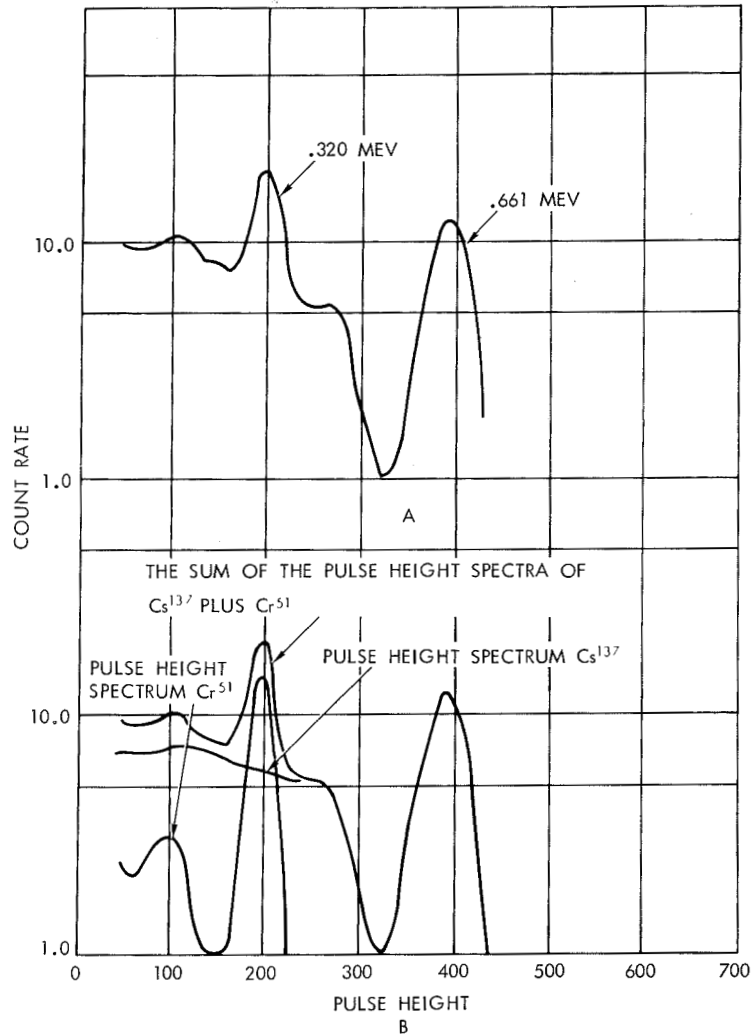


Figure 11-10. Pulse-height spectra of  $^{137}\text{Cs}$  and  $^{51}\text{Cr}$ ; using a  $3 \times 3 \text{ cm}$   $\text{NaI(Tl)}$  detector.

### DETECTOR EFFICIENCY

The response of a particular detector system can be evaluated in terms of a detection efficiency which depends on the geometry of the system and on the spatial and angular distribution of the incident flux being measured. Because source-to-detector distances in astronomical measurements are very much greater than

detector dimensions, spatial variations over the detector may be ignored. We use a rectangular coordinate system  $(x', y', z')$  fixed in the detector to describe positions within the volume of the detector system. We denote a spatially fixed coordinate system by the unprimed rectangular coordinates  $(x, y, z)$  and use  $(b, l)$  for the latitude and longitude angles. When one considers the application of the results derived in this section to  $\gamma$ -ray astronomy, the most convenient unprimed system will be the galactic system. The angles  $(b, l)$  will be used to describe the direction of the incident photons. The orientation of the detector system will be specified by giving the latitude and longitude of the  $z'$  and  $x'$  axes denoted by  $b_z', l_z'$  and  $b_x', l_x'$ , respectively.

### Definitions of Effective Cross-Sectional Area and Intrinsic Detection Efficiency

The geometry of a general situation is given in Figure 11-11. The  $x'$  and  $y'$  axes are not included in order to show more clearly the various angles and a photon flux from direction  $(b, l)$  entering the detector at point  $A(x', y', z')$ . The rectilinear path through the crystal along the incident photon direction is denoted by  $\overline{AB}$  with a distance  $\xi$ . We denote the photon flux which is differential in angle and energy by the quantity

$$f(\xi, b, l) = \frac{d^2 F}{d\Omega} d\xi \quad , \quad (11-15)$$

where

$$d\Omega = d(\sin b) dl \quad . \quad (11-16)$$

We can then compute  $C$ , the total number of photons per unit time and energy which will interact with the detector, by

$$C(\xi, b_z, l_z, b_x, l_x) = \int_{\Omega} \int_{s'} f(\xi, b, l) \times$$

$$\times \{1 - \exp[-\mu(\xi) \xi(B_z, l_z, b_x, l_x,$$

$$x', y', z', b, l)] dA_{\perp} d\Omega\}, \quad (11-17)$$

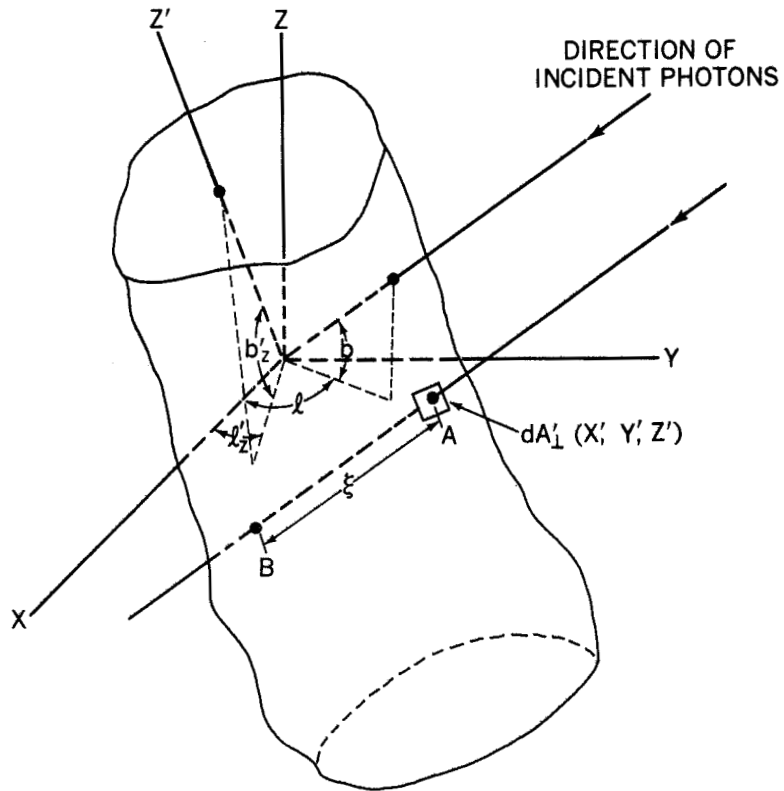


Figure 11-11. Geometric configuration for spatially fixed (unprimed) coordinate system and coordinate system fixed in the detector (primed).

where  $dA_{\perp}$  is the element of detector surface area perpendicular to the direction  $(b, l)$  at the point of entry  $A(x', y', z')$  and  $S'$  represents the integration over the surface of the detector where photons enter. The quantity,  $\mu$ , is the linear absorption coefficient which is energy dependent and represents then sum of the photoelectric, Compton, and pair production interactions. The quantity within the braces represents the probability that the photon will have at least one interaction within the crystal. Multiple interactions occur in times shorter than the decay of the scintillation produced in the detector and thus appear as a single interaction. These multiple interactions will change the amount of the energy deposited in the crystal but not the intrinsic efficiency.

The effective detector cross-sectional area is defined as

$$\eta = \frac{C}{\int_{\Omega} f d\Omega} \quad , \quad (11-18)$$

and the intrinsic detection efficiency as

$$\epsilon = \frac{C}{\int_{\Omega} \int_{s'} f d\Omega da_{\perp}} \quad . \quad (11-19)$$

The variability of  $\epsilon$  as a function of energy for three special flux distributions is illustrated in Figure 11-12 for a relatively symmetric crystal 10.16 cm long  $\times$  10.16 cm in diameter. More extreme shapes most likely will show greater differences because of increased proportions of short path lengths for an isotropic flux. Therefore, the quantities  $\eta$  and  $\epsilon$  are not useful in the case of an unknown photon distribution. They are also difficult to calculate for irregular detector geometries, but special cylindrical cases which are useful will be examined.

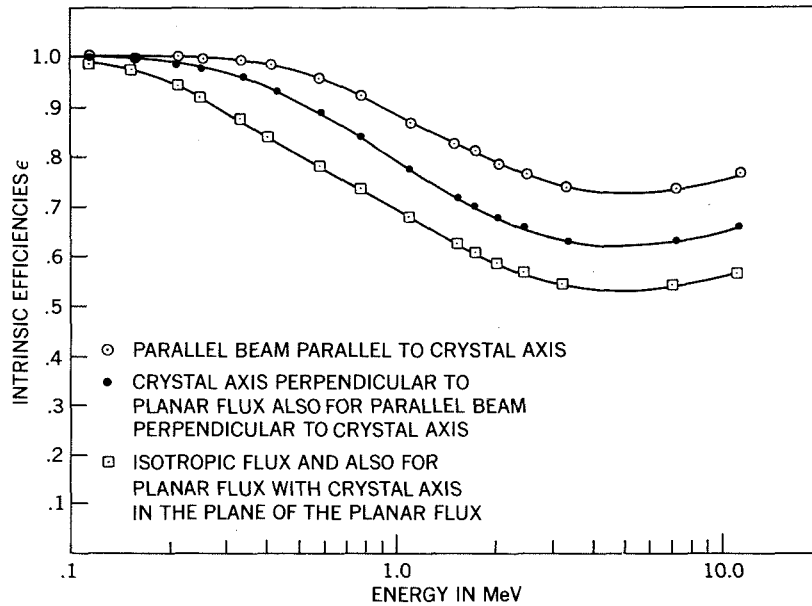


Figure 11-12. Intrinsic efficiencies as a function of energy for 10.16 cm  $\times$  10.16 cm (4 in.  $\times$  4 in.) cylindrical crystals.

### Response of a Cylindrical Detector to a Parallel Beam

We now specialize the geometry of the crystal to a right cylinder of height,  $H$ , and radius,  $R$ , with  $z'$  as the axis of symmetry and consider the flux distribution to be a plane wave coming from direction  $(b_0, l_0)$ . We do the plane wave case first since the results for a planar and an isotropic flux can be calculated in terms of the plane wave case. For a plane wave

$$f = P(\mathcal{E}) \delta(\sin b - \sin b_0) \delta(l - l_0) \quad (11-20)$$

Since we have cylindrical symmetry, the only angle of importance is the one between  $z'$  and the direction of the photon beam. We will denote this angle by  $\theta$  and it is given in terms of  $(b_0, l_0)$  and  $(b_{z'}, l_{z'})$  by

$$\cos \theta = \cos b_0 \cos b_{z'} \cos(l_0 - l_{z'}) + \sin b_0 \sin b_{z'} \quad (11-21)$$

and  $P(\xi)$  has units of photons/cm<sup>2</sup> s MeV. In this case we obtain

$$\begin{aligned}
 \eta(\xi, \theta) = & 2RH \sin\theta \left\{ 1 - \int_0^{1/2\pi} \cos\beta \left[ \exp\left(-\frac{2\mu R \cos\beta}{\sin\theta}\right) \right] d\beta \right\} \\
 & + \pi R^2 \cos\theta \left\{ 1 + \frac{4}{\pi} \int_0^{1/2\pi} \cos^2\beta \left[ \exp\left(-\frac{2\mu R \cos\beta}{\sin\theta}\right) \right] d\beta \right\} \\
 & - \frac{4R}{\mu} \sin\theta \cos\theta \left\{ 1 - \int_0^{1/2\pi} \cos\beta \left[ \exp\left(-\frac{2\mu R \cos\beta}{\sin\theta}\right) \right] d\beta \right\}
 \end{aligned} \tag{11-22}$$

for  $\tan\theta \geq 2R/H$ , and

$$\begin{aligned}
 \eta(\xi, \theta) = & 2RH \sin\theta \left\{ 1 - \int_{\alpha}^{1/2\pi} \cos\beta \left[ \exp\left(-\frac{2\mu R \cos\beta}{\sin\theta}\right) \right] d\beta \right. \\
 & \left. + \sin\alpha \left[ \exp\left(-\frac{2\mu H}{\cos\theta}\right) \right] \right\} \\
 & + \pi R^2 \cos\theta \left\{ 1 + \frac{4}{\pi} \int_{\alpha}^{1/2\pi} \cos^2\beta \left[ \exp\left(-\frac{2\mu R \cos\beta}{\sin\theta}\right) \right] d\beta \right. \\
 & \left. - \frac{2}{\pi} \left( \alpha + \frac{1}{2} \sin 2\alpha \right) \left[ \exp\left(-\frac{2\mu H}{\cos\theta}\right) \right] \right\} \\
 & - \frac{4R}{\mu} \sin\theta \cos\theta \left\{ 1 - \int_{\alpha}^{1/2\pi} \cos\beta \left[ \exp\left(-\frac{2\mu R \cos\beta}{\sin\theta}\right) \right] d\beta \right. \\
 & \left. - \sin\alpha \left[ \exp\left(-\frac{2\mu H}{\cos\theta}\right) \right] \right\},
 \end{aligned} \tag{11-23}$$

for  $\tan\theta \leq 2R/H$ , where  $\cos\alpha = H/2R \tan\theta$  and  $\cos\beta = \xi/2R$ .  
The intrinsic detection efficiency is then given by

$$\epsilon_p(\theta) = \frac{\eta_p(\theta)}{2RH \sin\theta + \pi R^2 \cos\theta} \quad (11-24)$$

This case is useful when one is dealing with a single distant point source since the detector counting rate will be given by

$$C_{ps}(\xi, \theta) = \eta_p(\xi, \theta) P(\xi) \quad (11-25)$$

for a given photon energy  $\xi$  and by

$$C_{ps}(\geq \xi_T, \theta) = \int_{\xi_T}^{\infty} \eta_p P(\xi) d\xi \quad (11-26)$$

for all photons above a threshold energy  $\xi_T$ .

### Response of a Cylindrical Detector to a Planar Flux

For simplicity of calculation we consider the planar or disk-like flux to lie in the plane  $b = 0$ . In this case

$$f = J(\xi) \delta(\sin b) \quad (11-27)$$

and  $J$  has units of photons/cm<sup>2</sup> s MeV rad. We wish to consider only two orientations of the cylindrical detector. Case (1) The  $z'$  axis lies in the plane  $b = 0$  (i.e.,  $z : z' = 0$ ). Case (2) The  $z'$  axis is perpendicular to this plane (i.e.,  $z \cdot z' = |z| \cdot |z'|$ ). For case (1), we find from Equation (11-21) that  $\theta = l - l_z$ , and we can

choose  $l_z = 0$  without loss of generality. Then we have, by performing the integration in Equation (11-17),

$$C_J(\mathbb{E}, b_z = 0) = J(\mathbb{E}) \int_0^{2\pi} \eta_p(\mathbb{E}, \theta) d\theta \quad (11-28)$$

Since

$$\int f d\Omega = 2\pi J(\mathbb{E}) \quad , \quad (11-29)$$

and

$$\int_{\Omega} \int_{s'} f d\Omega dA_{\perp} = 4(2RH + \pi R^2) J(\mathbb{E}) \quad , \quad (11-30)$$

we obtain

$$\eta_J(\mathbb{E}, b_z = 0) = \frac{2}{\pi} \int_0^{1/2\pi} \eta_p(\mathbb{E}, \theta) d\theta \quad , \quad (11-31)$$

and

$$\epsilon_J(\mathbb{E}, b_z = 0) = \frac{\int_0^{1/2\pi} \eta_p(\mathbb{E}, \theta) d\theta}{(2RH + \pi R^2)} \quad . \quad (11-32)$$

For certain purposes, it is useful to define an effective geometric factor in this case by

$$G_J(\mathbb{E}, b_z = 0) = \frac{C}{J(\mathbb{E})} = 4 \int_0^{1/2\pi} \eta_p(\mathbb{E}, \theta) d\theta \quad . \quad (11-33)$$

We note that  $G_J$  has units of  $\text{cm}^2 \text{ rad}$ . For the second case we have from Equation (11-21) that  $\theta = 1/2\pi$  and it follows

$$C_J(\mathcal{E}, b_{z'} = 1/2\pi) = 2\pi J(\mathcal{E}) \eta_p[\mathcal{E}, (1/2)\pi] \quad , \quad (11-34)$$

$$\eta_J[\mathcal{E}, b_{z'} = (1/2)\pi] = \eta_p[\mathcal{E}, (1/2)\pi] \quad , \quad (11-35)$$

$$\int_{\Omega} \int_{s'} f d\Omega dA' = 4\pi RHJ(\mathcal{E}) \quad , \quad (11-36)$$

$$\epsilon_J[\mathcal{E}, b_{z'} = (1/2)\pi] = \frac{\eta_p[\mathcal{E}, (1/2)\pi]}{2RH} \quad , \quad (11-37)$$

and

$$G_J[\mathcal{E}, b_{z'} = (1/2)\pi] = 2\pi\eta_p[\mathcal{E}, (1/2)\pi] \quad . \quad (11-38)$$

### Response of a Cylindrical Detector to an Isotropic Flux

In the case of an isotropic flux

$$f(b, l, \mathcal{E}) = I(\mathcal{E}) \quad , \quad (11-39)$$

where  $I(\mathcal{E})$  has units of  $\text{photons}/\text{cm}^2 \text{ s MeV sr}$ . For simplicity of calculation and without any loss of generality we take the  $(x', y', z')$  system exactly coincident with the  $(x, y, z)$  system. Then we find from Equation (11-21) that  $\theta = (1/2)\pi - b_0$  and

$$C_1(\mathcal{E}) = 4\pi I(\mathcal{E}) \int_0^{(\frac{1}{2})\pi} \eta_p(\mathcal{E}, \theta) d(\cos\theta) \quad (11-40)$$

$$\eta_1(\mathcal{E}) = \int_0^{(\frac{1}{2})\pi} \eta_p(\mathcal{E}, \theta) d(\cos\theta) \quad , \quad (11-41)$$

$$\int_{\Omega} \int_s f d\Omega dA_{\perp} = 2\pi^2 RI(H+R) \quad , \quad (11-42)$$

and

$$\epsilon_1(\mathcal{E}) = \frac{2}{\pi R(H+R)} \int_0^{(\frac{1}{2})\pi} \eta_p(\mathcal{E}, \theta) d(\cos\theta) \quad . \quad (11-43)$$

In this case we also define an effective geometrical factor by

$$G_1(\mathcal{E}) = \frac{C_1(\mathcal{E})}{I(\mathcal{E})} = 4\pi \int_0^{(\frac{1}{2})\pi} \eta_p(\mathcal{E}, \theta) d(\cos\theta) \quad , \quad (11-44)$$

and  $G_1$  has units of  $\text{cm}^2 \text{ sr}$ .

Further details of these efficiency calculations can be found in Trombka et al. (1974).

## Peak Efficiency

The efficiencies as defined above relate to the total interaction. In the analysis of pulse-height spectra, it may be more appropriate to study the area under the photopeak only. This area can be determined much more precisely than the total area for a given  $\gamma$ -ray energy. There are two major reasons for the difficulty in obtaining the total area. First, it is rather difficult to eliminate all scattering effects due to the surrounding materials. These will appear as pulses in the Compton continuum. Second, pulse-height analyzers cannot direct all pulses down to zero pulse height, for below certain pulse heights the electronic noise dominates the spectrum.

For a monoenergetic  $\gamma$ -ray incident upon a detector, let

- $A_p$  = area under the photopeak
- $A_t$  = area under the total pulse-height distribution
- $\epsilon_p$  = Intrinsic peak efficiency
- $P_t^p$  =  $A_p/A_t$  and is called the peak-to-total ratio

then

$$\epsilon_p = P_t^p \epsilon \quad (11-45)$$

For right-cylindrical crystals the peak-to-total ratio  $P_t^p$  does not change significantly as a function of distance along the axis of the cylinder (Francis et al., 1957; Miller et al., 1958). Figure 11-13 is a typical plot of  $P_t^p$  as a function of energy for two different geometries. Figure 11-14 is a plot of the intrinsic peak efficiency for a 24 percent (relative to a  $3 \times 3$  in. NaI(Tl) scintillation detector at 1.33 MeV) Ge(Li) detector. The efficiency has been determined for a parallel beam of  $\gamma$ -rays incident on the surface of the detector and perpendicular to the cylindrical axis of the detector. (Gordon et al., 1979). At low energies (less than 0.1 MeV) the efficiency drops because of absorption in the dead layer of the detector. The intrinsic efficiencies for the detection of the first and second escape peak are also shown.

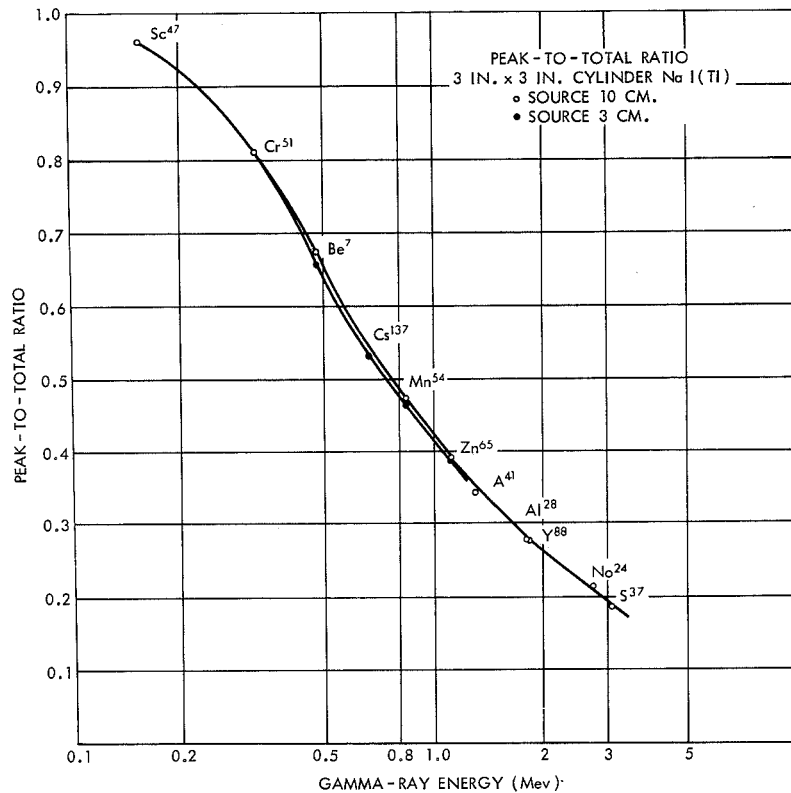


Figure 11-13. Peak-to-total ratio of a 3 x 3 in. cylinder of NaI(Tl) for source distances of 3 cm (closed points) and 10 cm (open points).

### Radiation Damage in Ge(HP) Detectors

Radiation damage in Ge(HP) detectors becomes a significant problem when they are used for extended spaceflight missions. Both high energy protons and high energy neutrons contribute to producing interstitial vacancy pairs in crystals by knocking atoms in the lattice out of their normal positions. Regions of very extensive damage can be produced. These regions may contain significant concentrations of donors and/or acceptor sites, and thus, provide trapping sites for holes and electrons. Radiation can cause degradation of the exposed surfaces which may lead to an increase in the detector leakage current. Radiation damage due to electrons and  $\gamma$ -rays seems to be negligible compared with that due to energetic neutrons and protons.

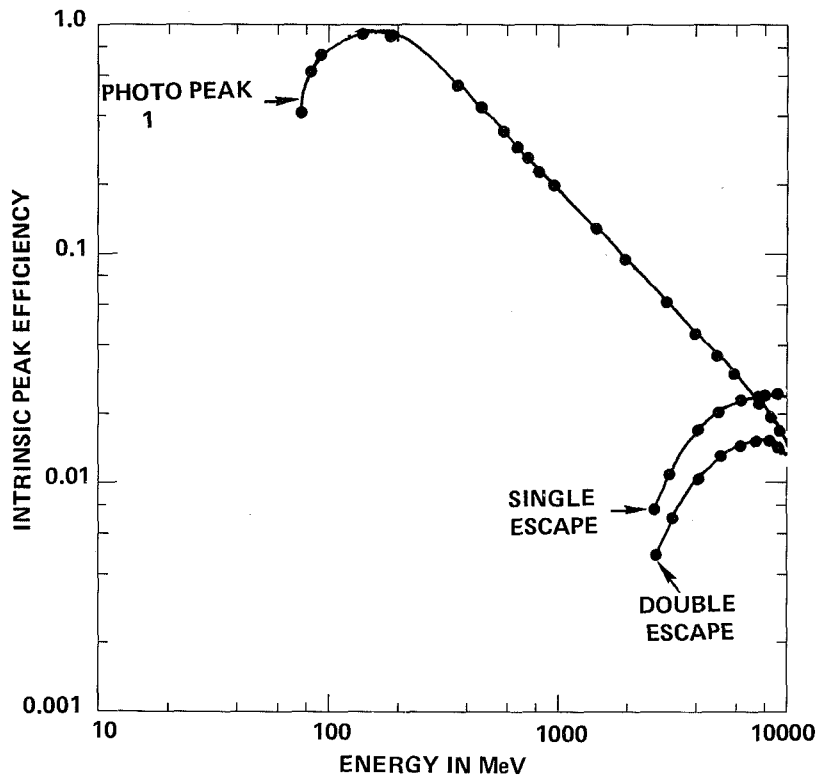


Figure 11-14. Intrinsic peak efficiency for a 100 Ge(HP) detector.

The radiation damage is reflected in the degradation of the detector resolution. This degradation can become observable when Ge detectors are exposed to fluxes about  $10^9$  neutrons  $\text{cm}^{-2}$  for fast neutrons and about  $10^7$  protons  $\text{cm}^{-2}$  for fast protons (Pehl et al., 1978a, 1978b). Fast neutron irradiation of Ge detectors produces predominantly defects which act as hole traps (Kraner et al., 1968). In conventional Ge(HP) and Ge(Li) coaxial detectors (*p*-type) used for  $\gamma$ -ray detection, the hole collection process dominates the signal, whereas when the electrode configuration is reversed (*n*-type), the electron collection process dominates the signal. Thus, the effects of radiation damage due to cosmic ray primaries and secondaries can be significantly reduced by using the *n*-type of material. In fact, it has been shown that the flux required to produce significant radiation damage can be increased by an order of magnitude (Pehl et al.,

1978a, 1978b). The *n*-type can only be produced in the Ge(HP) form.

Complete collapse of the energy resolution occurs when Ge(HP) detectors are annealed at 200°K after neutron irradiation; the acceptor concentration seems to increase greatly after such annealing. After neutron irradiation, detectors which may not exhibit radiation damage at liquid nitrogen temperatures may exhibit such damage after going through a room temperature thermal cycle.

Annealing Ge(HP) at 100°C for periods of hours has produced a very large recovery of energy resolution in radiation damaged detectors. Somewhat high temperature annealing (about 150°C) has been used and complete recovery has been achieved. Ge(Li) detectors, of course, cannot be annealed in order to improve energy resolution.

## DETECTOR FLIGHT SYSTEMS

The earlier chapters of this book have presented the results of  $\gamma$ -ray astrophysical observations. Measurements of  $\gamma$ -ray continua and discrete line spectra, and temporal and spatial distribution have required the design of different flight systems for  $\gamma$ -ray energies below 10 MeV. A number of such systems will be described here and for energies above 10 MeV in Chapter 12 a few typical systems will be described in order to illustrate methods of achieving the observational goals.

### The Apollo $\gamma$ -Ray Spectrometer Detector

The  $\gamma$ -ray detector assembly flown on Apollo 15 and Apollo 16 was composed of three major subassemblies: the electronics, the scintillation detector, and the thermal shield (Harrington et al., 1974). A partial view in cross section is shown in Figure 11-15. In flight this system was deployed at the end of a 7.5-meter boom in order to remove it far from both the spacecraft natural radioactivity and the spacecraft activity induced by the ambient cosmic ray flux.

The detector subassembly consisted of a right cylindrical NaI(Tl) crystal, about  $7 \times 7$  cm. A thin mantle of a scintillating plastic crystal, which was optically isolated from the primary NaI crystal, and both detectors were used in an anticoincidence

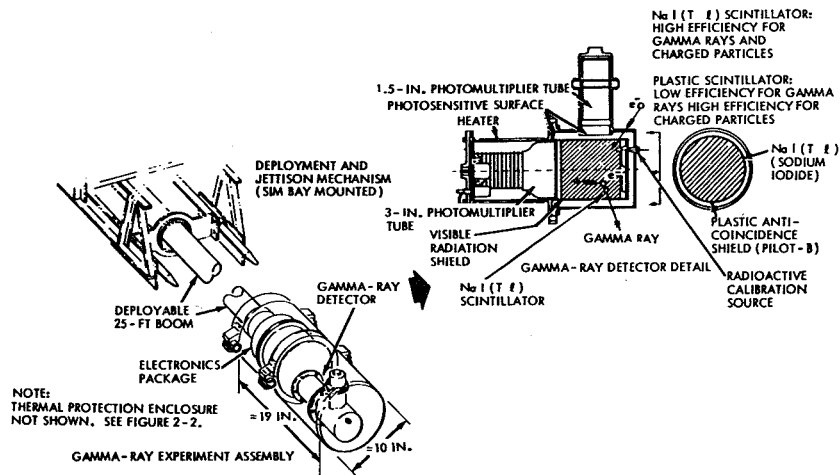


Figure 11-15. Apollo  $\gamma$ -ray detector detail.

mode. The plastic scintillator is transparent for all practical purposes to  $\gamma$ -rays with energies greater than 200 keV. Cosmic rays produce significant interactions in both detectors over the energy region of interest. Thus, the plastic shield will act as an active shield reducing the background produced by charged cosmic rays. In the case of Apollo, during translunar flight the cosmic ray background, relative to the  $\gamma$ -rays with energies greater than about 12 MeV, is about two orders of magnitude greater. Rejection efficiencies of the order of 99 percent for the anticoincidence systems would reduce the cosmic ray background as detected in the spectrometer to the same magnitude as the  $\gamma$ -ray flux. It was, therefore, difficult to detect the high energy (greater than 12 MeV)  $\gamma$ -ray flux on Apollo 15 and Apollo 16 during the translunar flight (Trombka et al., 1977).

Detector systems similar to the Apollo system were used by the United States on the Ranger Mission (Metzger et al., 1964) and by the Soviets during the Luna program (Vinogradov et al., 1968). The major difference in detector system design was in the method of observing the scintillations in the active plastic shield and inorganic central scintillation detector. The two systems were optically separated on the Apollo detector system and separate photomultipliers were used to observe the interactions. In both the Ranger and the Luna detector systems, a single photomultiplier was used to observe interaction in both the plastic and the inorganic scintillators. The fluorescence decay time in the

plastic and the inorganic detectors are significantly different. This is reflected as a difference in rise time observed at the output of the photomultiplier tube. The rise time of pulses produced in the plastic scintillator are much shorter than those produced in the inorganic scintillator, and that fact can then be used to discriminate between interactions occurring in the plastic detector and inorganic scintillator. This latter technique is called a "phoswitch."

### The Solar Maximum Mission (SMM) $\gamma$ -Ray Spectrometer

The  $\gamma$ -ray detector system carried aboard the SMM spacecraft is shown schematically in Figure 11-16 (Forrest et al., 1980).

The central (NaI(Tl)) detector system was designed with a large surface area in order to increase the sensitivity for detection of low intensity  $\gamma$ -ray flux. Furthermore, fine temporal resolution is required for studying the dynamics of  $\gamma$ -ray emission during solar flares. Good energy resolution is also of utmost importance in determining any line-broadening phenomena, as discussed in Chapter 4. Seven high resolution (7 percent FWHM for the 0.661-MeV line) detectors constitute the main portion of

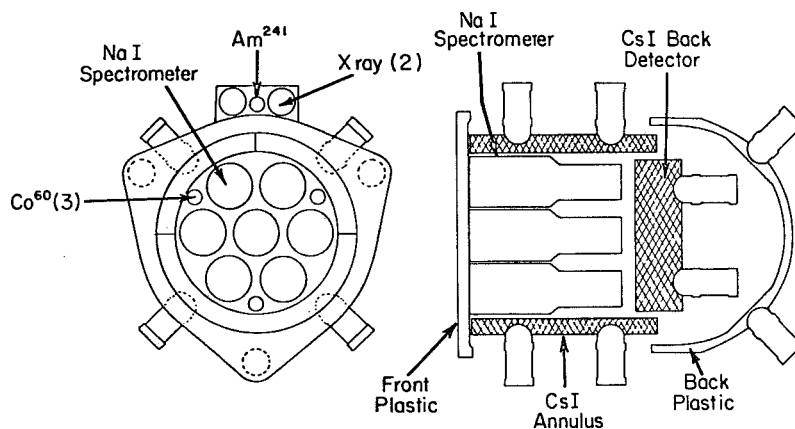


Figure 11-16. Schematic drawing of the SMM  $\gamma$ -ray spectrometer experiment showing the major subsystem components in top and cross-sectional side views (reprinted with permission from David J. Forrest, Forrest et al., 1980).

the  $\gamma$ -ray spectrometer system. Each of these components consists of a  $7.6 \times 7.6$ -cm integral line NaI(Tl) detector. The gain and zero of each of the seven detectors are automatically controlled so that all of the pulse-height scales are the same. An electronic servo loop is used to correct each output continuously to a common position. Three  $^{60}\text{Co}$  calibration sources (emitting 1.17-MeV and 1.33-MeV  $\gamma$ -ray energies) are used to achieve the automatic control (Forrest et al., 1972). A common pulse height analyzer could be used because all seven detectors were forced to a common gain. The presence of the  $^{60}\text{Co}$  did not significantly interfere with the measurements since transient events were being measured. Detailed background information can be obtained before and after the occurrence of a  $\gamma$ -ray burst associated, for example, with a solar flare. The calibration lines are subtracted by using these background measurements.

The gain of these detectors is set so that measurements are made up to 9 MeV (relative to the highest channel in the analog-to-digital converter). The lower level discriminator is set at 0.3 MeV. The digitized signals (out of the common ADC) are stored in two memories. One of these accepts only events associated with any single detector (singles mode) while the other memory accepts only events associated with two or more of the seven detectors (multiple mode). The two modes can be processed separately or summed.

The singles mode adds a further improvement to a discrete line  $\gamma$ -ray spectrometer. If the total energy of the  $\gamma$ -ray is lost in a given detector, it will appear as a signal in the photopeak. On the other hand, if a  $\gamma$ -ray is partially absorbed (in terms of energy loss to the detector), some of the energy, either by Compton scatter or annihilation radiation following pair production, may escape from the detector. The escaping  $\gamma$ -ray energy can interact in the other detectors or in the active shields and thus be rejected in the singles mode. The Compton continuum and first and second escape peaks can then be suppressed in the pulse-height spectra. The discrete lines will be enhanced, in a sense, relative to the continuum. In the sum modes, the total events occurring in the seven detector system can be obtained (multiple mode). This may be important for the detection of rather weak  $\gamma$ -ray fluxes where the total pulse-height spectrum may be needed to obtain statistically significant results.

The basic accumulation time for the singles mode and multiple mode pulse-height spectra is 16.38 seconds. Integral counts can be accumulated for 2-second intervals for three energy regions 4.2 MeV to 4.6 MeV, 4.6 MeV to 5.6 MeV and 5.6 MeV to 6.4 MeV. These regions can yield temporal information during flares concerning prompt  $\gamma$ -ray line emission from  $^{12}\text{C}$  and  $^{16}\text{O}$  at 4.4 MeV and 6.1 MeV, respectively, on a much finer time scale than can be differential energy spectral systems. There is one further integral window covering the energy range 300 keV to 350 keV which has an even finer time resolution (0.654 second) for fast time resolution study of hard X-ray bursts.

The energy range for spectral analysis can be increased up to 15 MeV by command. Evidence of the 15.11 MeV  $^{12}\text{C}$  line in very large flares can be investigated (Crannell et al., 1977). The thick CsI(Na) crystal at the back of the detector is also part of the high energy detector system. Events in the 10 to 100 MeV range occurring in the NaI and/or the CsI crystals are analyzed by separate pulse-height analysis. A matrix accumulation system is used in order to determine which of the observed interactions are associated with a single high energy detector and which elements are associated with  $\gamma$ -ray showers and interaction in more than one detector.

Two  $8 \times 0.6$ -cm thick NaI detectors are present. One has an Al filter and uses it to measure X-rays in the 10 to 80 keV range and the other has an Al-Fe filter and uses it to measure the X-ray flux in the 25 to 140 keV region. The basic purpose of the X-ray detectors is to provide corrected data for identification of the times when electron acceleration is occurring at the Sun. Photons and ions producing nuclear excitations are most likely to occur during these times.

Active plastic anticoincidence shields completely surround the  $\gamma$ -ray detector system. These shield elements are used to suppress the background produced by direct charged particle interactions, as well as the background  $\gamma$ -ray flux coming from all directions except from the Sun. The CsI and plastic elements shown in Figure 11-15 constitute the active shield. Care must be taken in using such active shields because they themselves can be a major source of induced  $\gamma$ -ray emission.

A similar type of shield detector design was used for the HEAO-C  $\gamma$ -ray spectrometer, except that the NaI(Tl) crystals

were replaced with Ge(HP) detectors (Jacobson, 1977; Mahoney et al., 1980). This system is capable of much better energy resolution than the one described above. Many of the background lines produced in the CsI shield have been observed during flight with this detector system.

An active  $\gamma$ -ray shield can be used in lieu of extending the detector system away from the spacecraft mass on a boom (the Apollo systems, as compared with the SMM system). The active shields are also used for obtaining directional resolution. The shield material contributes to the background. This background varies with time. For short times, the background can be relatively constant. In those cases where transient events of short duration are observed, the background subtraction obtained before and after an event can be used. For those cases where a weak constant source is to be observed, the background problem becomes quite serious. This is especially true in certain Earth orbits where the spacecraft passes through the South American Anomaly and where there is a varying geomagnetic field which will induce rather fast time variation in the induced background. The use of blocking active shields has been considered. In this design there are multiple detectors looking in the same direction. Half of these detectors are covered by an active shield, thereby allowing simultaneous source and background determination. The major difficulties with this approach are (1) the active blocking crystals become activated in space and contribute to the background and (2) the active shields are not completely opaque to the incident  $\gamma$ -ray flux. Furthermore, the  $\gamma$ -ray count rate can increase in the so-called "blocking crystal" configuration, compared with the unblocked detector. Great care must be taken in using such systems.

Some other examples of such detector systems can be found in Womack and Overbeck (1970), Nakano et al., (1973), and Metzger (1973).

### **The Compton Telescope**

A rather interesting detector design has been described by Herzo et al. (1975) which is based on the detection of a Compton scattering interaction of a  $\gamma$ -ray in a first detector followed by the detection of the Compton scattered photon in a second

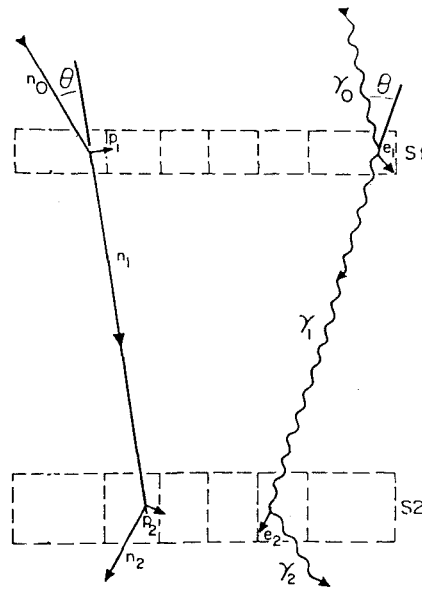


Figure 11-17. Schematic diagram of a double scatter telescope. Reprinted with permission from Herzo et al. (1975) and Nuclear Instruments and Methods.

detector. This method allows for the simultaneous determination of photon direction and energy. The method can be described using the two-dimensional representation of a so-called “double scatter” Compton telescope shown in Figure 11-17. Neutrons can also be detected in such a system.

The case for  $\gamma$ -ray detection is first considered. A  $\gamma$ -ray with energy  $\epsilon_0$  can interact in detector  $S_1$ ; and if the interaction is of the Compton scattering type, the scattered  $\gamma$ -ray  $\gamma_1$  emerges from  $S_1$  at some angle  $\theta$  with respect to the incident direction. The energy of the scattered  $\gamma$ -ray is  $\epsilon_1$ . The scattering occurs with an electron  $e_1$  at rest and  $E_1$  kinetic energy is imparted to this electron. Thus

$$\epsilon_0 = \epsilon_1 + E_1 \quad (11-46)$$

The Compton scattering process was discussed in Chapter 10 and the relationship between  $\theta$ ,  $\epsilon_1$ , and  $\epsilon_2$  was given in Equation (10-9), remembering that energy is expressed in electron rest mass energy units (i.e., 1.022 MeV is expressed as  $E = 2$  electron rest mass energy units). The scattering angle  $\theta$  can be written as

$$\theta = \cos^{-1} \left[ 1 - \left( \frac{1}{\epsilon_1} - \frac{1}{\epsilon_0} \right) \right]. \quad (11-47)$$

The  $\gamma$ -ray,  $\gamma_1$ , strikes the second detector,  $S_2$ , and can be totally absorbed or partially absorbed. If  $\gamma_1$  Compton scatters once in  $S_2$  and the scattered  $\gamma$ -ray,  $\gamma_2$ , escapes the detector,  $E_2$ , kinetic energy is imparted to electron  $e_2$  as a result of the scattering interaction and

$$\epsilon_1 = \epsilon_2 + E_2. \quad (11-48)$$

The pulse height measured is  $S_1$  due to the interaction of  $\gamma_0$  is  $E_1$ . Similarly,  $E_2$  is the pulse height measured in detector  $S_2$ . If, for example, total absorption of  $\gamma_1$  occurs in detector  $S_2$ , then  $\epsilon_2 = 0$ ,  $\epsilon_1 = E_2$  and Equation (11-47) can be written as

$$\theta_m = \cos^{-1} \left\{ 1 - \left[ \frac{1}{E_2} - \frac{1}{(E_1 - E_2)} \right] \right\}. \quad (11-49)$$

$E_1$  and  $E_2$  are measured. If total absorption does not take place in the second scintillator, the  $E_2 < \epsilon$  and true scattering angle  $\theta$  will be less than the values determined in Equation (11-47). Schönfelder et al. (1977) and Herzo et al. (1975) have developed a method for correcting the value  $E_2$  by a factor  $\alpha$ ; that is,  $\alpha E_2$  is used in Equation (11-47) for determining  $\theta$ . The factor  $\alpha$  is characteristic of the actual detector system and can be determined using Monte Carlo calculations.

The detector scintillators chosen for  $S_1$  and  $S_2$ , their thickness and separation are important in detector design. The detector  $S_1$  should have a large Compton cross section over the energy region of interest. If one studies the interaction cross section plate shown in Chapter 10, and Figures 10-1 to 10-6, it can be seen that lower  $Z$  materials (plastic scintillators) will be dominated by the Compton scattering over the energy domain 1 to 10 MeV. The detector,  $S_1$ , thus, should be liquid or plastic and thin to allow for single Compton scattering interactions. In order to achieve total absorption in  $S_2$ , on the other hand, total absorption is desirable. Thus, thicker and/or higher  $Z$  detector material should be used.

Higher energy neutron interaction processes are also shown

schematically in Figure 11-17. The incident neutron  $n_0$  scatters from a proton  $p_1$  in scintillator  $S_1$ . After scattering, the neutron with a lower energy can continue to move and strike detector  $S_2$ . The neutron can scatter again from  $P_2$  and the neutron  $n_2$  leaves the detector with a lower energy. The kinetic energy lost to the protons  $E_{p_1}$  and  $E_{p_2}$  is the measured pulse-height output signal from  $S_1$  and  $S_2$ . Over a large energy range (i.e., less than 100 MeV) neutron interaction can be differentiated from  $\gamma$ -rays by measuring the time of flight between the two detectors. The neutron velocities are less than the velocity of light for these energies. Above 100 MeV, the velocity of the neutron approaches the velocity of light and is, therefore, difficult to be differentiated. Below about 2 MeV, the proton recoil energy becomes too low to detect in the scintillation counters. This sets the lower limit to the energy sensitivity of the system.

The energy of the incident neutron  $E_{n_0}$  is given simply as

$$E_{n_0} = E_{p_1} + E_{n_1} \quad (11-50)$$

The scattering angle is given by

$$\tan\theta = \left( \frac{E_{p_1}}{E_{n_1}} \right)^{1/2} \quad (11-51)$$

Time-of-flight methods are used to reduce the background effects of high energy neutrons, as well as obtaining some information about the neutron energy spectrum in this energy domain. Gamma rays entering in any direction except through  $S_1$  can be rejected either by coincidence for the case of interaction in one detector or time-of-flight methods (when the  $\gamma$ -ray strikes detector  $S_2$  before  $S_1$ ). Active and passive shields surrounding the telescope are used to reduce the background produced by cosmic rays and the  $\gamma$ -ray emission from surrounding materials.

A number of Compton telescope designs have been proposed, tested, and flown. The following references describe a

number of such systems: Alvarez et al. (1973), Herzo et al. (1975), Schönfelder and Lichti (1975), Lichti et al. (1975), Schönfelder et al. (1977), Ryan et al. (1977) and White et al. (1977).

### Coded Aperture

Pinhole systems for imaging  $\gamma$ -ray-emitting objects have been considered for a number of years. Because the  $\gamma$ -ray fluxes are so low, a single pinhole would reduce the intensity far below other backgrounds, thus making such fluxes virtually undetectable. The concept of using a coded aperture was first introduced by Dicke (1968) and Ables (1968). The approach discussed in these papers involved replacing a single pinhole opening by many pinholes arranged randomly. The pinhole array is called the aperture. Each point on a self-luminous object deposits a shadow of the aperture on a focal plane. Subsequent processing of the picture yields the reconstructed image which should resemble the original object. The hole patterns of such an aperture significantly determine the signal-to-noise ratio obtained after image reconstruction. Many such patterns have been considered; but in this section, the Uniformly Redundant Array (URA), discussed by Fenimore and Cannon (1978), Fenimore (1978) and Cannon and Fenimore (1979), will be briefly described.

At this point, it must be emphasized that pinhole systems seem to be most applicable to soft  $\gamma$ -ray/hard X-ray measurements (i.e., less than 300 keV). This limitation can be attributed to a number of factors such as transparency of reasonable size pinhole arrays at higher energies, the problems of producing measurable pinhole arrays, and the importance of multiple Compton scattering at these energies. These factors contribute to a significant degradation in spatial resolution. Thus, for the higher energy domain, the other methods described in this chapter and Chapter 12 are more appropriate.

Essentially, a URA is a special kind of multiple pinhole mask in which the number of times a particular separation occurs between any pair of pinholes is the same for all separations. The separations are, thus, uniformly redundant. Ideally, URA's have the following properties: A point source is imaged through the URA mask onto a detector and casts a magnified shadow of the

URA mask on the detector. Subsequently, the same URA pattern, appropriately magnified, is used to correlate with the image to decode it and the reconstructed point source will be a spike superimposed on a constant background. This essentially means that the point spread function (autocorrelation function in this case) of a URA is a delta function with perfectly flat, but non-zero, side lobes. Furthermore, this flat and constant background can be removed if digital decoding is used. This is done by representing the holes in the URA as +1, and other locations as -1 instead of zero. This so-called balanced correlation method imposes the constraint that the point spread function be a delta function with zero side lobes. Because an extended object represents a superposition of point sources, the delta function point spread function is extremely important for the artifact-free reconstruction of extended objects.

In terms of a  $\gamma$ -ray telescope spectrometer the aperture is but one component. A position sensitive detector with spectroscopic capability is required. A Lixiscope (Low Intensity X-Ray Imaging Scope) is an example of such a detector (Yin et al., 1980). Figure 11-18 is a schematic diagram of the original Lixiscope detector (Yin et al., 1979). An incident X-ray and  $\gamma$ -ray image is first converted into a visible light image by a scintillator. The visible light image is then coupled by means of fiber optics to a micro-channel plate (MCP) visible light intensifier. The MCP intensifier, a high vacuum tube sealed by fiber-optic input and output face plates, is a self-contained unit. The incident visible light image from the scintillator is converted into an electron image by the photocathode deposited on the vacuum side of the input face plate. The electron image is focused by proximity to the input end of the MCP and multiplied within 12- $\mu$ m diameter microchannels, thus preserving positional integrity. The output electrons of the MCP are accelerated by about 5 KV to impinge upon an aluminized phosphor deposited on the output face plate to provide a much intensified visible light image.

In the design just described, single photons counting or energy sensitivity at the output was not possible due to limited gain and ion feedback problems associated with a single-state MCP. Using two MCP's in a chevron configuration, both single photon and energy discrimination was achieved (Yin et al., 1980). The energy resolution achieved is about a factor of two worse than that of a scintillation phosphor mounted on a single

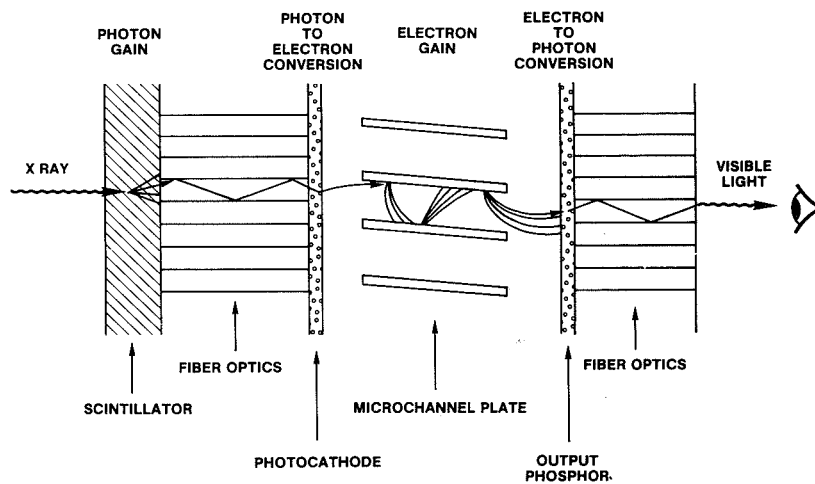


Figure 11-18. Schematic diagram of the original Lixiscope prototype.

photomultiplier tube. The important factor in the Lixiscope system is that both position and energy information can be achieved simultaneously.

The photon detection efficiency and the spatial resolution of the Lixiscope are governed by the scintillator; for example, a large number ( $10^2$ ) of visible light photons are produced in the scintillator by each absorbed X-ray, so that the probability of information loss after the initial absorption is negligibly small; and since the inherent spatial resolution of the MCP visible light image intensifier is about 30 line pair per mm, it is far superior to that of presently available scintillation materials and configuration for X-rays and  $\gamma$ -rays. A compromise must be reached between high quantum detection efficiency, which requires thick scintillators and high spatial resolution which requires thin scintillators. These constraints make the presently designed system useful only up to 250 keV.

Using the chevron configuration mentioned above, one can visually observe output scintillation due to single photon interaction. However, in the design of a  $\gamma$ -ray telescope for flight application, the output must be digitized. Digitizing vidicons and Lixiscope systems with digitizing anode outputs have been used. The feasibility of such a telescope design has been demonstrated (Yin et al., 1981).

## REFERENCES

- Ables, J.G., 1968, *Proc. Astro. Soc. Aust.*, **4**, 172.
- Adams, F., and Dams, R., 1970, *Applied Gamma-Ray Spectroscopy*, chap. 2 (New York: Pergamon Press, 1970), p. 21.
- Alvarez, L.W., Dauder, P.M., Smith, L.H., Buffington, A., Derenzo, S.E., Muller, R.A., Orth C., and Smoot, G., 1973, *The Liquid Xenon Compton Telescope, A New Technique for Gamma-Ray Astronomy*, serie. 14, issue 17. (Berkeley, Calif: Space Sciences Lab., 1973).
- Bertolini, G., and Coche, A., 1968, eds., *Semiconductor Detectors* (New York: John Wiley and Sons, Inc., 1968).
- Bird, L.L., 1956, *Tracerlog*, **78**, 12.
- Cannon, T.M., and Fenimore, E.E., 1979, *Appl. Opt.*, **18**, 1052.
- Crannell, C.J., Ramaty, R., and Crannell, H., 1977, *Proc. of the 12th ESLAB Symp.*, ESA SP-124, 213.
- Dicke, R.H., 1968, *Ap. J.*, **153**, L10.
- Fenimore, E.E., 1978, *Appl. Opt.*, **17**, 3562.
- Fenimore, E.E., and Cannon, T.M., 1978, *Appl. Opt.*, **17**, 337.
- Forrest, D.J., Higbie, P.R., Orwig, L.E., and Chupp, E.L., 1972, *Nucl. Instr. and Meth.*, **101**, 567.
- Forrest, D.J., Chupp, E.L., Ryan, J.M., Cherry, M.L., Gleske, I.U., Reppin, C., Pinkau, K., Rieger, E., Kanbach, G., Kinzer, R.L., Share, G., Johnson, W.N., and Kurfess, J.D., 1980, *Solar Phys.*, **65**, 15.
- Francis, J.E., Harris, C.C., and Trombka, J.I., 1957, *Variation of NaI(Tl) Detection Efficiencies with Crystal Size and Geometry for Medical Research*, ORNL 2204 (Oak Ridge, Tenn.:

Oak Ridge National Laboratory, 1979, College Park, Md.: Univ. of Md., Dept. of Chem., 1979), p. 225.

Gamble, R.L., 1955, Ph.D., Diss., Univ. of Texas.

Gordon, G.E., Walters, W.B., Zoller, W.H., Anderson, D.L., and Failey, M.P., *Non-Destructive Determination of Trace Element Concentrations*, Technical Report ORO-5173-008.

Harrington, T.M., Marshall, J.H., Arnold, J.R., Peterson, L.E., Trombka, J.I., and Metzger, A.E., 1974, *Nucl. Instr. and Meth.*, 118, 401.

Heath, R.L., Helmer, R.G., Schmittroth, L.A., and Cazier, G.A., 1965, *The Calculation of Gamma-Ray Shapes for Sodium Iodide Scintillation Spectrometers*, 39th ed., IDO 17017, AEC Research and Development Report, Physics, TID 4500.

Herzo, D., Koga, R., Millard, W.A., Moon, S., Ryan, J., Wilson, R., Zych, A.D., and White, R.S., 1975, *Nucl. Instr. and Meth.*, 123, 583.

Jacobson, A.S., 1977, *High Resolution Gamma-Ray Spectroscopy*, Paper presented at the 1977 Spring Meeting (Washington, D.C.: A.P.S., 1977).

Kelley, G.G., Bell, P.R., Davis, R.C., and Lazar, N.H., 1956, *Nucleonics*, 14, 53.

Kittel, C., 1953, *Introduction to Solid State Physics* (New York: Wiley, 1953).

Kraner, H.W., Chasman, C., and Jones, 1968, *Nucl. Instr. and Meth.*, 62, 173.

Lichti, G., Moyano, C., Schönfelder, V., 1975, *Proc. of the 14th Int. Cosmic Ray Conf.*, 4, 1423.

Mahoney, W.A., Ling, J.C., Jacobson, A.S., Tapphorn, R.M., 1980, *Nucl. Instr. and Meth.*, 178, 363.

- Metzger, A.E., 1973, in F.W. Stecker and J.I. Trombka, eds., *Gamma-Ray Astrophysics*, NASA SP-339 (Washington, D.C.: Government Printing Office, 1973) p. 97.
- Metzger, A.E., Anderson, E.C., VanDilla, M.A., and Arnold, J.R., 1964, *Nature*, **204**, 766.
- Miller, W.F., Reynolds, J., and Snow, W.J., 1958, *Efficiencies and Photofractions for Gamma Radiation on NaI(Tl) Activated Crystals*, ANL 5902, (Washington, D.C.: ANL, 1958).
- Mott, N.F., 1952, *Elements of Wave Mechanics* (Cambridge, Eng.: Cambridge University Press, 1952).
- Mott, M.E., and Sutton, R.B., 1958, in *Handbuch der Physik, Nucl. Instr. II.*, vol. XLV (Berlin: Springer-Verlag, 1958).
- Nakano, G.H., Imhof, W.I., Reagan, J.F., and Johnson, R.G., 1973, in F.W. Stecker and J.I., Trombka, eds., *Gamma-Ray Astrophysics*, NASA SP-339, (Washington, D.C.: Government Printing Office, 1973) p. 71.
- Neiler, J.H., and Bell, P.R., 1968, "The Scintillation Method" in  *$\alpha$ ,  $\beta$ , and  $\gamma$  Spectroscopy*, vol. I, ch. 5, ed. K. Siegbaum (Amsterdam: North-Holland Publishing Co., 1968), p. 245.
- Pehl, R.H., 1977, *Physics Today*, **30**, 50.
- Pehl, R.H., and Goulding, F.S., 1970, *Nucl. Instr. and Meth.*, **81**, 329.
- Pehl, R.H., Goulding, F.S., Landis, D.A., and Lenzlinger, M., 1968, *Nucl. Instr. and Meth.*, **59**, 45.
- Pehl, R.H., Varnell, L.S., Metzger, A.E., 1978a, *IEEE Trans. Nuc. Sci.* NS-25, no. 1, 409.
- Pehl, R.H., Madden, N.W., Elliott, J.H., Raudorf, T.W., Trammell, R.D., and Darken, Jr., L.S., 1978b, *Radiation Damage*

*Resistance Reverse Electrode of Coaxial Detectors*, LBL-8307 Lawrence Berkeley Lab. Tech. Report.

Price, W.J., 1958, *Nuclear Radiation Detector* (New York: McGraw-Hill, 1958).

Ryan, J.M., Dayton, B., Moon, S.H., Wilson, R.B., Zych, A.D., and White, R.S., 1977, *J. Geophys. Res.*, **82**, 3593.

Schönfelder, V., and Lichti, G., 1975, *J. Geophys. Res. Space Physics*, **80**, 3681.

Schönfelder, V., Graser, U., and Daugherty, J., 1977, *Ap. J.*, **217**, 306.

Seltzer, S.M., 1975, *Nucl. Instr. and Meth.*, **127**, 293.

Sietz, F., 1940, *The Modern Theory of Solids* (New York: McGraw-Hill, 1940).

Swank, R.K., and Buch, W.L., 1952, *Nucleonics*, **10**, 51.

Trombka, J.I., Metzger, A.E., Arnold, J.R., Matteson, J.L., Reedy, R.C., and Peterson, L.E., 1973, *Ap. J.*, **181**, 737.

Trombka, J.I., Vette, J.I., Stecker, F.W., Eller, E.L., and Wildes, W.T., 1974, *Nucl. Instr. and Meth.*, **117**, 99.

Trombka, J.I., Dyer, C.S., Evans, L.G., Bielefeld, M.J., Seltzer, S.M., and Metzger, A.E., 1977, *Ap. J.*, **212**, 925.

Vinogradov, A.P., Surkov, Yu. A., Chernov, G.M., Kirnozov, F.F., and Nazarkina, 1968, *Moon and Planets*, vol. 2, ed. A. Dolifus, (Amsterdam: North-Holland Publishing Company, 1968), p. 77.

White, R.S., Dayton, B., Moon, S.H., Ryan, J.M., Wilson, R.B., and Zych, A.D., 1977, *Ap. J.*, **218**, 920.

Womack, E.A., and Overbeck, J.W., 1970, *J. Geophys. Res.*, **75**, 1811.

Wright, G.T., 1954, *J. Sci. Instr.*, **31**, 462.

Yin, L., Trombka, J.I., and Seltzer, S., 1979, *Nucl. Instr. and Meth.*, **158**, 175.

Yin, L., Trombka, J.I., and Seltzer, S., 1980, *Nucl. Instr. and Meth.*, **172**, 471.

Yin, L., Trombka, J.I., Schmadebeck, R.L., Seltzer, S.M., and Bielefeld, M.J., 1981, *Proc. of the LA81 Symp. of the SPIE, Imaging Spectroscopy*, **268**, in press.



## Chapter 12

# Detectors for Energies Greater Than 10 MeV

### INTRODUCTION AND HISTORY

As noted in the last chapter, the detector telescopes used in  $\gamma$ -ray astronomy in general are more similar to particle detectors than to optical devices, since the high frequency of the radiation precludes the use of reflection or diffraction techniques, but the high energy content of each photon does enable them to be detected with scintillators, track imaging chambers, and solid state detectors. Within the  $\gamma$ -ray range, the basic design of the instrument changes as the energy of the  $\gamma$ -ray exceeds 10 to 20 MeV, and, therefore, moves from the region where the Compton effect predominates in the absorption of the  $\gamma$ -ray to that where electron pair production is most important. The electron pair process is a relatively attractive one from a  $\gamma$ -ray detector point of view, since essentially all of the  $\gamma$ -ray energy goes into two charged particles in one interaction, and a clear signature of the  $\gamma$ -ray can be recorded. Thus, in the energy range from 10 or 20 MeV to several times  $10^4$  MeV,  $\gamma$ -ray telescopes are usually built so that the electron pair may be seen and the properties of the electrons measured. Most of this chapter will be devoted to a discussion of these instruments.

As the  $\gamma$ -ray energy approaches  $10^5$  MeV, the intensities of celestial  $\gamma$ -rays become too low to be seen with space telescopes. (At present the upper limit for satellite experiments is only about  $3 \times 10^3$  MeV, but during the 1980's this limit should be extended upward by about a decade with the aid of much larger detectors.) Above  $10^5$  MeV, the energy of the individual photons is sufficiently high that they may be observed by telescopes on the

ground at night. This is accomplished by recording the atmospheric Čerenkov radiation emitted by relativistic charge particles produced as secondaries in the electromagnetic cascade that results from the interaction of the energetic photon with the atmosphere. This technique is only useful for examining source regions which are quite small in size, since the observations must be made against a high background of Čerenkov radiation light pulses produced by the isotropic charged particle cosmic radiation. The photon component from a source region will then appear as a spatial anisotropy in the light pulse distribution.

A number of factors have combined to cause the  $\gamma$ -ray realm to be the last of the major regions of the celestial electromagnetic spectrum to be examined. The interaction length for a  $\gamma$ -ray in the atmosphere is a small fraction of the total atmospheric depth. At first thought this may seem strange since  $\gamma$ -rays can travel through the entire disk of the galaxy with only about a 1 percent chance of being absorbed, while light can penetrate only about one-tenth of the distance from the Sun to the center of the galaxy. The explanation lies in the form of the matter. Light is strongly absorbed by the interstellar dust, but is little affected by the gas of our atmosphere. For  $\gamma$ -rays it is primarily the total amount of matter that is important, although the nuclear charge of the matter is also a factor, and there is almost  $10^4$  times as much matter along a path from the top of the atmosphere to ground level as there is along a typical path through the disk of the galaxy. Because the primary  $\gamma$ -rays interact in the atmosphere long before they reach the ground, it was not until the advent of scientific balloons and satellites that observations of the primary radiation could be made. Further, within the atmosphere another problem exists, namely the background of secondary  $\gamma$ -rays produced by cosmic rays interacting in the atmosphere. Even on very high altitude balloons carrying  $\gamma$ -ray telescopes to residual atmospheric pressures corresponding to only 1.5 to 4 g cm<sup>-2</sup>, this background makes observations of the very small celestial fluxes extremely difficult. In fact, at balloon altitudes only a few of the strongest celestial sources are visible above the atmospheric background. Finally, the very low fluxes have forced the development of rather large, sophisticated detectors and have required relatively large observing times. It is the

combination of the atmospheric background and the long observing times required which has forced high energy  $\gamma$ -ray astronomy to depend on satellite experiments for most of its observations.

It was recognized almost from the beginning that a high energy  $\gamma$ -ray telescope had to identify the electron pair unambiguously if it were to be successful, because the relatively rare  $\gamma$ -ray has to be clearly separated from the high background of charged particle cosmic radiation and the charged and neutral secondaries. Further, as was just suggested, the detecting instrument must be designed to record the  $\gamma$ -interactions selectively and have a very high efficiency for the rejection of other events. In addition, the detector must be able to provide information on the direction of arrival of the  $\gamma$ -ray and a measurement of its energy. Finally, the low flux demands that the detection efficiency must be high.

The earliest experiments developed in the late 1950's and early 1960's were of two basic types: (1) oriented nuclear emulsion stacks and (2) counter telescopes with anticoincidence shields. It was soon realized that celestial  $\gamma$ -ray intensities were quite low, making simple nuclear emulsion experiments impractical; but nuclear emulsions did have the property of being track imaging detectors, which in the form of spark chambers were to become the heart of the later  $\gamma$ -ray telescopes, and they led to upper limits approaching  $10^{-3}$  photons ( $E > 100$  MeV)  $\text{cm}^{-2}\text{s}^{-1}$  (Fichtel and Kniffen, 1965). The first of the counter telescopes to be flown in space was a scintillator-Cerenkov counter detector flown on Explorer 11 (Kraushaar and Clark, 1962; and Kraushaar et al., 1965). An improved version of the detector was flown on OSO-3 and led to the first certain measurements of celestial  $\gamma$ -rays. This latter detector (Clark et al., 1968) is shown in Figure 12-1. The top sandwich of crystal scintillators acts both as a converter of  $\gamma$ -rays and as part of the telescope defining the solid angle of the incident  $\gamma$ -ray. The other half of the telescope is the lucite Cerenkov detector, which responds to the Cerenkov light produced by one or both of the electron-positron pair particles produced in the converter, and is in coincidence with the scintillator sandwich. The detector system is surrounded by a large, very efficient anticoincidence dome to reject charged particles. Other scintillator-Cerenkov  $\gamma$ -ray telescopes were flown on Proton 2 and Cosmos 208, by Bratolyubova-Tsulukidze et al. (1969), on OSO-1 by Fazio and Hafner (1967), and on OSO-3 by Valentine et al. (1969).

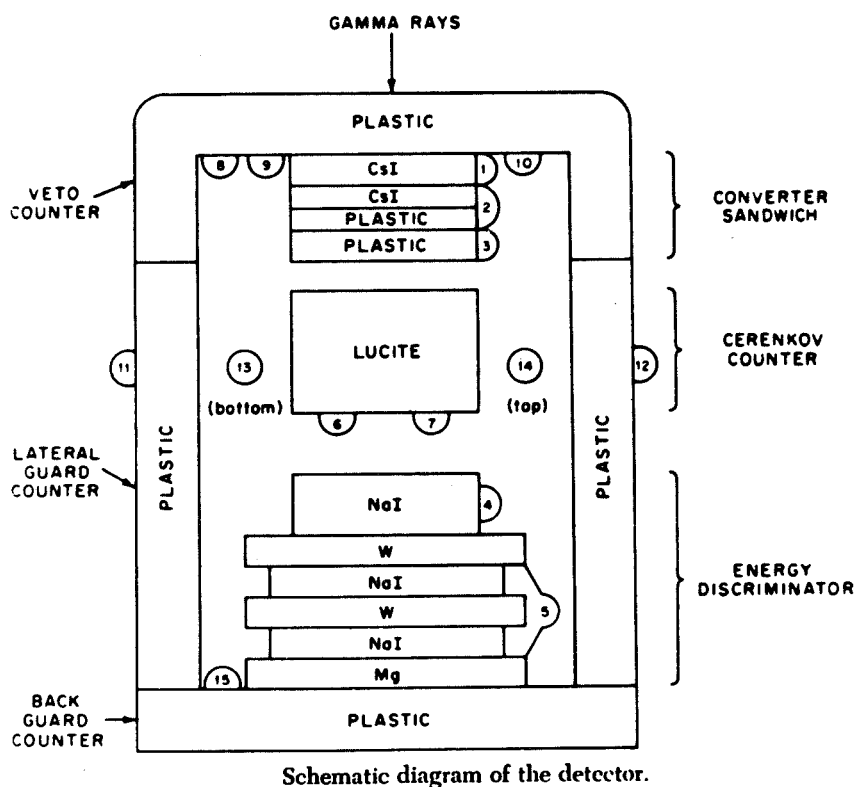


Figure 12-1. High energy  $\gamma$ -ray detector flown by Clark et al. (1968; reprinted with permission from Clark and the Canadian Journal of Physics) on OSO 3. This figure originally appeared in the Canadian Journal of Physics. This instrument led to the first certain measurement of high energy celestial  $\gamma$ -rays.

It became apparent, however, that more complicated techniques using picture-type detectors and large areas were required to see  $\gamma$ -ray point sources. Several investigators in the first part of the 1960's turned to the spark chambers as the heart of the high energy  $\gamma$ -ray detector system. A set of spark chambers provides a high discrimination picture-type device, which allows the experimenter to separate the desired electron-positron pairs from the other events which might satisfy the trigger conditions of the

telescope. Generally, the spark chamber assembly in a  $\gamma$ -ray telescope is surrounded by an anticoincidence system, and is triggered by a directional telescope coincidence signal in the absence of a signal from the surrounding anticoincidence detector. Figure 12-2 shows the SAS-2  $\gamma$ -ray telescope (Derdeyn et al., 1972), which is an example of this type of detector system.

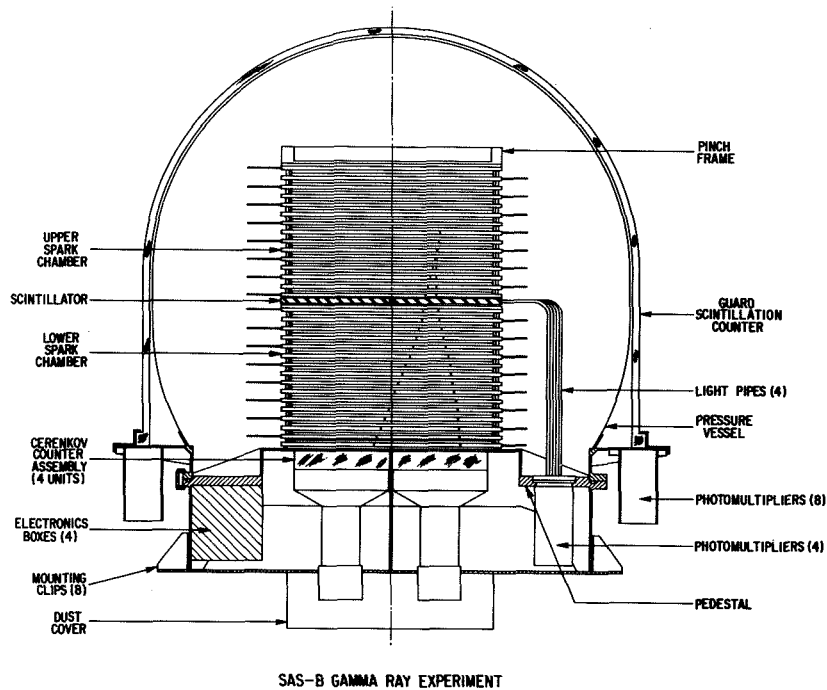


Figure 12-2. A schematic diagram of the  $\gamma$ -ray telescope flown on SAS-2 (Derdeyn et al., 1972).

Several different types of  $\gamma$ -ray telescopes have been developed and flown on high altitude balloons. The high altitude, thin (typically less than one thousandth of an inch) polyethylene balloon of large dimensions (typically 10 to 30 million cubic feet in volume when fully inflated at ceiling, although some of even larger dimensions have been flown) has proved a great asset to  $\gamma$ -ray astronomy in providing a means to place instruments above most of the atmosphere and to test detectors in an environment

similar to space. Figure 12-3 shows a high altitude balloon carrying a  $\gamma$ -ray detector just after launch.

Five distinctly different types of image chambers have been developed to the point of being included in a  $\gamma$ -ray telescope. They are the conventional optical spark chamber, the vidicon system, the sonic spark chamber, the proportional counter, and the multiwire magnetic core digitized spark chamber. Optical spark chambers using cameras and film were built and flown by several groups (Cobb et al., 1965; Frye and Smith, 1966; Board et al., 1968; and Neil et al., 1969). Vidicon systems were developed for the TD-1 satellite (Voges et al., 1973) and also for balloons (Helmken and Fazio, 1966; Fazio et al., 1968). A vidicon system will also be used on GAMMA-I. In this detector, the film is eliminated by using a vidicon tube which records the spark picture electronically. A somewhat different technique is used in the sonic chamber, which employs microphones to record the position of the spark through accurate timing signals. A chamber of this type was developed for a  $\gamma$ -ray telescope by Ogelman et al. (1966) and flown successfully on a balloon. A small sonic chamber was the first spark chamber in space, being flown on OGO-E by Hutchinson et al. (1969). Another  $\gamma$ -ray telescope including a spark chamber was flown on Cosmos 264 by Volobuev et al. (1969). A 4-gap spark chamber was placed under a one radiation length converter with the main objectives of the spark chamber being to see the shower development. A  $\gamma$ -ray telescope using proportional counters was developed by Albats et al. (1977) and flown on balloons.

Magnetic core spark chambers for  $\gamma$ -ray telescopes were developed at both the Goddard Space Flight Center (Ehrmann et al., 1967; Ross et al., 1969) and the Max-Planck Institute für Extraterrestrische Physik (Mayer-Hasselwander et al., 1972), proved on balloon flights, and then flown successfully in the SAS-2 (Derdeyn et al., 1972) and COS-B (Bignami et al., 1975)  $\gamma$ -ray telescopes, respectively. A magnetic core spark chamber system is also to be used on the planned GRO mission. The SAS-2 satellite provided the first detailed knowledge of the  $\gamma$ -ray sky and indication of the ultimate promise of  $\gamma$ -ray astronomy, while COS-B, following about three years later, significantly extended this knowledge, as has been seen in early chapters. These instruments will be described in detail in the Experimental Approach section of this chapter.

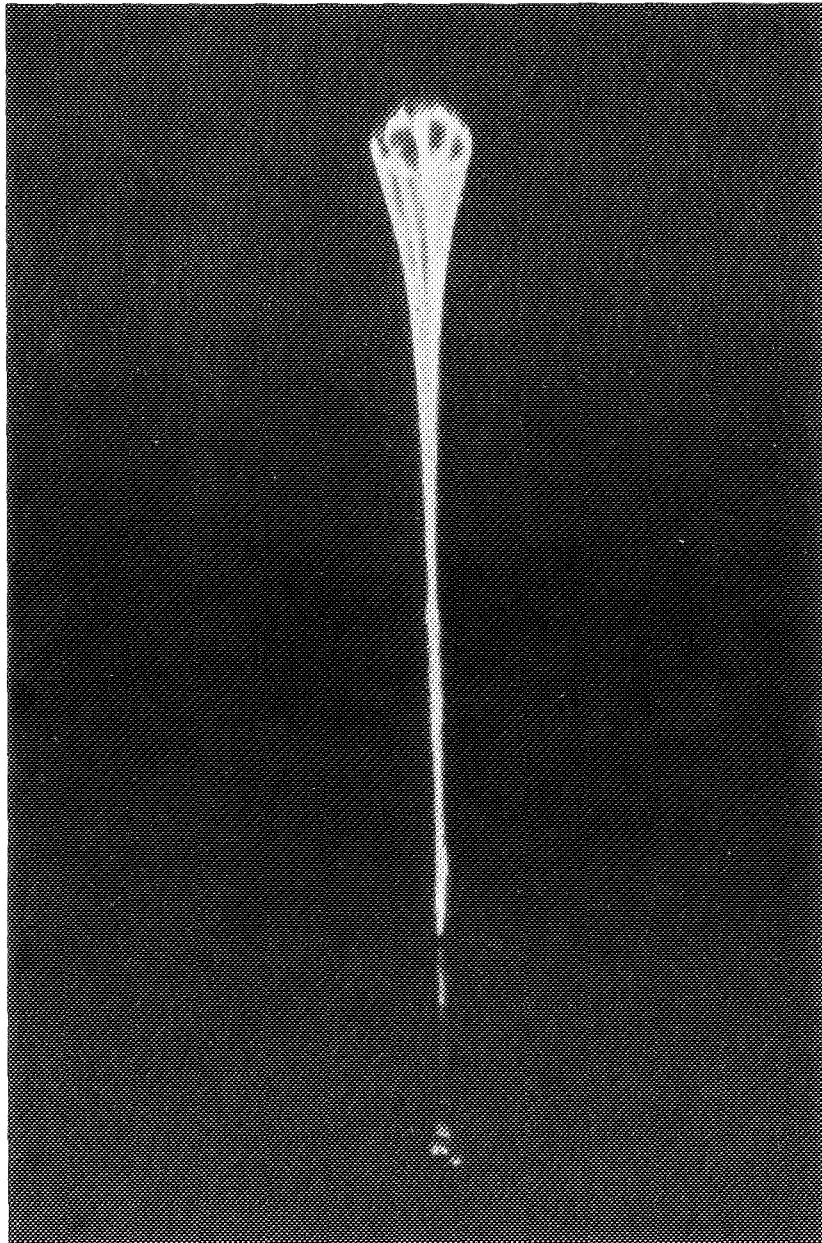


*Figure 12-3. A thin high altitude balloon rising through the atmosphere just after launch carrying a high energy  $\gamma$ -ray detector of the Goddard Space Flight Center. At float altitude, the balloon will have filled out to an approximately spherical shape.*

During the same period that  $\gamma$ -ray experiments were being developed to detect radiation in the 10 to  $10^4$  MeV range, work was proceeding on the ground to search for  $\gamma$ -rays above  $10^5$  MeV. The emission of Čerenkov light radiated by electrons in electromagnetic cascades in the atmosphere was discovered by Galbraith and Jelley (1953, 1955), who showed that light pulses from an air shower were detectable above the night sky background. Attempts were made in the 1960's and 1970's to detect point sources which could then justifiably be considered  $\gamma$ -ray sources since the distribution of arrival directions of primary charged particles in the same energy range which can initiate similar showers are diffuse. The basic concept of this type of detector is that a large steerable mirror focuses the light which is then recorded, normally by a set of photomultiplier tubes. Several variations to the basic technique have been developed and these are summarized by Porter and Weekes (1978). In spite of the very low flux levels in this energy range, it is now generally accepted that a few very high energy  $\gamma$ -ray sources have been detected by this general technique; these are the Crab pulsar, Cygnus X-3, and Centaurus-A.

At energies above a few times  $10^7$  MeV, it is possible for the secondary charged particles from a  $\gamma$ -ray induced shower to reach sea level. Electromagnetic cascades are expected to have a relatively small number of muons compared to cosmic ray-nucleon-induced showers; therefore, it was hoped that, in spite of the very low  $\gamma$ -ray fluxes, a point source might be detectable above the charged particle background. Thus far no clear evidence for a  $\gamma$ -ray source detected by this technique exists, and this experimental approach is no longer being strongly pursued.

## THE HIGH ENERGY GAMMA RAY INTERACTION

The basic interaction of the high energy  $\gamma$ -ray leading to an electron pair was discussed in Chapter 10. This treatment will be extended somewhat here to emphasize a few points which are particularly relevant to the design of a high energy  $\gamma$ -ray detector.

As in the case of radiation processes, the probability of a pair production interaction per radiation length depends only very slightly on atomic number or  $Z$ , particularly at high energies.

However, as shown in Figure 12-4, the importance of the Compton interaction in terms of the interaction probability per radiation length varies strongly with the nuclear charge of the material in which the interaction occurs. This feature results from the Compton interaction being basically one between a photon and electron, and therefore, the Compton process is proportional to  $Z$  rather than  $Z(Z + 1)$ . Thus, as the figure shows, the pair production process can be enhanced relative to the Compton process by using a high  $Z$  material in the detector, and this is normally done in high energy  $\gamma$ -ray detectors, since the pair production process is a more desirable one on which to make measurements.

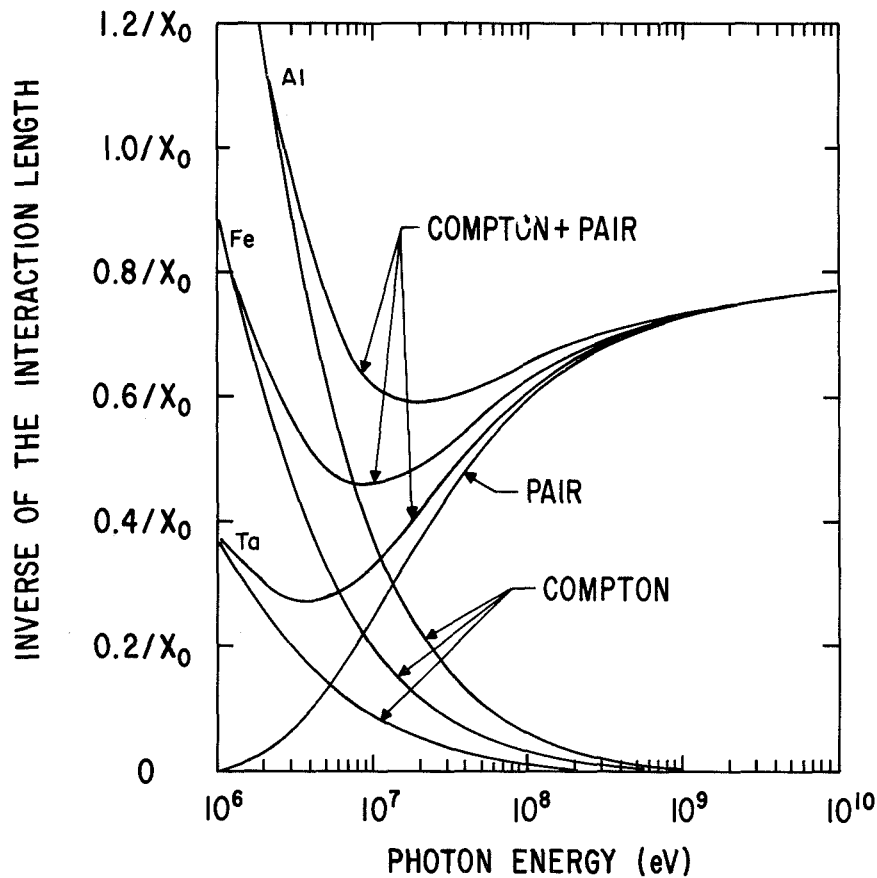


Figure 12-4. The inverse of the interaction length in terms of radiation lengths  $X_0$  for the Compton and pair production processes for three different materials.

The properties of the  $\gamma$ -ray must, in practice, be determined by measurements on the two secondary electrons. (At present, it does not seem practical to measure the very small fraction of the energy and momentum given to the target nucleus.) It is, of course, not possible to measure the electrons at the instant they interact in the detectors or without disturbing them. Hence, it is important to consider what happens to the secondary electrons. An electron undergoes a large number of Coulomb collisions as it passes through matter most of which produce very small angle deflections. Both the energy loss and the electron scattering are functions of the radiation length; thus, for a fixed distance measured in radiation lengths, they are unaffected by the selection of material. If the relevant layers in the detector are kept very thin so that energy loss is negligible over the length of the measurement of the electron's direction, and if there has not been a very improbable bremsstrahlung interaction in which a significant amount of energy has gone to a secondary photon, the mean square angle of scattering for an electron is given to a good approximation by the equation

$$\langle \theta^2 \rangle = \left( \frac{E_0}{\beta c P_e} \right)^2 \frac{x}{X_0} \quad (12-1)$$

where  $X_0$  is the radiation length,  $x$  is the distance transverse in radiation lengths, and  $E_0$  is approximately 21 MeV (Rossi, 1956). In any particle detector then, the scattering which occurs before the electron trajectories can be determined increases the uncertainty with which the arrival direction of the  $\gamma$ -ray is determined.

In attempting to measure the total energy of the photon by stopping the electron in an absorber such as a scintillator of some type, it is important to remember that not only the electron and positron must be absorbed, but also if an accurate energy estimate is to be obtained, the secondary bremsstrahlung radiation, and particularly, at low energies, the two 1/2 MeV photons formed

when the positron comes to rest and annihilates with an electron in the material. An alternate method for estimating the energy is to measure the average Coulomb scattering angle of each electron.

At high energies ( $> 10^5$  MeV) the emission from the cascade shower produced by the  $\gamma$ -ray in the atmosphere is used to study the properties of the  $\gamma$ -radiation study. When a very high energy photon interacts in the atmosphere and produces an electron pair, the secondary very high energy electrons in turn interact losing most of their energy through radiation. The photons in the  $\gamma$ -ray region in turn interact through either the pair formation or the Compton process. This sequence continues, and an electron-photon cascade develops. At each step the number of electrons and photons increases and their average energy decreases until the electrons' energies are sufficiently low that collision losses become more important than radiation. Their energy then goes largely into ionization and excitation of atoms. In the energy range from  $10^5$  to  $10^8$  MeV the secondary particles are heavily absorbed and detection of the shower particles is difficult. Further, the separation of the  $\gamma$ -ray from the enormously greater number of primary charged particles is very complex, although attempts have been made (O'Sullivan et al., 1978).

The Čerenkov light radiated by the electrons in the shower is not absorbed and may be detected on the ground on Moonless, clear nights at a dark site. Whereas the  $\gamma$ -ray shower Čerenkov light still has to compete on essentially equal terms with the much more numerous cosmic ray electron shower Čerenkov light events, the cosmic ray nucleons are somewhat less efficient in the production of Čerenkov light. The flux of optical Čerenkov photons from an air shower of even  $10^8$  MeV is modest, being only about  $10^3$  photons  $m^{-2}$  within 100 to 200 m of the shower axis (Porter and Weekes, 1978); nonetheless, as will be described in the next section of this chapter, it is possible to obtain useful results from this process.

## EXPERIMENTAL APPROACH

As the last two sections have suggested there are two quite different approaches to the detection of  $\gtrsim 10$  MeV  $\gamma$ -rays depending on the energy range, and each of these will be treated in this section. The discussion will be limited to the recent experimental

approaches and the improvements to be expected in the near future in these methods.

### **The 10 to $10^5$ MeV Region**

The  $\gamma$ -ray satellite instruments flown on SAS-2 and COS-B are quite similar in concept although there are some differences. They will be used as the examples of the high energy  $\gamma$ -ray telescopes of the 1970's. These instruments covered only a portion of this energy range primarily because of the limited size and weight available. Two high energy  $\gamma$ -ray satellite instruments, which, it is hoped, will fly on satellites in the 1980's, namely those on GAMMA-I and the Gamma Ray Observatory (GRO), will have greater capability as will also be described here.

The first of the satellites mentioned above was the high energy  $\gamma$ -ray magnetic core spark chamber telescope launched on SAS-2 on November 15, 1972 (Derdeyn et al., 1972). A schematic diagram of that  $\gamma$ -ray instrument is shown in Figure 12-2. The spark chamber assembly consists of 16 spark chamber modules above a set of 4 central plastic scintillators and another 16 modules below these scintillators. Thin tungsten plates, averaging 0.010 cm thick—corresponding to 0.03 radiation lengths—are interleaved between the spark chamber modules. In the upper half of the spark chamber assembly, these plates provide material for the  $\gamma$ -ray to interact with and produce an electron pair. The combination of the plates and spark chambers in the upper and lower halves provides a means of determining the energy of the electrons in the pair by measuring the average Coulomb scattering as they pass through the plates. The plates in the lower half of the spark chamber assembly also provide additional pictorial information used to identify the  $\gamma$ -ray.

The spark chamber assembly is triggered if a charged particle passes through one of the four square plastic scintillator tiles and the corresponding directional lucite Čerenkov counter immediately below, while, at the same time, there is no pulse in the surrounding plastic scintillator anticoincidence dome. Each of the four scintillator-Čerenkov counter telescopes acts independently of the others and has a full width half maximum (FWHM) opening angle of about  $30^\circ$ . The anticoincidence dome prevents

the spark chamber system from being triggered by charged particles, and the directional feature of the Čerenkov counter prevents the telescope from being triggered by upcoming particles which might stop above the central scintillator before reaching the anticoincidence dome.

Of the detector subsystems used in this  $\gamma$ -ray telescope, the spark chamber is one which was not described in Chapter 11 and deserves some attention. In general, a spark chamber consists of two planes to which a high voltage differential may be applied causing an electrical breakdown along the path or paths of charged particles which have passed through very recently and left an ionized path. Normally the voltage is applied within a few tenths of a microsecond and the rise time of the voltage pulse is as short as possible. The high voltages cause a free electron to produce an avalanche which, after reaching a critical size, leads to a breakdown. The voltage pulse height is chosen to be high enough to give a high efficiency (typically 96 percent) and good multiple track efficiency, but not so high as to produce undesired track spreading. It is also advantageous to keep the pulse profile short.

There are several types of readout systems for spark chambers besides the magnetic core one which was used on SAS-2 and COS-B, as noted at the beginning of this chapter. The magnetic core system has, however, proved to be desirable for  $\gamma$ -ray space telescopes for several reasons including suitability for spaceflight, capability for recording multiple tracks with high efficiency, good single track position accuracy, capability for resolving two close tracks, high reliability, low power consumption, reasonable cost, and two-dimensional readout. In the magnetic core spark chamber there are two planes of wires replacing the plates with the wires in one plane being orthogonal to those in the other. The individual wires are typically 1 mm apart and each threads a magnetic core. When a spark occurs the current flows down one wire, through the spark, and onto an orthogonal wire in the other plane setting the core on each wire, thereby giving the "x, y" position of each track at a given level. The third dimension in the picture is provided by the vertical assembly of spark chambers. The information contained in the set cores can be read out in the usual way by threading each core with two additional wires: one, a drive wire, which can be used to switch the core back to its "unset" state and the other, a sense wire, which sees an induced

voltage when a core is switched from one state to another. The cores are read out and reset in one operation which can occur very quickly so that the spark chamber is ready to be triggered again as soon as the capacitor in the high voltage pulser is recharged, and the satellite system is ready to receive data.

The information on spark locations is stored in a separate memory until it can be read out and transmitted by the satellite data and telemetry system. Since typically only 1 percent or less of the cores are set, it is more efficient to store the location of each set core rather than the knowledge of whether each core is set or not. There are also additional ways of compressing the data further.

In a  $\gamma$ -ray event, there are, of course, two tracks coming from a common vertex. It is desirable to know which track in one view corresponds to which track in the other. It is usually possible to determine the association on the basis of the track characteristics, such as Coulomb scattering or an occasional missing spark on a specific deck; however, to assist in correlating the two views, often a grid with the wires at  $45^\circ$  with respect to those in the other wire planes is placed at the bottom of the spark chamber stack assembly.

The main constituent of the spark chamber gas is now normally neon. It provides a very good multiple track efficiency as compared, for example, to argon which has a large breakdown time and, hence, larger fluctuations in spark formation time or oxygen, wherein the first fired electron from an oxygen molecule normally leads immediately to the only spark seen. A quenching agent is usually added to the gas to absorb ultraviolet light, thereby reducing spurious streamers and keeping the track narrow. Excessive amounts of the quenching agent will reduce efficiency; so, typically, one-half to one percent of a gas such as alcohol or ethane is used. Often a small amount (again one-half to one percent) of argon is added to take advantage of the Penning effect. This concentration allows enough collisions to occur to take advantage of the fact that the ionized states of argon lie below those of neon so that there is an enhancement of the number of electrons available during an avalanche. Gas purity is not as critical as in proportional chambers, but even very small quantities of electronegative gases must be rigorously avoided.

The detailed discussion and presentation of the theory of spark chambers and proportional counters, which have been used in a few  $\gamma$ -ray telescopes together with the relevant physics of the motions of ions in an electric field and spark formation is beyond the scope of this book, being a book-length subject in itself, and is well-treated elsewhere. The reader who is unfamiliar with this theory and wishes to pursue the subject, particularly in the light of the present context, is referred to the book by Peter Rice-Evans (1974).

In the case of SAS-2, each spark chamber module had a 25 cm by 25 cm active area with 200 wires in each plane. The two planes were separated by 3.6 mm. The material chosen for construction of the module was glass-bonded mica, selected for its low outgassing property, high dielectric strength, yield strength, and relative ease of machining as compared to most ceramics. (A ceramic called Macor which is somewhat easier to machine is planned to be used on GRO.) The spark wires were made of 0.10 mm diameter beryllium-copper. A "picture" of a  $\gamma$ -ray electron pair event obtained from the SAS-2 magnetic core data is shown in Figure 12-5.

The effective area of the SAS-2  $\gamma$ -ray telescope, which was limited by the size of the Čerenkov counters, was 540 cm<sup>2</sup>. The opening angle for detection of  $\gamma$ -rays was approximately 1/4 sr. The efficiency for detection of  $\gamma$ -rays was a function of energy with a value at very high energies of 0.22, and at 100 MeV of about 0.12. The efficiency and solid angle as a function of energy were determined by calibration at the National Bureau of Standards Synchrotron and the Deutsches Elektronen-Synchrotron (DESY). Timing accuracy for the arrival of each  $\gamma$ -ray to better than two milliseconds was obtained for the study of pulsed  $\gamma$ -ray sources.

By combining the energy and directional information for each electron, the direction and energy of the primary  $\gamma$ -ray was obtained. The uncertainty in the arrival direction for a  $\gamma$ -ray was about 2° two-dimensional r.m.s. at 100 MeV and reached 1° at high energies. The  $\gamma$ -ray energy threshold for useful information was not sharp, but was about 35 MeV. The energy of the  $\gamma$ -ray could be measured to about 200 MeV; above that energy the integral flux could be determined.

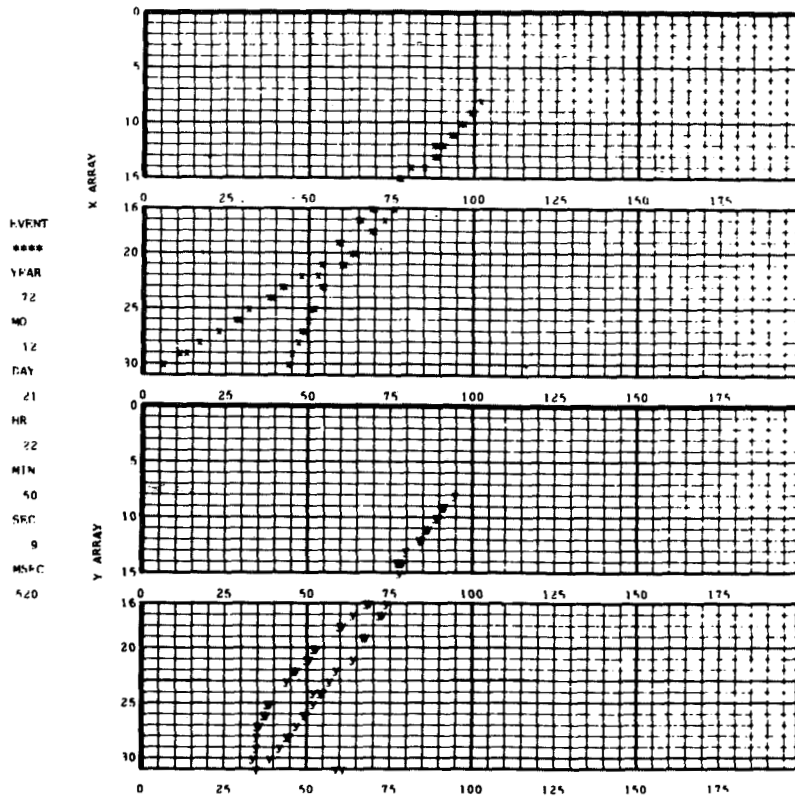


Figure 12-5. A celestial  $\gamma$ -ray event detected by SAS-2 and reconstructed from the telemetered data through a computer. The two orthogonal views of the same event are shown. The vertical scale has been compressed by a factor of about  $3\frac{1}{2}$  relative to the horizontal one so that the two views may be displayed more conveniently.

SAS-2 was launched from San Marco off the coast of Kenya into an approximately circular orbit with a  $2^\circ$  inclination and a 550 km altitude. The satellite was capable of being pointed in any direction, and viewed a particular region of the sky for about 1 week. Hence, typically, for approximately 0.36 of the orbit the detector pointed at the Earth, and for another approximately 0.08 of the orbit the Earth albedo  $\gamma$ -ray flux was high, leaving about 0.56 of the orbit for collection of celestial  $\gamma$ -ray data. Combined with a live time (the period when cores are not being read out and that  $\gamma$ -ray telescope is ready to accept another event) of about 90 percent, the portion of an orbit during which celestial data were collected was about 0.5.

The COS-B  $\gamma$ -ray telescope (Bignami et al., 1975), launched in August 1975, is similar in concept to the one flown on SAS-2. A schematic diagram of the COS-B instrument is shown in Figure 12-6. Its area and sensitivity were about the same as those of SAS-2. Having additional weight capability, the COS-B satellite was able to carry an energy-measuring crystal which allowed a measurement of the  $\gamma$ -ray energy to high energies, thereby permitting an extension of the measured energy spectrum. On the other hand, for various reasons, it did not contain the equivalent of the SAS-2 lower chamber, which proved to an advantage in the data analyses. An other major difference was that the COS-B satellite had a very high apogee, and, consequently, almost all of the orbit was available for viewing because occultation by the Earth prevailed during only a small fraction of the orbit. The

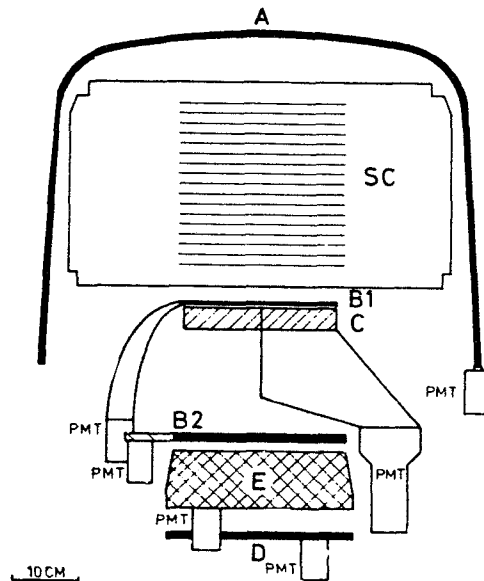


Figure 12-6. A schematic diagram of the  $\gamma$ -ray telescope flown on COS-B. The figure was supplied by the Caravan collaboration for COS-B, consisting of Space Science Department, ESTEC, Noordwijk, The Netherlands, University of Leiden, The Netherlands Centre d'Études Nucléaires de Saclay, France, University of Milan, Italy, University of Palermo, Italy; Max-Planck of Institut für Extraterrestrische Physik, Garching, FRG, and is reprinted here with the permission of Dr. H. Mayer-Hasselwander on behalf of this collaboration.

disadvantage was that the instrument saw the full cosmic ray intensity which created a  $\gamma$ -ray background from interactions in the thin thermal covering layer which for measurement of the diffuse background was not entirely negligible as it had been for SAS-2. Finally, the very long life of the COS-B experiment permitted much longer exposures and, hence, markedly improved statistics.

The GAMMA-I experiment is a joint effort of four Soviet and two French laboratories and is to be launched in the early 1980's. It is also similar in basic concept to the SAS-2 instrument. The sensitive area is about 2.6 times greater; the area solid angle factor is about the same because the viewing angle is smaller. It has an energy-measuring calorimeter which should be able to measure energies with significantly better accuracy than the energy-measuring element on COS-B. The  $\gamma$ -ray arrival direction will also be measured with greater accuracy. The upper spark chamber system is a 12-level wide-gap Vidicon system. With the aid of a mirror system, the picture of the sparks is recorded and digitized using a Vidicon tube. The directionality of the electron is determined by a time-of-flight system rather than a directional Čerenkov counter.

The time-of-flight system approach to the directional measurement, which will also be used in the high energy  $\gamma$ -ray telescope to be flown on the GRO, represents an important step forward. Because of the space required, it could not have been incorporated in the earlier missions, even if the low power space-flight quality electronics had been developed. The time-of-flight system provides both the coincidence telescope information and the directionality information. The basic unit consists of two charged particle detectors, which in this application are sheets of plastic scintillator separated by a distance large enough to measure the time of flight of a relativistic electron with sufficient accuracy to determine clearly whether it is traveling upward or downward. The time-of-flight technique has proved to be over an order of magnitude more efficient in rejecting undesired events than the previously used directional Čerenkov systems. The two plastic scintillators of each basic unit are separated by 70 cm in the GAMMA-I experiment and by 60 cm in the GRO high energy  $\gamma$ -ray telescope. In each instrument the total active area is covered by several of these basic units.

The high energy  $\gamma$ -ray telescope, to be flown on GRO in the second half of the 1980's, also retains the basic concept of the SAS-2 instrument, but has 10 times the area, over 20 times the area solid angle factor, improved angular resolution, and good energy resolution to the highest energies observable (expected to be about  $3 \times 10^4$  MeV, beyond which there will probably not be enough detectable photons from most sources even for an instrument of this size). A schematic diagram of this instrument is shown in Figure 12-7 (Fichtel et al., 1978; Hughes et al., 1980).

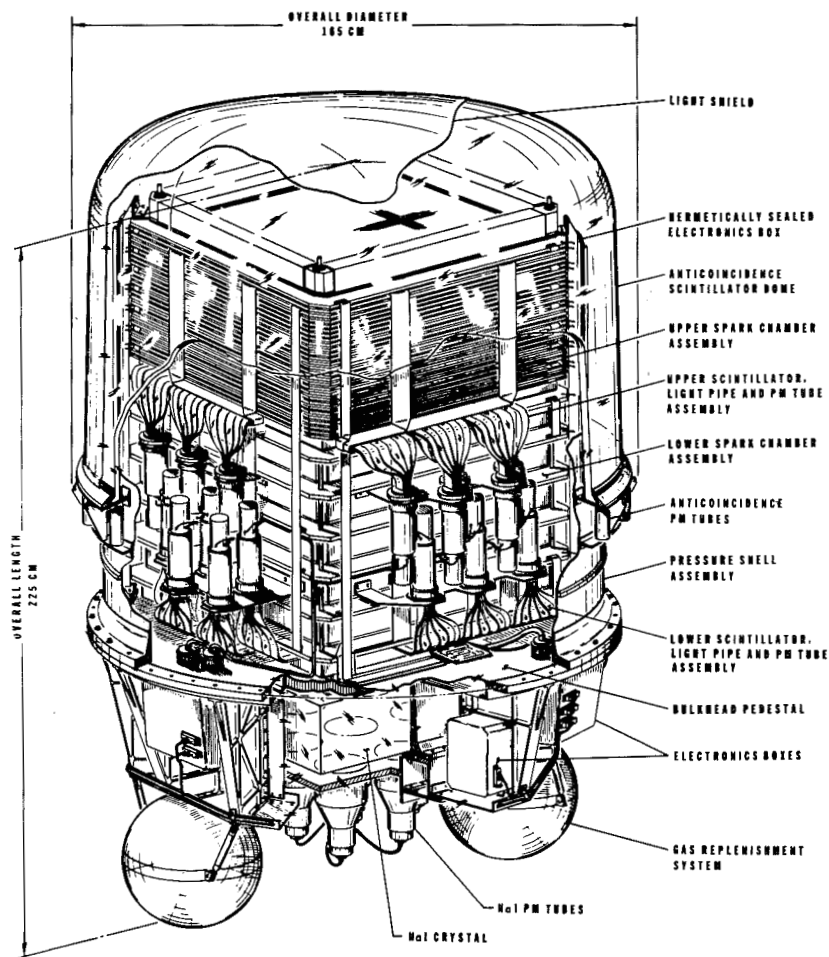


Figure 12-7. A schematic diagram of the  $\gamma$ -ray telescope planned to be flown on GRO (Fichtel et al., 1978).

The upper chamber consists of 28 magnetic core spark chamber modules interleaved with 0.02 radiation length plates. The directional time-of-flight coincidence system employs two 16-element layers of plastic scintillators, and has a total of 96 possible coincidence combinations. The energy of the  $\gamma$ -ray will usually be determined from measurements made in an 8-radiation length thick, 76 cm X 76 cm square NaI(Tl) scintillator crystal below the time-of-flight scintillator plane. The energy resolution of the proposed experiment is about 15 percent FWHM. In the lower energy range, the energy information from the crystal may be supplemented by multiple Coulomb scattering observations in the spark chamber assembly. The accuracy with which a source can be located depends on the energy spectrum shape, the intensity, and the location of the sources; for a strong source with a  $\pi$ -type spectrum, source locations of 5 to 10 arcmin should be achieved.

### **The Greater Than or About $10^5$ MeV Region**

As mentioned earlier in this chapter, at extremely high energies (above about  $10^5$  MeV) photons can be detected by instruments at sea level which record the Čerenkov light produced in the atmosphere from a series of interactions initiated by a single incident  $\gamma$ -ray. Figure 12-8 shows the 10-meter optical reflector of Smithsonian Astrophysical Observatory, Mt. Hopkins, Arizona. This reflector and others of this type scan a region of the sky where a source is suspected, and an attempt is made to detect a directional anisotropy among the air showers which is statistically significant. Several techniques have been used to enhance the sensitivity primarily by improving the signal-to-noise ratio (Porter and Weekes, 1978). A technique using two parallel large reflectors, each equipped with multiple detector channels to provide two images of the shower in Čerenkov light, appears to be one of the more promising approaches for the future (Weekes and Turver, 1977).

### **ANGULAR RESOLUTION**

In the 10 to  $10^5$  MeV energy range, the angular uncertainty within which a  $\gamma$ -ray arrival direction can be determined depends on four factors. The first involves the angular error introduced in

the initial interaction between the  $\gamma$ -ray and the detector material and was discussed in Chapter 10. The second factor discussed earlier in this chapter is related to the subsequent Coulomb scattering of the electrons which occurs in the material in the distance over which the electron directions are measured. The third related consideration is the accuracies to which the positions of the electrons can be measured and their relative energies determined. Finally, there is the matter of the accuracy of alignment of the telescope, its alignment to the aspect sensors, and the inherent accuracy of the aspect sensor. This last item, at least for satellites, is not a determining one in that accuracies well beyond those of the first three factors are readily achievable. The second and

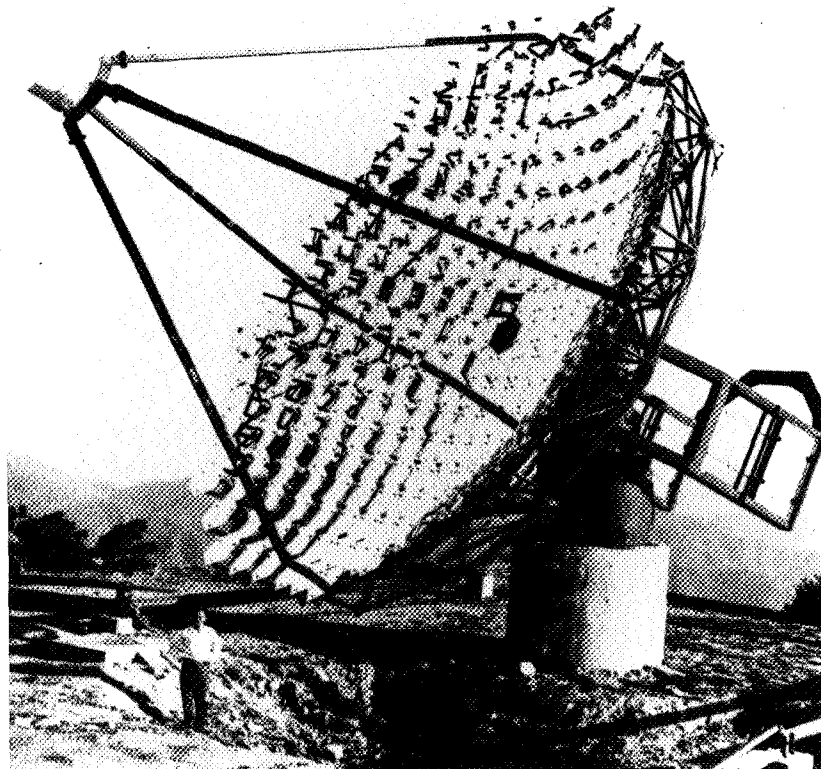


*Figure 12-8. Ten-meter optical reflector of the Smithsonian Astrophysical Observatory at Mt. Hopkins (reprinted with permission from Dr. T. Weekes, 1977 and the Smithsonian Astrophysical Observatory).*

third terms are rather complex in general; however, for a multiple thin plate chamber a reasonable approximation may be introduced. With these approximations, the angular uncertainty,  $\theta_u$ , is given by the expression

$$\theta_u = \left\{ \theta_{\gamma,ee}^2 + \left[ A_1 \frac{M_1^{1/2} L^{1/2}}{\xi} \right]^2 + \left[ A_2 \frac{B}{L} \right]^2 \right\}^{1/2}, \quad (12-2)$$

where  $M_1$  is the mass per unit length,  $L$  is the length over which the measurement is made, the  $A_i$ 's are constants, and  $B$  is a measure of the position accuracy.  $B$  is best determined experimentally, since it depends on track location accuracy and the ability to separate two tracks. The other consideration which enters is the ability to measure the relative energy of the electrons, since, for those events where the best choice of length occurs when two tracks exist, the best value of " $\theta_u$ " is the weighted average of two separate determinations, one for each electron.

When the detector is optimized for both angular accuracy and sensitivity, the three terms of Equation (12-2) are about equal. If the expression is minimized by selecting the optimum choice of  $L$ , which can be shown to be proportional to  $B^{2/3} \xi^{2/3} M_1^{-1/3}$  the following form is obtained:

$$\theta_u = \left\{ \theta_{\gamma,ee}^2 + \left[ A_4 \frac{M_1^{1/3} B^{1/3}}{\xi^{2/3}} \right]^2 \right\}^{1/2}, \quad (12-3)$$

where  $A_4$  is a constant. If  $B$  becomes very small, Equation (12-3) is no longer valid because the number of plates and position measurements cannot become arbitrarily large and the plate thickness

arbitrarily small with practical cost, power, and geometry considerations. Several conclusions can be drawn from Equation (12-3) concerning angular accuracy. First, the dependence on  $B$  is weak (effectively about a  $1/4$  power dependence when all terms are considered). Second, the dependence on  $M_1$  is similarly weak, and a reduction in  $M_1$  can only be achieved at the expense of sensitivity and thus decreased source locations accuracy. Finally, the angular resolution varies most strongly with energy (Remember that the dependence on  $\mathcal{E}$  in the first term which also does not depend on  $B$  or  $M_1$ ), and hence the higher energy  $\gamma$ -rays play an important role in obtaining the best possible angular accuracy. It is therefore important to identify these high energy  $\gamma$ -rays through a good energy measurement.

Figure 12-9 shows the angular accuracy achieved for a single  $\gamma$ -ray by SAS-2 and COS-B, what is expected for the GRO high energy  $\gamma$ -ray instrument, and the best that can be obtained if there were no errors other than those introduced by the  $\gamma$ -ray interaction itself. The figure shows that present instruments are already within a factor of two of this limit. Further, approaching this limit is difficult and costly. The options open for a major increase in angular accuracy appears to be as follows: the selection of the higher energy  $\gamma$ -rays, which would require much greater sensitivity; the reduction of the uncertainty in the error introduced by the initial interaction by detecting the recoil nucleus, which would require a major experimental advancement; and an active collimator, or coded aperture technique, which currently seems to present major obstacles for space application but perhaps not insurmountable ones.

Thus far, the discussion has been limited primarily to a single photon. A source can be located much more accurately by measuring the distribution of estimated arrival directions of a large number of  $\gamma$ -rays, and determining the error to which the centroid may be determined. The additional considerations which then also enter are the source strength, the instrument sensitivity, the diffuse celestial  $\gamma$ -ray intensity in the region of interest, the source energy spectrum (the more high energy  $\gamma$ -rays the better), and the viewing time. With the GRO instrument, 5 to 10 arcmin should be possible for the stronger sources.

In the region above  $10^5$  MeV, the accuracy with which the direction of a  $\gamma$ -ray can be determined depends on the nature of

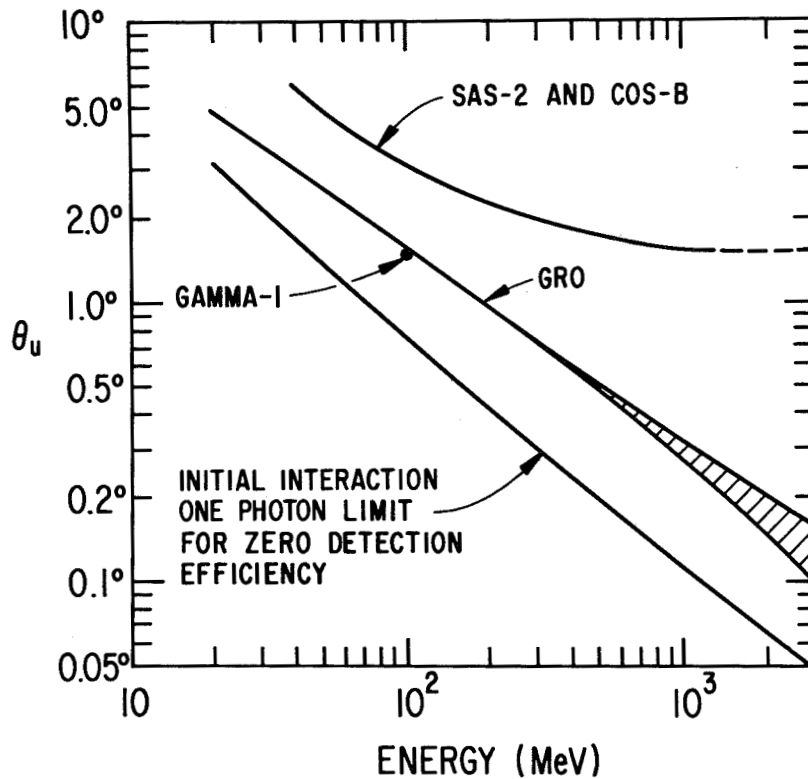


Figure 12-9. The projected root mean square (r.m.s.) uncertainty in arrival direction determination for single photons in several detectors and the initial interaction limit when all other errors are reduced to zero. See text for the detailed considerations. The SAS-2 curve is very close to that of COS-B, but not identical, being a bit lower at low energies and higher at high energies. For GAMMA-I, only the estimate at 100 MeV was known to the authors. At high energies there is a spread in values for GRO because the accuracy of the determination depends on where in the chamber the  $\gamma$ -ray interacted.

the development of the shower and how well the light distribution can be determined. At present a source can be located to about  $1^\circ$ . With future improvements principally concerned with measuring the Čerenkov light profile, it should also be possible to approach 5 to 10 arcmin for energies above  $10^6$  MeV.

## ENERGY RESOLUTION

The earliest experiments in the lower part of the high energy range depended primarily on measuring the Coulomb scattering of the electrons formed in the  $\gamma$ -ray interaction to obtain an estimate of the  $\gamma$ -ray energy, or even just on the opening angle of the pair alone. Considerations related to a practical detector having a fixed size and having to meet basic requirements led to a range of about 5 to 10 over which a fair estimate of the energy can be made from the Coulomb scattering measurements. The SAS-2 experiment, for example, was able to estimate the  $\gamma$ -ray energy to about 30 to 40 percent r.m.s. from 35 MeV to 200 MeV. Below that energy range, the secondary electrons were increasingly lost to scattering from the sides or to absorption. At the high energy end, a point is reached where a meaningful measurement is increasingly difficult to make, as the noise of the measurement begins to dominate. If the plates are made thicker to obtain meaningful scattering measurements at higher energy, the effective low energy threshold rises accordingly.

As payload weight restrictions lessened, detectors were added at the bottom of the telescopes to estimate the energy. As was noted earlier even a relatively simple shallow energy detector such as that flown on COS-B enhanced the experiment significantly, because although the accuracy in the 35 to 200 MeV energy range was about the same, the energy-absorbing crystal allowed measurements of similar accuracy to be made into the BeV range. The error results principally from escape of a variable fraction of the energy from the bottom and sides of the energy detector, and to a lesser degree from the inaccuracies associated with the measurements of the energy deposited in the energy-measuring device.

An obvious improvement can be achieved by using a larger and thicker but still fully active energy absorption counter. In the high energy  $\gamma$ -ray telescope to be flown on GRO, there will be an 8-radiation length thick NaI (TI) crystal covering the entire area. The energy resolution provided by this crystal is easy to measure and to calculate, and is about 6 percent r.m.s. (or equivalently better than 15 percent FWHM) for  $\gamma$ -ray energies less than about 1 GeV and increases very slowly with energy (Hughes et al., 1980). In addition to energy leakage fluctuations which

decrease with decreasing  $\gamma$ -ray energy, the realizable energy resolution in the telescope itself is influenced by two other instrumental factors in the range below 1 GeV. These are (1) the presence of about 0.6 radiation lengths of inert material above the crystal mostly in the form of the thin plates between the spark chambers, in which the electron-positron pair deposits a variable amount of energy, and (2) the possibility that one of the secondary particles either is scattered in this inert material and strikes the crystal close to its edge or misses it entirely. In the event analysis, however, partial corrections can be made for both of these effects. The spark chamber reveals the  $\gamma$ -ray conversion point and the subsequent track lengths for the secondary particle pair through the inert material for each event, and a correction can be made for the mean energy lost in this material below the conversion point. For a particle that fails to hit the crystal, an energy estimate can be made by observing its scattering in the upper and lower spark chamber arrays. The influence of both of these effects on the energy resolution can be determined by a Monte Carlo simulation of events in the telescope. Figure 12-10 shows the energy resolution expected for the GRO high energy

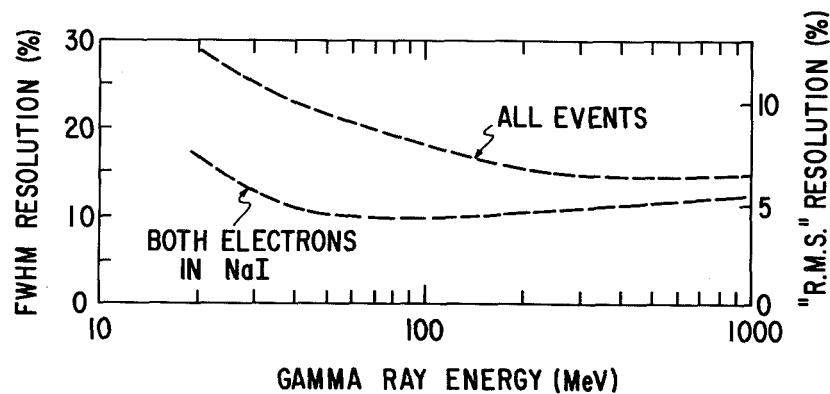


Figure 12-10. The estimated energy resolution of the high energy  $\gamma$ -ray instrument planned for GRO using all the information described in the text for all events and for those events in which both electrons of the pair strike the NaI(Tl) crystal for  $\gamma$ -rays entering at an angle of  $6^\circ$  with respect to the detector axis. The left axis gives the full width half maximum resolution and the right gives the effective equivalent root mean square resolution (Hughes et al., 1980).

$\gamma$ -ray instrument when these effects are included. A better energy resolution can be obtained for the class of events in which both secondary particles enter the crystal. These results are also shown in Figure 12-10. The fraction of triggers which fall into this class is approximately 50 percent at 300 MeV and increases with increasing  $\gamma$ -ray energy. At energies above 1000 MeV, the resolution is expected to degrade slowly from 15 percent FWHM to about 25 percent FWHM at 20 GeV because of fluctuations in energy leakage from the lower face of the crystal.

In the high energy realm above  $10^5$  MeV, the energy estimates are quite uncertain. However, the energy above which an integral flux can be determined, can be estimated with fair accuracy. With future imaging techniques, it should be possible to determine the energies of individual  $\gamma$ -rays to better than a factor of two, and, hence, there is the possibility of obtaining a much better spectral shape in this energy range.

## INSTRUMENT PERFORMANCE AND DATA ANALYSIS

As instruments have become more complex and the total amount of data has increased by orders of magnitude, the analysis of instrument performance and flight data has become an increasingly greater part of the total experiment effort. It is, therefore, appropriate that this subject also be treated here briefly.

In a satellite experiment, the software becomes important long before the post-launch data analysis phase. Computer programs are used to test the performance of individual subsystems, to verify the total instrument performance in the laboratory, to evaluate the data during the extensive instrument calibration at accelerators before launch, to monitor the instrument performance during environmental tests, and to examine the instrument's characteristics just prior to launch. Some of the same tests are also performed on the instrument after launch.

To present a simplified overview of the data analysis plan, the system planned for GRO, the high energy  $\gamma$ -ray telescope, is outlined in Figure 12-11 as an example (Fichtel et al., 1978). Its development has, of course, drawn from the SAS-2 and COS-B experience. Some of the major intermediate results desired are the sensitivity, energy,  $\gamma$ -ray event analysis, directional analysis, detector performance characteristics, and, of course, appropriate

checks on the software performance. Of these, the  $\gamma$ -ray event analysis requires the most time and attention. The computer program to analyze  $\gamma$ -ray events is designed to use a hierarchy of increasingly complex tests on spark chamber pictures in order to distinguish  $\gamma$ -ray initiated pair production events from other spark chamber triggers (e.g., interactions in the walls of the detector and single particle events). The simplest tests will be used to eliminate clearly unacceptable events with a minimum of processing. For those events which pass these tests, an attempt will be made to construct tracks through the sparks in the picture in such a way that the path could have been produced by an electron undergoing multiple Coulomb scattering. These tracks will then be examined using pattern recognition techniques to search for and discard events which are incompatible with  $\gamma$ -ray pair production. The remaining events will be examined relative to criteria defining a  $\gamma$ -ray electron pair. Events which are consistent

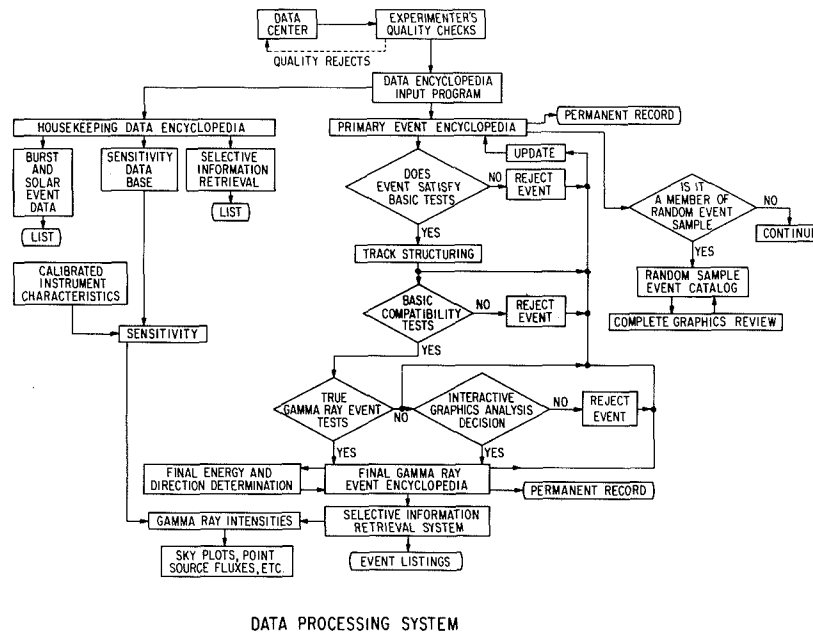


Figure 12-11. Greatly simplified block diagram of the planned data analysis software system for the GRO high energy  $\gamma$ -ray telescope (Fichtel et al., 1978).

with this form are then available for use without further processing. Those which have passed all the tests except this final one or which cannot be rejected with certainty will be identified for review on an interactive graphics unit, where they will be accepted or rejected. The accepted tracks will be examined to determine whether the track structuring is correct, and will be edited if necessary. At all stages of the processing, a random sample of all events will be visually examined on a graphics device. This sample will serve as a continuous monitor to verify the proper functioning of the automatic programs.

The  $\gamma$ -ray energy estimate will come primarily from the NaI(Tl) crystal. The energy deposited in the crystal will be determined by reference to the pre-launch calibration as well as to in-flight calibration measurements. However, determination of the actual  $\gamma$ -ray energy must also take into account features extracted from the spark chamber reconstruction of the particle trajectories. For example, energy corrections will be necessary if one or both electrons of a pair either miss the NaI(Tl) crystal completely or enter near its edge so that some of the energy is not recorded. In such cases, adjustments will be made to the estimated  $\gamma$ -ray energy by using the multiple Coulomb scattering energy estimates from the spark chamber data. A further small correction will also be required to account for the energy lost in the material above the NaI(Tl) crystal. An automatic cross check will also be made to determine whether the energy recorded in the crystal is compatible with that obtained from scattering measurements on the electron tracks. The final energy estimate will then be calculated and stored with the final  $\gamma$ -ray event analysis.

The  $\gamma$ -ray arrival direction will first be determined in experiment coordinates by means of an energy-weighted average of the electron directions near the point of pair production. The track lengths to be used for these direction calculations will be determined from both the NaI(Tl) and multiple scattering energy estimates. Appropriate transformations will then allow the computer to produce celestial and galactic coordinates.

The results of the  $\gamma$ -ray event analysis may then be combined with the sensitivity calculations and detector performance data to determine the  $\gamma$ -ray intensity as a function of celestial position and the energy spectra. The general approach to spatial and energy resolution, intensity and flux calculations, and error analysis is discussed in the next chapter.

## REFERENCES

- Albats, P., Denehy, B., Frye, G.M., Jenkins, T.L., Koga, R., and Schindler, S.M., 1977, *Proc. of the 12th ESLAB Symp.*, ed. R. Wills and B. Battrich, ESA SP-124, 287.
- Bethe, H.A., and Heitler, W., 1934, *Proc. Roy. Soc.*, **A146**, 83.
- Bignami, G.F., Boella, G., Burger, J.J., Keirle, P., Mayer-Hasselwander, H.A., Paul, J.A., Pfeffermann, E., Scarsi, L., Swanenburg, B.N., Taylor, B.G., Voges, W., and Wills, R.D., 1975, *Space Sci. Inst.*, **1**, 245.
- Board, S.J., Dean, A.J., and Ramsden, D., 1968, *Nucl. Instr. and Meth.*, **65**, 141.
- Bratolyubova-Tsulukidze, L.I., Grigorov, N.L., Kalinkin, L.F., Melioransky, A.S., Pryakhin, E.A., Savenko, I.A., and Yufarkin, V.Y., 1969, *Proc. of the 11th Int. Cosmic Ray Conf.*, **1**, 123.
- Clark, G.W., Garmire, G.P., and Kraushaar, W.L., 1968, *Can. J. Phys.*, **46**, S414.
- Cobb, R., Duthie, J.G., and Stewart, J., 1965, *Phys. Rev. Letters*, **15**, 507.
- Derdeyn, S.M., Ehrmann, C.H., Fichtel, C.E., Kniffen, D.A., and Ross, R.W., 1972, *Nucl. Instr. and Meth.*, **98**, 557.
- Ehrmann, C.H., Fichtel, C.E., Kniffen, D.A., and Ross, R.W., 1967, *Nucl. Instr. and Meth.*, **56**, 109.
- Fazio, G.G., and Hafner, E.M., 1967, *J. Geophys. Res.*, **72**, 2452.
- Fazio, G.G., Helmken, H.F., Cavrak, Jr., S.J., and Hearn, D.R., 1968, *Can. J. Phys.*, **46**, S427.
- Fichtel, C.E., and Kniffen, D.A., 1965, *J. Geophys. Res.*, **70**, 4227.

- Fichtel, C., Hofstadter, R., Pinkau, K., Bertsch, D., Favale, A., Hartman, R., Hughes, E.B., Kniffen, D., Mayer-Hasselwander, H.A., Rothermel, H., Schneid, E., Sommer, M., Thompson, D., 1978, Proposal for a High Energy Gamma Ray Telescope on the Gamma Ray Observatory.
- Frye, G.M., and Smith, L.H., 1966, *Phys. Rev. Letters*, **17**, 733.
- Galbraith, W., and Jelley, J.V., 1953, *Nature*, **171**, 349.
- Galbraith, W., and Jelley, J.V., 1955, *J. Atmos. Terr. Phys.*, **6**, 250.
- Helmken, H.F., and Fazio, G.G., 1966, *IEEE Trans. Nucl. Sci.*, NS-13, 486.
- Hughes, E.B., Hofstadter, R., Johansson, A., Rolfe, J., Bertsch, D.L., Cruickshank, W.J., Ehrmann, C.H., Fichtel, C.E., Hartman, R.C., Kniffen, D.A., Ross, R.W., Thompson, D.J., Pinkau, K., Rothermel, H., Sommer, M., Mayer-Hasselwander, H., Favale, A., and Schneid, E., 1980, *IEEE Trans. Nucl. Sci.*, NS-27, 364.
- Hutchinson, G.W., Pearce, A.J., Ramsden, D., and Wills, R.D., 1969, IAU Symp. 37.
- Kraushaar, W.L., and Clark, G.W., 1962, *Phys. Rev. Letters*, **8**, 106.
- Kraushaar, W., Clark, G., Garmire, G., Helmken, H., Higbie, P., and Agogino, M., 1965, *Ap. J.*, **141**, 845.
- Mayer-Hasselwander, H.A., Pfeffermann, E., Pinkau, K., Rothermel H., and Sommer, M., 1972, *Ap. J. (Letters)*, **175**, L23.
- Niel, M., Cassignol, M., Vedrenne, G., and Bouigue, R., 1969, *Nucl. Instr. and Meth.*, **69**, 309.
- Ogelman, H.B., Delvaille, J.P., and Greisen, K.I., 1966, *Phys. Rev. Letters*, **16**, 491.

- O'Sullivan, C., Fegan, D.J., McBreen, B., O'Brien, D., 1978, *Proc. of the 15th Int. Cosmic Ray Conf.*, 1, 188.
- Porter, N.A., and Weekes, T.C., 1978, "Gamma Ray Astronomy from  $10^{11}$  to  $10^{14}$  eV Using the Atmospheric Čerenkov Technique," Smithsonian Astrophysical Observatory, Special Report 381.
- Rice-Evans, P., 1974, *Spark, Streamer, Proportional, and Drift Chambers* (London: The Richelieu Press, 1974).
- Ross, R.W., Ehrmann, C.H., Fichtel, C.E., Kniffen, D.A., and Ogelman, H.B., 1969, *IEEE Trans. Nucl. Sci.*, NS-16, 304.
- Rossi, B., 1956, *High-Energy Particles* (Englewood Cliffs: Prentice-Hall, Inc., 1956), chaps. 2 and 5.
- Stearns, M., 1949, *Phys. Rev.*, 76, 836.
- Valentine, D., Kaplon, M.F., and Badhwar, G., 1969, *Proc. of the 11th Int. Cosmic Ray Conf.*, 1, 101.
- Voges, W., Pinkau, K., Koechlin, Y., Leray, J.P., Boella, G., Sironi, G., and Turner, M., 1973, *Proc. of the 13th Int. Cosmic Ray Conf.*, 1, 293.
- Volobuev, S.A., Galper, A.M., Kirillov-Ugryumov, V.G., Luchkov, B.I., Ozerov, Y.V., Rozental, I.L., Shermanzon, E.M., Grigorov, N.L., Kalinkin, L.F., Malioransky, A.S., Savenko, I.A., and Shashko, G.A., 1969, *Proc. of the 11th Int. Cosmic Ray Conf.*, 1, 127.
- Weekes, T.C., and Turver, K.E., 1977, *Proc. of the ESLAB Symp. on Recent Advances in Gamma Ray Astronomy*, 279.

# Chapter 13

## Analysis of Observational Spectra

### INTRODUCTION

The first step in the analysis of  $\gamma$ -ray energy loss spectra is their conversion to differential energy and differential angular photon spectra. This conversion can be carried out if the detector response and the background are both known. Once these parameters are known, there are many techniques that can be used to convert pulse-height spectra to photon spectra. A rather detailed compendium of analytic methods can be found in Carpenter et al. (1979). In the following section, a few of these techniques are discussed and background problems are considered.

The main emphasis in this chapter has been placed on the analysis of energy loss spectra in the lower  $\gamma$ -ray energy domain. Problems of transpositions from pulse height to photon space are most complex in this domain and the methods shown illustrate many of the problems which arise in the general analysis of energy loss spectra.

### GENERAL FORMULATION

Consider that photons with distribution  $T(\mathcal{E}, \Omega)$  are incident upon a detector, where  $\mathcal{E}$  is the energy and  $\Omega$  is the angular distribution relative to the detector. The photons interact with the detector and produce a distribution of energy losses or pulse heights at the detector output. The resulting pulse height is denoted by  $V$ . The response or energy loss mechanism for the

given detector geometry situation is denoted by  $\bar{S}(\mathcal{E}, V, \Omega)$ . The response function,  $\bar{S}(\mathcal{E}, V, \Omega)$ , when normalized, is a frequency distribution describing the probability that a  $\gamma$ -ray of energy  $\mathcal{E}$ , incident upon the detector with angular distribution  $\Omega$ , will be observed at pulse height  $V$ . The nature of these response functions was discussed in Chapter 11. Both theoretical and experimental methods can be used to determine  $\bar{S}(\mathcal{E}, V, \Omega)$  as discussed by Seltzer (1975). The angular distribution, with respect to the detector, will be fixed for the given experimental situation and the following definition can be used:

$$T(\mathcal{E}) = \frac{\int_{\Omega} \bar{T}(\mathcal{E}, \Omega) d\Omega}{\int d\Omega} , \quad (13-1a)$$

and

$$S(\mathcal{E}, V) = \frac{\int_{\Omega} \bar{S}(\mathcal{E}, V, \Omega) d\Omega}{\int d\Omega} . \quad (13-1b)$$

When a discrete or continuous distribution of  $\gamma$ -rays is incident upon the detectors, a pulse-height spectrum  $P(V)$  is obtained. The expression for  $P(V)$  can be written in terms of  $T(\mathcal{E})$  and  $S(\mathcal{E}, V)$  as follows:

$$P(V) = \int_0^{\mathcal{E}_{\max}} T(\mathcal{E}) S(\mathcal{E}, V) d\mathcal{E} . \quad (13-2)$$

The problem is to determine  $T(\mathcal{E})$  if  $P(V)$  and  $S(\mathcal{E}, V)$  are known.

One method for determining  $T(\mathcal{E})$  is to assume various forms of  $T(\mathcal{E})$  and obtain the product  $T(\mathcal{E}) S(\mathcal{E}, V)$  using sto-

chastic methods. The pulse-height spectrum is theoretically determined and compared to the observed pulse-height spectrum; chi-square tests are used to determine the best model fit.

Numerical methods can also be used to obtain a solution for  $T(\mathcal{E})$ . Equation (13-2) is rewritten as follows:

$$P_j \simeq \sum_i T_i S_{ij} \quad , \quad (13-3)$$

where  $i$  is the index for the average energy  $\mathcal{E}_i$  in the interval  $\Delta\mathcal{E}_i$ , and  $j$  is the index for the average  $V_j$  in the interval  $\Delta V_j$ . An exact solution to Equation (13-3) can be found by simple matrix inversion, but there is not a unique solution for Equation (13-3). The numerical form given by Equation (13-3) can be used as a solution to Equation (13-2) only under limited conditions. These conditions can be derived from information theory (Trombka, 1962; and Trombka and Schmadebeck, 1968). If a distribution has no oscillatory components with a frequency  $f$  greater than  $f_{\text{max}}$ , the Shannon sampling theorem asserts that samples at discrete points with a separation equal to or less than  $\frac{1}{2}f_{\text{max}}$  will completely describe the continuous distribution (Linden, 1959). The most rapidly changing region of the frequency distribution  $S(\mathcal{E}, V)$  can be shown to be the photopeak area. From a Fourier analysis of the photopeak region,  $\frac{1}{2}f_{\text{max}}$  is found to be equal to the half width at half maximum (HWHM). A set of monoenergetic response functions,  $S(\mathcal{E}, V)$ , which correspond to the average response function  $\overline{S(\mathcal{E}_j, V)}$  in  $\Delta\mathcal{E}_j$  and  $\mathcal{E}_j$  can be used in Equation (13-3) where the  $\mathcal{E}_j$ 's are chosen such that they are separated by HWHM at  $\mathcal{E}_j$  and  $\mathcal{E}_{j+1}$ . One can further show that the discrete channel samplings of the pulse-height spectra, as reflected by the channel width of the multichannel analyzer, must be no greater than HWHM in pulse-height units. This requires that there be at least two channels for every  $\mathcal{E}_j$  chosen. Thus, the pulse-height spectra sampling must be such that the data will yield an overdetermined set of measurements relative to the Equation (13-3).

Because of counting statistics and because the measurements yield an overdetermined set of data, a unique solution to Equation (13-3) does not exist. Least square analysis can be

used to determine a “best” solution. Using weighted linear least square techniques:

$$M = \sum_j \omega_j \left( P_j - \sum_i T_i S_{ij} \right)^2 \text{ to be a minimum } , \quad (13-3)$$

where  $\omega_j = \sigma_j^{-2}$ .  $\sigma_j^2$  is the variance in the determination of the counts in channel  $j$ .  $\sigma_j^2$  must include all effects in the data processing, such as background subtraction. The partial derivatives of  $M$  are taken with respect to the  $T_k$ 's and set equal to zero.

$$\frac{\partial M}{\partial T_k} = \sum_j \omega_j \left( P_j - \sum_i T_i S_{ij} \right) S_{jk} = 0 . \quad (13-4)$$

This can be written in matrix form as follows:

$$\tilde{S} \omega P - (\tilde{S} \omega S) \mathbf{T} = 0 , \quad (13-5)$$

where  $S$  is an  $m \times n$ , matrix of the response functions,  $\tilde{S}$  is the transpose of  $S$ ,  $\omega$  is the diagonal matrix of the weighting functions,  $T$  is a vector corresponding to the incident photon spectrum, and  $P$  is the measured pulse-height spectra.

Equation (13-5) can be solved for  $T$ , yielding

$$\mathbf{T} = (\tilde{S} \omega S)^{-1} \tilde{S} \omega P . \quad (13-6a)$$

A number of algorithms can be used to obtain a solution to Equation (13-6a). The particular method used depends on the answers to such questions as:

- Is it possible to invert the matrix  $(\tilde{S} \omega S)$ ?
- Are the components of the  $S$  matrix linearly independent?
- What is the nature of the  $\omega$  matrix?
- What is the effect of background, and how does one compensate for background in the calculation?
- How does one compensate for nonlinearities in the system?

### CALCULATION OF ERRORS

Before proceeding with the solution, we shall consider the problem of error calculation. These calculations can help determine qualitatively the confidence to be placed in the solution obtained and the linear independence of the components of the  $(\tilde{S} \omega S)$  matrix.

Once the  $T$ 's in Equation (13-6a) have been determined, it is possible to determine the mean square deviation in  $\mathbf{T}$ . If it is assumed that the  $S_{ij}$  is known to be without error or very small compared to the variance in the  $S_{ij}$ 's, then the error in the  $T_j$  calculation can be obtained under the assumption that the statistical variations in the determination of the  $T_j$ 's are caused by the statistical variation in the measurement of the  $P_i$ 's. Equation (13-6a) can also be written as follows:

$$T_j = \sum_i \sum_v C_{ij}^{-1} S_{iv} \omega_i P_i \quad , \quad (13-6b)$$

where  $\mathbf{C} = (\tilde{S} \omega S)$  is a symmetric matrix, the elements of  $\mathbf{C}$  are

$$C_{v\gamma} = \sum_i \omega_i S_{iv} S_{i\gamma} \quad , \quad (13-7)$$

and  $C^{-1}$  is the inverse of the matrix  $C$ ; that is

$$C(C^{-1}) = I \quad , \quad (13-8)$$

where  $I$  is the identity matrix, and

$$I_{\nu\lambda} = \sum_{\gamma} C_{\nu\gamma} C_{\gamma\lambda}^{-1} \quad (13-9)$$

is equal to 1 for  $\nu = \lambda$ , and is equal to 0 for  $\nu \neq \lambda$ .

From Equation (13-6b), it is seen that  $T_j$  is a linear combination of the  $P_i$ 's, since the  $\omega_i$ 's, the  $S_{ij}$ 's, and thus, the  $C_{ij}$ 's are constants. The variance in the determination of  $T_j$ ,  $\sigma^2(T_j)$ , can be written as a linear sum of the variance in  $P_i$  (i.e.,  $\sigma^2(P_i)$ ):

$$\sigma^2(T_j) = \sum_i \sum_{\nu} \sum_{\gamma} C_{\nu j}^{-1} C_{\gamma j}^{-1} S_{i\nu} S_{i\gamma} \omega_i^2 \sigma^2(P_i) \quad . \quad (13-10)$$

Now consider  $\omega_i \simeq b/\sigma_i^2$  Equation (13-10) then reduces to

$$\sigma^2(T_j) = b \sum_{\nu} \sum_{\gamma} C_{\nu j}^{-1} C_{\gamma j}^{-1} \sum_i \omega_i S_{i\nu} S_{i\gamma} \quad . \quad (13-11)$$

From Equation (13-7) it follows that

$$\sigma^2(T_j) = b \sum_{\nu} C_{\nu j}^{-1} \sum_{\gamma} C_{\nu\gamma} C_{\gamma j}^{-1} \quad , \quad (13-12)$$

and from the identity matrix in Equation (13-9)

$$\sigma^2 (T_j) = bC_{jj}^{-1} \quad (13-13)$$

The variance  $\sigma^2 (T_j)$  can be determined from the diagonal elements of the matrix  $C^{-1}$  and if  $b = 1$ , then  $\sigma^2 (T_j)$  is equal to  $C_{jj}^{-1}$ .

The goodness of fit  $X^2$  can be calculated as

$$X^2 = \frac{\sum_i \omega_i \left( P_i - \sum_j T_j S_{ij} \right)^2}{n - m} \quad (13-14)$$

where  $n$  is the number of channels used and  $m$  is the number of components in the  $S$  matrix. The equality given in Equation (13-13) holds if  $X^2 = 1$ . For other cases,  $\sigma^2 (T_j)$  should be modified as follows:

$$\sigma^2 (T_j) = bX^2 C_{jj}^{-1} \quad (13-15)$$

It can be shown further that the off diagonal elements,  $C_{\gamma\lambda}^{-1}$ , are the covariance between the  $\gamma$ th and the  $\lambda$ th component; the percentage of interference  $F_{\gamma\lambda}$  can then be calculated from

$$F_{\gamma\lambda} = \frac{\left( C_{\gamma\lambda}^{-1} \right)^2}{C_{\gamma\gamma}^{-1} C_{\lambda\lambda}^{-1}} \times 100\% \quad (13-16)$$

The  $F_{\gamma\lambda}$  can also be considered as a measure of whether the set of library components  $S$  is truly a linearly independent set, and thus, whether the  $(\tilde{S}\omega S)^{-1}$  matrix exists. If  $F_{\gamma\lambda} = 0$ , then the  $\gamma$ th and  $\lambda$ th components are linearly dependent, and if  $F_{\gamma\lambda} = 1$ , the two components have the same vector form but may differ by a constant.

## METHODS OF SOLUTION

In many of the questions for which Equation (13-6b) is used, the correlation coefficients are not small, and oscillations can be produced in the solutions. Constraints on the solutions can be used to damp out these effects. An extremely useful constraint requires that the least square solution be confined to the domain of positive values including zero. The problem of nonnegativity is considered in detail in Trombka (1962) and in Trombka and Schmadebeck (1968). In the following discussion a more general approach will be briefly presented.

In order to find a solution consistent with Equation (13-3) and requirements imposed by sampling theory, an overdetermined measurement of the pulse-height spectrum must be made. The overdetermined set can be reduced to a determined set utilizing the least square principle in Equations (13-6a) and (13-6b). The solution obtained selects those values of  $T_j$ 's for which  $M$  is an absolute minimum. This may yield results which are not consistent with physical constraints such as zero or positive intensities; the ratio of two or more line intensities in a spectrum is a constant, or a given nuclear species decays at a given rate as determined by a series of measurements. Such constraints can be imposed in place of the least square constraint. For simplicity let us consider Equation (13-5); it can be written using the definition of  $C$  given in Equation (13-7) and a vector  $\mathbf{B} = S \omega P$ , thus:

$$\mathbf{CT} = \mathbf{B} \quad (13-17a)$$

Consider the case of three energy groups with intensities  $T_1$ ,  $T_2$ , and  $T_3$ ; Equation (13-17a) can be written as the following set of simultaneous equations:

$$\begin{aligned} C_{11} T_1 + C_{12} T_2 + C_{13} T_3 &= B_1 \\ C_{21} T_1 + C_{22} T_2 + C_{23} T_3 &= B_2 \\ C_{31} T_1 + C_{23} T_2 + C_{23} T_3 &= B_3 \quad . \quad (13-17b) \end{aligned}$$

Consider now the following situation. The least square minimum values are required for  $T_1$  and  $T_2$ , but  $T_3$  is set such that  $T_3 = aT_2$ , that is the ratio of intensities be the constant  $a$ . The first two equations in the set given in Equation (13-17b) maintains that  $T_1$  and  $T_2$  retain their values based on a least square criteria, but the constraint replaces the least square criteria for the last equation; that is

$$\begin{aligned} C_{11} T_1 + C_{12} T_2 + C_{13} T_3 &= B_1 \\ C_{21} T_1 + C_{22} T_2 + C_{23} T_3 &= B_2 \\ 0 \cdot T_1 - a T_2 + T_3 &= 0 \quad , \quad (13-17c) \end{aligned}$$

and a new  $\mathbf{C}'$  matrix and  $\mathbf{B}'$  vector are formed:

$$\mathbf{C}' = \begin{vmatrix} C_{11} & C_{12} & C_{13} \\ C_{21} & C_{22} & C_{23} \\ 0 & -a & 1 \end{vmatrix}$$

$$\mathbf{B}' = \begin{pmatrix} B_1 \\ B_2 \\ 0 \end{pmatrix} .$$

The solution for  $\mathbf{T}$  can then be obtained

$$\mathbf{T} = (\mathbf{C}')^{-1} \mathbf{B}' . \quad (13-17d)$$

Many linear constraints can be imposed in this manner.

The nonnegativity constraints involve rather lengthy algorithms. One solution can be found in Trombka and Schmadebeck (1968).

#### COMPENSATION FOR GAIN SHIFT AND ZERO DRIFT

Gain shift can be considered as a compression or expansion of one pulse-height scale with respect to the second scale, whereas zero drift can be considered as a linear displacement of one scale with respect to the other. Thus, in general, these two changes can be expressed as

$$P_{ji} = gP_{ki} + \epsilon , \quad (13-18)$$

where  $P_{ij}$  is the channel number,  $i$  for spectrum  $j$ ,  $P_{ki}$  is the channel number,  $i$ , for spectrum  $k$ ,  $g$  is the gain shift, and  $\epsilon$  is the zero displacement. In order to perform the linear least square analysis,  $g$  must equal 1, and  $\epsilon$  must equal zero.

The spectrum to be changed is described by  $P_{ki}$ , the total counts in channel  $P_{ki}$  of spectrum  $k$ . To change the  $k$  spectrum so that it is on the same scale as the  $j$  spectrum, the following procedure is used (if  $g$  and  $\epsilon$  are known). The pulse-height scale,  $P_{ki}$ , is multiplied by  $g$ , and the intensity scale,  $P_{ki}$ , is divided by  $g$ .

It must be remembered that the pulse-height spectra can be considered as histograms. The integral under the pulse-height distribution must remain constant. This procedure for compensating for gain shift will keep this area a constant.

The spectra used in the least square analysis are included for integer values of pulse height which are separated by  $\Delta P_{ji} = 1$ . The gain is shifted by some value  $g$ , which would produce intensity,  $Y_{ji}$  values at fractional values of pulse height,  $P_{ki}/g$ , and cause  $\Delta P_{ki}$  to become either less than or greater than unity. Linear extrapolations between adjacent points in the pulse-height distribution are used to find the intercepts for the integer pulse-height values.

Compensation for a zero drift is accomplished by changing the pulse-height scale,  $g P_{ki}$ , to  $g P_{ki} + \epsilon$ . No operation on the intensity values,  $Y_{ki}$ , is needed for this linear displacement does not change the value of the integral under the pulse-height distribution. By using the linear extrapolation method previously mentioned, compensation for  $Y_{ki}$  being at noninteger values of  $g P_{ki} + \epsilon$ , and compensation for the fact that  $\Delta (g P_{ki} + \epsilon)$  may not be unity is obtained. Figure 13-1 shows the results of gain shifting on a spectrum with  $g = 0.70$  to match the library spectrum. The spectrum was obtained with a proportional counter filled with P-10 gas,\* and a 256-channel analyzer. Characteristic X-rays produced by  $\alpha$ -particle bombardment of sand samples were measured. The dots represent the measured spectrum, the triangles represent the gain shifted spectrum, the solid line shows the synthesized spectrum using the least square fit. The agreement is extremely good.

The computer program developed at the Goddard Space Flight Center\*\* will compensate for a constant value of gain shift or a zero drift, or, given a lower and upper limit for a gain shift or zero drift, will search for the proper value between the limits given. The criterion used to find the best gain shift,  $g$ , and zero drift,  $\epsilon$ , in the given interval is that values  $g$  and  $\epsilon$  be chosen such that chi-square defined in Equation (13-14) be a minimum. The procedure used to define this minimum chi-square is as

---

\*A 90 percent argon and 10 percent methan mixture.

\*\*Copies of the program may be purchased from COSMIC (Computer Software Management Information Center), University of Georgia, Athens, GA.

follows: The least square fit is performed for the minimum and maximum values of  $g$  in the given range. Then a fit is made for a value of  $g$  in the middle of the range. Again fits are made for values of  $g$  in the interval midway between the upper and middle value of  $g$ , and then the middle and lower value of  $g$ . The chi-square value obtained each time is always compared with the smallest value obtained previously. This process of halving the range and determining the smallest chi-square value for  $g$  is continued until the difference between two successive tests is smaller than some predetermined limit. In the case of the program developed at the Goddard Space Flight Center, experience has shown that this number is 0.01 for NaI (Tl) spectra. Once the value of  $g$  has been found, this gainshifted spectrum is used as the input spectrum to the zero drift search program. The same iterative process is used to determine the best value of  $\epsilon$  in the zero drift program as was used for the gain shift search.

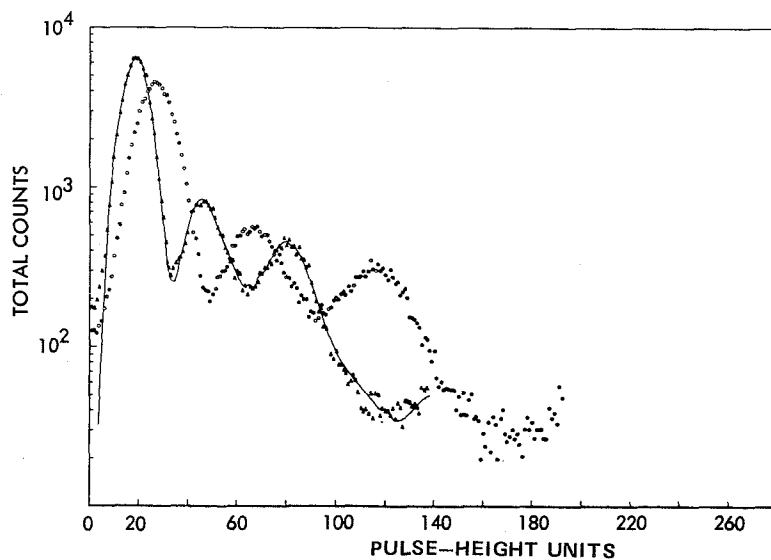


Figure 13-1. Effect of gain shift, X-ray fluorescence pulse-height units sample for silty sand from Hopi Butte, Arizona.

The precision to which the values can be determined depends strongly on the resolution of the detector system; the better this resolution, the sharper and steeper will be the shape of the

library function and the measured spectrum. The sharper the shape of these functions, the greater will be the change in chi-square for small changes in  $g$  or  $\epsilon$ . Furthermore, it has been found that the gain shift has greater sensitivity for the higher pulse-height region, while for the zero drift procedure, the lower pulse-height part of the spectrum shows greater sensitivity.

#### ANALYSIS OF MIXTURE OF DISCRETE LINES AND CONTINUUM

The technique used for the analysis of the Apollo 15  $\gamma$ -ray spectrometer data will be outlined below in order to demonstrate the application of the least square methods to the analysis of complex  $\gamma$ -ray pulse-height spectra (Trombka et al., 1979).

The methods for performing transformations from measurement space to photon space were outlined above. A major problem exists in the analysis of the lunar surface  $\gamma$ -ray emission spectra because there is a mixture of discrete lines and continuum. The natural activity due to potassium, thorium, and uranium and the induced activity due to cosmic ray and solar proton primary and secondary interaction with the lunar surface material (as discussed in Chapter 2) will produce discrete line  $\gamma$ -ray emission from the Moon. The magnitude and energy distribution of the discrete line spectrum can be used to infer the elemental composition of the lunar surface. The discrete line spectrum is superimposed on a continuous  $\gamma$ -ray emission spectrum. This continuum is caused by multiple scatter of the primary discrete line flux in the lunar surface material and a myriad of interactions of particles and  $\gamma$ -rays in the lunar environment. In order to obtain elemental composition information the discrete and continuous  $\gamma$ -ray components must be separated. This should be done simply by transforming the pulse-height spectrum to a photon spectrum and searching for the discrete lines which extend above the continuum. This problem is complicated by the determinations of the inverse matrix  $(\tilde{S} \omega S)^{-1}$ , Equation (13-6a). One obtains oscillations in the solution caused by interference between the components of the  $S$  matrix. These oscillations become most pronounced in the vicinity of discrete lines. The following technique has been used to minimize this interference problem.

A first estimate of the continuous component of the  $\gamma$ -ray

spectrum is obtained by transposing the pulse height to an energy spectrum (Equation 13-6a), eliminating all possible discrete lines and points on either side of those lines where oscillations occur, and finding the best fit over the total photon energy range, using spline techniques to fill in the regions where discrete line components have been removed. When this photon spectrum is determined, the pulse-height spectrum corresponding to this estimated continuous  $\gamma$ -ray spectrum can be obtained with the transformation given Equation (13-3). The continuum pulse-height spectrum is subtracted from the raw data to obtain a first estimate of the pulse-height spectrum of the discrete lines. This discrete line spectrum is then transformed to a photon spectrum (Equation 13-6a), and an estimate of the intensity of the discrete photon line intensity is obtained. These intensities are then used to obtain a second estimate of the discrete line pulse-height spectrum (Equation 13-3). This second estimate is subtracted from the raw data to obtain another estimate of the pulse-height spectrum of the continuous component. The process is continued as described until self-consistency is established. It has been found that about three iterations are required before there are no significant changes in the separated spectra.

Further refinements were required to arrive finally at the shape of the continuous spectrum for the Apollo lunar  $\gamma$ -ray measurements. An inflection point was found in the spectrum at around 4 MeV along with a lunar regional variation of the spectrum in the lower energy portion (less than 3 MeV).

The inflection point occurs where pair production becomes dominant over Compton scattering which acts as the major interaction process. The problem was resolved by the following procedure: obtain a total-orbit lunar spectrum, assume an average elemental surface concentration for various nuclear species, calculate the expected  $\gamma$ -ray discrete line spectra as detected at the spacecraft, and then subtract this component from the raw data. The continuum pulse-height spectra for energies above 4 MeV were calculated for various places over the lunar surface and were found to be independent of position. The shape of this spectrum is shown in Figure 13-2.

The lower energy portion ( $< 3$  MeV) of the spectrum was found to be spatially dependent and associated with scatter of the thorium, uranium, and potassium  $\gamma$ -ray emissions. Spectra

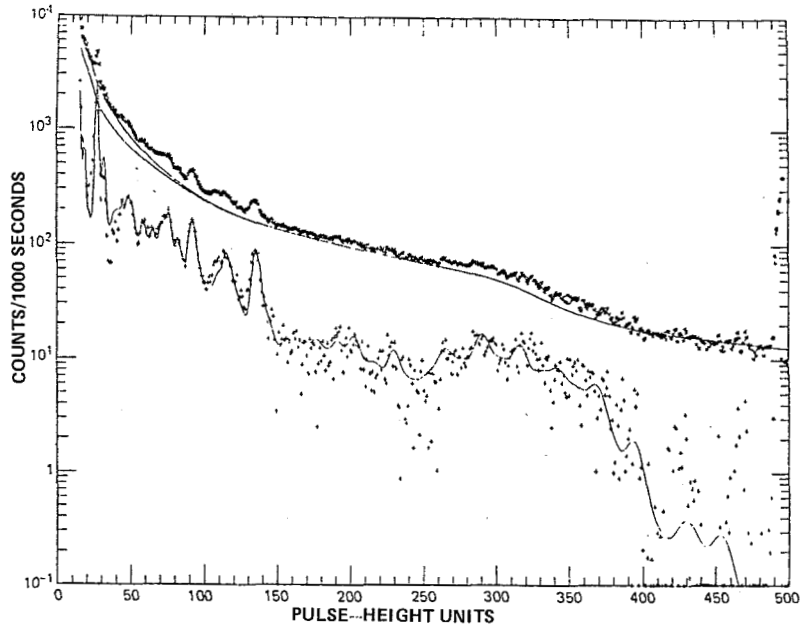


Figure 13-2. An example of an Apollo 16  $\gamma$ -ray spectrum for a lunar region of high radioactivity. The pulse-height spectra are the total signal (\*), the continuum for the lowest and highest values of natural radioactivity (upper -----), the resultant discrete line spectrum (+), and the best least squares fit to the discrete line spectrum (lower -----).

from the lowest to the highest concentrations of thorium, uranium, and potassium were obtained. Four levels were determined and found to be directly related to the integral count rate in the region from 0.55 MeV to 2.75 MeV. Differences between the pulse-height spectrum of the lowest activity level and those of the higher levels were obtained. The shapes were fitted to an exponential form

$$P_k(V) = A_k \exp(-BV) \quad , \quad (13-19)$$

where  $k$  is the integrated count rate for a specific lunar area region from 0.55 MeV to 2.75 MeV;  $P_k(V)$  is the continuous pulse-height spectrum for activity  $k$ ;  $B$  is a slope determined from the data; and  $A_k$  as a function of  $k$  is determined from the data. The parameter  $B$  was found to be independent of  $k$ . Figure 13-2 shows the continuum pulse-height spectrum for the lowest and the highest value of  $k$ . The shape and magnitude of this continuum spectrum greatly affected the elemental composition as determined by the least square method. The background shape was determined by using the pulse-height spectra integrated over hours of time. Once determined, they were used to subtract from spectra accumulated for significantly shorter periods of times (down to about 1000 seconds), and elemental abundances could be obtained for such elements as potassium, thorium, uranium, iron, silicon, and titanium. The shorter integration times allowed the determination of elemental composition for small regions over the Moon.

#### **ANALYSIS OF HIGH ENERGY RESOLUTION DISCRETE LINE SPECTRA**

High energy resolution detectors are now available for spaceflight application. If, for example, lines about 2 keV width are to be resolved, channel widths of less than 1 keV should be used in order to sample the pulse-height spectra properly. Thus, an 8000-channel analyzer would be required to sample the pulse-height spectrum up to 8 MeV. With this resolution hundreds of lines are resolvable and at least for discrete line studies, the techniques for matrix inversions utilizing monoenergetic response functions become too cumbersome. Automated methods for the analysis of such discrete line spectra have been developed. See, for example, Routti and Prussin (1969), Varnell and Trischuck (1969), Robinson (1970), Mills (1970), Slavić and Bingulac (1970), Bowman (1971), Gunnick and Niday (1972), Blok et al. (1975), Phillips and Marlow (1976), Carpenter and D'Agostino (1979).

A general outline of the approach used will be presented in the following discussion. The first step in the analysis requires the search for and recognition of the presence of a photopeak.

As was discussed earlier in this chapter, the photopeak is the most rapidly changing portion of the pulse-height spectrum when compared with such features as Compton edges or background continua. Thus, a variety of filter techniques can be used to determine the presence of a high frequency component in the presence of slowly varying components. These filter techniques essentially attempt to determine the change in slope averaged over a number of channels corresponding to the width of the peak (i.e., energy resolution of the spectrometer system). First and second derivatives of the measured pulse-height spectra can be obtained numerically. These derivatives can be calculated using a number of methods (e.g., spline methods and square wave, rectangular wave, second derivative of a Gaussian function and covariance, and zero area Gaussian function transforms). The transform methods have been incorporated in many of the automated and semiautomated search algorithms. The methods are described and compared in Phillips (1979). The least square transformation described in the earlier section is another example of these transform methods. The “oscillations” produced at the regions of the photopeak were discussed. The first and second derivatives over the slowly varying portion of the pulse-height distribution should be small or zero; in the vicinity of the photopeak these derivatives will be large. Once the transform is obtained statistically, significant first and second derivatives can be automatically determined, thus “flagging” the position of possible peaks.

Once the position of the peak is determined, a fit to the peak area in the region is attempted. The various components used in describing the peak area (Phillips, 1979) are as follows:

1. The peak ideally can be described as Gaussian given by

$$P_1(V) = A \exp - \left| \frac{V - V_0}{2\sigma^2} \right|^2 \quad (13-20)$$

where  $V$  is the pulse height or channel number,  $P_1(V)$  is the amplitude of the pulse-height spectrum at pulse height  $V$ ,

$V_0$  is the pulse height corresponding to the energy  $\mathfrak{E}_0$  of the incident  $\gamma$ -ray,  $A$  is a constant and  $\sigma^2 = a + b\mathfrak{E}_0$  for Ge detectors, for example, as discussed in Chapter 11.

2. Counts can be removed from the photopeak area by effects such as incomplete charge collection and pulse pile-up. It has been found that in an ideal detector system this effect can be described by an exponentially decaying distribution below the peak  $\exp |V - V_0/\beta|$  for  $(V - V_0) < 0$ . In an actual detector this distribution must be modified by the Gaussian smearing in the collection system; thus, this distribution will appear as

$$P_2 = \alpha \exp\left(\frac{V - V_0}{\beta}\right) \times \frac{1}{2} \operatorname{erfc}\left(\frac{V - V_0}{\delta} + \frac{\delta}{2\beta}\right), \quad (13-21)$$

where  $\alpha$  is normalizing amplitude; and if we set  $\mu = (V - V_0/\delta + \delta/2\beta)$ , the complementary error function,  $\operatorname{erfc}(\mu)$ , will be chosen so the  $1/2 \operatorname{erfc}(\mu) = 1$  for  $\mu \ll 0$ ,  $1/2 \operatorname{erfc}(\mu) = 1/2$  for  $\mu = 0$ , and  $1/2 \operatorname{erfc}(\mu) = 0$  for  $\mu \gg 0$ . This provides for a smooth cutoff centered at  $(V - V_0) = -\delta^2/2\beta$ ;  $\beta$  is determined experimentally for the particular detector and it is assumed that  $\delta^2 = \sigma^2$ .

3. A further skewing of the Gaussian toward lower pulse height has been noticed and attributed to surface effects. The magnitude of this effect,  $\tau$ , is about two to three orders of magnitude smaller than  $\alpha$ , the effect discussed in (2) above. In the form including the Gaussian noise measuring term of width,  $\mu$ ,  $P_3$  can be written as

$$P_3 = \tau \exp\left[\frac{(V - V_0)}{\nu}\right] \times \frac{1}{2} \operatorname{erfc}\left[\frac{(V - V_0)}{\mu} + \frac{\mu}{2\nu}\right], \quad (13-22)$$

where  $\nu$  is the slope and is an order of two larger than  $\beta$  (Equation 13-19).

4. The first and second escape peaks due to the absorption of  $\gamma$ -rays whose energies are greater than 2 MeV will have different shapes. Furthermore, annihilation  $\gamma$ -rays can Compton scatter in the detector with the energy given up adding to that of the escape peaks. Summing effects such as this can give the appearance of a step or discontinuity in the background above or below the peak. For lower energy  $\gamma$ -rays, Compton scattering into the detector from surrounding materials can also produce a significant step or ledge below the peak. If we define the step of amplitude as  $\chi$ , then the Gaussian spread contribution  $P_4$  is

$$P_4 = \chi \times \frac{1}{2} \operatorname{erfc} \left[ \frac{(V - V_0)}{\delta} \right] \quad (13-23)$$

5. The background continuum caused by such factors as Compton continuum from higher energy  $\gamma$ -rays, multiple scattering of  $\gamma$ -rays from the surroundings, etc. has been found to be well represented by a second order polynomial  $P_5$

$$P_5 = a + bV + cV^2 \quad (13-24)$$

The above five factors are the most important in fitting photo-peak regions. Other electronic distortion effects such as those due to improperly adjusted pole zero, pile up and insufficient base line restoration should also be taken into consideration in the peak analysis programs. It is best to adjust these latter effects electronically rather than in the analysis programs.

The amplitudes, slopes, and Gaussian smearing factors can

be determined from calibration sources and the data. Both linear and nonlinear least square methods can be used to fit the peak regions to determine the exact position and magnitude of the peak regions. Chi-square methods are used to determine whether the region is due to a single peak or multiple peaks. Automated computer methods such as HYPERMET (Phillips and Marlow, 1976) have been developed to automatically perform the type of analysis just described.

## SOURCES OF $\gamma$ -RAY BACKGROUND

In the earlier discussion, it has been assumed that the pulse-height spectra have had the interfering background removed. In Chapter 11, the use of active shields to reduce charged particle and  $\gamma$ -ray emission from the surrounding environment was discussed. These shields are very effective in reducing charged particle flux effects, but they are less effective in reducing  $\gamma$ -ray background. It is, therefore, important to understand the source of backgrounds in order to evaluate the magnitude of the interferences and, if possible, determine experimentally or theoretically the magnitude of the background that should be subtracted from the measured pulse-height spectra.

A number of sources of background interferences have been identified: photons due to cosmic ray and trapped particles primary and secondary interactions in the spacecraft, in the material surrounding the detector, and in the detector itself; natural radioactivity in the spacecraft; bremsstrahlung produced by high energy electrons; the diffuse  $\gamma$ -ray background; atmospheric  $\gamma$ -rays; and scattered  $\gamma$ -rays produced in planetary surfaces and atmospheres.

In the following section, a brief description of the major background components are described. The magnitude of these various components will be indicated relative to the measurements of the diffuse  $\gamma$ -ray spectra carried out during Apollo 15 and Apollo 16 (Trombka et al., 1976). Further details of the identification and computation of the background components can be found in Dyer et al. (1975a and 1975b), Trombka et al. (1976) and Dyer et al. (1980). Figures 13-3a and 13-3b show energy loss spectra of the various background components measured with the Apollo 15 and Apollo 16  $\gamma$ -ray spectrometer during translunar flight.

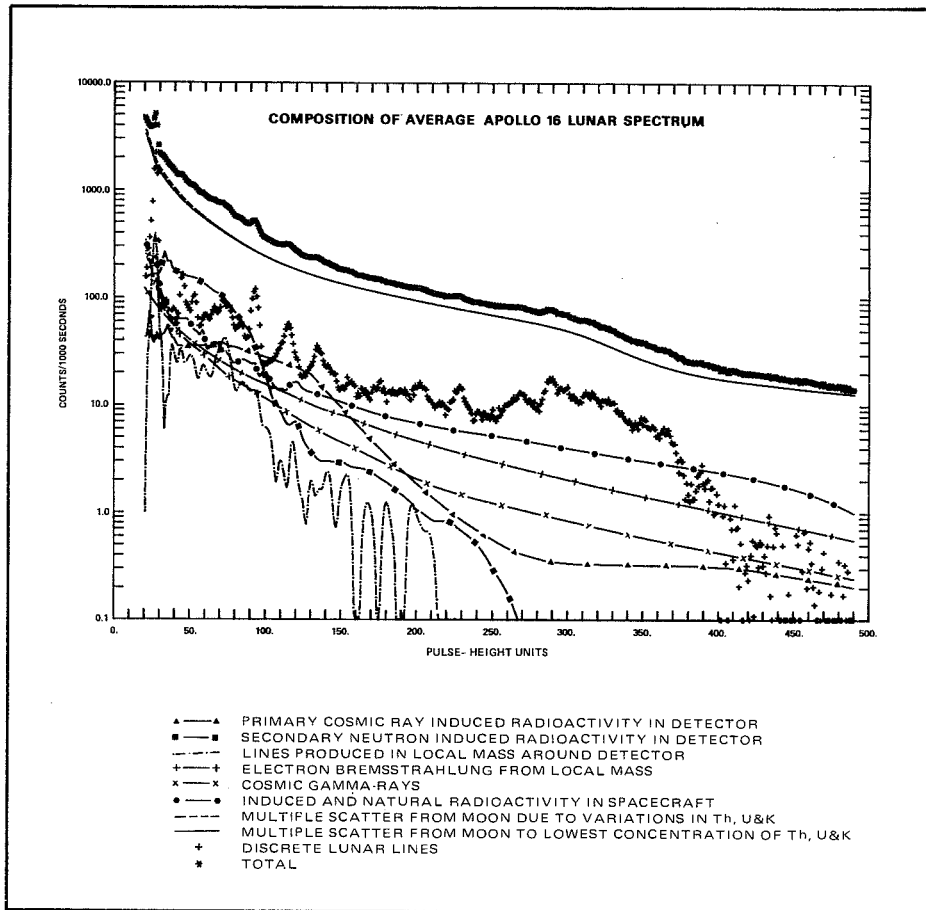


Figure 13-3a. The total pulse-height spectra observed at full (7.6 m) boom extension in Apollo 15 and Apollo 16 are compared with the calculated levels of various backgrounds discussed in the text. The latter are shown for the Apollo 16 measurement. The only component to change significantly is the electron bremsstrahlung, which, at the time of Apollo 15, was approximately half the value shown.

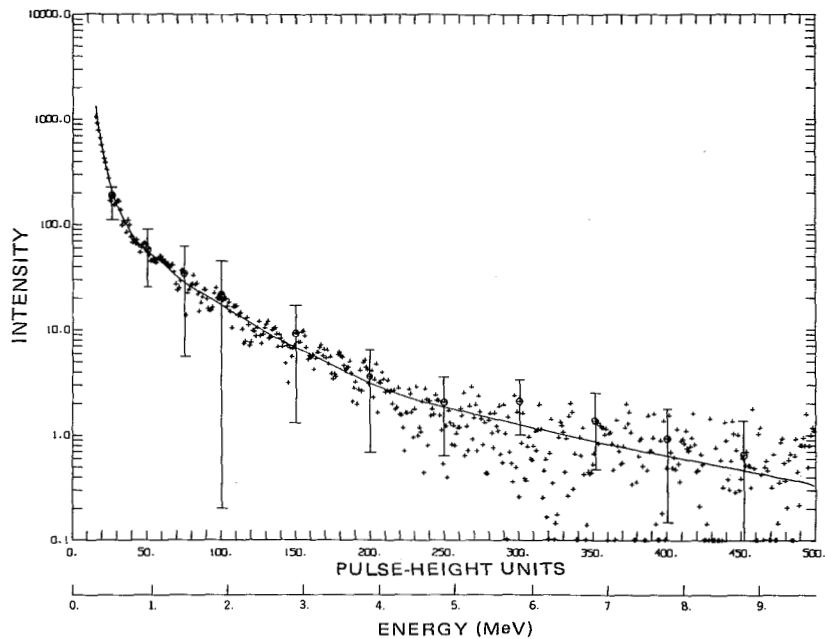


Figure 13-3b. The pulse-height spectrum (shown) of the cosmic  $\gamma$ -ray component obtained after the subtraction of all backgrounds is compared with the pulse-height spectrum (equivalent) of the unfolded photon spectrum. Error bars are plotted every 25 or 50 channels and include the effect of statistics and the uncertainties in the subtraction of backgrounds.

### Direct Charged Particle Detector Counts

Charged particles can interact in the mass of the detector portion of the  $\gamma$ -ray spectrometer producing a pulse similar to  $\gamma$ -ray pulses. Active charged particle shields can be used to decrease significantly the magnitude of this background component. The Apollo  $\gamma$ -ray spectrometer with an active charged particle shield (Harrington et al., 1974) was described in Chapter 11. This system worked well over the energy range up to about 10 MeV (Trombka et al., 1973). Above 10 MeV, the cosmic ray flux is orders of magnitude higher than the  $\gamma$ -ray flux for the Apollo spectrometer system, and thus, small changes in the rejection efficiency of the active shield changed the observed pulse-height spectrum significantly (Trombka et al., 1976). In near-Earth orbit, the primary cosmic

ray flux will be decreased due to the Earth's magnetic field. Trapped radiation can cause similar problems in active shields and possibly prevent counting during passage through such regions.

### **Natural Radioactivity**

Many sources of natural radioactivity can be found aboard spacecraft, for example, thoriated magnesium, radioactive sources used for space charge dissipation, radioactive tracers used in quality control of electronic components, and thoriated optical lenses. A survey of sources found aboard the Apollo spacecraft was carried out (Metzger and Trombka, 1972), and may be useful when considering potential radiation background problems in spaceflight experiments and spacecraft design. In terms of the Apollo mission, these sources of background were found to contribute a much lower  $\gamma$ -ray flux than the cosmic ray and trapped particle induced radiation.

The Apollo  $\gamma$ -ray spectrometer pulse-height spectrum of the background contribution due to natural radioactivity is included in the spacecraft component shown in Figure 13-3a.

### **Spacecraft Component**

Cosmic ray primary and secondary interactions in the spacecraft provide a major background component. The interactions in a planetary body and discussed in Chapter 3 are the same as those that produce  $\gamma$ -ray emission from the spacecraft material. This component can be significantly reduced by placing the detector on the end of a boom extended away from the mass of the spacecraft. The  $\gamma$ -ray detector on Apollo was extended 7.6 m from the spacecraft surface. The spacecraft component detected with the detector at this distance is shown in Figure 13-3a.

In those cases where the detector cannot be extended away from the spacecraft, active CsI or NaI shields can be used to reduce the background from the spacecraft. These systems were used on a High Energy Astronomy Observatory (HEAO) and Solar Maximum Mission (SMM) spacecraft. The SMM  $\gamma$ -ray spectrometer system was described in Chapter 11. However, the materials

used in the active shields can contribute to the induced background; thus, great care must be taken in selecting materials for such active shields.

### **Electron Bremsstrahlung**

The translunar pulse-height spectrum measured during the Apollo 15 and Apollo 16 missions are shown in Figure 13-3a, and an overall change in magnitude can be seen. This change is about 15 percent over all of the energy scale. At the time of the Apollo 16 missions (April 1972), there was a quiet time, a low energy electron flux increase, possibly of Jovian origin (Teegarden et al., 1974). The electron flux measured during Apollo 16 in the energy domain from 3 to 12 MeV was found to have increased by a factor of about two over that measured during Apollo 15. These higher energy electrons can produce bremsstrahlung radiation due to interactions in materials surrounding the detector. It is believed that the difference in the magnitude of the pulse-height spectra measured by Apollo 15 and Apollo 16 can be attributed to the change in low energy electron flux (Trombka et al., 1976). The pulse-height spectrum due to the bremsstrahlung component is shown in Figure 13-3a.

### **Cosmic Ray and Trapped Particle Induced Radioactivity in the $\gamma$ -Ray Detector**

Cosmic ray primaries and trapped particle interactions within the  $\gamma$ -ray detector can produce prompt or delayed  $\gamma$ -ray and particle emissions. The prompt interactions discussed in Chapters 3 and 4, relative to the Sun and planets, are the important processes producing detector activation. The delayed emissions are a major source of background. They are a result of the buildup of radioactive states which decay with a variety of delays, depending on the lifetimes of the numerous individual excited levels. Since the induced radioactivity is within the detector, both  $\gamma$ -rays and charged particles produce interactions. For high proton energies (in the GeV range), light fragments and their decayed products are produced which deposit most of their energy in the detector; Tables 13-1, 13-2, 13-3, and 13-4 list source of the major radio-

Table 13-1  
Isotope List for Activation of Na I/Cs I Crystals by Inner Belt Protons

Isotope	Half-Life	Major Features		Quantity Produced by 1000 Interactions			
		$\beta^+$ continuum end point (MeV)	$\gamma$ -ray peaks (keV)	Inner belt		155 MeV	
				Na I	Cs I	Na I	Cs I
$^{133m}\text{Ba}$	38.9 h		283		2.9		0.8
$^{133}\text{Ba}$	7.2 y		473		2.9		0.8
$^{131}\text{Ba}$	12.0 d		656, 409, 252		36.4		8.4
$^{129}\text{Ba}$	2.2 h	2.45	256, 171		16.2		8.7
$^{128}\text{Ba}$	2.4 d		308, EC		6.5		8.9
$^{127}\text{Ba}$	18.0 m	4.1			3.6		6.3
$^{126}\text{Ba}$	97.0 m	1.8			2.6		4.7
$^{132}\text{Cs}$	6.5 d		702		39.2		41.6
$^{131}\text{Cs}$	9.7 d		EC		33.8		43.6
$^{130}\text{Cs}$	30.0 m	2.99	EC		22.2		29.7
$^{129}\text{Cs}$	32.0 h		451		15.0		21.4
$^{128}\text{Cs}$	3.8 m	3.93	476		10.4		15.7
$^{127}\text{Cs}$	6.2 h	2.1			7.2		11.6
$^{126}\text{Cs}$	1.6 m	4.8			7.0		12.1
$^{125}\text{Cs}$	45.0 m	3.07	146		6.7		11.6
$^{124}\text{Cs}$	26.5 s	5.9			5.9		10.5

**Table 13-1 (continued)**  
**Isotope List for Activation of Na I/Cs I Crystals by Inner Belt Protons**

Isotope	Half-Life	Major Features		Quantity Produced by 1000 Interactions			
		$\beta^+$ continuum end point (MeV)	$\gamma$ -ray peaks (keV)	Inner belt		155 MeV	
				Na I	Cs I	Na I	Cs I
$^{123}\text{Cs}$	5.9 m	3.1			4.1		7.2
$^{122}\text{Cs}$	4.5 m	6.6			2.2		3.0
$^{131\text{m}}\text{Xe}$	11.8 d		164		9.7		12.4
$^{129\text{m}}\text{Xe}$	8.0 d		236		8.1		11.7
$^{127\text{m}}\text{Xe}$	75.0 s		300, 175, 124	4.5	9.4	1.9	11.6
$^{127}\text{Xe}$	36.4 d		408, 236	4.5	9.4	1.9	11.6
$^{125\text{m}}\text{Xe}$	57.0 s		252, 141, 111	26.5	21.7	6.1	12.0
$^{125}\text{Xe}$	17.0 h		277, 222, 87.92	26.5	21.7	6.1	12.0
$^{123}\text{Xe}$	2.08 h	2.7	211, 182	20.1	20.8	11.1	17.9
$^{122}\text{Xe}$	20.1 h		272, EC	8.7	9.9	7.3	10.7
$^{121}\text{Xe}$	38.8 m	3.8		3.6	3.6	3.9	4.1
$^{126}\text{I}$	13.02 d	$\beta^-$ 1.25	1452, 698	61.0	45.4	64.7	51.9
$^{125}\text{I}$	60.14 d		673	51.1	42.1	65.3	58.3
$^{124}\text{I}$	4.18 d	3.16	1357, 635	32.7	27.1	43.6	38.4
$^{123}\text{I}$	13.2 h		191	21.5	18.6	30.6	27.0
$^{122}\text{I}$	3.62 m	3.1	596, EC	14.4	13.4	21.9	19.9

Table 13-1 (continued)  
Isotope List for Activation of Na I/Cs I Crystals by Inner Belt Protons

Isotope	Half-Life	Major Features		Quantity Produced by 1000 Interactions			
		$\beta^+$ continuum end point (MeV)	$\gamma$ -ray peaks (keV)	Inner belt		155 MeV	
				Na I	Cs I	Na I	Cs I
$^{121}\text{I}$	2.12 h	2.4	843, 244	10.8	10.9	14.2	14.1
$^{120}\text{I}$	1.30 h	5.6	594	8.2	7.3	13.7	11.1
$^{119}\text{I}$	19.0 m	3.5	289	9.3	7.0	18.4	12.8
$^{125\text{m}}\text{Te}$	58.0 d		145	15.1	9.7	19.4	12.4
$^{123\text{m}}\text{Te}$	117.0 d		248, 88.5	13.4	8.7	20.0	12.9
$^{121\text{m}}\text{Te}$	154.0 d		294, 81.8	10.1	6.8	16.3	10.8
$^{121}\text{Te}$	17.0 d		605, 538	10.1	6.8	16.3	10.8
$^{119}\text{Te}$	15.9 h		1790, 730, 575	7.3	5.3	12.4	8.7
$^{119\text{m}}\text{Te}$	4.7 d		2350, 1400, 464, 301, 183	7.3	5.3	12.4	8.7
$^{118}\text{Te}$	6.0 d		EC	11.9	9.7	20.5	15.0
$^{117}\text{Te}$	61.0 m	3.5	750	8.9	6.6	12.0	8.4
$^{116}\text{Te}$	2.50 h		124	4.3	3.3	5.8	4.0
$^{120}\text{Sb}$	15.9 m	2.7	EC	6.1	4.1	10.2	6.6
$^{120}\text{Sb}$	5.8 d		2520, 1500, 1380, 319, 119	6.1	4.1	10.2	6.6

Table 13-1 (continued)  
Isotope List for Activation of Na I/Cs I Crystals by Inner Belt Protons

Isotope	Half-Life	Major Features		Quantity Produced by 1000 Interactions			
		$\beta^+$ continuum end point (MeV)	$\gamma$ -ray peaks (keV)	Inner belt		155 MeV	
				Na I	Cs I	Na I	Cs I
$^{119}\text{Sb}$	38.0 h		53	16.0	10.5	24.9	16.2
$^{118}\text{Sb}$	3.50 m	3.7	EC	6.1	4.1	9.1	5.9
$^{118\text{m}}\text{Sb}$	5.10 h		2600, 1510, 1370, 1120, 323, 70	6.1	4.1	9.1	5.9
$^{117}\text{Sb}$	2.8 h		187	8.1	5.9	14.2	9.6
$^{116}\text{Sb}$	15.0 m	4.6	1322, 989	3.9	2.9	4.8	3.2
$^{116\text{m}}\text{Sb}$	60.0 m	4.6	2929, 1867, 1634, 1089, 673, 574, 268, 128	3.9	2.9	4.8	3.2
$^{115}\text{Sb}$	31.0 m	3.0	2750, 528	5.6	4.3	7.0	4.8
$^{114}\text{Sb}$	3.3 m	6.3		2.1	1.7	2.5	1.7
$^{22}\text{Na}$	2.6 y	2.8	1275	24.6	0.0	26.5	0.0

Note: y = years; d = days; h = hours; m = minutes; s = seconds; EC = electron capture.

Table 13-2  
 Example Isotopes Produced in Apollo Na I Crystals by the Cosmic Ray Flux

Isotope	Half-Life	Major Features		Cross Section at 1.6 GeV (mbarn)	Decay Rates ( $\text{Min}^{-1}$ ) After 9 d in Flight	
		$\beta^+$ continuum endpoint (MeV)	$\gamma$ -ray peaks (keV)		from cosmic rays	from secondary neutrons
$^{126}\text{I}$	13.02 d	$\beta^+$ 2.14 $\beta^-$ 1.25	1452, 698, EC	57.2	14.4	146.0
$^{124}\text{I}$	4.18 d	3.16	1357, 635	24.4	12.5	129.5
$^{123}\text{I}$	13.2 h		191	17.7	12.5	
$^{119}\text{Te}$	15.9 h		1790, 730, 675	10.5	13.9	
$^{117}\text{Te}$	61.0 m	3.5	750	8.4	11.1	
$^{119}\text{Sb}$	38.0 h		53	15.7	27.9	
$^{117}\text{Sb}$	2.8 h		187	17.5	20.3	
$^{116}\text{Sb}$	15.0 m	4.6	1322, 989	9.2	13.5	
$^{116\text{m}}\text{Sb}$	60.0 m	4.6	2929, 1867, 1634, 1089, 673, 574, 268, 128	9.2	6.1	
$^{115}\text{Sb}$	31.0 m	3.0	2750, 528	19.4	12.9	
$^{111}\text{In}$	2.83 d		443, 273, 198	15.2	13.0	
$^{110}\text{In}$	69.1 m	3.93	684	7.1	4.7	

Table 13-2 (continued)  
 Example Isotopes Produced in Apollo Na I Crystals by the Cosmic Ray Flux

Isotope	Half-Life	Major Features		Cross Section at 1.6 GeV (mbarn)	Decay Rates ( $\text{Mo}^{-1}$ ) After 9 d in Flight	
		$\beta^+$ continuum endpoint (MeV)	$\gamma$ -ray peaks (keV)		from cosmic rays	from secondary neutrons
$^{110}\text{In}$	4.9 h		3210, 2510, 2230, 1570, 911, 684	7.1	4.7	
$^{24}\text{Na}$	15.0 h	$\beta^-$ 4.17		0.0	0.0	30.2
Example light fragments						
$^{20}\text{F}$	11.03 s	$\beta^-$ 7.03		7.6	6.6	
$^{18}\text{F}$	109.8 m	1.66		9.1	8.5	
$^{15}\text{O}$	122.2 s	2.76		7.5	6.0	
$^{16}\text{N}$	7.1 s	$\beta^-$ 10.42		4.9	3.9	
$^{12}\text{B}$	0.02 s	$\beta^-$ 13.37		3.7	3.3	
$^8\text{Li}$	0.844 s	$\beta^-$ , $\alpha$ 16.1		2.7	1.9	
$^6\text{He}$	0.802 s	$\beta^-$ 3.51		9.3	14.5	

Note: y = years; d = days; h = hours; m = minutes; s = seconds; EC = electron capture.

**Table 13-3**  
**Major Radioactive Isotopes Produced in Germanium by Trapped Radiation**

Isotope	Half-Life <sup>a</sup>	End Point of $\beta^-$ Continuum (MeV)	Prominent Lines (keV)	Number Produced per 1000 Interactions
<sup>76</sup> As	26.5 h	$\beta^-$ 2.97		2.07
<sup>74</sup> As	17.9 d	$\beta^-$ 1.36, $\beta^+$ 2.56	607	14.9
<sup>73</sup> As	80.3 d		EC (11.1)	37.3
<sup>72</sup> As	26.0 h	$\beta^+$ 4.36	641, 797, 846, 905 1061, 1476, 2091, 2212, 2251, 2519, 2921, 3011, 3751	35.0
<sup>71</sup> As	62.0 h	$\beta^+$ 2.01	186	40.9
<sup>70</sup> As	52.0 m	$\beta^+$ 6.24	611, 681, 761, 921, 1051, 1131, 1261, 2041	15.7
<sup>69</sup> As	15.0 m	$\beta^+$ 3.9		
<sup>75</sup> Ge	82.0 m	$\beta^-$ 1.20		12.0
<sup>71</sup> Ge	11.4 d		EC (10.4)	53.1
<sup>69</sup> Ge	38.0 h	$\beta^-$ 2.225	EC, 330, 583, 798, 882, 1117	24.6
<sup>68</sup> Ge	275.0 d		EC(10,4)	11.4
<sup>67</sup> Ge	19.0 m	$\beta^+$ 4.4		3.6

Table 13-3 (continued)  
Major Radioactive Isotopes Produced in Germanium by Trapped Radiation

Isotope	Half-Life <sup>a</sup>	End Point of $\beta^-$ Continuum (MeV)	Prominent Lines (keV)	Number Produced per 1000 Interactions
<sup>75</sup> Ga	2.0 m	$\beta^-$ 3.30		0.97
<sup>74</sup> Ga	7.9 m	$\beta^-$ 5.60		3.29
<sup>73</sup> Ga	4.9 h	$\beta^-$ 1.55		8.98
<sup>72</sup> Ga	14.1 h	$\beta^-$ 4.00		21.3
<sup>70</sup> Ga	21.1 m	$\beta^-$ 1.66		32.5
<sup>68</sup> Ga	68.3 m	$\beta^+$ 2.92	EC(9.7), 1088	40.9
<sup>67</sup> Ga	78.0 h		EC, 101, 195, 216, 306, 398	31.4
<sup>66</sup> Ga	9.4 h	$\beta^+$ 5.175	1049, 2758	19.2
<sup>65</sup> Ga	15.2 m	$\beta^+$ 3.26	125, 162, 216, 760	10.0
<sup>64</sup> Ga	2.6 m	$\beta^+$ 7.07		1.66
<sup>72</sup> Zn	46.5 h	$\beta^-$ 0.45		0.51
<sup>71m</sup> Zn	4.0 h	$\beta^-$ 2.91		0.93
<sup>71</sup> Zn	2.4 m	$\beta^-$ 2.61		0.93
<sup>69m</sup> Zn	13.8 h		439	3.65
<sup>69</sup> Zn	57.0 m	$\beta^-$ 0.90		3.65
<sup>65</sup> Zn	245.0 d	$\beta^+$ 1.35	EC (9.0), 1124	21.6

Table 13-3 (continued)  
Major Radioactive Isotopes Produced in Germanium by Trapped Radiation

Isotope	Half-Life <sup>a</sup>	End Point of $\beta^-$ Continuum (MeV)	Prominent Lines (keV)	Number Produced per 1000 Interactions
<sup>63</sup> Zn	38.4 m	$\beta^+$ 3.366	EC 678, 971	4.2
<sup>62</sup> Zn	9.3 h	$\beta^+$ 1.69	EC 51, 519, 599	1.28
<sup>64</sup> Cu	12.8 h	$\beta^-$ 0.57, $\beta^+$ 1.68	EC(8.3)	6.0
<sup>62</sup> Cu	9.8 m	$\beta^+$ 3.94	EC	6.7
<sup>61</sup> Cu	3.32 h	$\beta^+$ 2.24	EC, 76, 292, 388, 538, 663, 948, 1158, 1198	2.80
<sup>58m</sup> Co	9.0 h		25	1.3
<sup>58</sup> Co	71.3 d	$\beta^+$ 2.309	818, 872, 1682	0.65

<sup>a</sup>Isotopes with half-lives of less than 1 minute are not included.

**Note:** y = years; d = days; h = hours; m = minutes; s = seconds; EC = electron capture.

Table 13-4  
Major Radioactive Isotopes Produced in Germanium Under Cosmic Ray Bombardment

Isotopes	Half-Life	Endpoint of $\beta^-$ Continuum (MeV)	Prominent Lines (keV)	Cross Section at 1.6 GeV (mbarn)	Decay Rate $\text{Min}^{-1}$ at Saturation
$^{75\text{m}}\text{Ge}$	48.0 s		139	2.7	2.0
$^{75}\text{Ge}$	82.0 m	$\beta^-$ 1.2		2.7	4.0
$^{73\text{m}}\text{Ge}$	0.53 s		54, 13.5, 67.5	11.9	15.60
$^{71\text{m}}\text{Ge}$	20.0 m		23, 175, 198	12.3	9.2
$^{71}\text{Ge}$	11.4 d		EC (10.4)	12.3	18.4
$^{69\text{m}}\text{Ge}$	5.1 $\mu\text{s}$		85	7.1	5.3
$^{69}\text{Ge}$	38.0 h	$\beta^+$ 2.225	EC, 330, 583, 798, 882, 1117	7.1	10.6
$^{68}\text{Ge}$	275. d		EC (10.4)	6.4	4.8
$^{73}\text{Ga}$	4.9 h	$\beta^-$ 1.55		9.0	6.7
$^{72\text{m}}\text{Ga}$	0.036 s		99	5.4	4.0
$^{72}\text{Ga}$	14.1 h	$\beta^-$ 4.0		5.4	8.1
$^{70}\text{Ga}$	21.1 m	$\beta^-$ 1.66		16.8	12.6
$^{68}\text{Ga}$	68.3 m	$\beta^+$ 2.92	EC (9.7), 1088	23.1	22.1
$^{67}\text{Ga}$	78.0 h		EC, 101, 195, 216, 306, 398	20.7	15.5
$^{66}\text{Ga}$	9.4 h	$\beta^+$ 5.175	1049, 2758	13.3	9.9

Table 13-4 (continued)  
Major Radioactive Isotopes Produced in Germanium Under Cosmic Ray Bombardment

Isotopes	Half-Life	Endpoint of $\beta^-$ Continuum (MeV)	Prominent Lines (keV)	Cross Section at 1.6 GeV (mbarn)	Decay Rate $\text{Min}^{-1}$ at Saturation
$^{65}\text{Ga}$	15.2 m	$\beta^+$ 3.26	125, 162, 216, 760	7.4	5.5
$^{69\text{m}}\text{Zn}$	13.8 h		439	5.7	4.3
$^{69}\text{Zn}$	57.0 m	$\beta^+$ 0.901		5.7	8.6
$^{67\text{m}}\text{Zn}$	9.3 $\mu\text{s}$		93	4.3	18.7
$^{65\text{m}}\text{Zn}$	1.6 $\mu\text{s}$		54	13.4	15.5
$^{65}\text{Zn}$	245. d	$\beta^+$ 1.349	EC (9.0), 1124	13.4	26.5
$^{63}\text{Zn}$	38.4 m	$\beta^+$ 3.366	EC 678, 971	7.4	5.5
$^{64}\text{Cu}$	12.8 h	$\beta^-$ 0.573, $\beta^+$ 1.678	EC (8.3)	9.6	7.2
$^{62}\text{Cu}$	9.8 m	$\beta^+$ 3.94	EC	12.3	9.2
$^{61}\text{Cu}$	3.32 h	$\beta^+$ 2.236	EC, 76, 292, 388, 588, 663, 948, 1158, 1198	7.6	5.7
$^{58\text{m}}\text{Co}$	10.6 $\mu\text{s}$		80	4.7	3.5
$^{58\text{m}}\text{Co}$	9.0 h		25	4.7	7.0
$^{58}\text{Co}$	71.3 d	$\beta^+$ 2.300	818, 872, 1682	4.7	10.5
$^{57}\text{Co}$	270. d		22, 129, 143	9.9	7.4
$^{55}\text{Fe}$	2.6 y		EC(6.5)	9.8	7.3
$^{54}\text{Mn}$	303. d		841	11.2	8.4

Table 13-4 (continued)  
Major Radioactive Isotopes Produced in Germanium Under Cosmic Ray Bombardment

Isotopes	Half-Life	Endpoint of $\beta^-$ Continuum (MeV)	Prominent Lines (keV)	Cross Section at 1.6 GeV (mbarn)	Decay Rate $\text{Min}^{-1}$ at Saturation
$^{51}\text{Cr}$	27.8 d		EC (5.5), 325	10.0	7.5
$^{49}\text{V}$	330. d		EC(5.0)	10.3	7.7
$^{48}\text{V}$	16.00 d	$\beta^+$ 4.013	950, 988, 1317, 2246, 2300, 3229, 3245	4.6	3.4
$^{44\text{m}}\text{Sc}$	2.44 d		271	2.4	1.8
$^{44}\text{Sc}$	3.92 h	$\beta^+$ 3.647	1160	2.4	3.6
$^{28}\text{Al}$	2.31 m	$\beta^-$ 4.635		5.4	4.0
$^7\text{Bc}$	53.0 d		478	12.2	9.1
$^6\text{He}$	0.8 s	$\beta^-$ 3.510		8.1	6.1
				$\Sigma = 343.5$	$\Sigma = 347.5$

Note: y = years; d = days; h = hours; m = minutes; s = seconds; EC = electron capture.

active species produced in NaI, CsI, and Ge by cosmic rays and inner belt protons.

Secondary neutrons are produced as a result of primary charged particle interactions with the detector and surrounding materials. Both fast and thermal neutron interactions can produce significant induced radioactivity in  $\gamma$ -ray detectors. The relative effect of cosmic ray primary and secondary neutron interactions for Apollo  $\gamma$ -ray measurements are shown in Figure 13-3a. These effects dominated over the induced activity produced by passage through the Earth radiation belts (Trombka et al., 1976; Dyer et al., 1975b).

The background produced by a given nuclear species depends on the decay mode. In those cases where the  $\gamma$ -ray emission is preceded by a charged particle decay, the energy loss spectra will be observed as the sum of the charged particle and  $\gamma$ -ray energy loss, since, in terms of the detection system, these decays are simultaneous. Theoretical calculations of the pulse-height spectra observed as a result of the decay of  $^{124}\text{I}$  and  $^{24}\text{Na}$  in a NaI detector are shown in Figure 13-4 and Figure 13-5.  $^{124}\text{I}$  is a neutron-deficient nuclide. The line features can be attributed to the electron capture decay branch. Positron emission followed by  $\gamma$ -ray decay produces the underlying continuum. In the case of a neutron-rich nuclide such as  $^{24}\text{Na}$ , electrons' emission always precedes the  $\gamma$ -ray decay; thus, only a continuum is observed (see Figure 13-5).

A method of calculation for assessing the magnitude and spectral shape of induced activity in a  $\gamma$ -ray detector has been developed. The method is described in detail in Dyer et al. (1980). Induced activity in the Apollo  $\gamma$ -ray spectrometer and OSO-7  $\gamma$ -ray detector are considered in detail. The contribution of primary cosmic ray particles, trapped particles, and their secondaries depends on the flight parameters, the detector type and geometry, and the size of the spacecraft.

### **Atmospheric and Planetary Surface $\gamma$ -Ray Interactions**

Multiple scattered  $\gamma$ -ray radiation contributed about 80 percent of the background for the measurement made near the lunar surface. The magnitude of this effect was discussed in an earlier section and is shown in Figure 13-2.

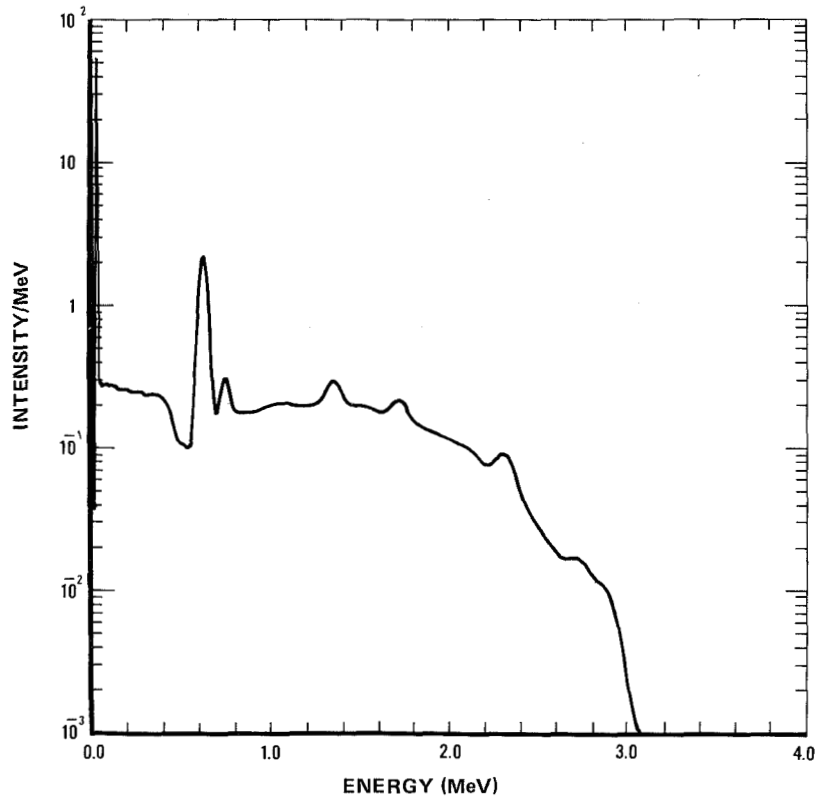


Figure 13-4. Computed response function for  $^{124}\text{I}$  decay inside the Apollo 7  $7\text{ cm} \times 7\text{ cm}$  NaI(Tl) crystal. The underlying continuum results from several  $\beta^+$  branches, while the line features result from electron capture modes.

For experiments onboard spacecraft in Earth orbit or near planetary bodies with atmospheres, charged and neutral particle interactions will produce discrete line  $\gamma$ -ray emission. Natural radioactive elements in the atmosphere are a further source of discrete line  $\gamma$ -ray emission. Multiple scattering of these  $\gamma$ -rays

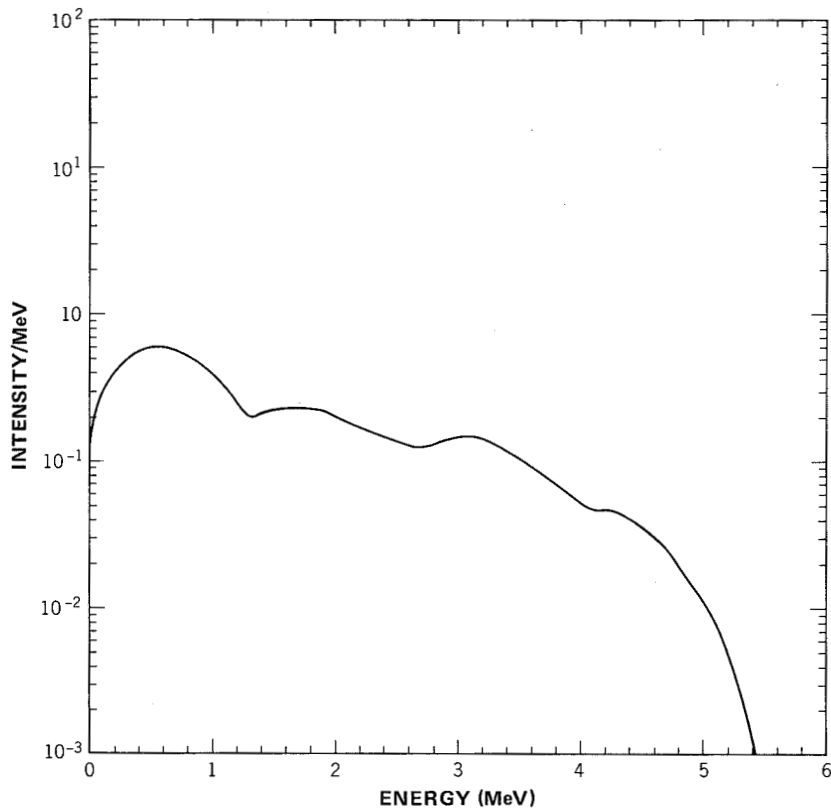


Figure 13-5. Computed response function for  $^{24}\text{Na}$  decay inside the Apollo 7 cm  $\times$  7 cm Na I (Tl) crystal. The continuum results from  $\beta^-$  spectra shifted by coincidence with one or more emitted  $\gamma$ -rays.

and annihilation radiation produce a continuum and a 0.511 MeV line. In Earth orbit the background will be modulated by the longitudinal and latitudinal variations in the magnetic fields and the variations in the trapped radiation belts, which change the exciting particle flux. Details of studies of terrestrial atmospheric  $\gamma$ -rays can be found in Daniel and Stephens (1974), Kinzer et al.

(1974), Thompson (1974), Lichti et al. (1975), Ling (1975), Imhof et al. (1976), and Ryan et al. (1977).

### **Diffuse or Cosmic $\gamma$ -Rays**

The diffuse  $\gamma$ -ray spectrum was discussed in Chapter 9. The pulse-height spectrum of this component as measured by the Apollo  $\gamma$ -ray spectrometer is shown in Figure 13-3b.

Table 13-5 summarizes the contribution of the various background components measured during translunar flight by the Apollo  $\gamma$ -ray spectrometer.

### **Background in High Energy $\gamma$ -Ray Detector**

In the high energy  $\gamma$ -ray region where the pair production process dominates and a picture-type device is normally used (as described in Chapter 12) the background in a well designed  $\gamma$ -ray telescope is very low. Since the electron pair is actually seen,  $\gamma$ -rays from unacceptable directions may be eliminated by analysis of the pair, and in the case of an unusual set of signals from counters that are not associated with a  $\gamma$ -ray, but still triggers the picture chamber, the event will be rejected in the subsequent pictorial analysis. It is also true that in such a satellite telescope the rate of these "false triggers" is not high enough to have a significant effect on the live time of the instrument.

The background problem then reduces to the small number of  $\gamma$ -rays in an acceptable solid angle which results from charged particles interacting in the small amount of material composing the light cover and thermal blanket above the anticoincidence dome and, at the same time, not producing any charged particles which enter the anticoincidence system. These events are indeed rare because the great majority of the primary particles, which must be reasonably energetic to produce the  $\gamma$ -ray in the first place, lead to at least one charged particle and usually several which enter the anticoincidence dome. Although both are rare, the two most likely types of interactions which can lead to the  $\gamma$ -ray coming from an interaction in the overlying material without an anticoincidence signal are as follows: (1) a grazing incidence primary whose narrow cone of secondaries also does not enter the anticoincidence dome and from which there are no

**Table 13-5**  
**Composition of Apollo Spectrum (percentage contribution)**

Energy (MeV)	Spacecraft		Bremsstrahlung		Neutron		Cosmic Ray		Discrete Lines		Cosmic	
	A15	A16	A15	A16	A15	A16	A15	A16	A15	A16	A15	A16
0.4-0.8 . . . . .	18	15	12	19	12	11	12	11	15	16	31	27
0.8-2.0 . . . . .	15	13	14	23	9	8	28	24	11	12	22	20
2.0-5.0 . . . . .	20	17	19	30	6	5	33	29	3	3	19	17
5.0-10.0 . . . . .	40	33	26	42	0	0	11	10	0	0	23	16

**Note:** A15 is Apollo 15; A16 is Apollo 16.

wide angle charged secondaries and yet there is still a very wide angle  $\gamma$ -ray in the telescope acceptance angle, and (2) an approximately vertical primary charged particle for which there is charge exchange and for which there are no forward moving charged secondaries and there is a high energy  $\gamma$ -ray. Calculations can be performed to estimate the number of  $\gamma$ -rays produced in this way from the known cosmic ray intensity and trapped particle background. The calculations are long, but reasonably accurate, and they may be verified by exposing the  $\gamma$ -ray telescope to high energy particle beams from accelerators. The background level is most relevant in comparison to the weak diffuse celestial radiation, which it is desired to measure. Figure 13-6 shows such a

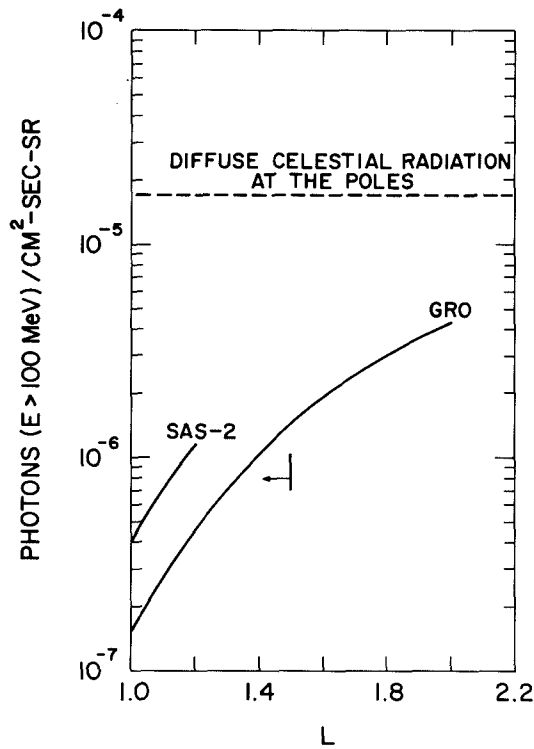


Figure 13-6. Comparison of calculated background  $\gamma$ -radiation for the planned GRO high energy  $\gamma$ -ray telescope as a function of the geomagnetic coordinate  $L$ , with the diffuse celestial radiation at the galactic poles for  $E > 100$  MeV. A similar curve for the SAS-2 instrument, which is supported by calibration results using high energy protons, is shown for comparison. GRO should spend about 85 percent of its time at  $L$  values less than 1.5.

comparison for the SAS-2  $\gamma$ -ray telescope, which had the lowest background level of any high energy  $\gamma$ -ray satellite telescope flown thus far, and for the planned GRO high energy  $\gamma$ -ray telescope.

## REFERENCES

- Berger, M. J., and Seltzer, S. M., 1972, *Nucl. Instr. and Meth.*, **104**, 317.
- Blok, H. P., DeLange, J. C., and Schotman, J. W., 1975, *Nucl. Instr. and Meth.*, **128**, 545.
- Bowman, W. W., 1971, *Nucl. Instr. and Meth.*, **96**, 135.
- Carpenter, B. S., D'Agostino, M. D., and Yule, H. P., ed., 1979, *Computers in Activation Analysis and Gamma-Ray Spectroscopy*, DOE Symposium Series 49, CONF 780421, NTIS, (Springfield, Va.: U.S. Dept. of Commerce, 1979).
- Daniel, R. R., and Stephens, S. A., 1974, *Rev. Geophys. Space Phys.*, **12**, 233.
- Dyer, C. S., Trombka, J. I., Metzger, A. E., Seltzer, S. M., Bielefeld, M. J., and Evans, L. G., 1975a, *Proc. of the 14th Int. Cosmic Ray Conf.*, **1**, 2.
- Dyer, C. S., Trombka, J. I., Schmadebeck, R. L., Eller, E., Bielefeld, M. J., O'Kelley, G. D., Eldridge, J. S., Northcutt, K. J., Metzger, A. E., Reedy, R. C., Schonfeld, E., Seltzer, S. M., Arnold, J. R., and Peterson, L. E., 1975b, *Space Sci. Instr.*, **1**, 279.
- Dyer, C. S., Trombka, J. I., Seltzer, S. M., and Evans, L. G., 1980, *Nucl. Instr. and Meth.*, **173**, 585.
- Gunnink, R., and Niday, J. B., 1972, "Computerized Quantitative Analysis by Gamma-Ray Spectrometry" Program GAMANAL, UCRL-51061, vols. 1-4.
- Harrington, T. M., Marshall, J. H., Arnold, J. R., Peterson, L. E., Trombka, J. I., and Metzger, A. E., 1974, *Nucl. Instr. and Meth.*, **118**, 401.
- Imhof, W. L., Nakano, G. H., and Reagan, J. B., 1976, *J. Geophys. Res.*, **81**, 2835.

- Kinzer, R. L., Share, G. H., and Seeman, N., 1974, *J. Geophys. Res.*, **79**, 4567.
- Lichti, G., Moyano, C., and Schönfelder, V., 1975, *Proc. 14th Int. Cosmic Ray Conf.*, **4**, 1423.
- Linden, D. A., 1959, *Proc. IRE*, **47**, 39.
- Ling, J. C., 1975, *J. Geophys. Res.*, **80**, 3241.
- Metzger, A. E., and Trombka, J. I., 1972, *Proc. National Symposium on Natural and Manmade Radiation in Space*, ed. E. A. Warman, NASA TM X-2440.
- Mills, S. J., 1970, *Nucl. Instr. and Meth.*, **81**, 217.
- Phillips, G. W., 1979, *Computers Activation Analysis and Gamma-Ray Spectroscopy*, in B. S. Carpenter, M. D. D'Agostino, and H. P. Yule, eds., CONF-780421; (Springfield, Va.: U.S. Dept. of Energy, Technical Information Center, 1979), p. 197.
- Phillips, G. W., and Marlow, K. W., 1976, *Nucl. Instr. and Meth.*, **137**, 525.
- Robinson, D. C., 1970, *Nucl. Instr. and Meth.*, **78**, 120.
- Routti, J. T., and Prussin, S. G., 1969, *Nucl. Instr. and Meth.*, **72**, 25.
- Ryan, J. M., Dayton, B., Moon, S. H., Wilson, R. B., Zych, A. D., and White, R. S., 1977, *J. Geophys. Res.*, **82**, 3593.
- Seltzer, S. M., 1975, *Nucl. Instr. and Meth.*, **127**, 293.
- Slavić, I. A., and Bingulac, S. P., 1970, *Nucl. Instr. and Meth.*, **84**, 261.
- Teegarden, B. J., McDonald, F. B., Trainor, J. H., Webber, W. R., and Roelof, E. C., 1974, *J. Geophys. Res.*, **79**, 3615.

- Thompson, D. J., 1974, *J. Geophys. Res.*, **79**, 1309.
- Trombka, J. I., 1962, "On the Analysis of Gamma-Ray Pulse Height Spectra," Ph.D. Dissertation, University of Michigan.
- Trombka, J. I., and Schmadebeck, R. L., 1968, *A Numerical Least-Square Method for Resolving Complex Pulse Height Spectra*, NASA Report SP-3044, 170.
- Trombka, J. I., Dyer, C. S., Evans, L. G., Bielefeld, M. J., Seltzer, S. M., and Metzger, A. E., 1971, *Ap. J.*, **212**, 925.
- Trombka, J. I., Metzger, A. E., Arnold, J. R., Matteson, J. L., Reedy, R. C., and Peterson, L. E., 1973, *Ap. J.*, **181**, 737.
- Trombka, J. I., Eller, E. L., Schmadebeck, R. L., Dyer, C. S., Reedy, R. C., Barr, D. W., Gilmore, J. S., Prestwood, R. L., Bayhurst, B. P., Perry, D. G., Smith, A. E., Cordi, R. C., Pehl, R. H., Eldridge, J. S., Schonfeld, E., and Metzger, A. E., 1976, *ASTP Preliminary Science Report*, NASA TMX-58173.
- Trombka, J. I., Schmadebeck, R. L., Bielefeld, M. J., Evans, L. G., Metzger, A. E., Haines, E. L., Dyer, C. S., Seltzer, S. M., Reedy, R. C., and Arnold, J. R., 1979, *Computers in Activation Analysis and Gamma-Ray Spectroscopy*, B. S. Carpenter, M. D. D'Agostino, and H. P. Yule, eds., CONF-780421; (Springfield, Va.: U.S. Dept. of Energy, 1979), Technical Information Center, p. 26.
- Varnell, L., and Trischuck, J., 1969, *Nucl. Instr. and Meth.*, **76**, 109.

# **PART VI**

# **THE FUTURE**

## ***Chapter 14***

## ***Prospects for Gamma Ray Astronomy***



## Chapter 14

# Prospects for Gamma Ray Astronomy

In the previous chapters, it has been illustrated that  $\gamma$ -ray astronomy is moving from the discovery phase to the exploration phase and that the rich promise of  $\gamma$ -ray astrophysics noted by theorists in the late 1940's and 1950's is becoming a reality. Gamma rays have now been "seen" from the Sun, solar system bodies, compact galactic objects, the interstellar medium, and active galaxies. Also detected has been a diffuse radiation of possible exceptional cosmological significance, low energy  $\gamma$ -ray bursts of unknown origin, and a high energy  $\gamma$ -ray source with no obvious counterpart at other wavelengths.

Looking first at the future prospects for the study of the solar system, the Solar Maximum Mission (SMM) currently in orbit should add substantially to our knowledge of discrete solar  $\gamma$ -ray lines before the end of its life. However, there are no present plans to perform solar  $\gamma$ -ray observations during the period of solar minimum. The next major effort for studying  $\gamma$ -ray emission from the Sun is likely to be undertaken during the next solar maximum period at the end of the 1980's and beginning of the 1990's. Large area, detection systems with good energy and time resolution should be used. At that time,  $\gamma$ -ray imaging capable of spatial resolution of the order of 10 arcminutes or better should be available for at least the softer  $\gamma$ -ray region. The results obtained by the Gamma Ray Experiment (GRE) aboard the SMM spacecraft will significantly influence future designs of solar  $\gamma$ -ray systems.

In the first two decades of solar system exploration with spacecraft, close-up observations of Mercury, Venus, Mars, Jupiter, Saturn, and the Moon have been made, and our understanding of the solar system has been revolutionized. A remarkable and complex picture of the planets and their satellites is beginning to emerge from planetary observations. For example, Venus has a very dense and hot atmosphere, whereas Mars has a very rarified atmosphere. In both cases, carbon dioxide ( $\text{CO}_2$ ) is the major constituent of the atmosphere, instead of nitrogen as in the case of the Earth. On the other hand, Titan has an atmosphere with about as much nitrogen as the Earth. The Galilean satellite, Io, has an atmosphere of ionized sodium. Mars has giant volcanoes larger than any on Earth, while the Moon has large basalt-filled maria. Yet neither Mercury, Mars, nor the Moon have developed plate tectonic features such as appear on the Earth. Meteorite impacts seem to have played a universal role in shaping the surface of the terrestrial planets and satellites, particularly early in their history. Gamma ray observations made during planetary missions have made significant contributions to our understanding the evolution and dynamics of our solar system.

The U.S. planetary probe, Galileo, has been approved for flight in the 1980's. The Galileo program will investigate the environment of Jupiter and study the Galilean satellites in detail. ESA is planning the Giotto program involving a flyby of Halley's Comet. There are no plans to include  $\gamma$ -ray spectrometers aboard these space probes. The Soviets plan to continue their Venera program to Venus, with plans for the Venera spacecraft to fly past Halley's Comet on its way to Venus. A  $\gamma$ -ray spectrometer aboard the Venera spacecraft will perform measurements of the Venus surface, and an X-ray fluorescence spectrometer is planned to be included on-board in order to perform elemental analysis of collected samples.

Plans for comet and asteroid rendezvous missions, as well as Mars, Mercury, and Moon orbiters, are presently under consideration for flight during the later part of the 1980's and early part of the 1990's. Both remote sensing and close-observation  $\gamma$ -ray spectrometer systems are being considered for such missions. The experience gained during the United States Apollo program and Soviet Luna, Mars, and Venera programs indicate

that high energy-resolution detectors would be highly desirable on such future flight missions. A number of balloon flights and the HEAO-C mission have demonstrated the feasibility of flying such systems on planetary space probes. Soft  $\gamma$ -ray imaging systems to study hard X-ray and soft  $\gamma$ -ray emissions produced by solar wind interactions in the Comet and planet environment are also being developed.

Turning to  $\gamma$ -ray astrophysics beyond the solar system, it has been noted at several points in the book that the next steps would greatly enhance our knowledge of several different astrophysical phenomena. These include: (1) the dynamic, evolutionary processes associated with neutron stars and black holes, as well as with  $\gamma$ -ray-emitting objects whose nature is still a mystery; (2) possible direct evidence of nucleosynthesis, the elemental building process in nature; (3) exploration of our galaxy in the  $\gamma$ -ray range with particular regard to regions difficult to observe at other wavelengths; (4) the origin and dynamic pressure effects of the cosmic rays; (5) study of high energy particles and energetic processes in other galaxies, especially radio galaxies, Seyfert galaxies, and quasars; and (6) cosmological clues including direct evidence bearing on the matter-anti-matter symmetric big bang theory and on primordial black hole emission.

Experimentally these astrophysical goals require a set of large individual experiments that may advantageously be combined into a substantial Shuttle-launched free-flying spacecraft. These instruments should have the capability to survey high energy  $\gamma$ -ray sources and diffuse emission with energy resolution around 15 percent and point-source sensitivity of  $10^{-7}$  photon  $\text{cm}^{-2} \text{s}^{-1}$ , and better off the galactic plane, and with about 5 to 10 arcmin angular resolution on strong sources. For low energy  $\gamma$ -rays the energy resolution should be similar and the sensitivity approximately  $10^{-5}$  photon  $\text{cm}^{-2} \text{s}^{-1}$  or better. Nuclear  $\gamma$ -lines need to be identified, at a sensitivity level of the order of  $10^{-5}$  photon  $\text{cm}^{-2} \text{s}^{-1}$  or better in order to analyze the interstellar medium and supernova shells. Gamma ray bursts require instruments able to study spectral and temporal behavior, as well as to locate the sources as well as possible. The technology now exists to build the appropriate instruments, and development has progressed to the point where construction of flight units can occur.

The Gamma Ray Observatory (GRO) mission, which would achieve these goals, is now being undertaken by NASA. An artist drawing of an early concept of GRO is shown in Figure 14-1. GRO will be placed into orbit around the Earth by the Space Shuttle at an altitude of about 400 kilometers. The observatory would be expected to have an active life in space of about two years. The results will have important bearing on most of the astrophysical problems discussed in this book.

Before GRO, there will be GAMMA I, which was described in Chapter 12. The improved sensitivity and  $\gamma$ -ray directional accuracy, relative to satellites that have already flown, should allow better definition of the characteristics of the galactic plane and provide better position information on many of the localized excesses already observed, as well as possibly adding to the number of observed extragalactic sources.

The missions to be launched in the mid-1980's when combined with the satellites close to the Earth including GRO should provide a powerful long baseline network for the accurate location of the low energy  $\gamma$ -ray bursts. The Venera series and possible planetary, cometary, or asteroidal satellites can contribute to this network in an important way. The long baselines available in this network together with the already existing accurate timing should provide substantially improved position determinations, which should clearly identify the objects from which these bursts come if they are in fact clearly seen at other wavelengths. In addition, the presently planned GRO burst detector will be able to observe time variations down to 0.1 ms for strong sources and to detect spectral variations on relatively short time scales. These observations will allow the study of models of emission mechanisms and source geometry in detail.

As mentioned earlier, at extremely high energies (above about  $10^5$  MeV), photons are detected by instruments at sea level which record the Čerenkov light produced in the atmosphere from a series of interactions initiated by a single incident  $\gamma$ -ray. Improved detector systems of this type should be forthcoming in the 1980's. The search for additional very high energy  $\gamma$ -ray sources and the measurement of their properties including the time history and at least some spectral information is of fundamental importance in understanding the processes in nature which can lead to greater than  $10^{11}$  eV  $\gamma$ -rays.

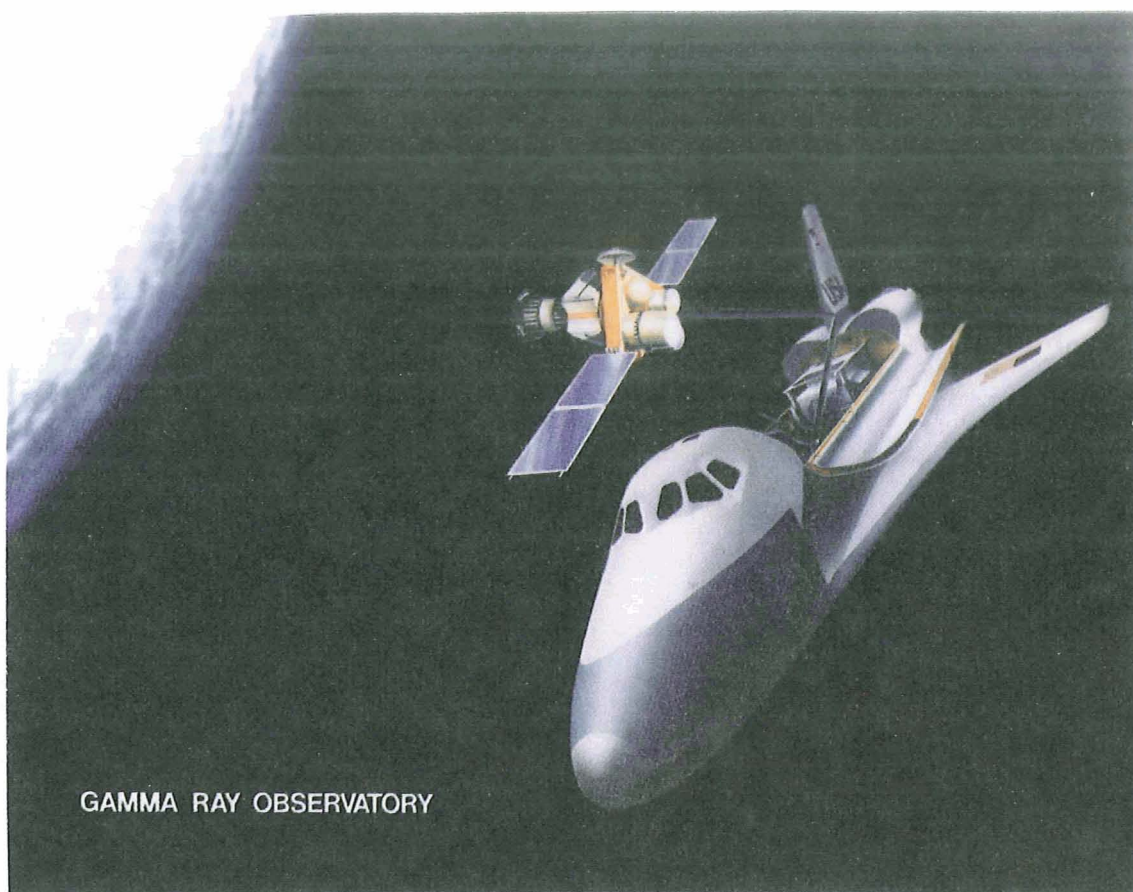


*Figure 14-1. Artist's rendition of an early concept of the Gamma Ray Observatory (photo courtesy of the National Aeronautics and Space Administration).*

We have seen that  $\gamma$ -ray astronomy offers an entirely new look at our galaxy and the universe. It is a young, growing science, developed to the point that its potential for fundamental contributions to astronomy and astrophysics in the near future is large. With the study of cosmic  $\gamma$ -rays, the forces of change, the formative processes in the galaxy and interstellar clouds, rapid expansion processes, explosions, the largest energy transfers, very high energy particle acceleration, and even the fundamental process of the creation of elements are all directly examined. From the results that will be obtained, a new insight into creation and evolution will be realized, as well as a better understanding of the ways in which the universe is continually changing.



## List of Symbols

The following list of symbols is intended to include all of those which are commonly used throughout the book. Symbols peculiar to an individual subject are defined in the chapter in which they are used and are not necessarily listed here.

<p><math>A</math> Atomic Mass Number</p> <p><math>\text{\AA}</math> Angstrom (<math>10^{-8}</math> cm)</p> <p><math>B</math> Magnetic Flux Density</p> <p><math>b</math> Galactic Latitude</p> <p><math>\beta</math> Reduced Velocity (<math>v/c</math>)</p> <p><math>c</math> Velocity of Light</p> <p><math>\chi</math> Goodness of Fit Parameter</p> <p><math>\times</math> Pair Production Interaction Cross Section</p> <p><math>d</math> Days</p> <p><math>E</math> Kinetic Energy</p> <p><math>e</math> Electronic Charge</p> <p><math>\&amp;</math> Photon Energy</p> <p><math>\epsilon</math> Efficiency</p> <p><math>f</math> Frequency</p> <p><math>g</math> Grams</p> <p><math>H_0</math> Hubble Constant</p> <p><math>h</math> Planck Constant</p> <p>Hours</p> <p><math>\hbar</math> <math>h/2\pi</math></p> <p><math>I</math> Moment of Inertia</p> <p><math>J</math> Intensity [<math>t^2 t^{-1} \Omega^{-1}</math>]</p> <p><math>j</math> <math>dJ/d\&amp;</math> [<math>t^{-1} \Omega^{-1} \&amp;^{-1}</math>]</p> <p><math>l</math> Galactic Longitude</p> <p>Mean Free Path</p> <p><math>\lambda</math> Wavelength</p> <p><math>M</math> Mass of an Object</p> <p>Particle Mass (except electron)</p>	<p><math>m</math> Electron Mass</p> <p>Minutes</p> <p><math>\mu</math> Linear Absorption Coefficient</p> <p><math>\mu_m</math> Mass Absorption Coefficient</p> <p><math>N</math> Number Density</p> <p><math>n</math> Neutron</p> <p><math>\nu</math> Frequency</p> <p><math>P</math> Pulsar Period</p> <p><math>p</math> Proton</p> <p><math>\Phi</math> Particle Flux [particles <math>t^{-2} t^{-1}</math>]</p> <p><math>Q</math> Source Strength [(photons or energy) <math>t^{-1}</math> or (photons or energy) <math>t^{-1} t^{-3}</math>]</p> <p><math>q</math> Source Function [(photons or energy) <math>t^{-3} t^{-1} \&amp;^{-1}</math>]</p> <p><math>q_0</math> Deceleration Parameter</p> <p><math>R</math> Range</p> <p><math>r</math> Radial Distance</p> <p><math>\rho</math> Mass Density</p> <p><math>s</math> Seconds</p> <p><math>T</math> Temperature</p> <p><math>t</math> Time</p> <p><math>\tau</math> Characteristic Time</p> <p>Photoelectric Cross Section</p>
---	---

$\sigma$	Microscopic Cross Section	$v$	Particle Velocity
	Standard Deviation	$\omega$	Angular Velocity
	Compton Interaction	$W$	Atomic Weight
	Cross Section	$X$	Depth [ $(m t^2)$ ]
$\Omega$	Solid Angle	$X_0$	Radiation Length
	Angular Frequency	$Y$	Years
	Cosmological Density	$Z$	Charge
	Parameter		Atomic Number
$U$	Total Energy	$z$	Red-Shift Parameter
$V$	Volume	$\odot$	Solar (as subscript)
	Pulse Height or Energy		
	Loss		

## Subject Index

### Absorption

- atmosphere, 306, 307
- coefficient, *see* Cross sections
- Compton interaction, 305, 313, 313, 315; *see also* Cross sections
- pair production, 170, 305, 307, 312, 315, 332; *see also* Cross sections
- photoelectric effect, *see* Cross sections

Acceleration, 113, 132, 133, 142, 145

### Activation

- cosmogenic (by cosmic ray), *see* Nuclear  $\gamma$ -ray lines
- measurements of OSO, Apollo 17, Apollo-Soyuz, *see* Background components
- nuclear activation by neutrons, *see* Nuclear  $\gamma$ -ray lines
- of CsI, NaI, and Ge, *see* Background components
- of spacecraft, *see* Background components

Alpha backscatter experiment, *see* Surveyor

Analysis of digital spectra, *see* Pulse height and digital spectra

Andromeda galaxy (M31), 168

### Annihilation, 67-73

- matter, antimatter, 67, 100, 106, 170, 197-198, 208, 209
- positronium, 68-73
- singlet state, 71-73
- triplet state, 71-73
- see also* Cross sections

Anticoincidence shield, 307, 309, 316; *see also* Detectors

Apollo 15 and 16  
 diffuse spectrum measurement, 204, 209  
 gamma ray burst, 149, 150, 151

Background components (detector), 50  
 atmospheric and planetary surface  $\gamma$ -ray interactions, 50, 373, 374-375  
 cosmic ray and trapped particle interactions, 50, 204, 306, 307, 321, 356, 358, 377  
 cosmic ray and trapped induced activation in detector, 50, 204, 356, 360-363, 374, 374-375, 375, 377, 360  
 electron bremsstrahlung, 356, 357, 377  
 high energy  $\gamma$ -ray detector, 321  
 natural radioactivity, 356, 357, 359, 377  
 spacecraft component, 356, 357, 359, 377

Balloons (large scientific), 7, 306, 309, 310, 311

Big bang model, 187, 197, 198, 203, 208-210, 218, 219, 387

Blackbody radiation, 103, 104, 188, 215

Black holes, 5, 8, 107, 143-146, 168, 170, 173, 174, 176, 203, 218, 387

BL lacertae objects, 165, 168, 178-180, 213 215

Bremsstrahlung  
 background source, *see* Background components  
 nonthermal electron, 84, 85, 99, 101, 102, 103, 217, 314  
 thermal electron, 150

Broadening (of spectral lines), *see* Doppler shift

Carbon-12  
 excited states and  $\gamma$ -ray emissions (4.4 MeV and 15.11 MeV lines), 67, 68, 82, 84, 87, 88, 89, 91, 108, 290, 291

Centaurus A, *see* Radio galaxies

Čerenkov, 9, 218, 306, 307, 308, 312, 315, 316, 317, 319, 328

- Compton  
 gamma ray production, 100, 101, 103, 105, 112, 116, 123, 124, 169, 170, 173, 175, 215, 217  
 gamma ray absorption, 305, 313, 313, 315  
*see also* Cross sections
- Compton scattering, 67, 84, 264; *see also* Cross sections, Response functions, and Detector efficiencies
- Compton telescope, *see* Detectors
- COS-B, 7, 113, 114, 118-119, 119, 120, 121, 134, 135, 137, 138 147, 147, 148, 178, 310, 317, 320, 321, 321, 322, 327, 328, 329, 331
- Cosmic rays  
 activation by, cosmogenic, 38, 39-42  
 distribution in galaxy, 110-113  
 gamma ray background, produced by, 306, 356-373  
 galactic  $\gamma$ -ray production, 99-107, 116, 121, 123, 124, 167  
 general, 4, 99-105, 110-113, 121-124, 140, 142, 143, 166, 167, 192, 193, 203, 217, 218, 312, 315, 387  
 interactions, 5, 33, 99-107, 140, 142, 143, 312  
 production of  $\gamma$ -ray by  $\pi$ -meson secondaries, 99  
*see also* Nuclear  $\gamma$ -ray lines and Neutrons
- Cosmological red shift, 67, 174, 190-195, 198, 211, 212
- Cosmology, 187-199, 204, 208, 209, 211, 213
- Crab nebula, 8, 9, 133, 135, 136, 137, 138, 139, 143, 312
- Cross sections  
 bremsstrahlung, 102, 103, 105, 230, 231, 244, 245  
 Compton, 103-105, 230, 231, 234-239, 240, 242-244, 247  
 definitions (mass, linear, electronic, energy loss, radiation length, and range), 229, 230, 231, 232  
 ( $e^+$ ,  $e^-$ ) annihilation, 233, 241, 248  
 energy scattering by Compton process, 242-244, 294-295  
 pair production, 230, 231, 233, 234-239, 240, 241, 242, 248, 313, 313  
 $\pi^0$ -meson production, 100-101, 105  
 photoelectric, 230, 232, 233, 234-239, 248  
*see also* Detector efficiency

Cygnus, 121, 144, 146, 147, 147, 312

#### Detectors

- alkali-hallide scintillation counters, 247
- angular resolution, 324-329
- background in, *see* Background components
- Čerenkov counters, 218, 307, 308, 312, 316, 319, 322, 324, 328, 388
- Compton telescope, 292-295
- efficiency, 274-286
- energy, resolution of, 254-256, 261-263, 314, 324, 328-330
- gamma ray spectrometers, *see* OSO, Apollo, Ranger, Mars, Venera, SMM, HEAO/C
- Ge(Li) and Ge(HP) spectrometers, 247, 257-264
- high energy, 305-333
- lixiscope (Low Intensity X-Ray Scope), 297-298
- NaI(Tl) scintillators, 247, 248, 287, 288 289, 307, 308, 308, 324, 329, 330, 333
- nuclear emulsions, 307
- phoswitch, 288
- photomultiplier tube, 251-254
- plastic scintillator, 234, 248, 287, 288, 307, 308, 316, 322-323
- radiation damage, 285-287
- response function (NaI(Tl) and Ge), 264-274, 373-375, 374, 375
- solid state (band theory), 248-250, 258-261, 263-264
- spark chambers, 308, 309, 310, 316-324, 330, 332, 333
- time-of-flight system, 324
- X-rays, 386
- see also* Apollo, COS-B, OSO-3, OSO-7, SAS-2, and SMM

Doppler shift, 67, 68, 71, 73, 74, 84

Electrons, 99, 100, 102-105, 107, 123, 124, 145, 169, 170, 192, 198, 217, 207, 313, 314, 315, 326, 330

Electron-positron annihilation, 100, 106, 107, 170, 198, 315; *see also* Annihilation

Elementary particles, 100, 197, 198, 208

Energy loss, 138, 139, 247, 314, 337

Galaxies, 5, 6, 7, 8, 165-180, 193, 203, 210-217, 219, 385  
active, 168-180, 192, 210-217, 219, 385  
local, 166-168  
spiral, 8, 108, 165, 168, 171  
*see also*, BL lacertae objects, Magellanic clouds, Quasars, Radio galaxies,  
and Seyfert galaxies

GAMMA-I, 310, 316, 322, 328, 388

Gamma ray bursts, 131, 145, 148-152, 287, 388

Gamma ray lines, *see* Nuclear  $\gamma$ -ray lines, Annihilation, and Natural radio-  
activity

Gamma Ray Observatory (GRO), 310, 316, 319, 322, 323, 327, 328,  
329, 330, 331, 332, 378, 379, 388, 389

Gamma ray remote sensing, *see* Apollo, Luna, Mars, and Ranger

Ge(Li) spectrometers, *see* Detectors

Helium nuclei, 100, 106, 110, 188

High Energy Astronomical Observatory (HEAO), 289, 291, 359

Hubble Parameter ( $H$ ), 187, 188, 190-194, 195, 197

Hydrogen, 100, 107-110, 124, 167, 195, 205, 206  
capture line (2.223 MeV), 5, 84, 91

Interstellar matter, 107-110

Interstellar magnetic field, *see* Magnetic fields

Jupiter, 360, 386

K-mesons, 100

Lifetime of cosmic rays, 111

Lithium drift germanium, *see* Detectors Ge(Li)

Luna 10 and 11, 8, 49, 288

Lunakhod, 9

Magellanic clouds, 152, 167, 168

Magnetic bremsstrahlung, *see* Synchrotron radiation

Magnetic fields  
galactic, 99, 111, 112, 113  
pulsars, 133

Mars, 8, 50, 386

Mars 4 and 5, 9, 26, 50

Moon, 8, 26, 386

Neutrons  
albedo, 27, 82  
capture, *see* Nuclear  $\gamma$ -ray lines  
inelastic scatter, *see* Nuclear  $\gamma$ -ray lines  
secondary (from cosmic rays), 33, 82  
solar flare processes, 67, 82, 89, 91

Neutron stars, 8, 132-140, 148, 387

NGC 4151, *see* Seyfert galaxies, NGC 4151

Nuclear  $\gamma$ -ray lines, 8, 67, 68, 105-107, 141, 142, 387  
activation, 43-46, 48, 75  
inelastic scatter (charged and neutral particles), 38, 39-42, 67, 68, 74-82  
natural radioactivity, 32, 34-35  
prompt capture (charged and neutral particles), 38, 43-46, 67, 68, 74, 75, 76, 77-82  
spallation, 74, 76, 77-81

Nucleosynthesis, 107, 140, 141, 387

OSO-3, 7, 113, 204, 308

OSO-7, 86, 87, 88

Oxygen 16  
excited states of (6.12 MeV and 15.11 MeV lines), 68, 82, 84, 87, 88, 90

398 *GAMMA RAY ASTROPHYSICS*

Pair production, 170, 264, 290, 305, 307, 312, 313, 313, 315, 332; *see also*  
     Cross sections and Detectors

Photoelectric effect, *see* Cross sections and Detectors

$\pi^+$ -mesons, 68, 100, 106, 145, 197

$\pi^0$ -mesons, 67, 68, 77, 85, 86, 99, 100, 101, 145, 197, 324

Pin hole camera, *see* URA

Positrons, 68-73, 84, 100, 106, 170, 198, 307

Positronium, *see* Annihilation

Pulsars, 8, 131, 132-140, 146

Pulse height and digital spectra
     compensation from gain shift and zero drift, 346-347
     discrete line analysis, 352-355
     methods of measurements derived from information theory, 339
     relationship to photon spectrum 337-341
     transformation method, 339-346, 349-352

Quasars
     general, 165, 168, 174, 176-178, 211-213, 214, 387
     3C273, 169, 176-178, 210, 211

Radio galaxies
     general, 165, 168, 169, 173-174, 175, 387
     CEN-A, 9, 169, 173-174, 175, 176, 210, 312

Radioactive capture, *see* Nuclear  $\gamma$ -ray lines

Radioactivity, *see* Nuclear  $\gamma$ -ray lines

Ranger, 8, 49, 50, 289

Red shift, 171, 174, 190-195, 198, 211, 212

SAS-2, 113, 115, 116, 117, 120, 121, 134, 137, 138, 139, 140, 147, 148,  
     173, 179, 204, 206, 209, 215, 309, 309, 310, 317, 319, 320-323, 328,  
     329, 331, 378, 379

Scintillation detectors, *see* Detectors

Seyfert galaxies

general, 165, 168, 169, 171-173, 176, 210, 211, 212, 387  
NGC 4151, 169, 171-173, 210, 211

Solar flares, 67-91

conclusions regarding  $\gamma$ -ray observations, 88, 89, 90-91  
gamma ray productions, *see* Nuclear  $\gamma$ -ray lines, Annihilation  
Neutron production, *see* Neutrons  
specific flares, 86, 87, 88, 89, 90-91

Solrad, 27

SMM (Solar Maximum Mission), 89-91, 385

Gamma Ray Experiment (GRE), 89-91, 289-293

Solar system evolution, 20-23, 25-26, 49, 54, 58-62

Nebular movestic, 5, 20-21  
Planetesimal, dualistic, 20-21

Solid state detectors, *see* Detectors

Spallation, 38, 47; *see also* Cross sections and Nuclear  $\gamma$ -ray lines

Spectra (specific), 57, 88, 101, 103, 104, 120, 137, 147, 150, 351

Supernovae, 6, 107, 113, 133, 140-143, 148, 152

Surveyor, 8

$\alpha$ -backscatter experiment, 8, 50

Synchrotron radiation, 4, 84, 100, 101, 105, 111, 114, 133, 169, 173, 175

21-cm line, 4, 108, 114, 124, 204, 215, 216

Uniform Redundant Array (URA), 296, 297

Vela pulsar, 8, 9, 133, 134, 135, 136, 139, 143

Venera 8, 9, and 10, 9, 26, 50, 386

Venus, 50, 51, 386; *see* Venera

Viking, 9

X-ray fluorescence spectrometer, 50

X-rays

general, 133, 135, *136*, *137*, 144, 146, *147*, 147, 149, *150*, 169,  
170, 171, 173, 174, *175*, 176, 178, *179*, 180, 203, 210, 211, 212,  
213, 215, 216, 217, 218

emission from the moon, planets, comets, and asteroids, 26, 27,  
28, 29, 30, 31, 32

X-ray remote sensing spectrometers, *see* Apollo, SMM, and Viking

